UNIVERSITY OF ASTON IN BIRMINGHAM

A STUDY OF THE SCATTERING OF FAST NEUTRONS IN LARGE SAMPLES

Thesis submitted for the Degree of

Doctor of Philosophy

by

Sattar P.T. Anvarian, B.Sc., M.Sc.

Department of Physics

June 1982

A STUDY OF THE SCATTERING OF FAST NEUTRONS IN LARGE SAMPLES

Thesis for Degree of Ph.D.

by

Sattar P. T. Anvarian

The University of Aston in Birmingham

SUMMARY

In the present work, the elastic scattering of fast neutrons from iron and concrete samples were studied at incident neutron energies of 14.0 and 14.4 Mev, using a neutron spectrometer based on the associated particle time-of-flight technique. These samples were chosen because of their importance in the design of fusion reactor shielding and construction.

Using the S.A.M.E.S. accelerator and the 3 M v Dynamitron accelerator at the Radiation Centre, 14.0 and 14.4 Mev neutrons were produced by the T(d, n)^{4}He reaction at incident deuteron energies of 140 keV and 900 keV mass III ions respectively. The time of origin of the neutron was determined by detecting the associated alpha particles. The samples used were extended flat plates of thicknesses up to 1.73 mean free paths for iron and 2.3 mean free paths for concrete. The associated alpha particles and fast neutrons were detected by means of a plastic scintillator mounted on a fast focused photomultiplier tube.

The differential neutron elastic scattering cross-sections were measured for 14 Mev neutrons in various thicknesses of iron and concrete in the angular range from zero to 90°. In addition, the angular distributions of 14.4 Mev neutrons after passing through extended samples of iron were measured at several scattering angles in the same angular range. The measurements obtained for the thin sample of iron were compared with the results of Coon et al. The differential cross-sections for the thin iron sample were also analyzed on the optical model using the computer code RAROMP. For the concrete sample, the angular distribution of the thin sample was compared with the cross-sections calculated from the major constituent elements of concrete, and with the predicted values of the optical model for those elements. No published data could be found to compare with the results of the concrete differential cross-sections. In the case of thick samples of iron and concrete, the number of scattered neutrons were compared with a phenomological calculation based on the continuous slowing down model. The variation of measured cross-sections with sample thickness were found to follow the empirical relation $\sigma = \sigma_o e^{\alpha x}$. By using the universal constant "K", good fits were obtained to the experimental data.

In parallel with the work at 14.0 and 14.4 Mev, an associated particle time-of-flight spectrometer was investigated which used the ^{2}H(d,n)^{3}He reaction for 3.02 Mev neutron energy at the incident deuteron energy of 1 Mev.

Key words: Neutron/Elastic Scattering/Cross-sections/Extended Samples/ Iron and Concrete

SA/AJC/AEC
10.5.1982

ACKNOWLEDGEMENTS

I would like to express my deep gratitude to Dr. A.J. Cox my supervisor, for his continued help and guidance throughout the research project. I wish to acknowledge Professor S.E. Hunt, the Head of Physics Department, for his interest in this project. I also wish to thank Dr. P.N. Cooper of the Nuclear Physics group for many valuable discussions during this work.

I also wish to thank the University of Tabriz and the Ministry of Science and Higher Education of Iran for providing part of the research grant.

I wish to thank Mr. T. Kennedy and the secretarial staff and Miss L. Riding for their assistance. Thanks are also due to Mr. J. Phull of the Nuclear Research Laboratory and Mr. F. Lane and other staff of the physics workshop for their help.

I wish to acknowledge the Radiation Centre staff for their assistance. I also wish to thank Miss A. Clarke for her excellent typing of the present thesis.

I am very grateful to my mother and all of my family for their moral and financial support throughout the project.

Finally, I wish to express my gratitude to my wife, Pari, and my son and daughter, for their moral support, patience and understanding throughout the whole project.

S.P.T. Anvarian

University of Aston in Birmingham

1982

LIST OF CONTENTS

CHAPTER THREE

NEUTRON AND CHARGED PARTICLE DETECTION

CHAPTER FIVE

DIFFERENTIAL CROSS-SECTION MEASUREMENTS

LIST OF TABLES

LIST OF FIGURES

CHAPTER ONE

CHAPTER ONE

GENERAL INTRODUCTION

1.1 INTRODUCTION

The mechanism of nuclear interactions and nuclear structure can be investigated by the scattering of a nuclear particle with a nucleus. It has been found that experimental values of the differential cross-sections for elastic scattering of fast neutrons by nuclei can provide considerable information concerning the neutron nucleus interaction.

Systematic observations of nuclear reactions over a wide range of nuclei and energies are of interest from the point of view of pure nuclear physics and applied physics. Specifically fast neutron elastic scattering data are frequently requested for the purpose of reactor core and shielding design.

The demand for scattering information for the development of nuclear theory, ie the study of the differential cross-section of fast neutrons scattered in materials of different thicknesses is of interest both from the point of the theory of neutron passage through matter and from the point of view of shielding calculations for fusion reactors. Also the nuclear performance of the blanket and shield in a fusion reactor will have a substantial impact on the overall operation of reactor. Therefore, it is necessary to have experimental verification of the nuclear data that will be used to carry out the nuclear design calculations. The experimental results provide the necessary data for calculating and selecting shielding materials, since both the average distance travelled by neutrons before absorption and the number of elastic collisions required to lose a given fraction of initial energy is a function of the angular dependence of the scattering cross-sections.

In the design of an experiment it is sometimes necessary to collimate and shield from the fast neutrons. A knowledge of the differential

cross-sections and spectrum of neutrons transmitted through materials is required to optimize the design of composite sheilds.

In the present work measurements are made on the scattering of 14.0 and 14.4 Mev neutrons by different thicknesses of Iron and Concrete, as these measurements are important for construction of fusion reactors.

The experimental procedure and theoretical results are given in the following sections.

1.2 THEORIES OF NUCLEAR REACTIONS

1.2.1 The Statistical Compound Nucleus Theory

According to wave mechanics the neutron is treated as a wave instead of a rigid sphere. The interaction between the incoming neutron and the nucleus is represented by a finite complex potential. According to Bethe[1] the neutron sees the nucleus as an attractive potential well with specified depth and radius. Elastic scattering and transmission can be explained using the concept of the potential well. However, Bethe[1] showed that this theory in its original form, was unable to account for the variation of cross-sections with energy, capture cross-sections and the wide spacing of resonances.

The observation of very sharp resonances at very low neutron energies was an additional problem. In order to explain these resonances and other features of nuclear reactions Bohr[2] proposed the compound nucleus theory which has been extremely useful in the interpretation of nuclear reactions.

According to this theory, the nuclear reaction takes place in two stages:

(1) The incident particle is absorbed by the target nucleus, giving away all its energy in collisions with the nucleons of the target. The incident particle becomes part of the target nucleus, and a compound nucleus thus formed.

(2) The compound nucleus disintegrates by ejecting a particle or a γ-ray leaving the resultant nucleus in an excited state.

If the emitted and incident nucleons are the same, and the residual nucleus is returned to its ground state, then the process is known as *compound elastic scattering* or sometimes *resonance elastic scattering*. On the other hand, if the emitted particle leaves the residual nucleus in an excited state the process is called *compound inelastic scattering*.

As in compound nucleus theory, the energy of the incident particle is shared among the nuclear particles before re-emission can occur, the decay of the compound nucleus is independent of the way in which it was formed, depending only on the quantum parameters of the system, i.e. energy, and angular momentum.

One of the most serious failures of the compound nucleus theory is its inability to account for the large scale energy dependance of the total neutron cross-section. However, for a certain class of reaction such as (n, n'), (n, p) and (n, α) induced by high energy neutrons in medium-weight nuclei, it remains the most complete and easily accessible description of the reaction.

As a replacement for the compound nucleus model Weisskopf[4, 5] proposed a model in which nuclear reactions proceed in three stages:

(A) An *independent-particle stage*, in which the bombarding particle retains its identity and interaction with the target nucleus as a whole.

(B) A *compound-system stage*. This stage contains all the processes which produce the absorption.

(C) A *final stage*, in which the reaction products separate from each other. The independent stage can be represented by what is usually referred to as the *optical model*. The description of this model is given in detail in section (1.2.3)

The statistical model of compound nucleus formation is particularly

applicable to isotopes of medium to high mass number. The excitation energy of the compound nucleus which is just the incident neutron energy plus the binding energy of the captured neutron, is then great enough so that the conditions of the statistical model apply.

This model is not able to explain, the forward peaking shown by the elastic scattering at higher energies, nor did it make any provision for any dependence of the nuclear forces on spin, specifically spin-orbit coupling. Under these conditions, it can be shown that the predictions of the statistical model correspond to the particles and nuclei involved having zero spin.

The cross-section for neutron interaction that involve the compound nucleus as an intermediate state can be written as [3]:

$$\sigma_S(E_C) = \sigma_{CN}(E_C) \frac{\Gamma_n}{\Gamma} \qquad \ldots\ldots (1.1)$$

where Γ_n = the Neutron width, gives the probability per unit time that the state decays by neutron emission.

Γ = total width, i.e. sum of the probabilities for all possible processes.

$\frac{\Gamma_n}{\Gamma}$ = Is the relative probability that the compound nucleus decays by the emission of a neutron.

and $\sigma_{CN}(E_C)$ = the cross-section for the formation of the compound nucleus.

In general, the cross-section for the formation of the compound nucleus by an incident neutron of energy E is given by Hauser and Feshbach[6] as:

$$\sigma_c = \sum_{\ell} (2\ell + 1)\, \pi \lambda\!\!\!^{-2}\, T_\ell(E) \qquad \ldots\ldots (1.2)$$

where σ_c = the cross-section for incoming particle waves of angular momentum ℓ.

$\lambda\!\!\!^{-}$ = the wave length of the incoming neutron

and $T_\ell(E)$ = the transmission coefficient or penetration factor for the target nucleus for waves of this ℓ and $\lambda\!\!\!^{-}$.

1.2.2 Direct Reaction Theory

Many different types of nuclear reaction have been explained by the compound nucleus theory. This model is predominant at lower neutron energies. However, in the energy range $10 < E < 20$ Mev, the angular distribution of the emitted particles can be explained by the direct interaction mechanism. On the basis of this theory, the reaction is assumed to take place without the formation of the intermediate compound nucleus state.

For high bombarding energies or for light nuclei, excitation of a single particle in the target nucleus may occur as a result of direct interaction between the incident neutron and a single nucleon in the target nucleus.

The characteristic of direct interactions are:

(i) Emission of excess particles of high energy in comparison with the number expected according to the statistical theory.

(ii) Forward peaking of the higher energy particles of the emission spectrum.

The theory of direct interaction assumes that in a reaction process the first event is a collision between the incident particle and a nucleon near the surface of the target nucleus. If a mean free path of the order of nuclear dimensions is assumed, the struck nucleon may emerge from the nucleus without the formation of a compound nucleus and the direct process is complete.

At higher energies, the direct interaction processes do not show the

sharp resonances of the compound nucleus model, the resonances are broad, and the number of high energy particles emitted is much higher than expected from the compound nucleus theory.

1.2.3 The Optical Model

In the general account of nuclear reactions, it has been shown that both direct and compound nucleus processes can contribute to any reaction. As the energy rises, the compound elastic cross-section rapidly becomes negligible compared with the direct cross-sections. For energies below 10 Mev the direct interaction model is unable to account for the nature of the isotropic distributions of the differential cross-section measurements. However, the behaviour of cross-sections were not entirely explained by these models.

To explain the variation of cross-sections at different energies, Fernbach, Serber and Taylor[7] proposed the optical model, in which the nucleus was not considered to be totally absorbing, but only partially absorbing and partially refracting to the wave associated with incident neutron. This model is an intermediate position between the compound nucleus model with its high absorption and the shell model with its weak absorption. The optical model introduced the simplification that, the interaction between an incident nucleon and the individual nuclear constituents cna be represented by a two body potential.

In order to take account for both scattering as well as absorption, the interaction potential is represented as:

$$U_{OPT}(r) = U_R(r) + i\,W_I(r) + V_{SO}(r) \qquad \ldots\ldots (1.3)$$

where $U_R(r)$ = the real central potential

$W_I(r)$ = the imaginary potential

and $V_{SO}(r)$ = the spin orbital potential

The real central potential which is almost always taken to have the form: $- V_R f(r, R, a)$ with:

$$f(r, R, a) = [1 + \exp (\frac{r - R}{a})]^{-1} \quad \ldots\ldots (1.4)$$

is the *Woods-Saxon* form factor [8]. The imaginary potential has been taken to have a volume form, a surface form, or a mixture of surface and volume terms. The spin-orbit potential is generally taken to have the Thomas form. The forms of the above potentials are given in Section(6.2).

The real part of the potential accounts for the scattering and the imaginary part explains absorption.

This model has been proved to be applicable to a variety of incident particles, particularly neutrons and protons. Using this model, the observed resonances in the cross-section at various mass numbers, as a function of energy can be predicted as can, the forward peaking of the neutron differential elastic scattering cross-section at higher energies.

In general the relation between the total cross-section (σ_T), the shape elastic cross-section (σ_{SE}) and the reaction cross-section (σ_R) can be written as:

$$\sigma_T = \sigma_{SE} + \sigma_R \quad \ldots\ldots (1.5)$$

where σ_R arises mainly from the presence of the imaginary potential. The experimentally observed elastic scattering cross-section is the sum of σ_{SE} and σ_{CE} i.e.

$$\sigma_E = \sigma_{SE} + \sigma_{CE} \quad \ldots\ldots (1.6)$$

where σ_{CE} is the compound elastic cross-section.

However, for incident neutron energies above 6 MeV, compound elastic scattering is negligible, hence equation (1.5) and (1.6) give:

$$\sigma_T = \sigma_{SE} + \sigma_R = \sigma_E + \sigma_R \quad \ldots\ldots (1.7)$$

This model enables the differential cross-section $\sigma(\theta)$ and the quantities in equation (1.7) to be calculated.

1.3 NEUTRON INTERACTION WITH MATTER

The interactions of neutrons as a result of its lack of charge are different from the interaction of charged particles with matter. They are not affected by the electrons in the atom or by the positive charge of the nucleus. As a result, neutrons pass through the atomic cloud, and interact directly with the nucleus. Thus the interactions of neutrons with the nucleus depend only on the distribution of nuclear matter within the nucleus, on the neutron energy and on the matter through with which they interact. The principle interactions of neutrons with matter are:

(I) Elastic scattering (n, n)

(II) Inelastic scattering (n, n')

(III) Radiative capture (n, γ)

(IV) Absorption with charged particle emission, e.g. (n, p) and (n, α)

(V) (n, 2n) and similar reactions

(VI) Fission, (n, f)

Of the above reactions, only the first two are significant in the present work and are discussed in the next sections.

1.3.1 Elastic Scattering

In elastic scattering, a neutron emerges with the same energy as the incident neutron in the centre of mass system of reference. However,

this means that in the Laboratory system, it may lose a maximum amount of energy:

$$E_{max} = E_o \frac{4Mm}{(M + m)^2} \quad \ldots\ldots (1.8)$$

where m is the mass of the neutron,

and M is the mass of the nucleus under investigation. In this process, the neutron strikes the nucleus, which is almost always in its ground state during the process, which involves only a transfer of kinetic energy between the neutron and the nucleus. Elastic scattering predominates in lighter nuclei. There are two principal mechanisms of elastic interaction:

"*potential scattering*" in which energy of the incident is not shared with other nucleons (i.e. without forming compound nucleus) is scattered, or "*resonance scattering*" in which, the neutron is assimilated by the nucleus which subsequently decays by giving off a neutron with energy equivalent to that carried into the nucleus by the incident neutron.

Standard conservation of energy and momentum equations give the energy of the neutron after the collision as:

$$E' = E_o \frac{A^2 + 2A \cos \phi + 1}{(A + 1)^2} \quad \ldots\ldots (1.9)$$

or, $$E' = \tfrac{1}{2} E_o [(1 + \alpha) + (1 - \alpha) \cos \phi] \quad \ldots\ldots (1.10)$$

where E' = the energy of the scattered neutron,

E_o = the energy of the incident neutron,

$\alpha = (\frac{A - 1}{A + 1})^2$, here, A is the atomic weight of the scatterer.

and ϕ = the angle of scattering in the centre of mass system.

Hence, the relationship between the angle of centre-of-mass (ϕ) and the Laboratory angle (θ) is given by:

$$\cos\theta = \frac{1 + A\cos\phi}{(A^2 + 2A\cos\phi + 1)^{\frac{1}{2}}} \qquad \ldots\ldots (1.11)$$

The energy of scattered neutron at an angle θ in the Laboratory system is given by:

$$E' = \frac{E_o}{(A+1)^2}\left[\cos\theta + (A^2 - \sin^2\theta)^{\frac{1}{2}}\right]^2 \qquad \ldots\ldots (1.12)$$

In collision with heavier nuclei, a neutron loses a fraction of initial energy, so with increasing mass of the struck nucleus, the maximum fractional energy loss in a single collision decreases. However, for light nuclei, e.g. hydrogen, neutron can lose all its energy in one collision.

1.3.2 Inelastic Scattering

When inelastic scattering occurs, the kinetic energy of the incident neutron is divided among the kinetic energy of the emitted neutron, the kinetic energy of the struck nucleus, and the excitation energy of the nucleus. In other words, in an inelastic scattering collision, some of the kinetic energy of the neutron is converted into the excitation energy of the target nucleus, a neutron of lower kinetic energy is then emitted, leaving the target nucleus in an excited state. This excitation energy will be emitted as γ-radiation or the internal conversion, as the nucleus goes to its ground state.

In an inelastic collision, the initial energy of the neutron must exceed the minimum excitation energy of the target nucleus. The threshold energy of neutron which makes inelastic scattering process possible is

given by: [3]

$$E_{th} = \frac{A + 1}{A} \varepsilon_1 \qquad \ldots\ldots (1.13)$$

where E_{th} = inelastic theshold energy,

ε_1 = the energy of a given excited state of the target nucleus

The energy of neutron after inelastic scattering "E′" is given by: [3].

$$E' = \frac{E}{(A + 1)^2} \left(1 + \frac{1}{\gamma^2} + \frac{2 \cos\phi}{\gamma}\right) \qquad \ldots\ldots (1.14)$$

Here $$\gamma = \frac{1}{A}\left[\frac{AE}{AE - (A + 1)\varepsilon}\right]^{\frac{1}{2}} \qquad \ldots\ldots (1.15)$$

where ϕ = angle of scattering in the centre-of-mass system,

E and E'are the laboratory energies of the incident and inelastic neutron respectively,

and ε = energy of the excitation level of the corresponding nucleus.

The angle of emission of the inelastic neutron in the Laboratory and in the centre-of-mass system are related by: [3]

$$\tan\theta = \frac{\sin\phi}{\gamma + \cos\phi} \qquad \ldots\ldots (1.16)$$

where θ = angle in the laboratory system,

ϕ = angle in the centre-of-mass system,

and γ is defined by equation (1.15)

Neutrons which are inelastically scattered by heavy nuclei can undergo large fractional energy losses until they are scattered below the inelastic threshold.

1.4 FUSION REACTORS

1.4.1 Nuclear Fusion Reactions

The production of energy by the nuclear Fusion of light elements represents a vast resource for mankind. In order to make a reactor, reactions must be chosen which have:

(i) a large Q-value, and

(ii) a large cross-section

The most efficient thermonuclear fuel is obviously an equimolar mixture of deuterium and tritium, since this charged particle reaction has the highest known cross-section. From both an economic and a nuclear standpoint, the only practical fuel for a thermonuclear reactor is deuterium and Lithium as the primary fuel. The former is abundant and available as a common isotope of hydrogen which presently known and inferred reserves of Lithium, extractable at present, have a fusion energy content of about 10^3 Q(1Q = 10^{21}j).

From a practical point of view, only the D-D and the D-T reactions have been considered. However, the D-T reaction with an energy output of 17.6 Mev, and a relatively high cross-section of about 5 barns at 110 KeV is much more favourable. The alpha particle carries of 3.5 Mev which is considerable and could constitute a major sources of heating of the fusion plasma. The maximum cross-section for the above reaction occurs at lower energies than the D-D reaction. On the other hand, deuterium which is necessary for this reaction occurs in nature with an abundance of 1 in 6500 atoms, while tritium which is radioactive with a half-life of 12.26 years has to be manufactured. It has, therefore, to be bred via reactions, induced by the neutrons produced by the (D-T) reaction. Neutrons from the thermonuclear reactions could be slowed

down in a suitable moderator containing ^{6}Li (due to its relatively high cross-section for (n,t) reactions):

$$^{6}Li + n \rightarrow {}^{4}_{2}He + {}^{3}_{1}H + 4.6 \text{ Mev} \quad \ldots\ldots (1.17)$$

In the fusion plant itself.

In the case of ^{7}Li with fast neutron, the reaction will be:

$$^{7}Li + n \rightarrow {}^{3}_{1}H + {}^{4}_{2}He - 2.4 \text{ Mev} + n' \text{ (slow)} \quad \ldots\ldots (1.18)$$

The tritium-producing reactions make Lithium an excellent candidate for a major blanket material. For this tritium breeding the plasma volume has to be surrounded by a blanket consisting of Li.

Figures (1.1) and (1.2) show the variation of cross-section via energy for ^{6}Li and ^{7}Li respectively.

1.4.2 Fusion Reactor System

The basic configuration of a fusion reactor is shown in Figure (1.3). All recoverable thermal energy and tritium are produced on the inner blanket. The first wall, and its coolant channel are the most important part of the blanket, because energy densities are highest there. Also, the cooling efficiency of the wall coolant is of major importance, since economic considerations demand the highest possible power densities at the vacuum wall.

The major coolants which have been considered are: molten Lithium fluoride, organic liquids, gases, Lithium Nitrate, water and Lithium beryllium fluoride.

Fused Lithium beryllium fluoride can be used as a coolant material, because of its thermal and radiation stability, and also the use of Be

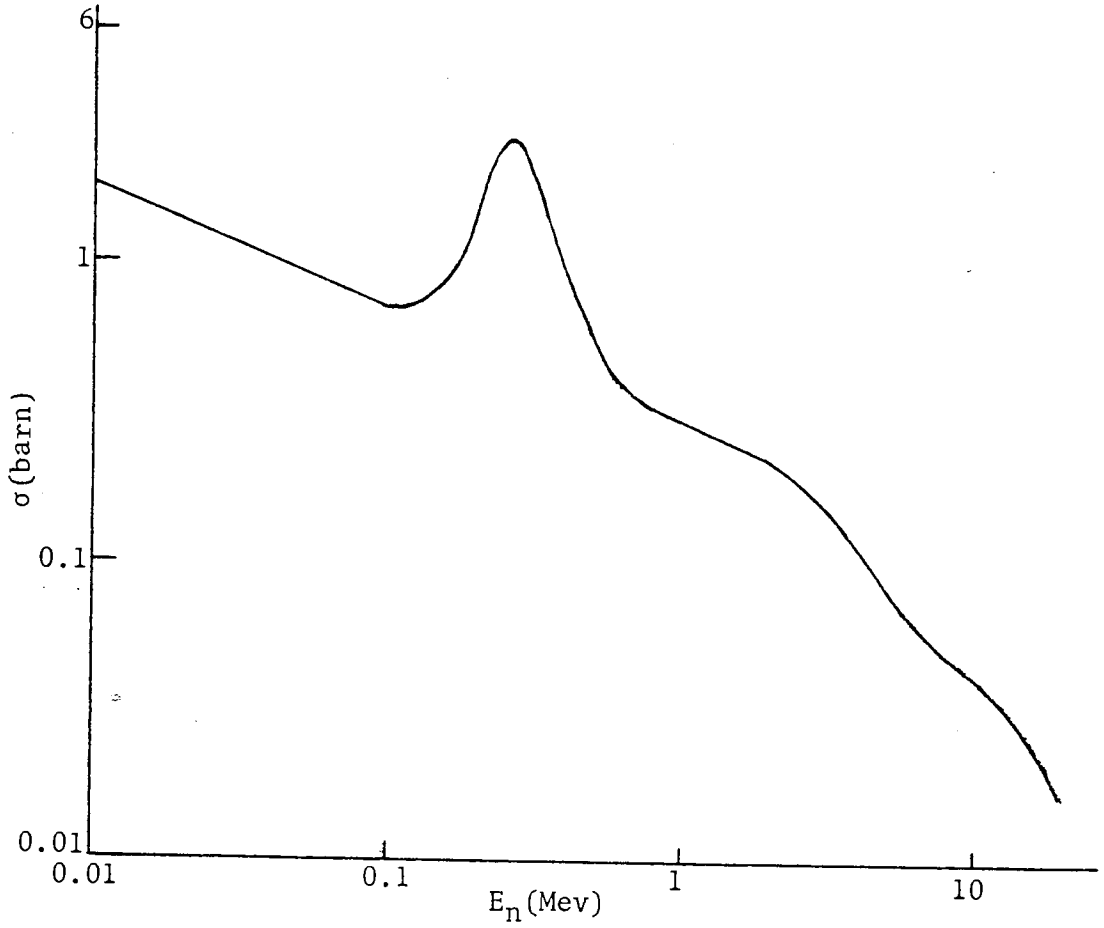

Fig(1.1) $^{6}Li\ (n,t)^{4}_{2}He$ cross-section versus energy[9]

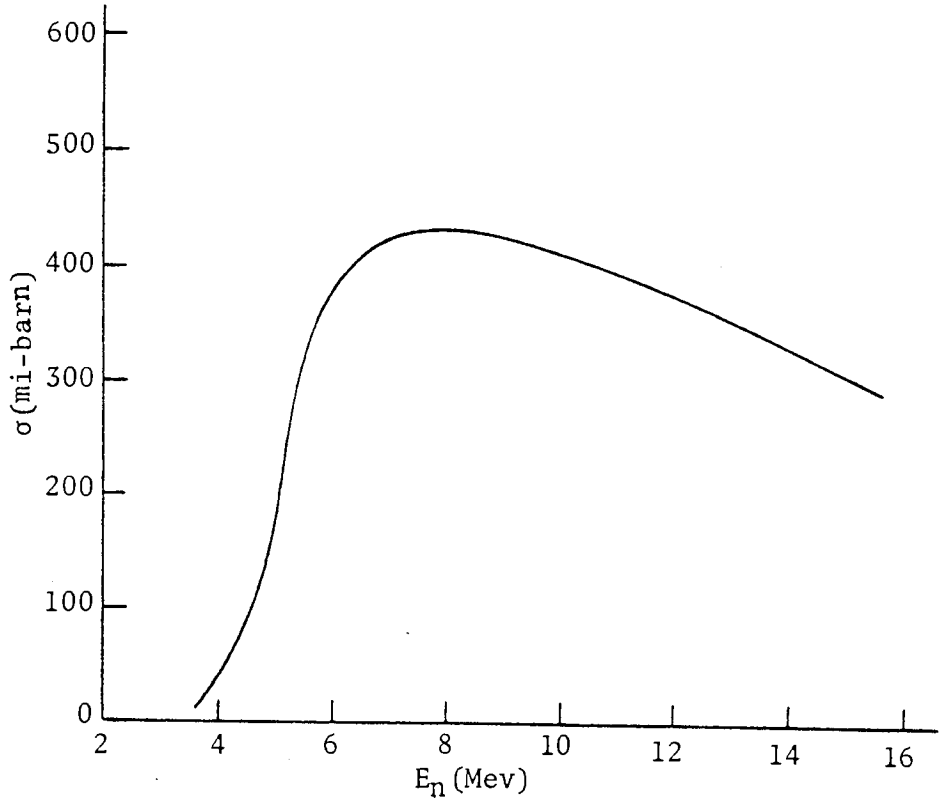

Fig(1.2) $^{7}Li\ (n, tn')^{4}_{2}He$ cross-section versus energy [9]

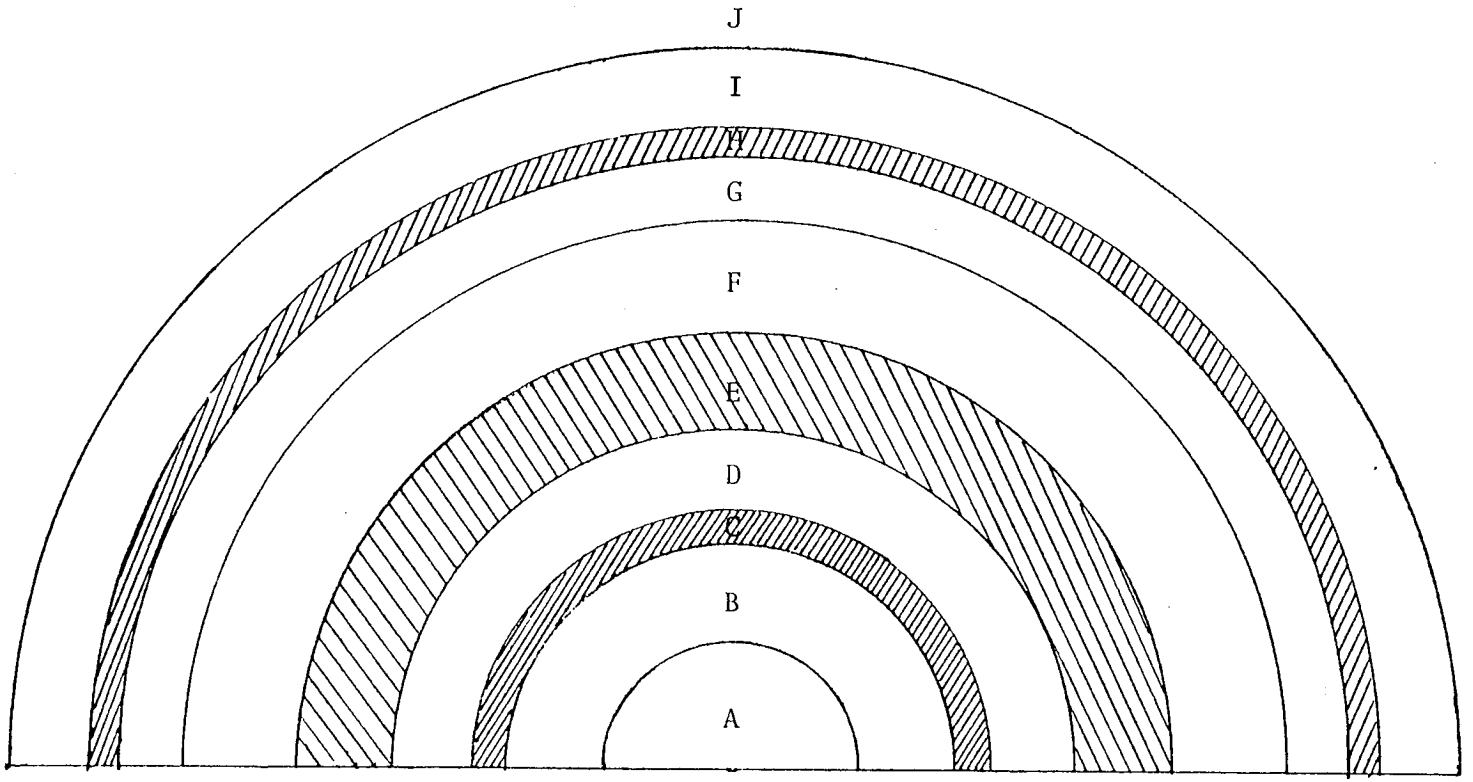

A - plasma 10^8 K°

B - vacuum

C - first wall > 620°C

D - Lithium blanket

E - Graphite

F - Lithium coolant

G - Neutron shielding (water)

H - γ-shield (lead)

I - Super conducting coils 4°K (- 268°C)

J - Biological shield

Figure (1.3) Section of possible fusion reactor [10]

may lead to higher tritium regeneration than use of others. However, because of toxicity problem with Be, usually, molten Lithium fluoride is used as a coolant.

For first wall, materials such as: Niobiom, titanium, molybdenum and steel are most likely to be used. However, molybdenum appears to be the best material, because it has a low vapour pressure, and good mechanical properties at high temperature. Also it provides (n, 2n) multiplication at high neutron energies without serious thermal neutron radiative capture.

As a structural material within the blanket vanadium and Graphite are recommended.

The properties and characteristics of materials which are useful as a γ-ray and neutron shielding for fusion reactor, are discussed in the next section.

1.5 REACTOR SHIELDING

The nuclear reactor is one of the most intense sources of neutrons and γ-radiation available. The problem of reactor shielding is a great deal more complicated than that of shielding a simple source of γ-radiation.

In a reactor the principle sources of radiation are neutrons and gamma radiation, in the core itself, however radioactive coolant flowing in heat exchangers and irradiated fuel elements in storage pits may provide additional sources of gamma radiation. Neutrons passing from the core into the shield produce more gamma radiation as a result of (n, γ) reactions in the shield.

Fast neutron intensities are attenuated by reducing the energy of the neutrons until they are in thermal equilibrium with their surrounding. As thermal neutrons they can then be captured by suitable materials. When

the energy of neutron is greater than few Mev, it may transfer part of its energy by the inelastic scattering process to the struck nucleus. This process is quite probable for heavy nuclei, and less so for the lighter nuclei. In the case of elastic scattering, heavy nuclei are relatively ineffective and light nuclei are most effective. Thus the shield must have some light elements in it, otherwise there would be no really effective mechanism to reduce the neutron energy when it was below 1 Mev. It is advantageous to have heavy materials in the shield as at high neutron energies their inelastic scattering cross-section will be a major slowing down process. Iron and other heavy materials have been used extensively in reactor shields, either in solid sheets, or distributed uniformly in concrete.

When a shield is suitably divided into alternating regions of iron and concrete, the attenuation of the γ-rays and neutrons proceeds at more or less the same rate through successive layers, the overall size and weight of the shield is reduced over that of a concrete shield alone. [11].

In reactor some materials like steel and lead must be interposed between the core and the shield to attenuate the reactor radiations. Such shieldings are called thermal shields. It should be high density, high thermal conductivity and high atomic number. It should be also stable under irradiations. Other material such as cadmium alloyed with lead can be used.

The sources of gamma rays are, inelastic scattering of fast neutrons, the various capture processes in the system. Thus a good gamma-ray shielding material is that it should contain some high density elements. Materials such as lead and steel are the ones most commonly used because of their relatively low price.

The choice of shielding materials is greatly influenced by size,

weight and space economy. Concrete is one of the cheapest and effective shielding materials.

In the present work, the interaction of 14 Mev neutrons with iron and concrete materials were studied. The properties of iron and concrete are discussed in detail in Chapter (5).

1.6 THE RESEARCH PROGRAMME

The aim of the present work was to study the elastic scattering of 14 Mev neutrons from different thicknesses of Iron and concrete materials. The reason for this is that neutron scattering through these materials is important for the design of reactor shielding. Also little information is available, in order to calculate the cross-section of the scattered neutrons from broad, thick slabs of materials which are used for shielding, or for other purposes around nuclear reactors.

Fast neutron elastic scattering cross-section data are of general interest in pure physics, but have also found wide applications in fusion and fission reactor physics. In reactor physics, there is need for data for a large number of isotopes from the light elements to the heaviest ones. Generally speaking, the two types of fast neutron data involved in reactor design are:

Inelastic scattering, and the angular distribution of elastically scattered neutrons. As it was impossible to study all the above reactions, and materials, in this work only the elastic scattering of 14 Mev neutrons on Iron and concrete materials, and 14.4 Mev neutrons on iron samples were studied.

In addition an associated particle time-of-flight system was investigated for the $^{2}_{1}H\ (d,n)^{3}_{2}He$ reaction with 3.02 Mev neutron energy.

Finally, accurate neutron scattering measurements provide data for a detailed study of the properties of the nuclear optical model.

Using T (d, n)$^4_2$He reaction, and an associated particle time-of-flight technique, the elastic scattering of 14 Mev and 14.4 Mev neutrons from Iron and concrete of various thicknesses was studied and the differential cross-sectoins were determined.

The thickness of the scattering sample used was up to 1.7 mean free paths for Iron and about 2.3 mean free paths for concrete for the neutron energies under consideration.

From the literature survey undertaken at the beginning of this work for iron, the differential elastic scattering cross-section of 14 Mev neutrons is reported by Yuasa[12] for large scattering angles between 70° and 170°. Wilmore and Hodgson[13] and Bjorklund and Fernbach[14] have calculated theoretically the elastic scattering cross-section for iron and some of the other elements using the optical model.

Elliot[15] has reported the differential elastic scattering cross-sections of Fe, Ta, Bi and S, using cylindrical geometry for 14 Mev neutrons, between 5° and 55°.

Coon et al[16] have reported neutron elastic differential cross-section for iron using cylindrical geometry for 14.5 Mev neutrons.

In the case of concrete, the literature search revealed an absence of elastic scattering data for 14 Mev neutrons. Most of the reported work is about dose rate measurement[17-19] and the neutron attenuation measurement [20-23].

The aim of the present work was to provide data on the angular distribution for extended samples of iron and concrete between 25° and 90° with respect to the direction of neutron beam.

Using the optical model parameters obtained by Becchetti and Greenlees[24], the elastic scattering data for the thin iron and concrete samples was compared with the predictions of this model. For extended samples, this work provided the data of angular distribution, using a model based on the continuous slowing down density.

CHAPTER TWO

CHAPTER TWO

EXPERIMENTAL METHODS USED TO STUDY THE $T(d,n)^4_2He$ REACTION

2.1 NEUTRON SOURCE

Depending upon the energy and the intensity of the neutron beam, different kinds of source which can be used to provide beam of neutrons. By bombarding a suitable target with particles from an accelerator, neutrons can be produced. The energy spectrum of neutron depends upon the nature of the particles and their kinetic energy, and on the target material.

The most common reactions used to produce neutrons are those involving deuterium, because the coulomb barrier between the incident deuteron and light target nucleus is small. These reactions are:

$$^2_1H + ^2_1H \rightarrow ^3_2He + ^1_0n + 3.26 \text{ Mev} \quad \ldots\ldots (2.1)$$

and

$$^2_1H + ^3_1H \rightarrow ^4_2He + ^1_0n + 17.587 \text{ Mev} \quad \ldots\ldots (2.2)$$

As it is mentioned before, second reaction is preferred because of large Q-value, and high cross-section. As a comparison, the cross-sections for the above reactions as a function of deuteron energy are shown in Figure (2.1). Electrostatic generators are convenient sources of neutrons, since they are able to accelerate particles with a continuously variable energy and with a small energy spread. A number of other charged particle induced reactions such as $^9Be\ (\alpha,n)^{12}_6C$ (Q = 5.708 Mev) are applied to neutron generation. In this case, a higher incident particle energy is required, although this reaction has low yield neutrons. In this work the above reactions were used to produce 3.0 Mev and 14 Mev neutrons respectively.

Two accelerators which were used to produce neutrons are discussed in the next sections.

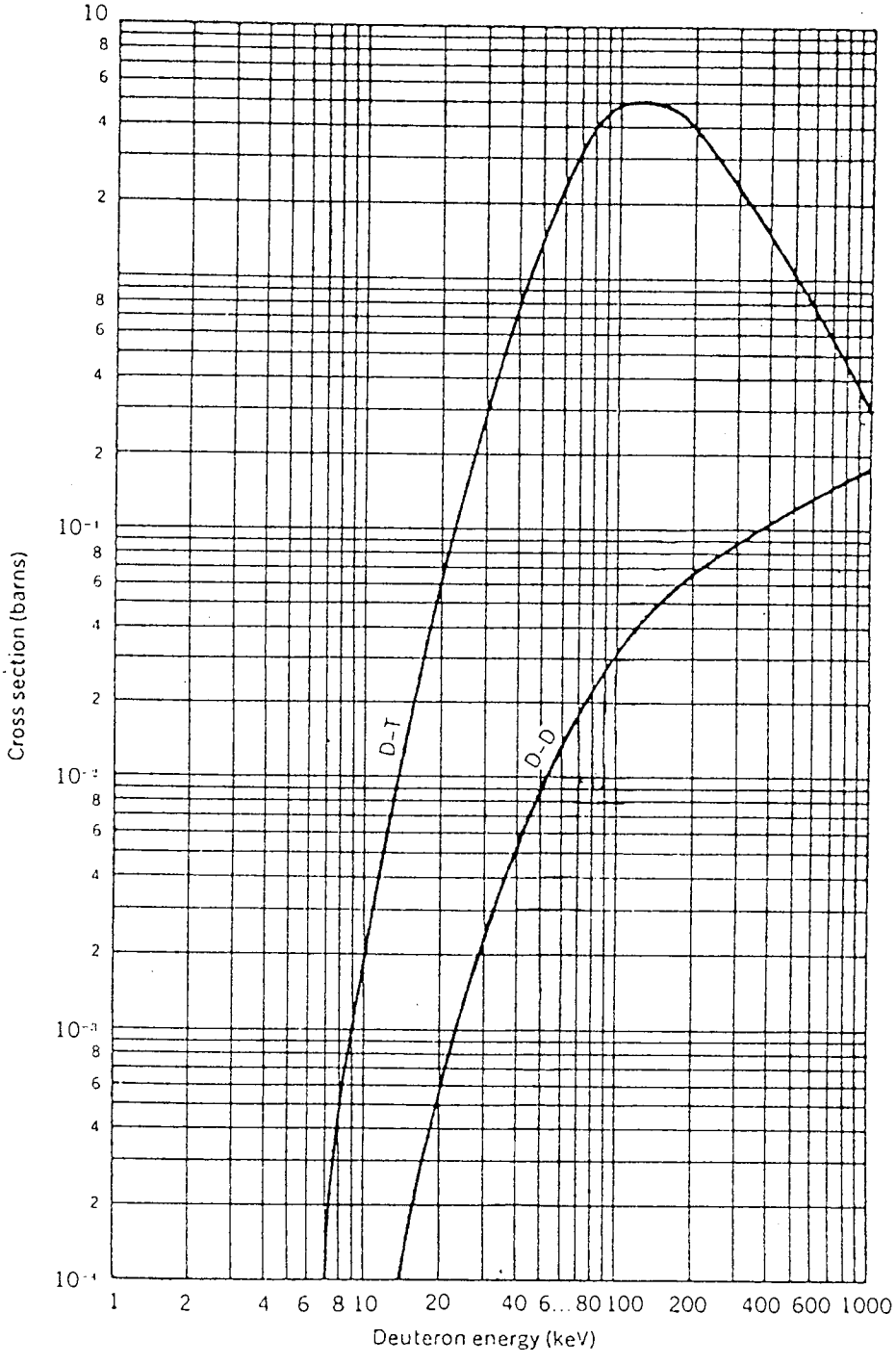

Figure (2.1) Comparison of the cross-section for (D-T) and (D-D) reactions [25]

2.1.1 The S.A.M.E.S. Accelerator

The use of 14 Mev neutron generators in research using the (D-T) reaction is becoming more and more general. Using titanium-tritiated target and low energy S.A.M.E.S. type J. accelerator, 14 Mev neutrons were produced.

The acceleration voltage was supplied by an electrostatic generator hermetically sealed in a hydrogen atmosphere. The voltage was continuosly variable from 0 to 160 kV and the generator could deliver 2mA at 150 kV with a stability of ± 1% [26].

The Ion source, excited by a 100 MHz R.F. oscillator was supplied with deuterium gas through a thermally activated palladium leak. Using a potential variable from 0 to 6 Kv, the ions were extracted and had a maximum output current of 600 μA. The ions are concentrated at the entrance of the extraction canal by a magnetic field coil located at the base of the ion source bottle. An oil-immersed Cockcroft-Walton generator situated inside the high voltage terminal of the accelerator, supplied 0-45 Kv potential to the focusing electrode. The S.A.M.E.S. accelerator is shown in figure (2.2). The target and detectors and other experimental system were placed several metres away from the accelerator.

The accelerator was operated from the control panel which was shielded behind a concrete wall.

2.1.1.1 Beam Line and Target Assembly

The target assembly was fixed at the end of a 5 metre long beam line. Two pumping stages were used to maintain the vacuum, the pressure in the main stage connected to the accelerator was about 2×10^{-6} torr. The auxiliary pumping stage was positioned at the other side of the beam line, near the target assembly. To stop oil, depositing on the target, and provide a good vacuum on the target, a liquid nitrogen cold finger was

Figure (2.2) The S.A.M.E.S. Accelerator

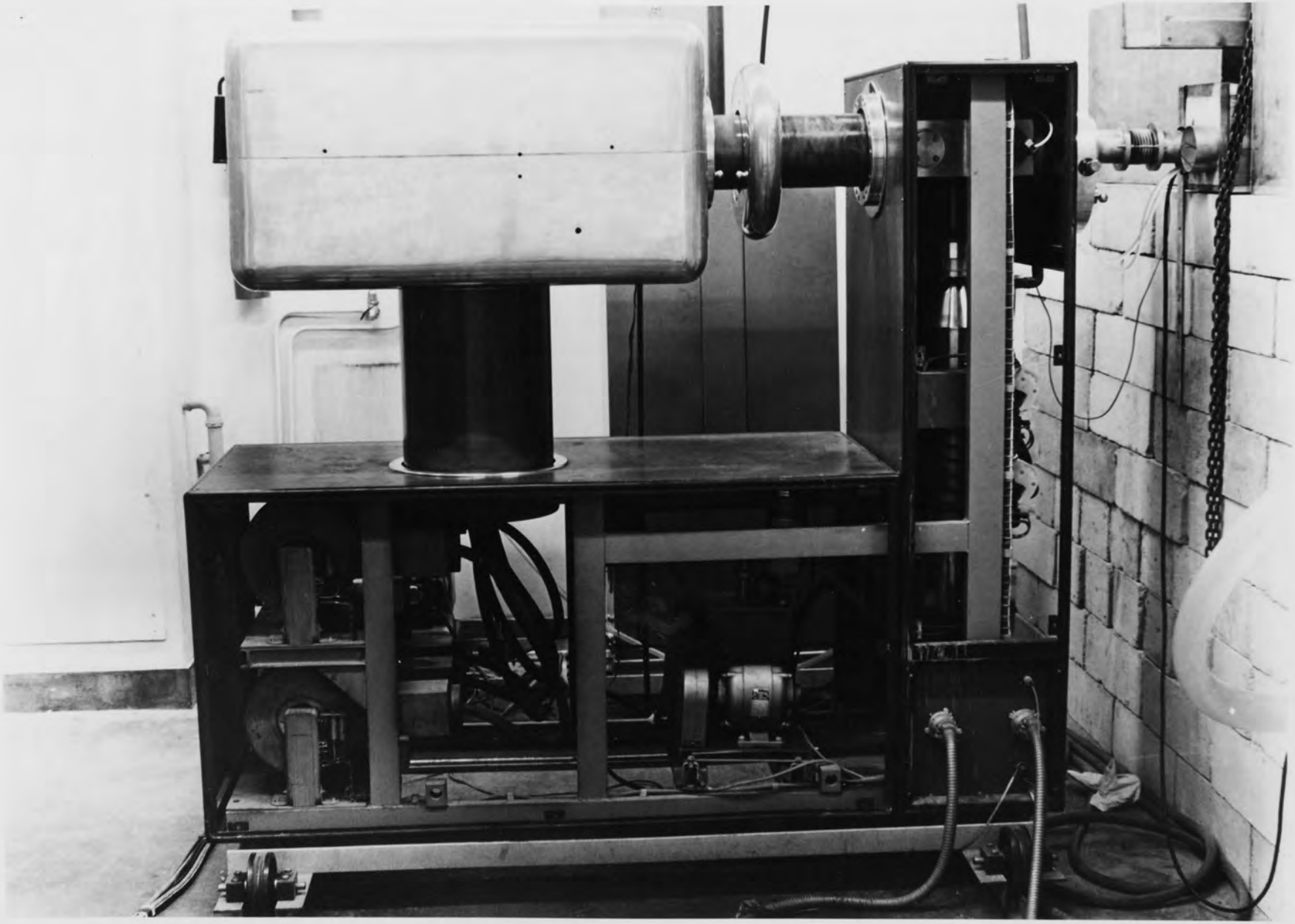

positioned above the auxiliary pumping stage.

To focus the beam onto the target an extra pair of electrostatic quadrupole lenses were connected in the tube, the voltage on the quadrupole lenses was ± 1.85 kV. This system has been discussed in detail by Baynham[27].

To optimize the current on the target, a pair of electrostatic deflector plates, between the quadrupole lenses and the target assembly, were used to control the beam. The voltage on the deflector plate was ≃ - 1.5 kV.

A small aperture (10 mm. x 1 mm.) was fixed at 20 cm. behind the target to define the deuteron beam.

An annular (Ti T) target supported in a rectangular stainless steel chamber was supplied by Multivolt LTD. The outer diameter of the target was 14.3 cm and 31.8 mm wide, which contained about 6.2 m Ci of the tritium per cm^2. The target was rotated at about 10 r.p.m. with a small electric motor and was water cooled.

The alpha detector was fixed to the target assembly at right angles to the beam direction.

The target assembly is shown in figure (2.3). Figure (2.4) shows the auxiliary pumping system together with the target assembly.

2.1.2 Sample Position

For deuteron energy of 140 keV with the α-particle emission at 90° to the beam direction, the neutrons were emitted at 83° to the beam direction, as determined from the kinematics of $T(d,n)^4_2He$ reaction.

The scattering sample was placed normal to the most intense neutron emission angle (i.e.83°) and at 20 cm. from the T Ti target. At this distance, all the neutrons completely intercepted the sample, as defined by the associated alpha particles.

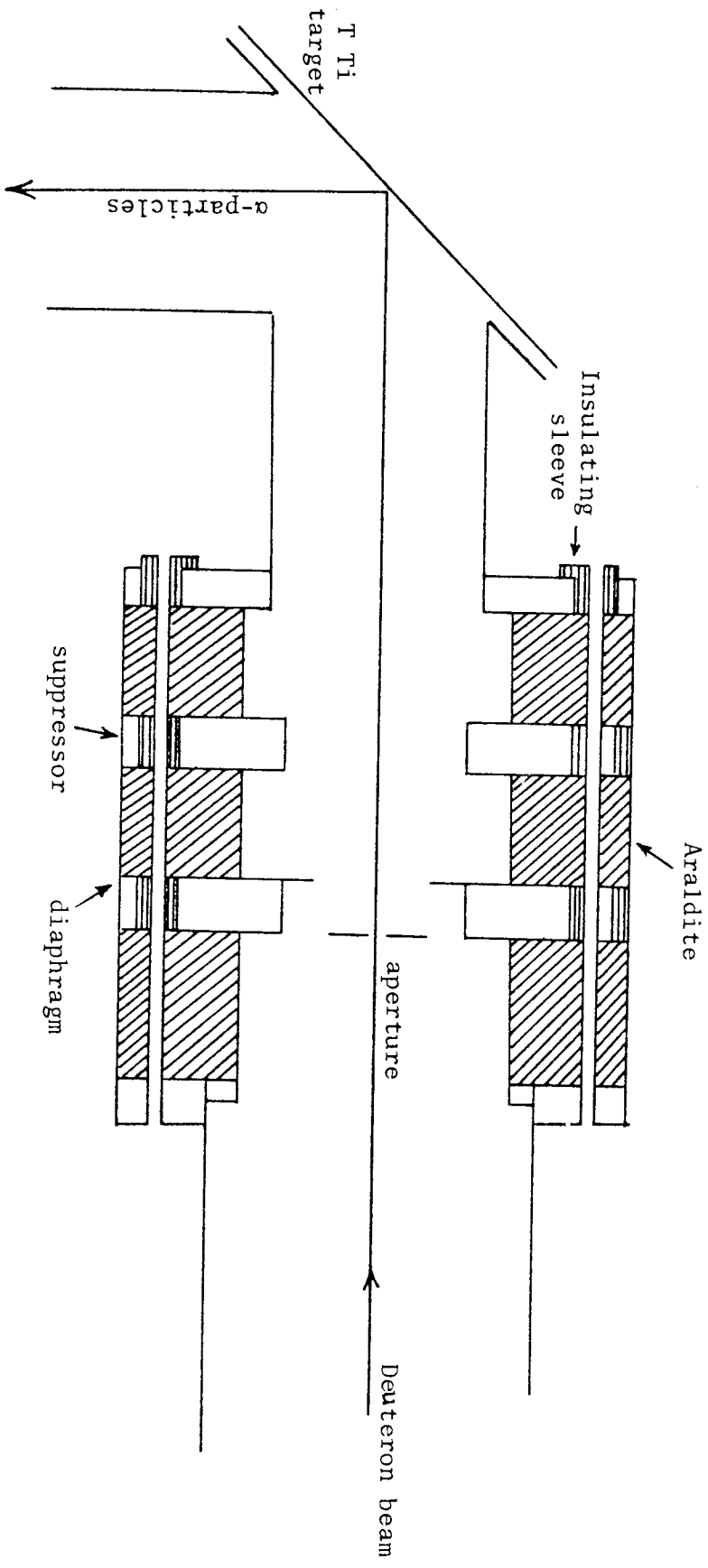

Figure (2.3) The 90° branched target assembly

Figure (2.4) Target assembly with auxiliary pumping system

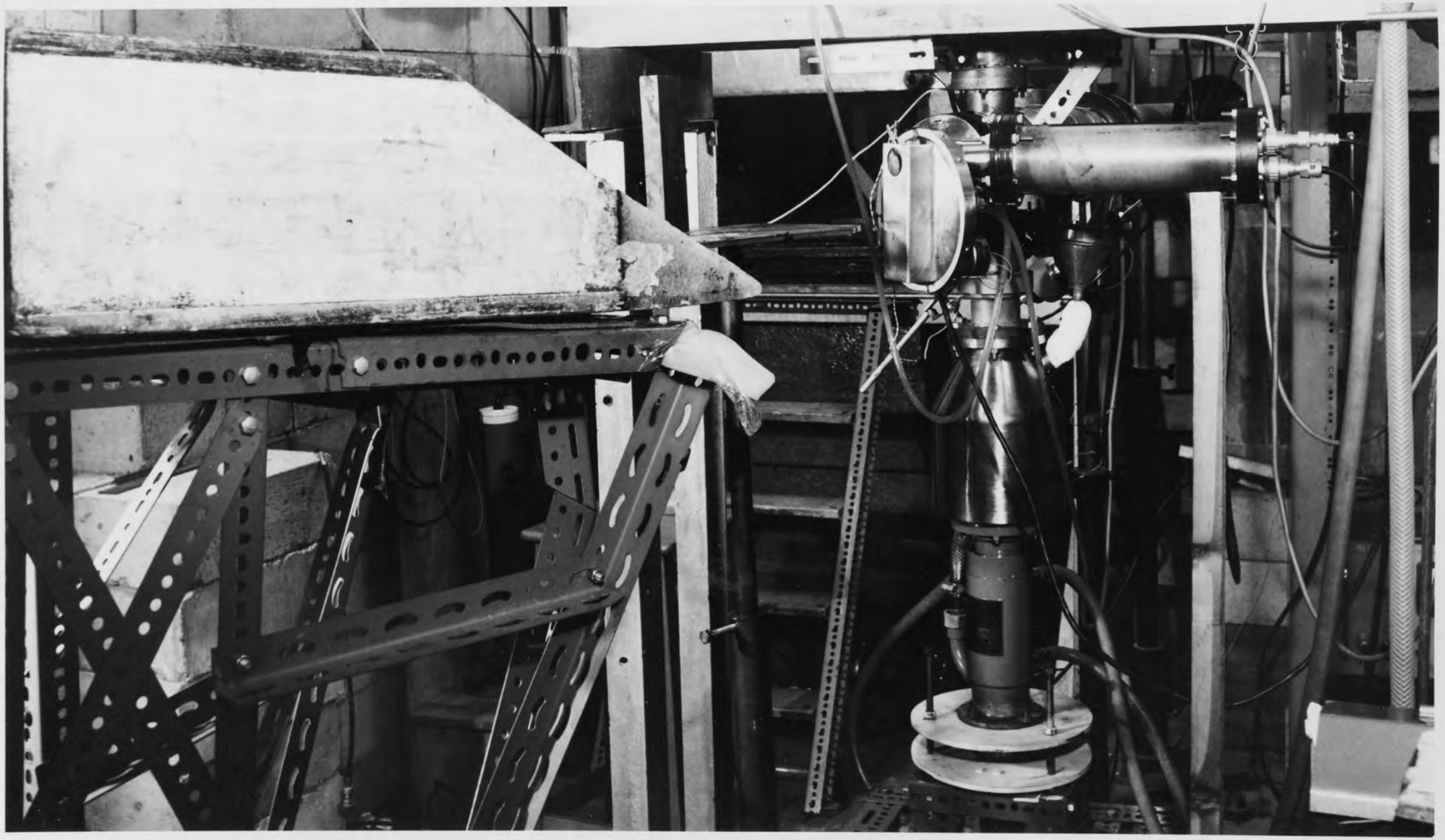

The cross-sectional area of the neutron beam as limited by the alpha-detector aperture, was 4.3 cm. x 2.4 cm. The flight path from the centre of sample to the face of the neutron detector was fixed at 140 cm.. The scattering angle varied from 0° to 90° with respect to the neutron beam direction.

The sample holder was a steel base fixed to the Laboratory floor, surmounted by a flat steel plate of 20 cm. x 25 cm..

Measurements for deuteron energies above 150 keV were not possible with the S.A.M.E.S. accelerator. Further measurements for higher deuteron energies were carried out at Birmingham University, Radiation Centre, using a 3 Mev Dynamitron accelerator. 14.4 Mev neutrons were obtained from the D-T reaction with 900 keV mass III* deuteron beam. Neutrons were emitted at 78° to the deuteron beam direction. The scattering sample was placed normal to this angle at 25 cm. from the target. The distance from the centre of scattering sample to the face of neutron detector was kept to be the same as before. Again, the scattering angle range was varied from 0° to 90° to the neutron beam direction. Experimental results are given in chapter five. The cross-sectional area of the sample is radiated by the neutrons, was 5.3 cm. high by 3.0 cm. wide.

2.1.3 Dynamitron Accelerator

The Dynamitron Accelerator is a high voltage particle accelerator designed to produce a maximum of 30 kw of beam power at a maximum potential of 3 Mv. The main characteristic of Direct accelerators such as Dynamitron can be summarized as:

(1) Production of a continuous beam

(2) The type of particle being accelerated can be changed easily.

(3) High energy stability

* N.B. The mass of deuteron beam consist of $(HD)^+$

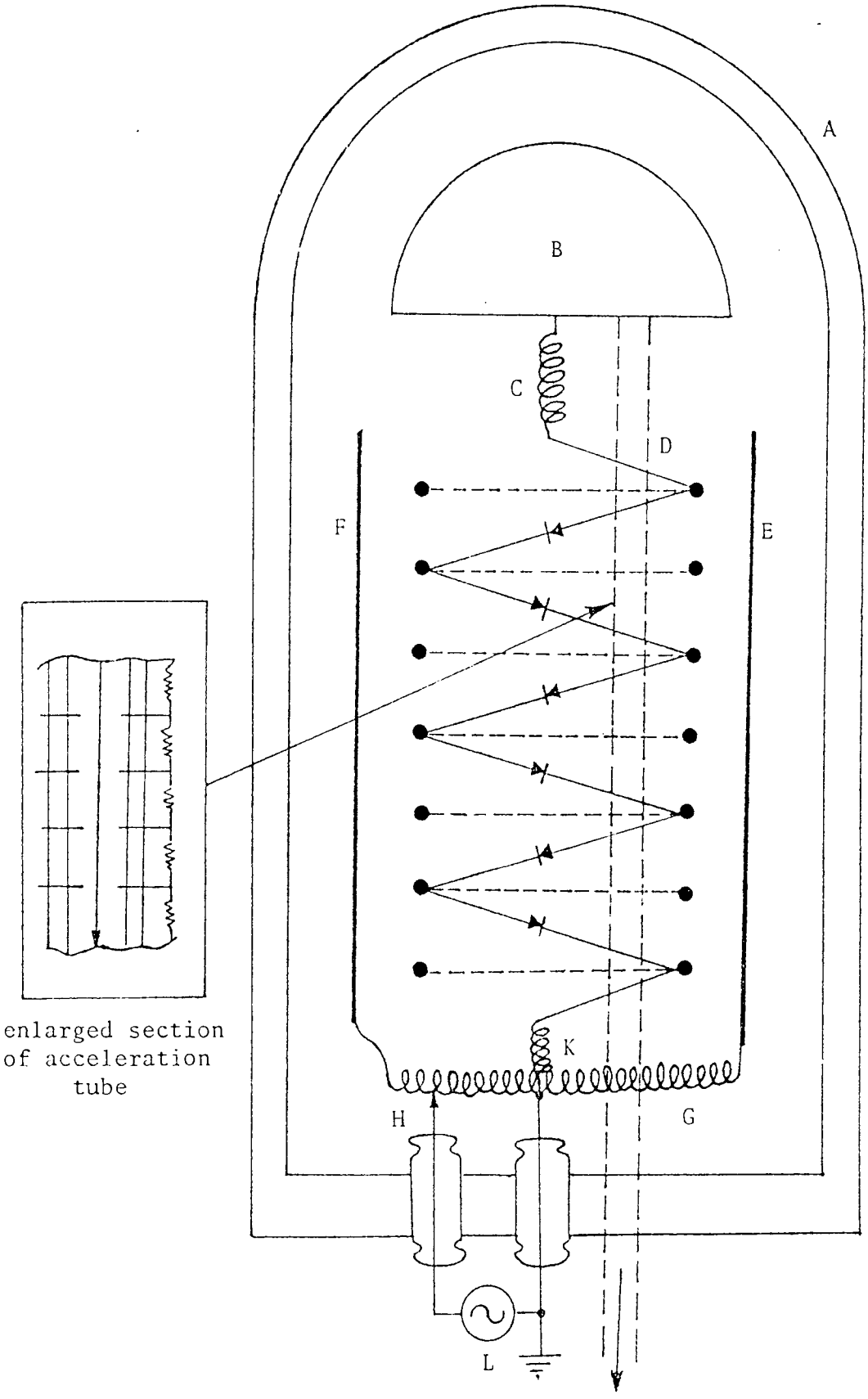

● - Corona ring

A - Pressure Vessel

B - H.V. terminal Electrode

C and K - r.f. chokes

D - Beam tube

E and F - r.f. electrodes

H - resonant circuit

L - r.f. oscillator

G - toroidal coil

Figure (2.5) Schematic Diagram of vertical section through a vertical Dynamitron Accelerator [28]

(4) The beam energy spread is small

(5) The beam energy can be varied easily over a wide range.

Three major sections comprise a complete Dynamitron accelerator system, these are:

(A) The voltage generator

(B) The accelerator tube

(C) The ion source

A schematic diagram of the Dynamitron system is shown in figure (2.5).

Basically, it is a variable energy potential drop device capable of terminal potentials from about 800 kV to 3 Mv. The power supply in this case is a multi-stage rectifier system powered by a high R.F. oscillator, operating at about 130 KHz. The power is fed to two large semi-cylindrical plates (the dees) inside the pressure vessel which are capacitively coupled to semi-conductor rings located about the acceleration column. From the base of the machine up to the terminal 32 solid state rectifier modules in the form of a chain are placed on each side of structure to prevent corona. The rectifications of the R.F. over these 64 rectifier stages produces the D.C. potential on the terminal.

The Dynamitron can accelerate electrons or positive ions. In the electron mode up to 10 mA of beam can be produced, however, in the positive mode, the specification for the machine is, e.g. 2 mA of protons at 3 Mv. This structure in addition to providing a high current capability, has three fundamental properties that are critical to its success, these are:

Relatively small quantities of stored energy on the insulated column structure, a uniform cylindrical section over the length of the column structure for optimum electrostatics, and a self-healing dielectric in the event the terminal or column structure discharge to ground.

Figure (2.6) The Column of Dynamitron Accelerator

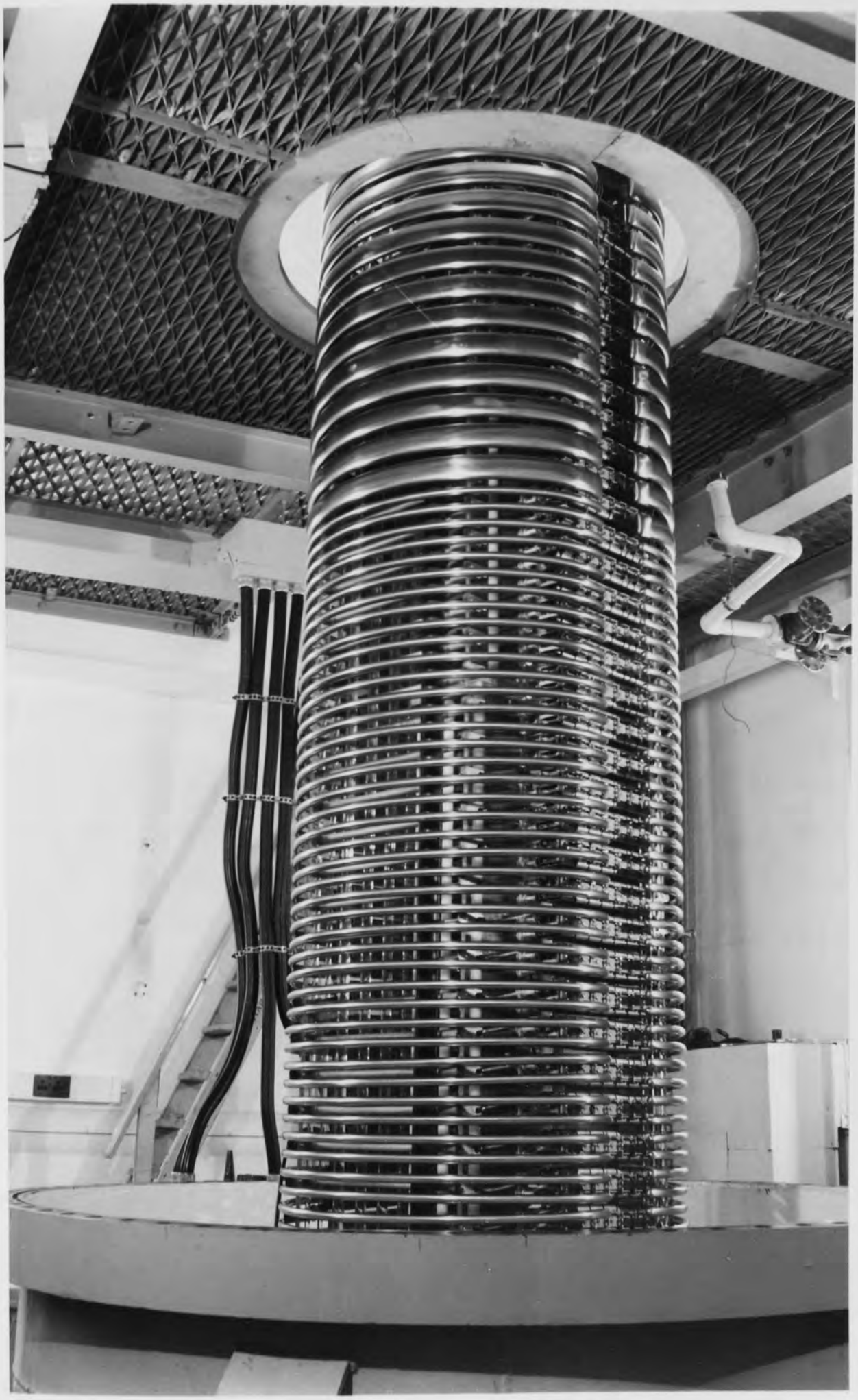

The tube is located concentrically within the centre line of the column, since the primary structural material is glass. The acceleration column of Dynamitron is shown in figure (2.6).

Ions are produced in a duoplasmatron ion source, and either hydrogen, helium or deuterium can be used. In order to separate the different ions produced, the source is placed at an angle to the acceleration column and the ions bent into the line of the accelerator by a permanent magnet. Adjustment of the potential used to extract the ions from the source prior to insertion into the magnetic field selects which mass ion passes through the analyser. However, if after acceleration the beam is taken through an angle in one of the bending magnets, the masses will be almost fully separated.

The beam from the machine is not entirely monoenergetic, there is a ripple of a 1 kV at 1Mv, and the size of ripple increases with machine energy. The current is measured on a digital voltmeter (DVM) reading across a 500 ohm resistor in the control panel. A Keithley electrometer was used as it provides the range of inputs and accuracy required. The beam after emerging from the accelerator column enters the magnet room. In this room the beam passes into the first bending magnet, "the H-magnet" and then to second bending magnet, "the C-magnet", which can either permit the beam to continue on at 45° or bend it through a further 45°, as in the present work, to service the beam into the low scatter cell.

A Hewlett-Packard computer system is used to collect the data.

2.1.3.1 Target Chamber and Beam Collimator

With the Dynamitron accelerator, a "T" shaped stainless steel target chamber was used. Figure (2.7) shows the target assembly with the target holder.

Part 'A' was connected to the beam tube by a flange. Again, the

A :Accelerator tube

B :Beam collimator

C :Deuteron beam

D :To the Alpha detector

E :Target holder

F&G:Water inlet and outlet

H :Target disc

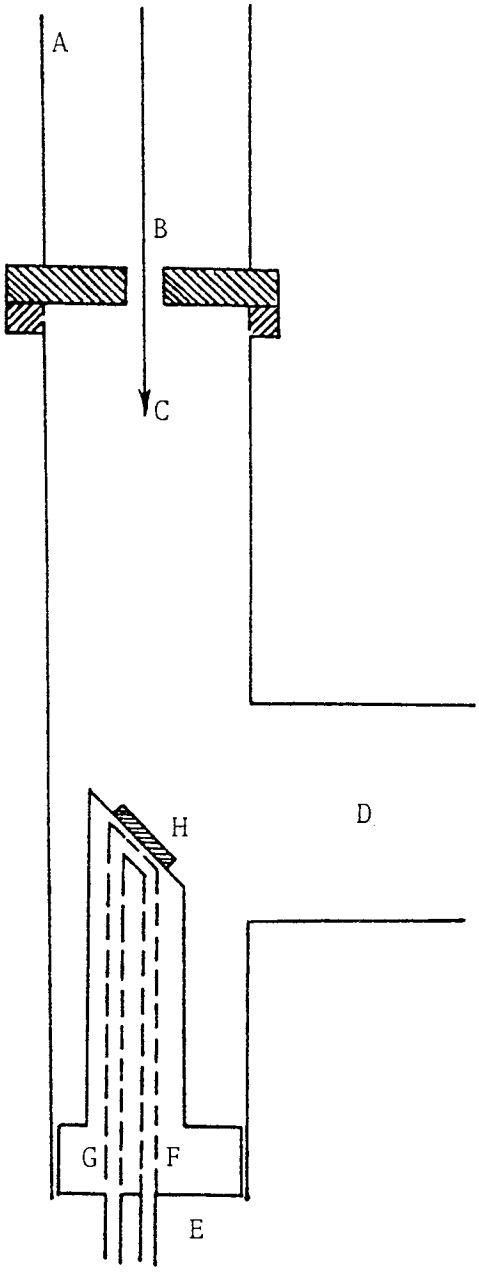

Figure (2.7) The Target Assembly

alpha-detector was fixed at 90° to the beam line.

The neutron source was a tritiated titanium substrate deposited on a copper backing, supplied by the Amersham Radio-Chemical Centre of U.K.A.E.A. It was positioned onto the holder at 45° to the beam direction and was water cooled.

The area of the target used was restricted by the two stainless steel and tantalum aperture plates, with internal diameters of 10 mm and 3 mm respectively with 2 cm. distance between the two.

The apertures were electrically insulated from the beam line and target assembly.

Figure (2.8) shows the position of the collimators and connecting pipe of the target assembly. A sketch of the target chamber with target assembly is shown in figure (2.9).

2.2 SAMPLE SCATTERING GEOMETRY

To reduce the relative background from the material around the sample in the Laboratory and to reduce the magnitude of the correction, which must be made to the cross-section measurements, the shape of the scattering material and relative shielding is important. The three most common arrangements are:

(A) Cylindrical geometry

(B) Ring geometry, and

(C) Flat plate geometry

2.1.1 Cylindrical Geometry

Figure (2.10 - a) shows the cylindrical geometry in which the sample is in the form of a cylinder or sphere, placed in the neutron beam. For small samples, the symmetry almost guarantees an accurate measurement of

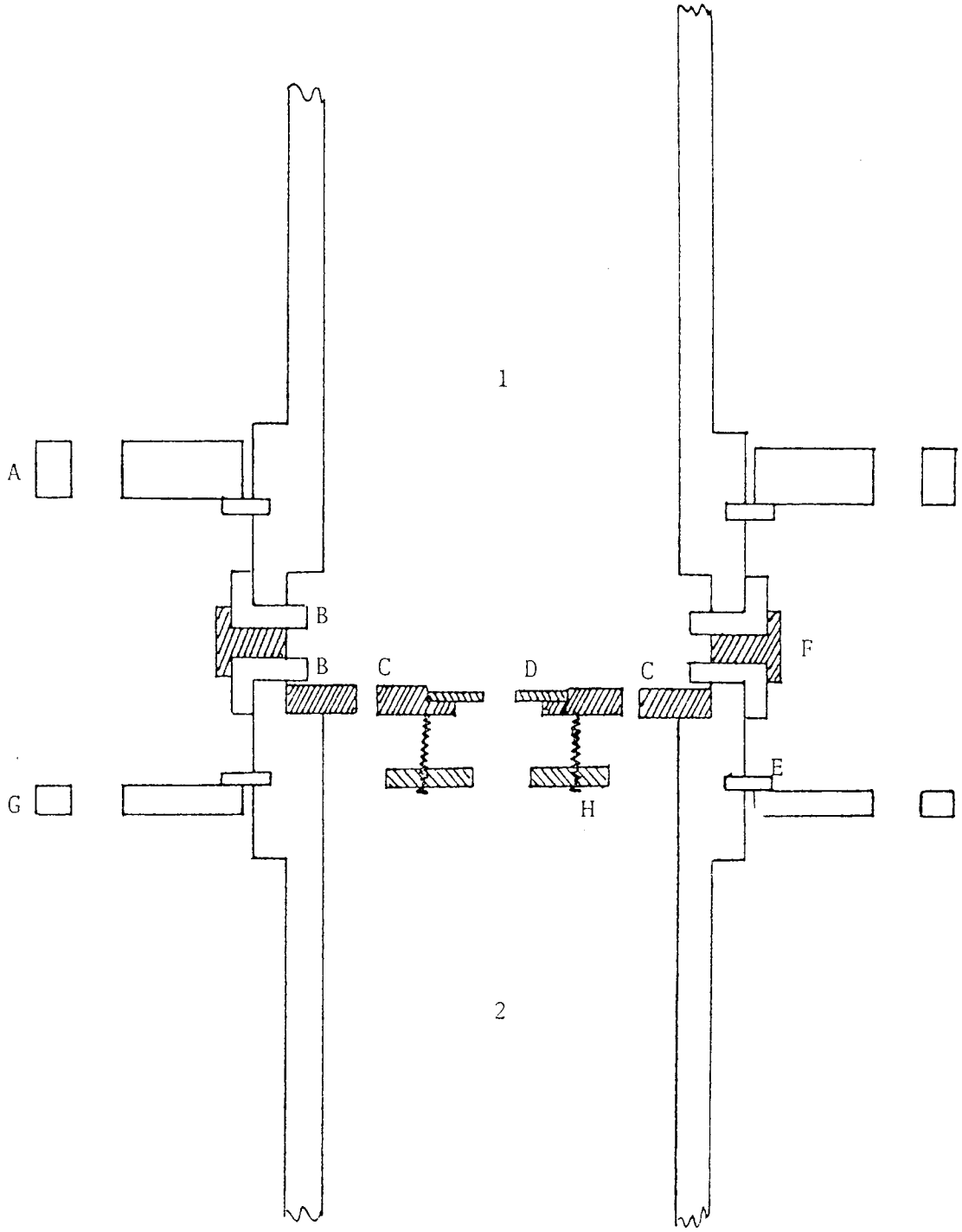

1 - Pipe of target chamber

2 - Roughing out port

A - Bakelite ring

B - 'O' ring

C - Aluminium holder

D - Tantalum foil

E - Spring clips

F - Aluminium spacer

G - Stainless steel

H - Stainless steel collimator

Figure (2.8) Connection pipe of the target chamber and position of the collimators to the beam line

Figure (2.9) Beam line and target chamber assembly

the angular variation of the scattering. In this geometry however, an error in positioning the sample alters the effective thickness. This technique has been used by some authors[29-30]. Blech et al[31] have derived a formula to correct the intensity for multiply scattered neutrons in cylindrical specimens.

2.2.2 Ring Geometry

In this geometry, a ring shaped scatterer is used. This was the first scattering geometry used in differential cross-section measurements. These employed large ring samples, and Fe or Cu shadow cones,[32-34]. A ring of material was mounted on the 0° axis with respect to the neutron source. The detector was also mounted on the 0° axis and shielded from the source by a shadow cone also on the axis, as shown in figure (2.10-b).

The advantage of this geometry is that, for a given angular resolution and thickness of scatterer, more material can be used, hence a greater intensity can be obtained. However, there are many disadvantages:

(1) There is difficulty for many elements in constructing large ring shaped scatterers, because of cost.

(2) It is a relatively poor geometry method, since the detector must be close to a large scatterer, and hence large goemetrical corrections must be made to the data.

(3) The detector must be shielded from the most intense flux at zero degree , while the scattering sample sees a lower flux.

(4) In this geometry, since the distances between sources, sample and detector change with scattering angle, these distances must be determined separately for each angle.

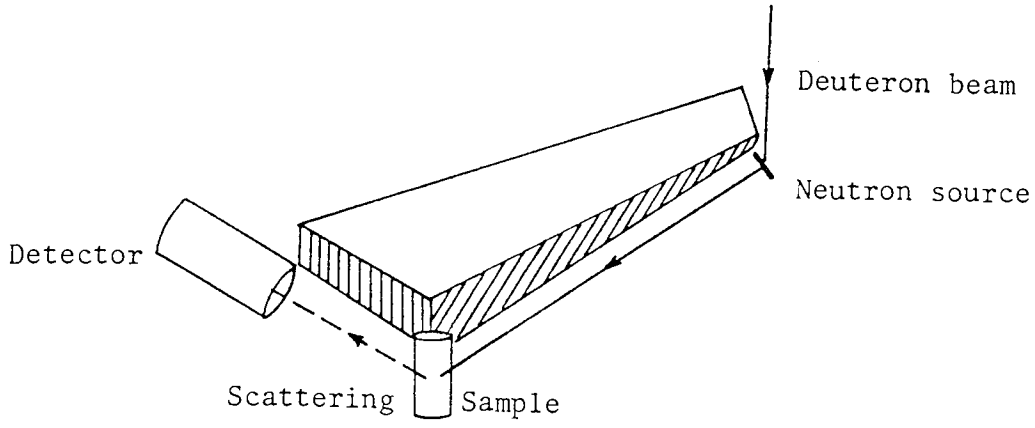

(a) Cylindrical geometry

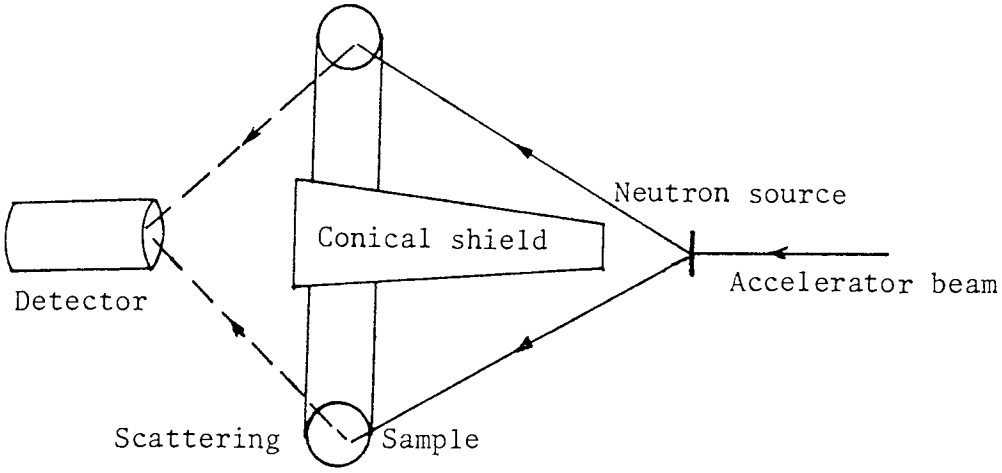

(b) Ring geometry

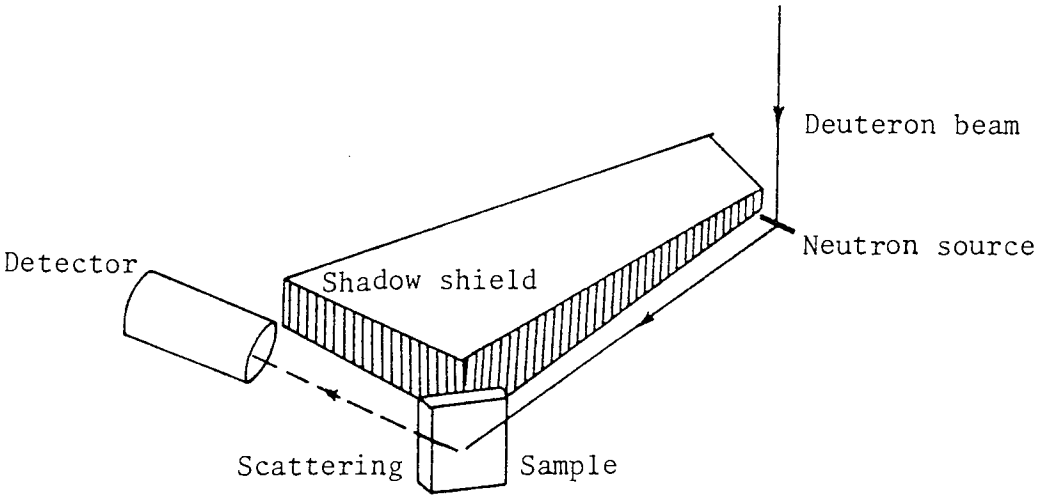

(c) Flat plate geometry

Figure (2.10) Sample Scattering Geometry

2.2.3 Flat Plate Geometry

In this geometry, the sample is in the form of flat plates. In order to reduce the multiple scattering correction, usually a thin flat plate sample is used. One of the advantages of this geometry is that, the target sample can be made wider, to subtend completely the defined neutron beam. By rotating the detector, the angular distribution of the scattered neutron can be obtained over the whole angular range. In this geometry, a massive shielding must be used around the detector to reduce the background. To stop the direct beam, a shadow bar of paraffin wax, Iron or tungsten is placed between the sample and detector assembly. Figure (2.10-c) shows the flat plate geometry.

In the present work, because of above advantages, and disadvantages of other two geometries, flat plate geometry was used.

2.3 NEUTRON TIME-OF-FLIGHT TECHNIQUE

The measurement of the intensity and energy distribution of neutrons emitted from nuclear reactions is an important source of information in the study of nuclear structure and nuclear reaction mechanisms.

The measurement of neutron energy spectra is, of course, complicated by the lack of a versatile energy-sensitive neutron detector. With the development of electronic techniques and scintillation materials with responses in the nano second range the time-of-flight technique has become quite a widely used technique for the energy measurement of fast neutrons. [35].

A relatively simple method for measuring neutron energies based on the measurement of velocity has been in use for many years. Dunning et al[36] developed a neutron velocity selector to measure the low energy part of the spectrum of neutron from a fast neutron source. In 1938

Alvarez[37] used the time-of-flight technique to discriminate between fast and low energy neutrons. In the past twenty years, two general techniques have been developed, to measure the differential scattering cross-section of fast neutrons:

(A) measurement of the gamma-ray production by inelastic scattering as the residual nucleus de-excites. [39-40].

(B) Direct measurement of the scattering neutron energy and angular distribution [35].

In the present work this technique was adopted to measure the differential elastic scattering cross-section of fast neutrons from reactor shielding materials.

Time-of-flight technique require the establishment of two time signals, relating to neutron production and detection. An essential part of the time-of-flight measurement is therefore, the precise determination of the time of origin of the particles. If the neutron source and detector are separated by a fixed distance L, known as the flight path, then the time it takes to travel this known distance is uniquely related to the velocity and hence the energy of the neutron, which can be written as follows:

$$t = \frac{L}{V} = 72.3\ E^{-\frac{1}{2}}L \qquad \text{n.sec} \qquad \ldots\ldots (2.3)$$

where L = path length in metres

and E = energy of neutron in Mev

In the relativistic region, for a given neutron energy E_n, using the result of special relativity, the time can be obtained as [38].

$$E_n = E_o[(1 - V^2/C^2)^{-\frac{1}{2}} - 1] \qquad \ldots\ldots (2.4)$$

$$E_n = E_o[(1 - L^2/t_n^2 C^2)^{-\frac{1}{2}} - 1] \qquad \ldots\ldots (2.4)$$

Assuming the units of energy are Mev, and those of length and time are metre and n.sec. then:

$$t_n = \frac{3.3356\ L}{E_o\left[1 - \left(\frac{E_o}{E_n + E_o}\right)^2\right]^{\frac{1}{2}}} \quad \text{n.sec.} \qquad \ldots\ldots (2.5)$$

where E_o = rest energy of the neutron = (939.553 Mev)

At E_n = 1 Mev the difference between the relativistic and non- relativistic calculations of $(\frac{t_n}{L})$ is about 0.057 n.sec.

If the overall timing uncertainty is $\frac{dt}{t}$ (FWHM) then the neutron energy resolution for a time-of-flight spectrometer is given by the formula:

$$\frac{dE}{E} = 2\,\frac{dt_n}{t_n} \qquad \ldots\ldots (2.6)$$

In equation (2.6) dt_n is the uncertainty from all sources. The timing uncertainty includes jitter in the detector and electronics, uncertainty in the length of the flight path.

There are at present several different designs of time-of-flight neutron spectrometers for fast neutrons, all of them are characterized by the measurement of the time elapsed between the time a neutron is produced at the target, and the time at which it is detected. The time differences can be measured by a time to pulse-height converter whose pulse height output is directly proportional to the time difference of the two pulses arriving at the converter inputs. This pulse-height distribution can then be recorded on a multichannel pulse-height analyzer.

For the determination of the zero time, with low energy accelerators, there are two general methods:

(1) The pulsed beam method

(2) The Associated particle method

2.3.1 The Pulsed Beam Technique

In the pulsed beam technique, the source is usually a nuclear reaction induced by ion bombardment, the neutrons are produced in short bursts, which mark the beginning of the flight time, the end of the flight path is determined by a signal from the neutron detector. There is, however, a spread in time because of dispersion in the deceleration and migration times. [41]. The pulsed source method is therefore, limited to those assemblies for which the dispersion is small compared to the flight time. In fact, the time of arrival of a neutron at the detector is measured relative to a pulse derived once per cycle from the r.f. voltage, from this time, the neutron energy can be obtained.

Cranberg and Levin[43] applied this technique for the first time to neutron energy measurement. The pulsed beam technique can be used for all reaction in which the neutrons are produced by an ion beam.

2.3.2 The Associated Particle Method

The associated particle method was the first time-of-flight technique to be developed for the measurement of fast neutron energies. [35, 42]. In this technique the recoil product of the reaction which is produced with the neutron is detected in coincidence with the neutron. The time between the detection of a neutron and of its production is measured, and from this time the neutron energy is calculated. The two features of the associated particle method are:

(1) The accelerator can be operated with constant beam current

(2) The detection of the recoil product of the reactor in a certain

solid angle subtended at the source means that an associated or coincident neutron was produced and has been scattered toward the scattering sample.

This technique is mainly used at low deuteron bombarding energy with the $(T,n)^4He$ and $D(d,n)^3He$ reactions [44]. On the other hand it has a higher signal to noise ratio,and is particularly useful in conjunction with low energy accelerators, which are easy to operate [45].

In this technique, it is easier to measure the emission rate of the associated particle than that of the neutron, e.g. in the $T(d,n)^4He$ reaction, the helium particle can be detected with 100% efficiency by a scintillation or solid state detector. This is used as the zero time marker, the neutron associated with this α-particle proceeding to the scatterer when it has been scattered towards a second detector that detects the neutron and provides the second time pulse corresponding to the end of its flight.

In order to obtain better timing precision, the alpha detector should be located near to the target, to reduce the alpha time-of-flight dispersion arising from small variations in alpha energy due to spread in angle. The associated particle method with the $T(d,n)^4He$ and $D(d,n)^3He$ reactions was adopted for use in the present work.

2.4 KINEMATICS OF $T(d,n)^4_2He$ REACTION

The determination of the energy of the neutron emitted from a given nuclear reaction as a function of the angle of observation and the incident particle energy can be calculated in a very direct manner from the equations for conservation of energy and momentum.

The (D-T) reaction may be studied either by accelerating deuterons beam onto tritium titanium target, or by accelerating deuterons through thin foil into the tritium gas target, or bombarding tritium absorbed in

zirconium or other metals.

As the neutrons and alpha particles share the Q-value in the inverse ratio of their masses, at zero deuteron bombarding energy, the neutron carries off an energy of 14.0 Mev and the alpha particles ≃ 3.5 Mev.

In considering scattering collisions two convenient frames of references are used. These are the Laboratory (L) system, and the centre-of-mass (C) system. The schematic representation of a nuclear disintegration is shown in figure (2.11).

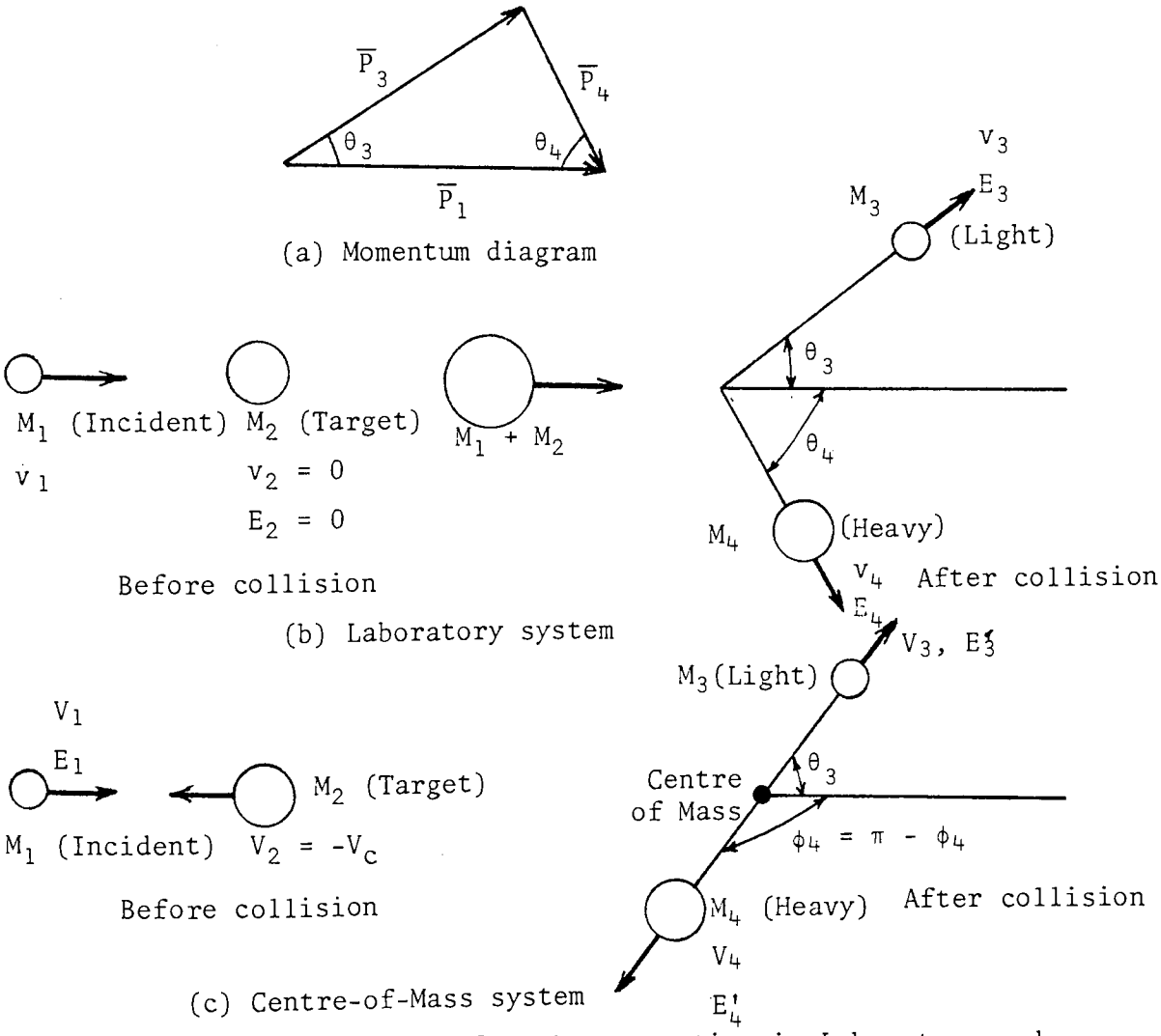

Fig. (2.11) Representation of nuclear reaction in Laboratory and centre-of-mass system of coordinates.

In the Laboratory system, a particle of mass M_1, speed v_1, and kinetic energy E_1 is incident on a nucleus of mass M_2, (initially at rest).

After collision, the light particle of mass M_3, speed v_3, and kinetic energy E_3, emerges at an angle θ_3 to the original direction and the residual nucleus of mass M_4, speed v_4, and kinetic energy E_4 emerges at an angle of θ_4 to the incident direction respectively.

To find the energy of incident particles it is necessary to apply:

(1) The conservation of momentum along and perpendicular of the incident direction, yields:

$$P_1 = P_3 \cos\theta_3 + P_4 \cos\theta_4 \qquad \ldots\ldots (2.7)$$

$$0 = P_3 \sin\theta_3 + P_4 \sin\theta_4 \qquad \ldots\ldots (2.8)$$

(2) The conservation of energy, yields:

$$Q = (E_3 + E_4 - E_1) \equiv (M_1 + M_2 - M_3 - M_4)C^2 \qquad \ldots\ldots (2.9)$$

The combination of equations (2.7) and (2.8) gives:

$$P_4^2 = P_1^2 + P_3^2 - 2 P_3 P_1 \cos\theta_3 \qquad \ldots\ldots (2.10)$$

using $P^2 = 2ME$ and equation (2.9), solving for the particle M_3 (in non-relativistic region), the energy of light particle, i.e. neutron can be obtained:

$$E_3 = E_1 \frac{M_1 M_3}{(M_3 + M_4)^2}\{ 2\cos^2\theta_3 + \frac{M_4(M_3 + M_4)}{M_1 M_3}\left(\frac{Q}{E_1} + 1 - \frac{M_1}{M_4}\right)$$

$$\pm 2\cos\theta_3\left[\cos^2\theta_3 + \frac{M_4 (M_3 + M_4)}{M_1 M_3}\left(\frac{Q}{E_1} + 1 - \frac{M_1}{M_4}\right)\right]^{\frac{1}{2}}\} \qquad \ldots\ldots (2.11)$$

or simply solving equation (2.9) and (2.10) for Q yields:

$$Q = E_3\left(1 + \frac{M_3}{M_4}\right) - E_1\left(1 - \frac{M_1}{M_4}\right) - \frac{2\sqrt{M_1 M_2 E_1 E_3}}{M_4}\cos\theta_3 \qquad \ldots\ldots (2.12)$$

defining the quantities

$$K = \frac{\sqrt{M_1 M_3 E_1}}{M_3 + M_4} \cos\theta_3 \qquad \ldots\ldots (2.13)$$

and $$L = \frac{M_4 Q + E_1(M_4 - M_1)}{M_3 + M_4} \qquad \ldots\ldots (2.14)$$

it yields:

$$\sqrt{E}_3 = [K \pm (K^2 + L)^{\frac{1}{2}}] \qquad \ldots\ldots (2.15)$$

The reaction is possible when $\sqrt{E}_3$ is real and positive.

In relativistic region, the energy of neutron has been calculated by Horstmann and Liskin[46,71].

Figure (2.12) shows the variation of neutron energy with angle for different deuteron energies in the Laboratory system for the non-relativistic region.

2.4.1 The Angular Relationship of the Associated Particles

Due to kinematics of the reaction, the neutrons and their associated alphas are not emitted in exactly opposite directions.

The angular range of neutrons defined by alpha particles emitted at 90 ± 6° to the deuteron beam direction has to be calculated. The kinetics of $T(d,n)^4He$ reaction have been investigated by many workers, [47-48, 71, 94].

Benvensite and Zenger[47] give equation (2.16) which relates angles of emission of the neutron and alpha-particle in the Laboratory system viz:

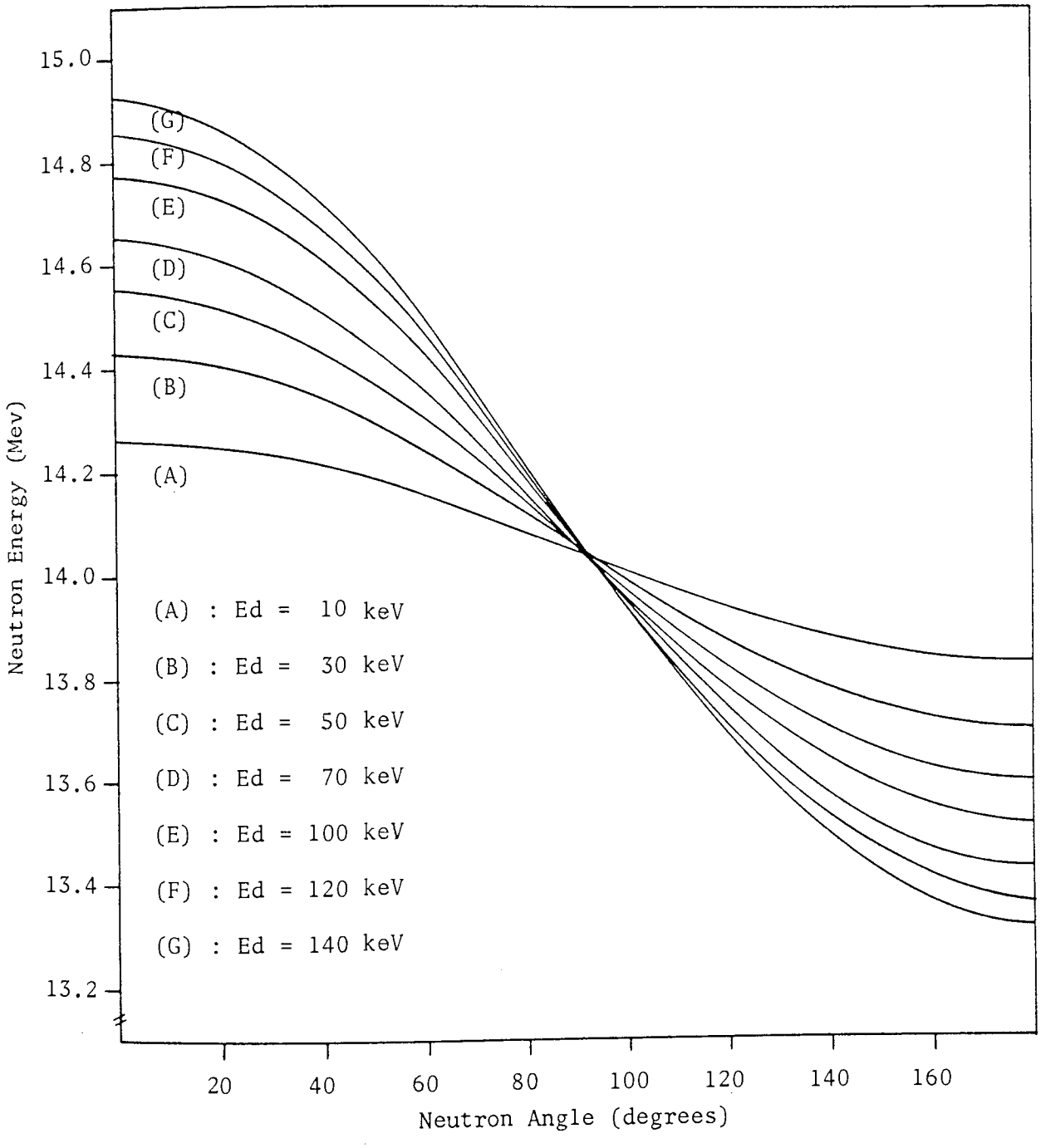

Figure (2.12) Variation of Neutron energy with the angle of emission of the (T-D) reaction at various incident deuteron energies

$$tg\ \theta_\alpha = \frac{\frac{1}{2}\sin 2\theta_n + \sin\theta_n \left(\frac{1}{\gamma^2} - \sin^2\theta_n\right)^{\frac{1}{2}}}{-\sin^2\theta_n + \cos\theta_n \left(\frac{1}{\gamma^2} - \sin^2\theta_n\right)^{\frac{1}{2}} - \frac{M_\alpha}{M_n}} \quad \ldots\ldots (2.16)$$

Here, $\gamma = \frac{V_{c.m.}}{v'_n}$, where $V_{c.m.}$ is the velocity of the centre of mass frame, in the Laboratory system and v'_n is the neutron velocity in the centre of mass system.

The value of γ can be found from the relation:

$$\frac{1}{\gamma^2} = \frac{M_\alpha}{M_n} \cdot \frac{M_d + M_T}{M_d} \left(\frac{M_T}{M_d + M_T} + \frac{Q}{E_o}\right) \quad \ldots\ldots (2.17)$$

where Q = Energy released in the reaction (Q ≃ 17.6 Mev), M_α, M_d, M_T and M_n are the masses of alpha, incident deuteron, Triton, and neutron particles respectively, and E_o is the energy of the incident deuteron beam.

Hanson et al[48], by using the conservation of momentum and momentum diagram Figure (2.11-a) have found the following simple relation between alpha and neutron angles:

$$\sin\theta_\alpha = \left(\frac{M_n\ E_n}{M_\alpha\ E_\alpha}\right)^{\frac{1}{2}} \sin\theta_n \quad \ldots\ldots (2.18)$$

The variation of θ_α and the corresponding θ_n for various deuteron energies is shown in Figure (2.13).

A computer programme in Basic was written to calculate the energy and angular relationship between neutron and alpha particles from(D-T) reaction. The layout of this computer programme is shown in Appendix B.

The Angular straggling of α-particle in the target has been investigated by Connell[49], who found an uncertainty of ¼° in the results of calculation, which is negligible compared to the angular resolution of the system which is about ± 6°.

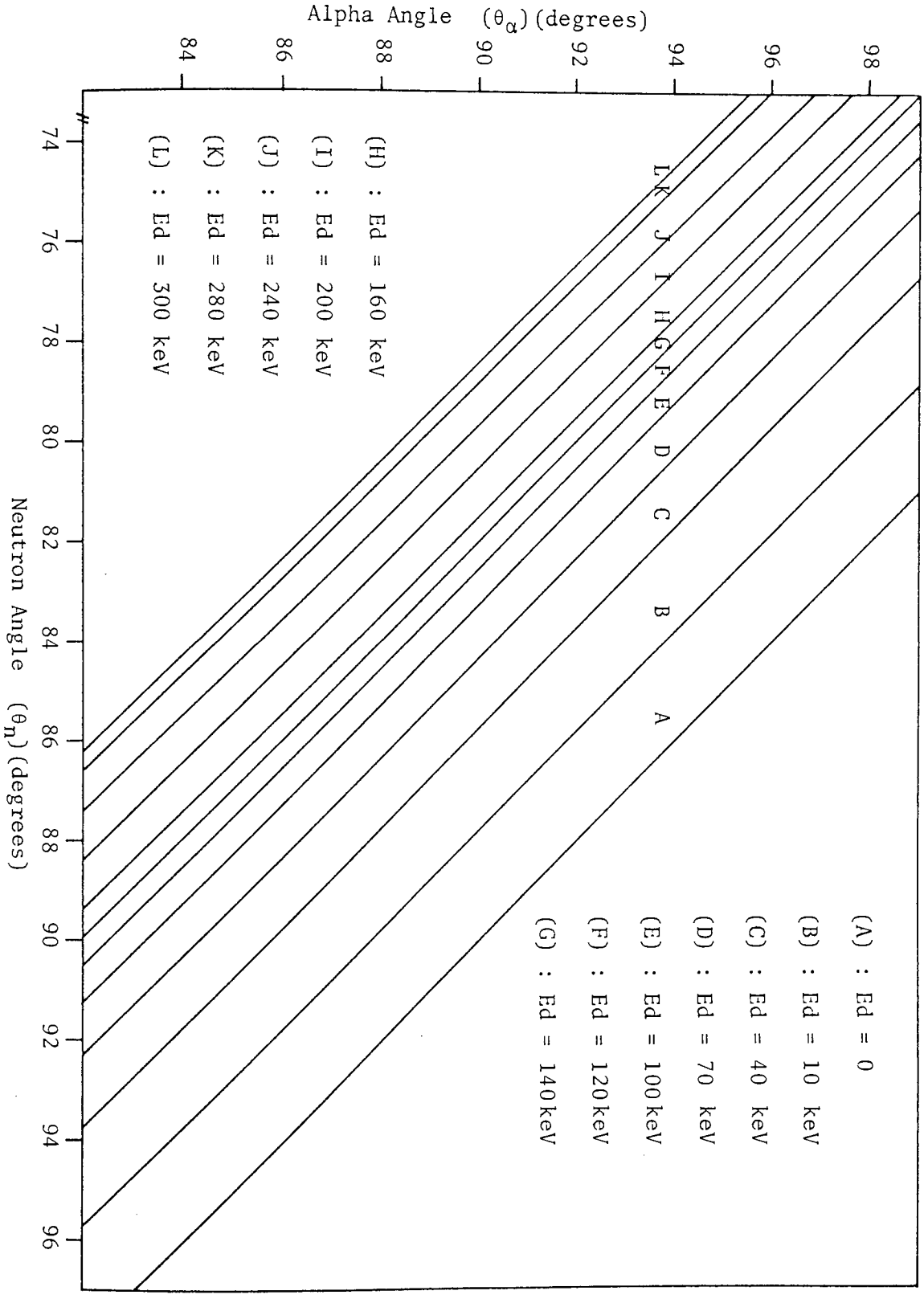

Figure (2.13) Relation between ^4_2He and Neutron Laboratory angles at various incident deuteron energies

2.4.2 The Anisotropy Factor

The two coordinate systems are shown in figure (2.11). The centre-of-mass system is a convenient frame reference to analyse the dynamics of collision. To transfer the differential cross-section from centre-of-mass system to Laboratory frame, an anisotropy factor, i.e. $\frac{d\omega'}{d\omega}$ is required, where $d\omega'$ and $d\omega$ are elements of solid angle in the centre-of-mass and Laboratory system respectively.

Brockmann[50] have investigation the effects of anisotropic scattering in neutron transport and slowing down processes of the neutrons.

The ratio of solid angles is given by:

$$\frac{d\omega}{d\omega'} = \frac{\sin\phi_n \, d\phi_n}{\sin\theta_n \, d\theta_n} \qquad \ldots\ldots (2.19)$$

where (ϕ_n) and (θ_n) are the neutron emission angles in the centre-of-mass and Laboratory frame respectively.

The relation between the centre-of-mass angle ϕ_n and the Laboratory angle θ_n is given by [47]:

$$\cos\phi_n = -\gamma \sin^2\theta_n + \cos\theta_n \, (1 - \gamma^2 \sin^2\theta_n)^{\frac{1}{2}} \qquad \ldots\ldots (2.20)$$

where γ is as defined previously. By differentiating of equation (2.20) and rearranging gives:

$$\frac{d\omega'}{d\omega} = \frac{\gamma[\cos\theta_n + (\frac{1}{\gamma^2} - \sin^2\theta_n)^{\frac{1}{2}}]^2}{(\frac{1}{\gamma^2} - \sin^2\theta_n)^{\frac{1}{2}}} \qquad \ldots\ldots (2.21)$$

Figure (2.14) shows the variation of the neutron anisotropy factor with neutron emission angle θ_n for various deuteron energies.

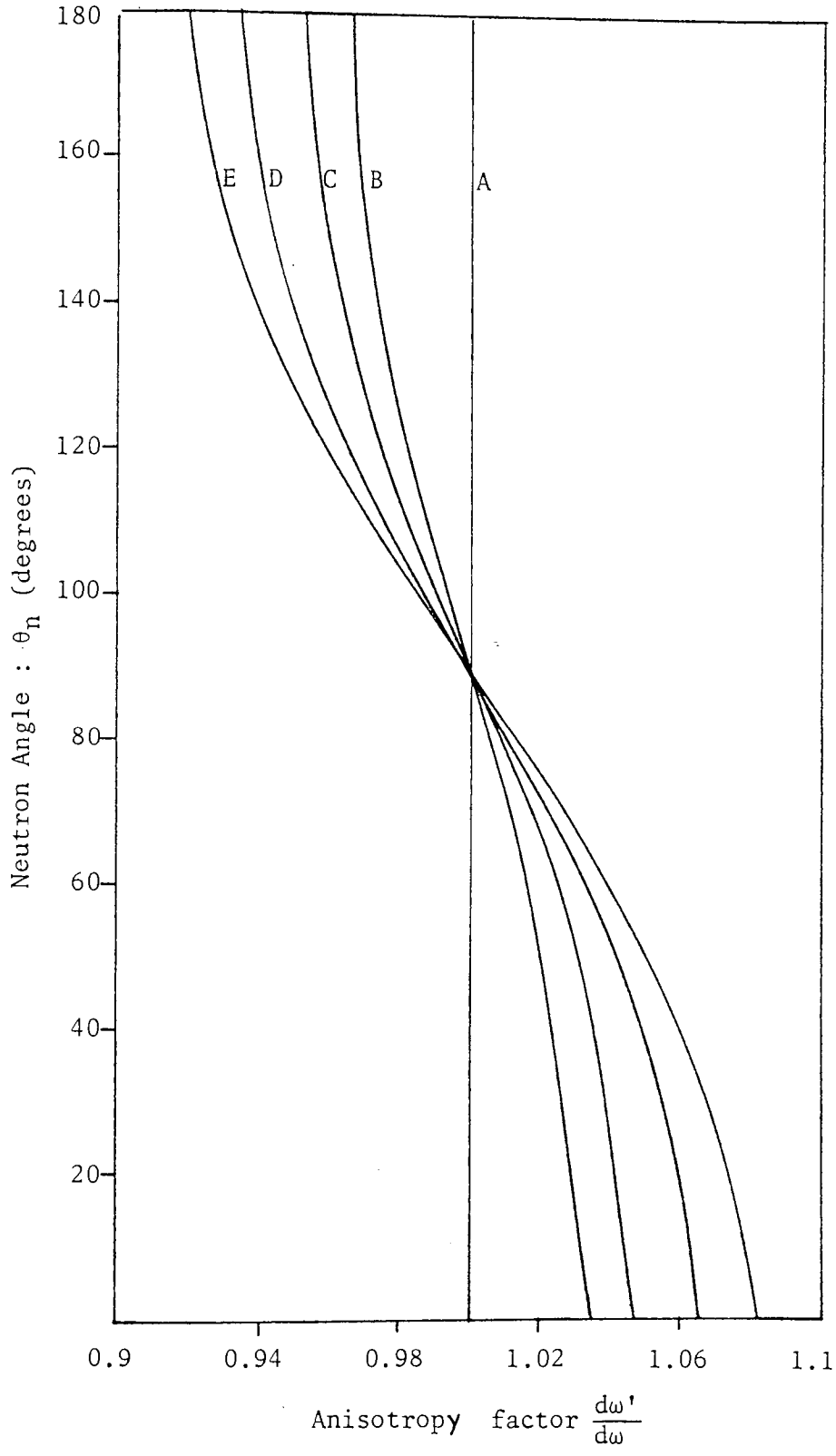

(A) : Ed = 0 (B) : Ed = 50 keV (C) : Ed = 100 keV

(D) : Ed = 200 keV (E) : Ed = 300 keV

Figure (2.14) The neutron anisotropy factor as a function of neutron angle θ_n

2.5 TIME-OF-FLIGHT ELECTRONICS SYSTEM

A block diagram of the electronics used with the associated particle method is shown in Figure (2.15). By using a time-to-pulse height converter (NE 4670) whose pulse height output is directly proportional to the time interval of the two pulses arriving at the converter inputs, the time differences between the "*start*" and the "*stop*" pulses can be measured.

The fast negative output pulses from the anode of the neutron photomultiplier tube are fed into a coaxial cable through an emitter follower, which provides a suitable drive and matching into the coaxial cable. The coaxial cable was connected into the input of constant fraction discriminator (Ortec 463) which accepted pulses whose amplitudes were higher than the theshold level. The pulse at the discriminator output was fed into the "*start*" of the time to pulse height converter.

The anode output of the alpha detector after passing through a coaxial cable is fed into a 100 MHz discriminator system (Ortec 436). The negative output of the discriminator was fed through a gate and delay generator (Ortec 416A) whose delay time is continuously variable from 100 n sec. to 110 μ sec. This delayed signal was used to the stop of the time converter.

By connecting the output pulses of the time converter to the multichannel pulse height analyser, time spectra at different angles were obtained.

To obtain the total number of alpha particles the positive output of the 100 MHz discriminator was fed into a scaler (NE 4681) and a rate meter (Elscint-RM-N-1).

The time converter had a variable time conversion range between (0-50) n sec. to (0-200) μ sec. In this work, the 100 n. sec. time range was used.

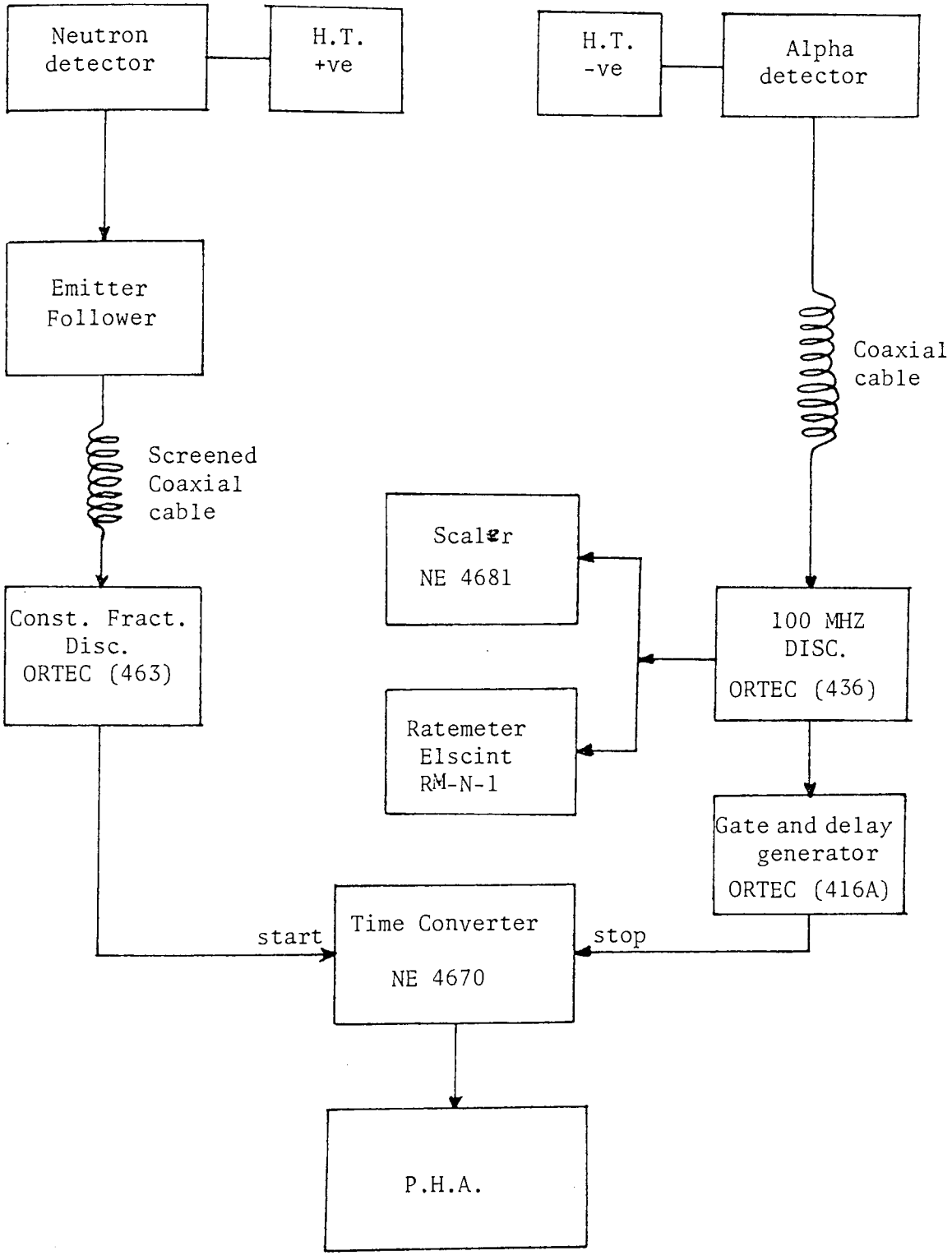

Figure (2.15) Block diagram of time-of-flight electronics system

2.6 THE NEUTRON YIELD

From the theory of the yield of a nuclear reaction, the total yield of neutrons per incident deuteron of energy E is given by:

$$Y(E) = \int_0^E \frac{N_t \cdot \sigma(E) \cdot dE}{dE/dx} \qquad \ldots\ldots (2.22)$$

where Y (E) = the yield of reaction per incident beam particle for a beam of energy E emitting and coming to the rest in the target.

E = the energy of the incident deuterons,

$\sigma_{(E)}$ = the cross-section at a deuteron energy E for the $T(d,m)^4He$ reaction.

N_t = the number of tritium nuclei per unit volume,

and dE/dx = the stopping power of the deuteron in the Ti T target.

The neutron yield per unit solid angle and per incident deuteron energy at a neutron emission angle θ_n can be calculated by:

$$Y(\theta_n) = \int_0^{E_{max}} \frac{\frac{d\sigma}{d\omega} \cdot N_t}{dE/dx} dE \qquad \ldots\ldots (2.23)$$

where $\frac{d\sigma}{d\omega}$ is the differential cross-section per steriadian at a deuteron energy E and neutron angle θ_n.

2.6.1 The Energy Loss of Deuterons in (Ti T) Target

There are no experimental data available on the rate of energy loss for deuterons in (Ti T) target. The rate of loss of energy in Ti-T can be calculated by assuming Bragg's law, if the rates of loss in the constituents $(\frac{dE}{dx})_{Ti}$ and $(\frac{dE}{dx})_T$ are known. The energy loss can be calculated from the relation:

$$(-\frac{dE}{dx})_{Ti\ T} = (\frac{48}{48 + 3\alpha})(\frac{dE}{dx})_{Ti} + (\frac{3}{48 + 3\alpha})(\frac{dE}{dx})_T \qquad \ldots\ldots (2.24)$$

where α = Tritium loading factor

i.e. the number of tritium atoms per titanium

$(\frac{dE}{dx})_{Ti}$ = the energy loss of deuterons in Titanium

and $(\frac{dE}{dx})_{T}$ = the energy loss of deuterons in Tritium.

Warshaw[51] has obtained the stopping power of proton in Al, Cu, and other elements for proton energy of 50 keV to 350 keV(corresponding to deuteron energies 100-700 keV). By assuming that the energy loss is a function of the velocity of the particle, i.e.

$$(\frac{dE}{dx})_{proton}(E) = (\frac{dE}{dx})_{deuteron}(2E) \quad \ldots\ldots (2.25)$$

Benvensite and Zenger[47] using above equation have been calculated $(\frac{dE}{dx})_{Ti}$.

Figure (2.16) shows the rate of energy loss of deuterons in titanium.

The stopping power of deuterons in Tritium was obtained using the proton data of Reynold et al[52].

Assuming the loading factor α = 1 in the calculation, the rate of energy loss of incident deuterons in the target will be:

$$(-\frac{dE}{dx})_{Ti\ T} = 0.94117\ (\frac{dE}{dx})_{Ti} + 0.05882\ (\frac{dE}{dx})_{T} \quad \ldots\ldots (2.26)$$

Gunnersen and James [53] and Granta et al[54] have assumed the tritium loading factor (α) as 1.5 and 1.3 respectively. However, Benvensite and et al[55] have discussed the value of loading factor α, and have found that, a change of a factor 3 in the loading factor will yield a 10% change in the $(\frac{dE}{dx})_{Ti\ T}$.

Table (2.1) shows the energy loss value for deuterons in Ti, T and Ti T target.

Figure (2.17) shows the rate of energy loss of deuterons in titanium

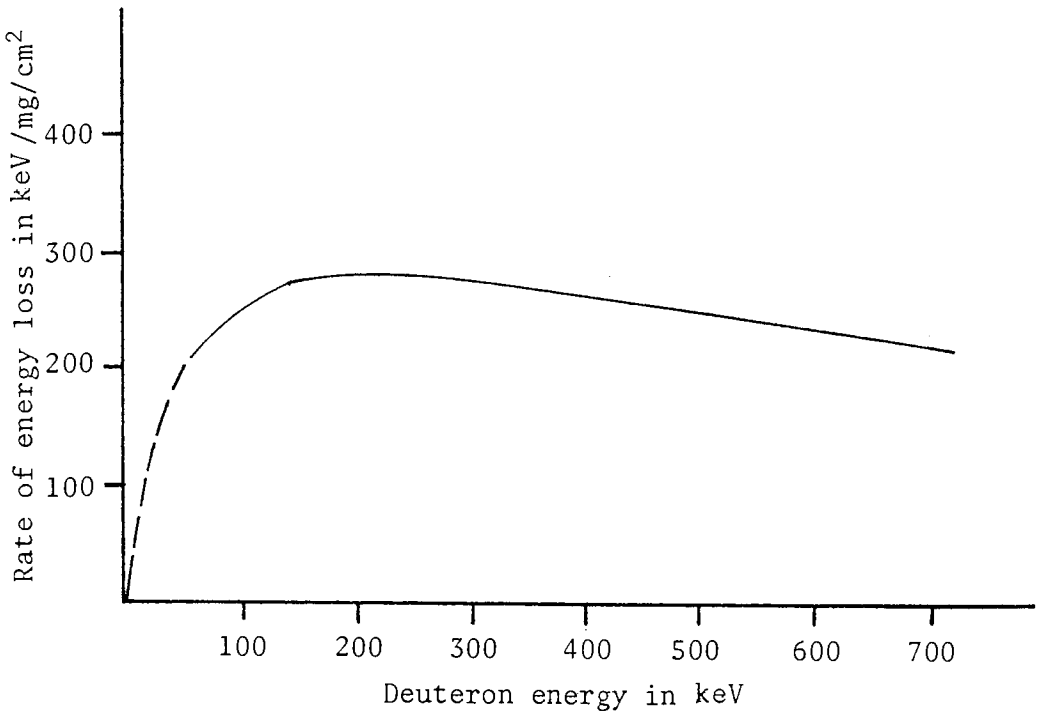

Figure (2.16) The rate of energy loss of deuterons in titanium [47]

tritiated target. For deuteron energies between (300-500 keV) the data are taken from reference [47].

2.6.2 Number of Tritium Nuclei per cm^3, "N_t"

It is assumed that the loading factor (α) of tritium to titanium is constant and equal to unity, throughout the thickness of target material. The value of N_t was obtained as follows:

The density of the target material is:

$$\rho_{Ti\ T} = \frac{(48 + 3)_{Ti\ T}}{(48)_{Ti}} \times \rho_{Ti} \times 0.85 \qquad \ldots\ldots (2.27)$$

The density of Ti is 4.54g /cm^3, and the factor 0.85 arises from the

Table (2·1)

Energy Loss Values for Deuterons in Ti, T and (Ti T) Target

(Values are in keV/mg/cm^2)

E (keV)	$(\frac{dE}{dx})_T$ [47,53]	$(\frac{dE}{dx})_{Ti}$ [47,53]	Calculated $(\frac{dE}{dx})_{Ti\ T}$
10	≃ 490	59	84.4
15	≃ 600	88	118.1
20	≃ 704	108	143.1
25	802	132	171.4
30	890	149	192.6
35	960	163	209.8
40	1023	177	226.8
45	1081	187	239.6
50	1128	193	247.9
60	1183	210	267.2
70	1238	223	282.7
80	1268	233	293.9
90	1281	242	303.1
100	1290	252	313.1
110	1294	260	320.8
120	1295	265	325.6
130	1288	269	328.9
140	1281	273	332.3
150	1271	276	334.5
160	1251	278	335.2
170	1231	280	336.9
200	1211	286	340.4
225	1084	285	332.0
250	≃ 1007	≃ 283	325.6
275	≃ 976	≃ 279	320.0
300	≃ 965	≃ 272	313.0

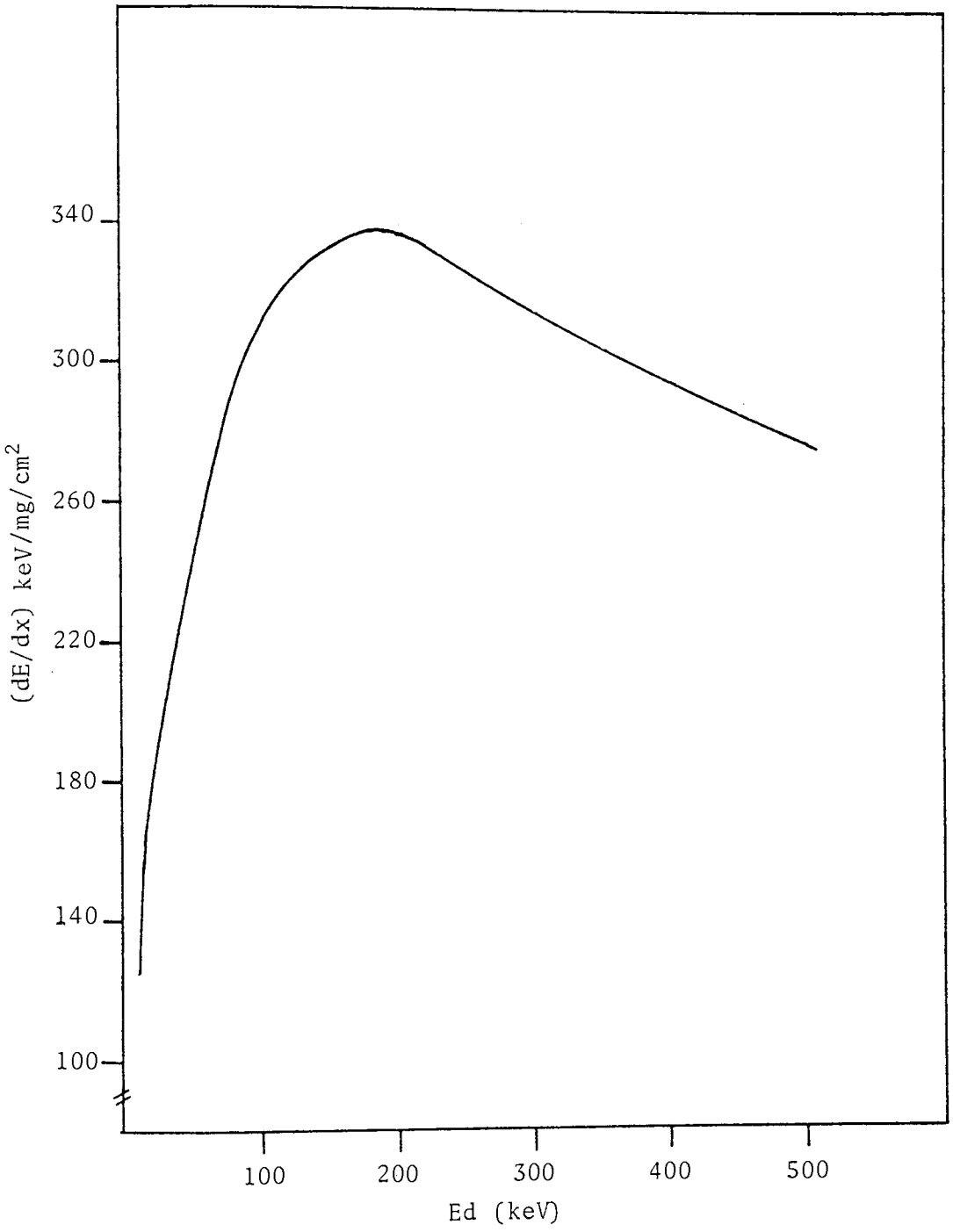

Figure (2.17) The rate of energy loss of deuterons in (Ti T) target keV

15% expansion of titanium during tritiation. The number of N_t of tritium atom/cm^3 is then:

$$N_t = \frac{\rho_{Ti\ T} \times A_o}{A_{Ti\ T}} = \frac{4.22 \times 6.023 \times 10^{23}}{(48 + 3)} = 4.98 \times 10^{22} \text{ atoms/cm}^3$$

2.6.3 Differential Cross-section for the $T(d,n)^4He$ Reaction

The values of differential cross-section of the $T(d,n)^4He$ reaction have been given by Conner, Bonner et al[56] for 10-1732 keV and by Arnold et al[57] for 7.5-120 keV deuterons energy. Argo et al[58] have found that the angular distribution of the neutrons is isotropic in the centre-of-mass system for deuteron energies below 600 keV, and Allen, Pool[59] have reported that up to 200 keV deuteron energy the distribution is isotropic in the centre-of-mass system. Benvensite et al[47] have measured the differential cross-sections for incident deuterons energy up to 500 keV.

Figures (2.18), (2.19) and (2.20) show the differential cross-section of (T-D) reaction from 10 keV up to Ed = 10 Mev. The data of Figure (2.18) were used in the present calculation.

Applying numerical intergration to equation (2.23) and using values of $(\frac{dE}{dx})_{Ti\ T}$, the differential cross-sections and Anisotropy factors, the neutron yield per incident deuteron energy per unit solid angle was obtained from the expression:

$$Y = N_t \sum \frac{\frac{d\sigma}{d\omega'} \times \frac{d\omega'}{d\omega}}{\frac{dE_d}{dx}} dE_d \qquad \ldots\ldots (2.28)$$

Figure (2.21) shows the relative neutron yield as a function of deuteron energy.

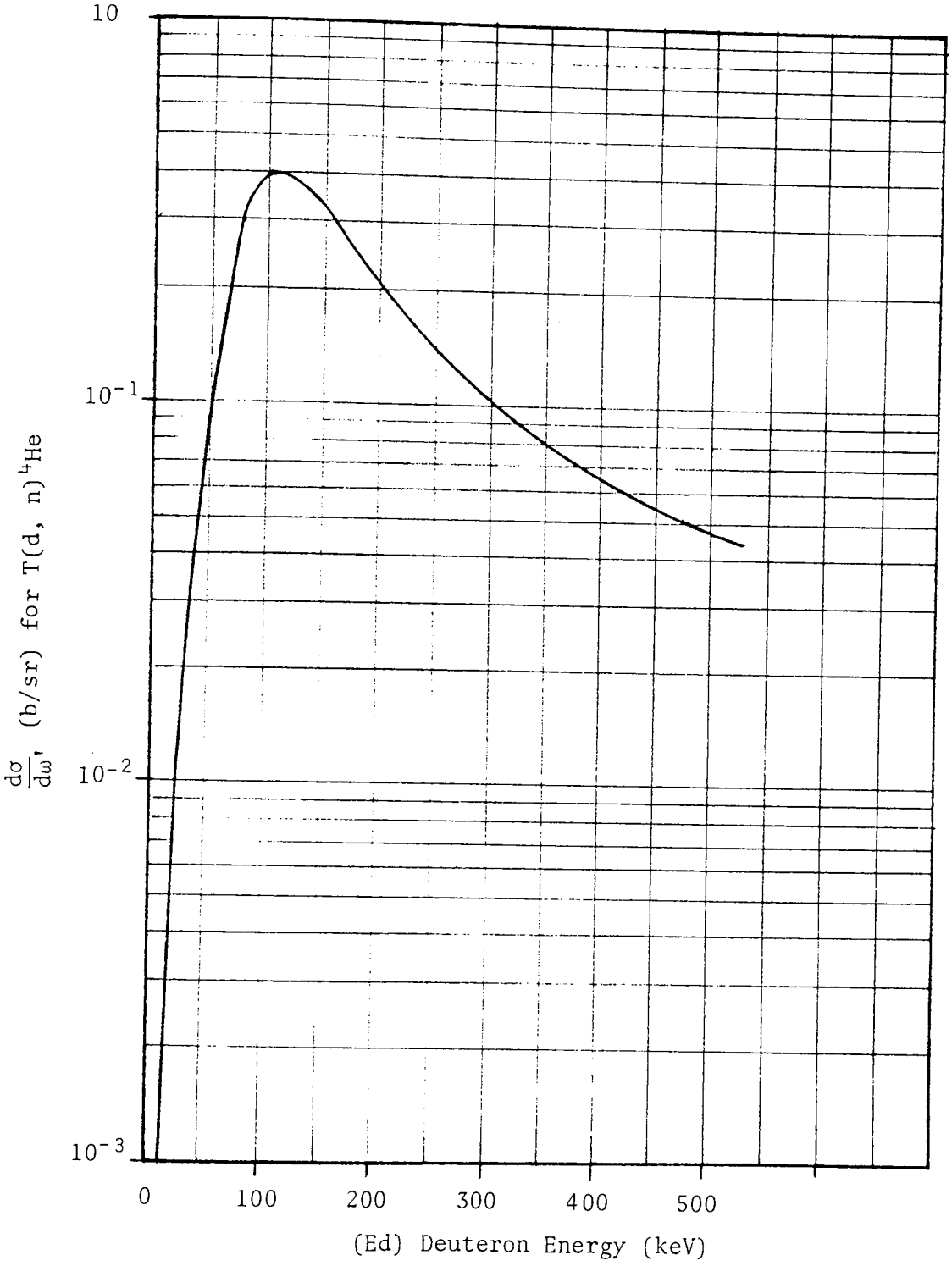

Figure (2.18) Differential cross-section for the production of neut rons from the T(d, n)^{4}He Reaction [47]

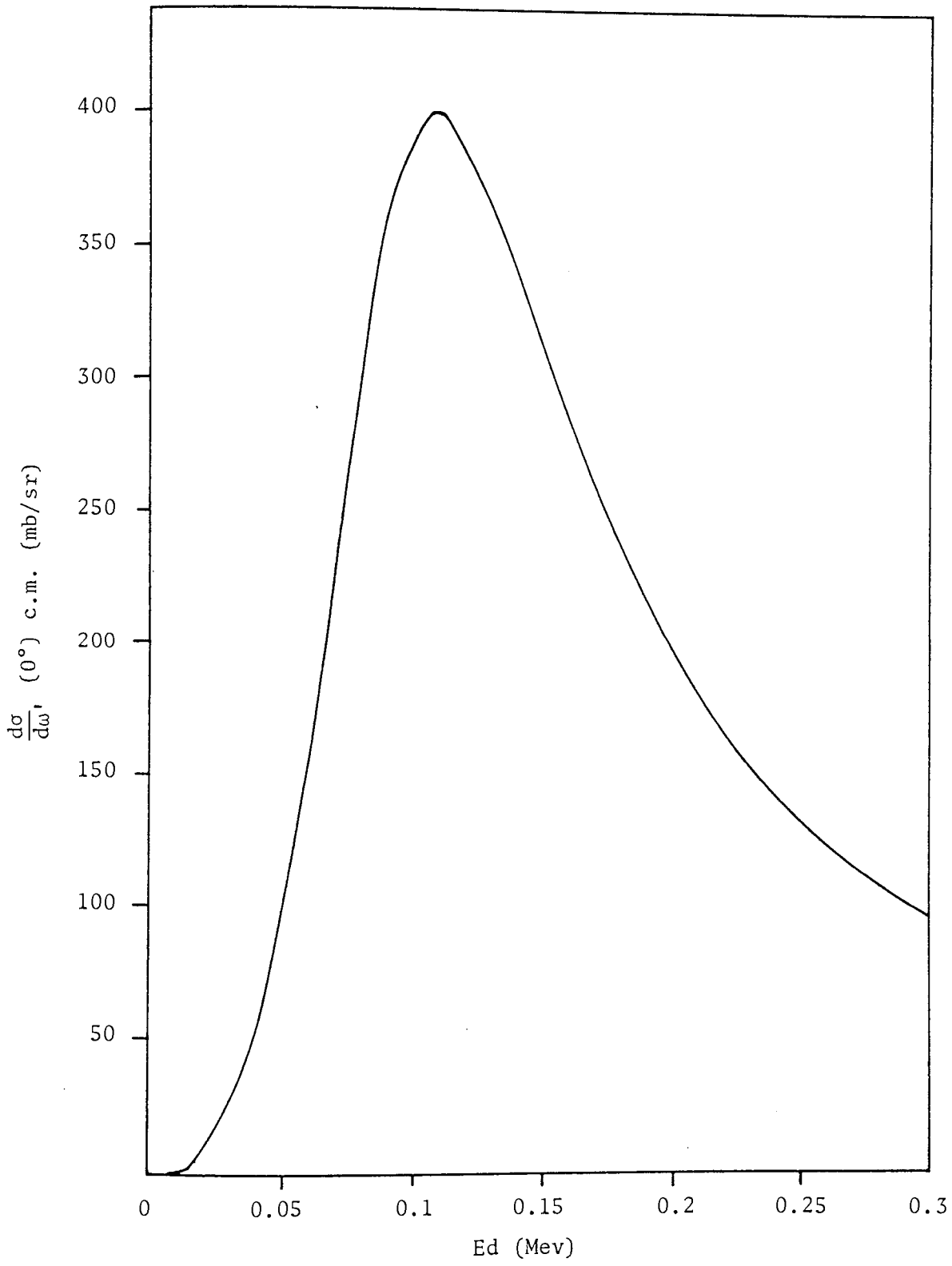

Figure (2.19) Differential cross-section of T(d, n)^{4}He reaction at (0) deg. in centre-of-mass system [60-61]

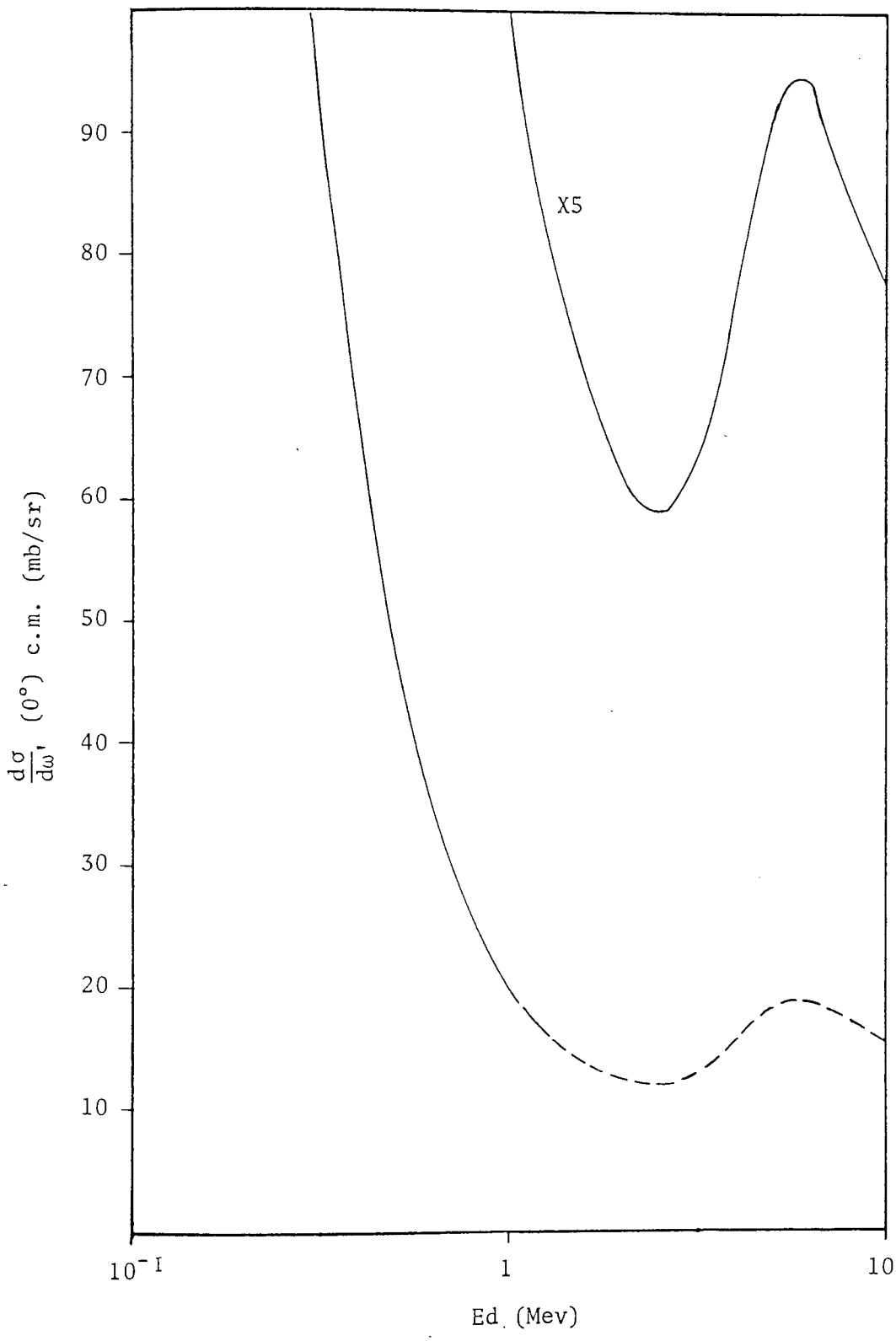

Figure (2.20) Differential cross-section of T(d, n)^{4}He reaction at (0°) in centre-of-mass system [60-61]

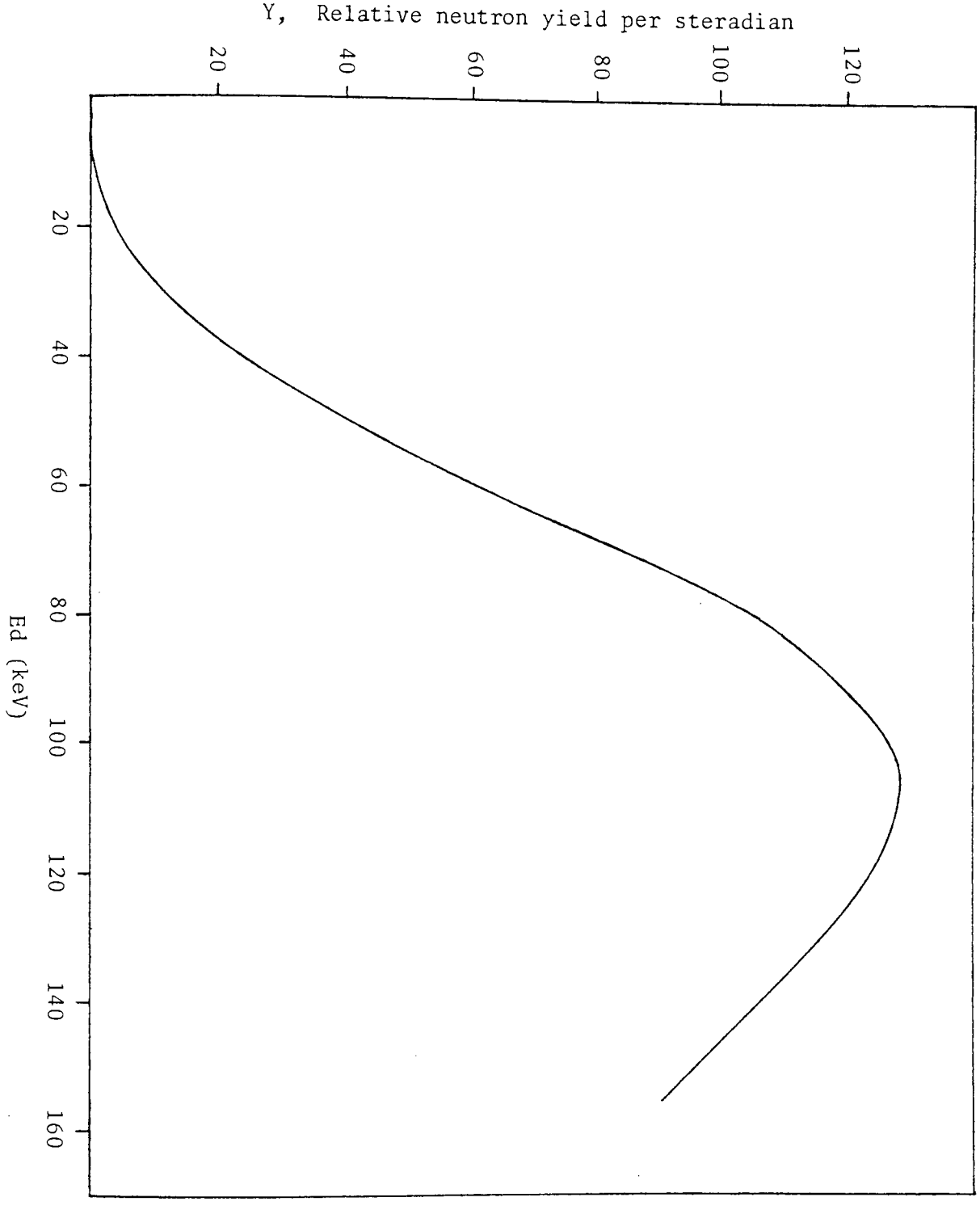

Figure (2.21) The relative neutron yield as a function of deuteron energy

2.6.4 The Neutron Beam Profile

It has been shown that the neutron angle varies with the deuteron energy, and the relative neutron yield varies with E_d. The relative neutron yield at each angle θ_n, is described by the neutron beam profile, and can be calculated using the information of figure (2.13) and figure (2.21) which give the variation of neutron angle with alpha particle angle, and the neutron yield with deuteron energy respectively.

For each neutron angle the area under the curve of figure (2.21) in the energy interval of Ed_1 to $Ed_2 = Ed_1 + dE_d$ is proportional to the neutron yield for that deuteron energy interval. Thus the relative neutron yield at each angle θ_n, as defined by the alpha-detector, can be calculated.

The calculated neutron beam profile as defined by the alpha particles produced at 90 ± 6° is shown in figure (2.22). The curve was obtained using 1° steps for each neutron angle.

The FWHM of the neutron beam profile is 12° and the total width of the associated neutron beam is 17°.

2.6.5 The Neutron Line Shape

The line shape refers to the energy spread of the neutrons striking the sample. The energy spread of the neutron is influenced by a number of factors:

(1) if the primary beam of charged particles inducing the reaction has a spread in energy, the neutrons produced will likewise share this spread.

(2) the solid angle of the alpha detector with respect to the target

(3) the other factor is the degradation of the incident beam in the target material.

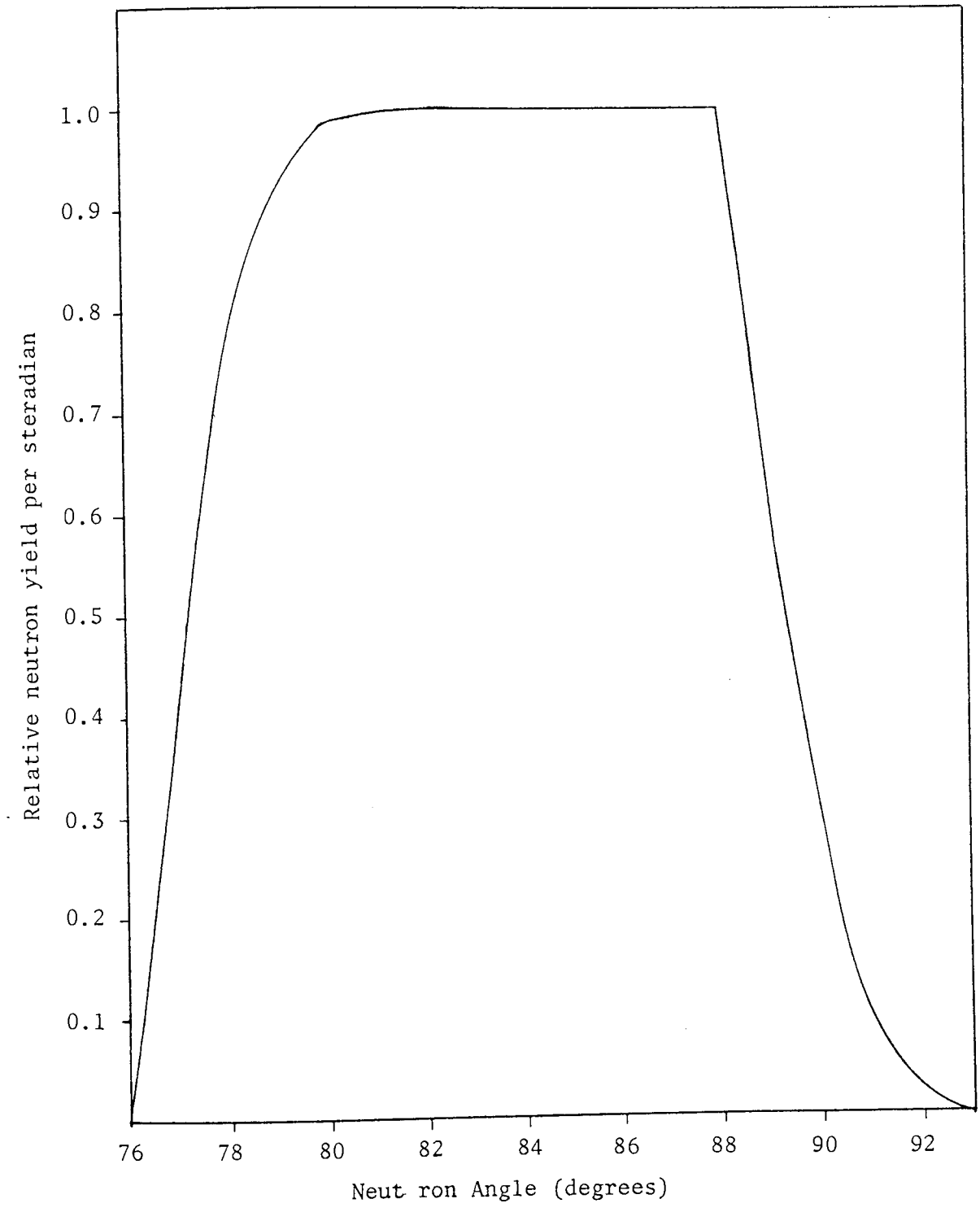

Figure (2.22) The neutron beam profile, defined by the 90 ± 6° alpha detector

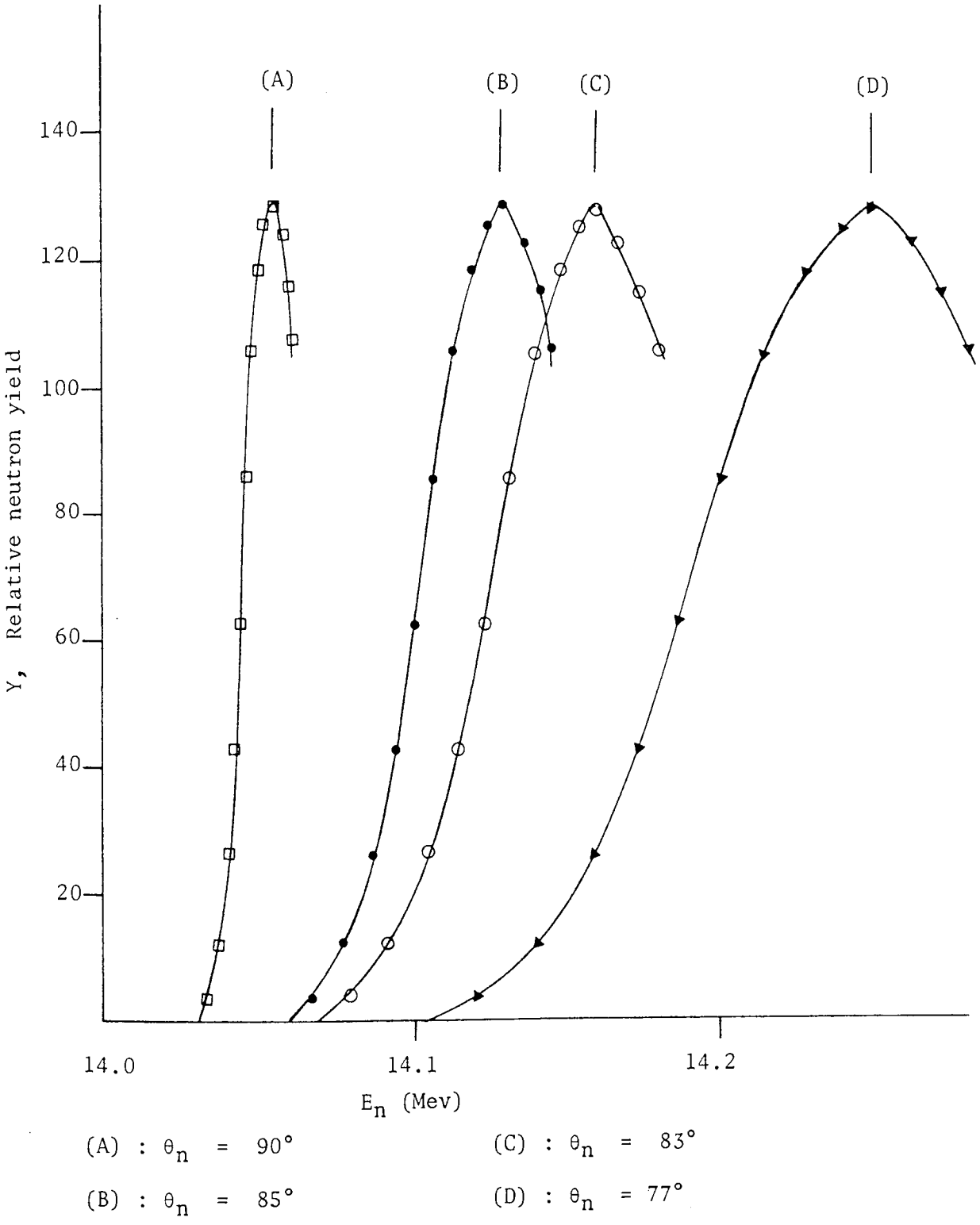

Figure (2.23) The neutron line shape for different values of θ_n

The neutron energy is given by equation (2.11) which is a function of neutron angle and deuteron energy. The abscissa of the Line shape is the neutron energy resulting from the equation (2.11), and the ordinate is proportional to the neutron yield in the Laboratory system. It is determined from the equation (2.28), i.e.

$$Y(\theta_n, E_d) \alpha \frac{\frac{d\sigma}{d\omega'} \times \frac{d\omega'}{d\omega}}{\frac{dE_d}{dx}} dE_d \qquad \ldots\ldots (2.28)$$

The neutron Line shapes for various neutron angles are shown in Figure (2.23).

2.7 THE SPECTROMETER RESOLUTION

The resolution is usually defined in terms of the full width of the peak at half maximum amplitude (FWHM).

The time resolution of the spectrometer was measured by observing the direct neutron beam spectrum at 83° to the incident deuteron beam direction. The FWHM of the spectrometer was 2.5 ± 0.2 n.sec. Figures (2.24) and (2.25) show the time spectra at zero degrees to the incident neutron beam direction. The full width at 1/10 maximum was obtained as 3.9 ± 0.4 n.sec. which is shown in figure (2.24).

In the measurement of the time spectrum, several factors will affect to the time resolution of the spectrum. The overall time spread Δ_T, which may be written as:

$$\Delta T^2 = \Delta T_p^2 + \Delta T_d^2 + \Delta T_s^2 + \Delta T_E^2 \qquad \ldots\ldots (2.29)$$

where ΔT_p = represents the uncertainty in the neutron production time

ΔT_d = the time uncertainty in the neutron detection times

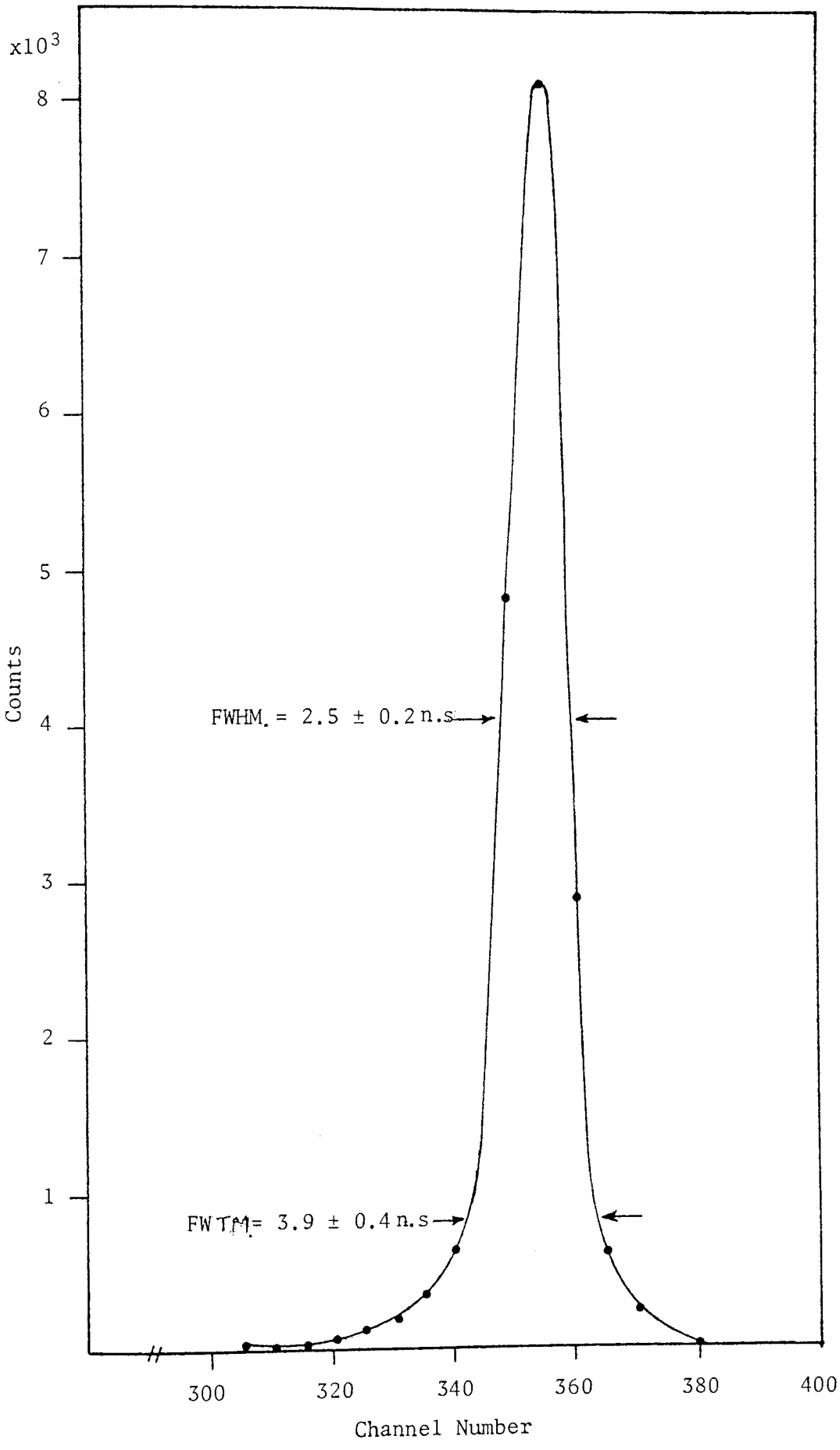

Figure (2.24) Time spectrum at zero degree without sample for 14 Mev neutrons

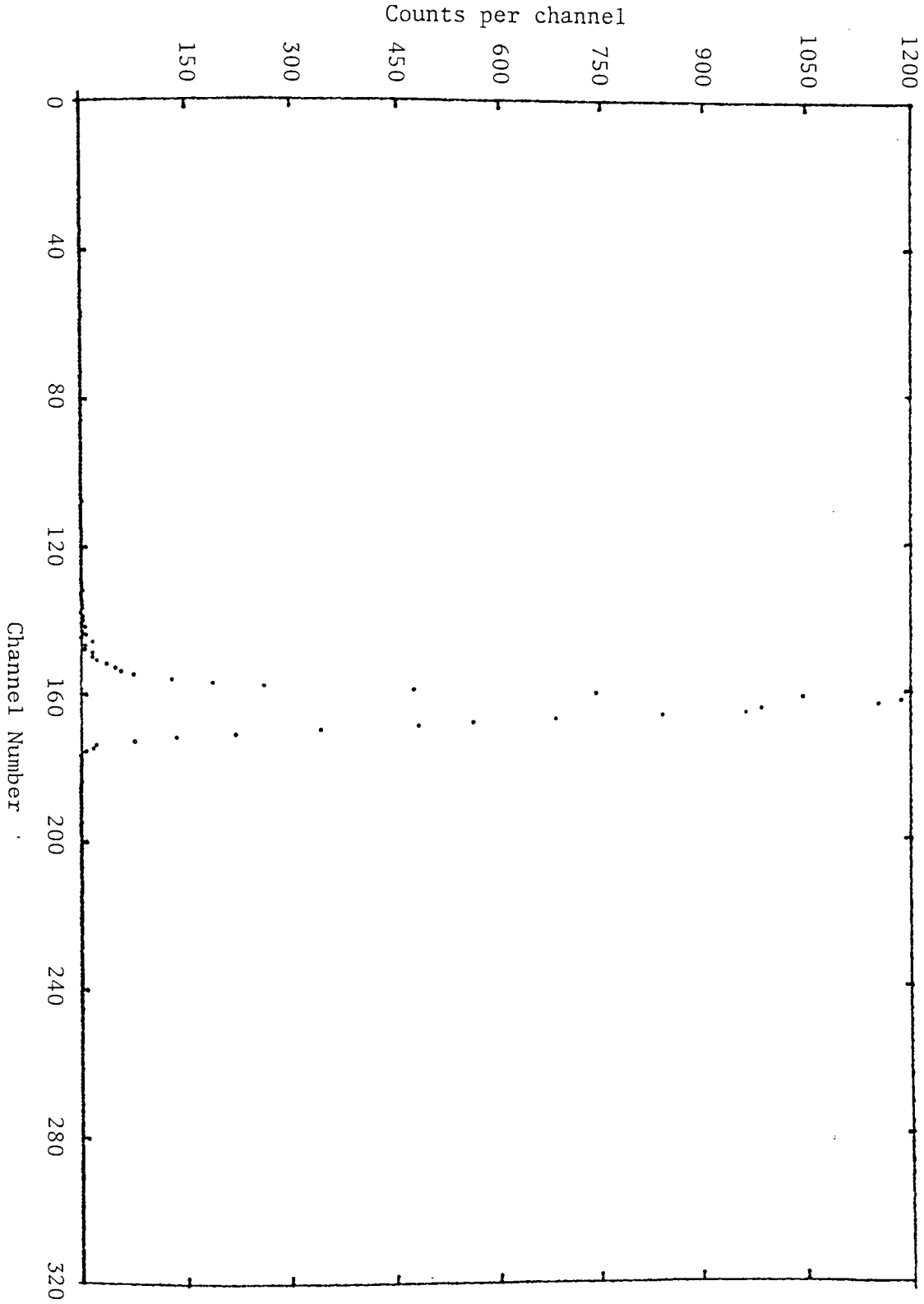

Figure (2.25) Time spectrum at 0° without sample for 14.4 Mev neutrons

owing to the thickness of the detector.

This time uncertainty in the scintillation counter has been discussed by Mosznski and Bengtson[62] and can be due to some factors:

(a) the energy transfer from the detected nuclear particles to the optical levels in the scintillator

(b) the finite decay time of light emitting states in the scintillator and the light yield of the scintillator as a function of the energy of the detected radiation.

(c) variation of the light collection from the scintillator at the photo cathode.

(d) variation of the transit time of the photo electrons

(e) variation of the multiplication process in the electron multiplier.

ΔT_S = the time uncertainty due to finite neutron energy spread, and finally,

ΔT_E = the time uncertainty in the electronic system.

The energy spread of the alpha particles due to the 12° angular range subtended by the alpha detector was 70 keV.

A typical time spectra from the 2 cm. Iron sample at 25° and 5 cm concrete material at 35° are shown in figure (2.26) and figure (2.27) respectively.

In the present work, with the resolution of the neutron detector, it was not possible to resolve elastic neutron peak from the first inelastic peak of iron, from excited state with 0.846 Mev, nor some of the elements in the concrete. The detailed explanation is given in chapter 5.

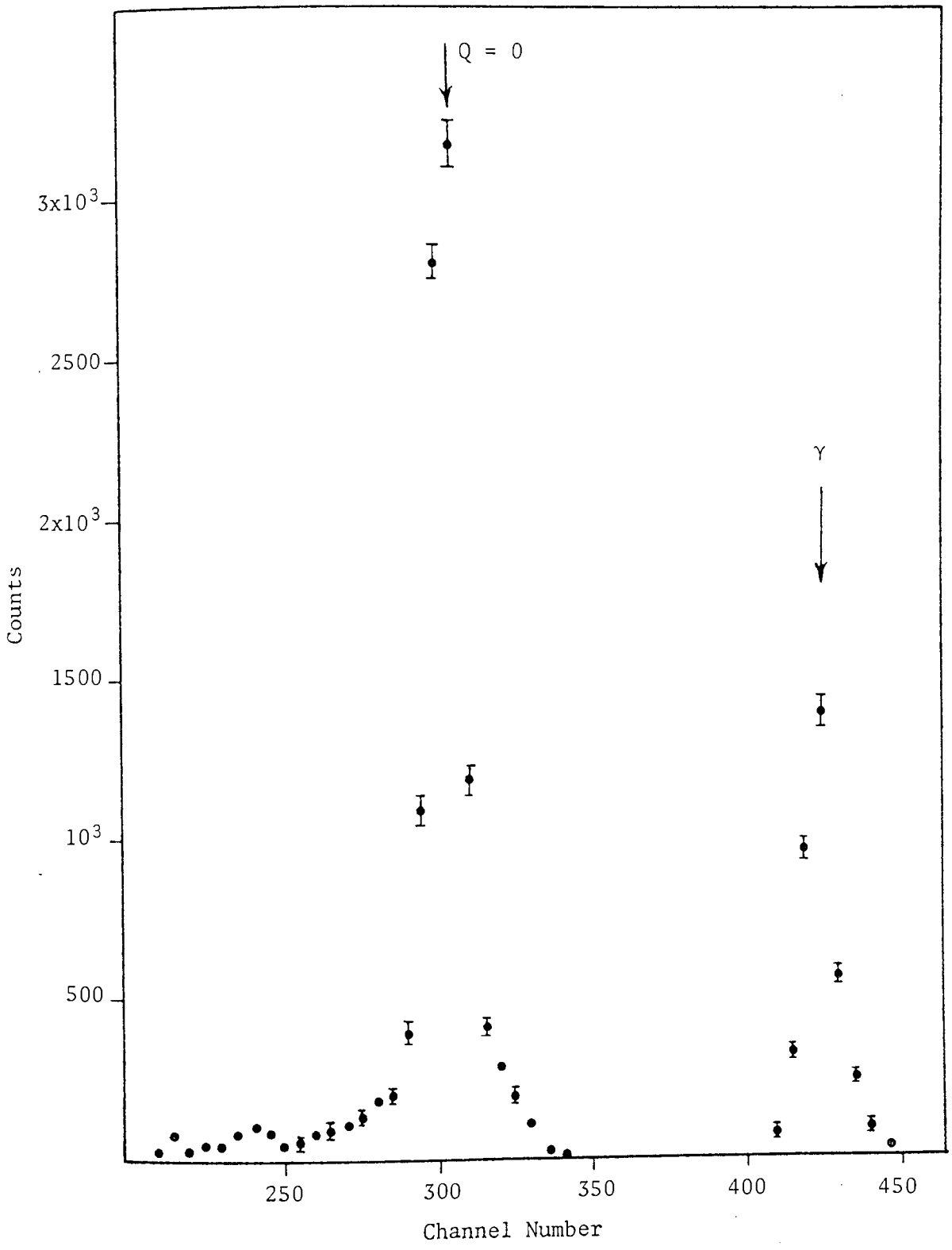

Figure (2.26) Typical time-spectrum for scattering in 2 cm. thick Iron at $\theta_n = 25°$

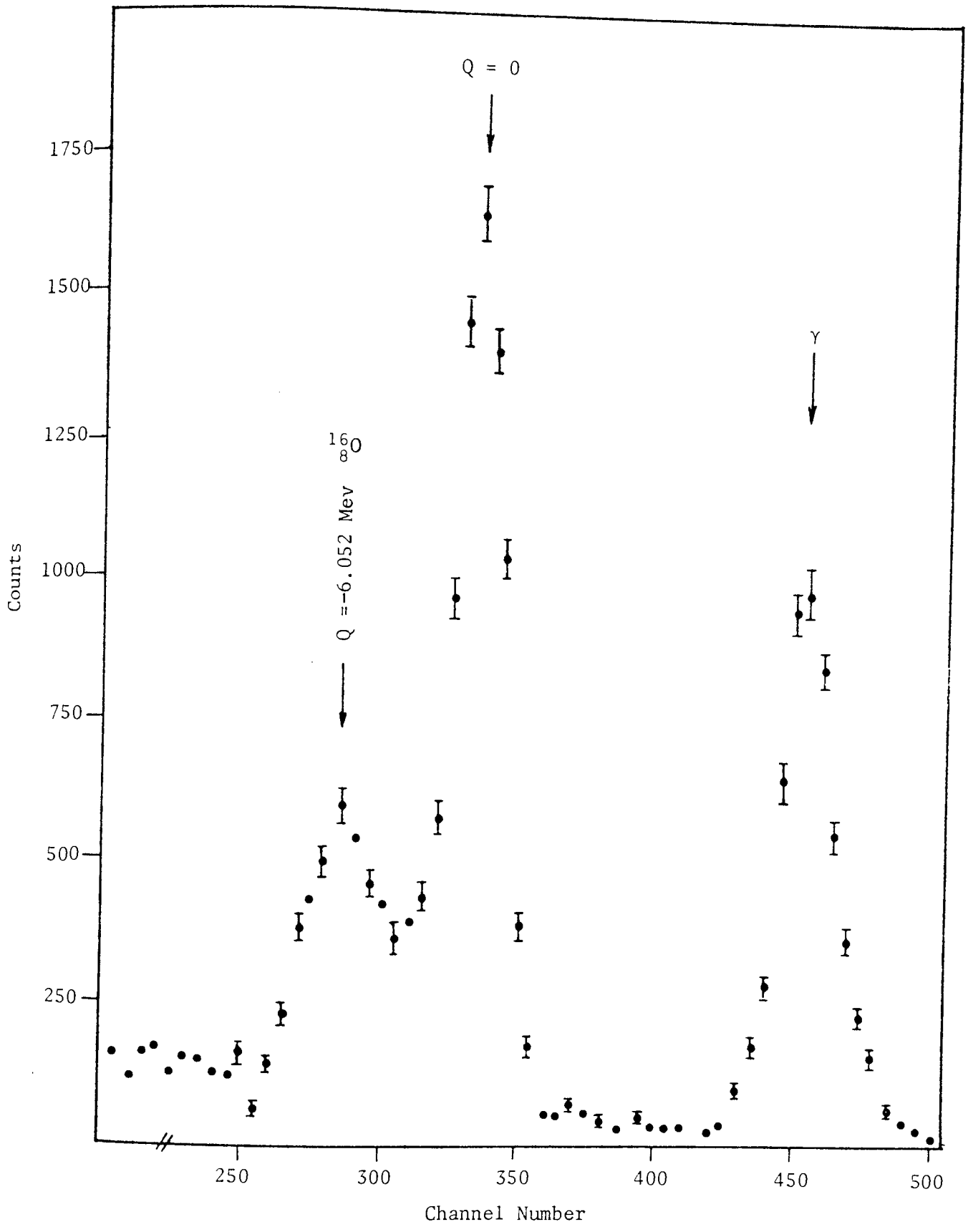

Figure (2.27) Typical time-spectrum for scattering in 5 cm. Thick Concrete sample at $\theta_n = 35°$

CHAPTER THREE

CHAPTER THREE

NEUTRON AND CHARGED PARTICLE DETECTION

3.1 INTRODUCTION

The neutron is an electrically neutral particle, it cannot therefore be detected with the usual detectors employed for ionizing radiation. It is therefore detected indirectly using nuclear reactions, that produce charged particles. The most widely used method of fast neutron detection is to use an organic scintillator, and the (n,p) scattering process. The interaction transfers some portion of the neutron kinetic energy to the target nucleus, resulting in a recoil nucleus. By far the most popular target nucleus is hydrogen. The cross-section for neutrons elastic scattering from hydrogen at E_n = 14 Mev is about 0.7 barn, and ($\sim$ 2.5 b for 2.5 Mev neutrons) and its energy dependence is well known.

In this scattering the neutron can transfer up to its entire energy in a single collision with a proton nucleus, whereas only small fraction of energy can be transferred in collision with heavy nuclei. Table (3.1) shows the maximum fraction of the incoming neutron energy that can be transferred to a recoil nucleus in a single collision for different target nuclei, which were calculated from kinematics of nuclear reactions, (see section 2.4), i.e.

$$E_R = \frac{4A\ E_n}{(A+1)^2} \cdot \cos^2\theta \qquad \ldots\ldots (3.1)$$

where E_R = energy of the recoil nucleus (in Lab. system)

A = mass of the target nucleus/neutron mass

θ = scattering angle of the recoil nucleus in the laboratory coordinate system

and E_n = incoming neutron kinetic energy

In a head-on collision of the incoming neutron with target nucleus i.e. ($\theta \simeq 0$), the equation (3.1) can be written as:

$$(E_R)_{max.} = \frac{4A\ E_n}{(1 + A)^2} \qquad \ldots\ldots (3.2)$$

Table (3.1)

Maximum Fractional Energy Transfer in

Neutron Elastic Scattering

Target Nucleus	A	$(E_R/E_n)_{max}$
$^{1}_{1}H$	1	1.000
$^{2}_{1}H$	2	0.889
$^{3}_{2}He$	3	0.750
$^{4}_{2}He$	4	0.640
$^{12}_{6}C$	12	0.284
$^{16}_{8}O$	16	0.221

The resulting recoil protons from the (n,p) reaction are relatively easy to detect for fast neutrons and serve as the basis for a wide variety of fast neutron detectors.

3.2 CHOICE OF DETECTOR

Organic scintillators are widely used for detecting nuclear radiations. The early development of organic scintillation detectors and scintillation mechanisms have been discussed by Birks[63], and development

since 1964 on the characteristics of scintillation and properties of various organic scintillators are discussed by Brooks[64]. The organic scintillation detector has been widely used to detect neutrons with energies of a few Mev.

Different types of scintillators, e.g. organic crystals (anthracene, or stilbene), organic liquids (e.g. NE 213), and plastics (e.g. NE 102) have been developed for various applications.

Scintillators normally respond directly to the ionization generated by charged particles. Neutral radiations (e.g. gamma rays and neutrons) are detected if they produce recoil electrons or recoil nuclei respectively within the scintillator material. These materials emit light when bombarded with nuclear radiations. The ideal scintillation material should convert the kinetic energy of charged particles into detectable light with a high scintillation efficiency, and this conversion should be linear, i.e. the light yield should be proportional to deposited energy, the decay time of the induced luminescence should be short, so that fast signal pulses can be generated, and finally the material should be of good optical quality.

In scintillation detectors, the light is normally detected by a photomultiplier tube, which gives a large pulse at the anode.

The main characteristics of organic scintillators which have to be considered are [64].

(1) The variation of response with energy for different types of charged particles.

(2) The absolute scintillation efficiency, the response resolution and the associated energy resolution

(3) the fast timing characteristics.

For organic scintillation detectors high efficiencies (accurate to

< 1 to 10%) are possible over a wide energy range (∿ 100 keV to 100 Mev) with energy resolution from 3 to 30% above 100 keV[66].

There are three advantages of using recoil protons. First, the energy of the recoil protons is much higher than any other recoil nucleus. Second, the n-p elastic scattering cross-section is high, and third, up to 20 Mev, the neutron-proton scattering has isotropic angular distribution in the centre-of-mass coordinate system [65].

In general the counters chosen for the detection of fast neutron should have the following characteristics:

(A) detection of minimum ionizing particles, since a greater light output of the scintillator for higher ionizing particles improves the resolution

(B) high efficiency

(C) good discrimination against gamma-ray background

(D) good pulse height resolution for neutron spectroscopy

(E) neutron detectors for fast neutrons should have low efficiency for slow neutrons, to reduce the background from neutrons with energies below the region of interest.

However, the sensitivity of organic scintillators to gamma-rays relatively high. Using electronics and time-of-flight techniques, it is possible to discriminate against gamma-rays in a mixed gamma and neutron environment.

In this work a plastic scintillator type NE 102A was used and it is discussed in section (3.3)

3.3 PLASTIC SCINTILLATOR NE 102A

Among different scintillators the ones which have found wide application as neutron detectors are:-

(A) liquid organic scintillators

(B) plastic scintillators

There are close similarities in the behaviour of plastic and liquid scintillators, however, among the practical problems of liquid scintillators, when used as large volume detectors, is needed for a resistant and strong containing vessel, and difficulties in handling large volumes. Because of the ease with which plastics can be shaped and fabricated, they have become an extremely useful form of organic scintillators.

Plastic scintillators are available with a good selection of standard sizes of rods, cylinders and flat sheets, and because the material is relatively inexpensive, plastics are often the practical choice of large volume solid scintillators.

Swank and Buck[67] have found the most promising scintillator material was TPB. (1, 1, 4, 4-tetraphenyl-butadine: C_{28} H_{22}) in polyvinyltoluene because the pulse height production was greater than the other several polystyrene solution specimens. In addition they have shown that polyvinyltoluene (PVT) is an efficient scintillator solvent.

In the present work a plastic scintillator type NE 102A with 50.8 mm thick and 50.8 radius manufactured by the Nuclear Enterprised Ltd. was used, as it seems to ensure, the best compromise between large light yield short fluorescence decay time, and good light transmission properties.

The light output has a rise timeof 0.9 n.sec and an exponential decay time with a time constant t_c = 2.4 n.sec [68].

The timing uncertainty of plastic scintillator due to variations in flight times to different detection points in the detector can be found from the relation:

$$dt = \frac{\ell}{\sqrt{(2E_n/m)}} \qquad \ldots\ldots (3.3)$$

where ℓ = the thickness of the detector

m = the neutron mass

and E_n = the Energy of neutron incident on the detector

For 14.0 Mev neutrons the time uncertainty for ℓ=5 cm. NE 102 A scintillator was $\sim$ 1 n. sec and for 2.5 Mev neutrons for the same detector, timing uncertainty = 2.28n.sec.

3.4 ENERGY DISTRIBUTION OF THE RECOIL PROTONS

From the kinematics of neutron collision in the centre-of-mass co-ordinate (c.o.m. system), for incoming neutrons with energy E_n, the energy of recoil nucleus E_R is given by the equation:

$$E_R = \frac{2A\ E_n}{(1 + A)^2}(1 - \cos\phi) \qquad \ldots\ldots (3.4)$$

where A = mass of target nucleus/neutron mass

ϕ = scattering angle of the neutron in the c.o.m. system

E_R = energy of the recoil nucleus

and E_n = energy of the incident neutron

In order to convert to the Laboratory coordinate system (Lab), ($\phi = 2\theta$) the following transformation can be used:

$$2\cos^2\theta = 1 - \cos\phi \qquad \ldots\ldots (3.5)$$

where θ = scattering angle of the recoil nucleus in the Laboratory coordinate system.

When combined with equation (3.4), the recoil nucleus energy will be the same as equation (3.1), i.e.

$$E_R = \frac{4A\ E_n}{(1 + A)^2}\cos^2\theta \qquad \ldots\ldots (3.1)$$

From table (3.1) it is seen that for a proton (A = 1) the neutron can transfer all of its energy in a head-on collision. Hence, for neutron-proton scattering equation (3.1) becomes:

$$E_p = E_n \cos^2\theta \qquad \ldots\ldots (3.6)$$

We must also consider the way in which the recoil energies are distributed between a minimum of zero and the maximum given in table (3.1).

If we define $\sigma(\phi)$ as the differential scattering cross-section in the (c.o.m. system), then by definition, the probability that the neutron will be scattered into an angular region $d\phi$ about ϕ is:

$$p(\phi)\, d\phi = 2\pi \sin\phi d\phi \cdot \frac{\sigma(\phi)}{\sigma(s)} \qquad \ldots\ldots (3.7)$$

where $\sigma(s)$ = total scattering cross-section integrated over all angles.

Using the relation:

$$p(E_R)\, dE_R = -p(\phi)\, d\phi \qquad \ldots\ldots (3.8)$$

where E_R is the energy of recoil nuclei in Laboratory system. By differentiation of equation (3.4), the probability of creating a recoil energy with energy in dE_R about E_R is:

$$p(E_R) = \frac{(1 + A)^2}{A} \cdot \frac{\sigma(\phi)}{\sigma_s} \cdot \frac{\pi}{E_n} \qquad \ldots\ldots (3.9)$$

From equation (3.9), the probability of observing the proton energy from E_p to $E_p + dE_p$ in a shortway is:

$$p(E_p) \propto \frac{1}{E_n} \qquad \text{where } 0 \leq E_p \leq E_n$$

$$\text{and} \qquad = 0 \qquad \text{where } E_p > E_n \qquad \ldots\ldots (3.10)$$

Equation (3.9) shows that the shape expected for the recoil continum is the same as the shape of differential scattering cross-section $\sigma(\phi)$ as a function of centre-of-mass scattering angle of neutron.

For neutron-proton collisions below E_n = 20 Mev it has been found that the scattering is isotropic in the centre-of-mass system[69,65].Thus, $\sigma(\phi)$ does not change with ϕ, and is equal to a constant $\frac{\sigma_s}{4\pi}$.

Therefore, the expected proton recoil energy distribution is a rectangular spectrum, extended from $E_p = 0$ to $E_p = E_n$ as shown in figure (3.1).

3.5 SCINTILLATOR EFFICIENCY

Precise knowledge of the efficiences of these scintillators is necessary to obtain the minimum possible error in the final results.

The efficiency of an organic scintillator is defined as the ratio of the number of recoil protons to the number of incident neutrons. The detection efficiency of a device based on recoil protons can be calculated from the scattering cross-section σ_s. If only one kind of nuclei are present in the detector, the efficiency is simply given by:

$$\varepsilon = \frac{N_1}{N_0} = 1 - \exp(-n\,\sigma_s\,x) \qquad \ldots\ldots (3.11)$$

where n = the number of target nuclei/unit vol.

N_0 = flux of incident neutron all of energy E_0

N_1 = number of recoil nuclei produced in the scintillator

and x = path length through the detector for incident neutrons.

At energies less than about 12 Mev, (n-p) scattering is the dominant neutron interaction in hydrogen media [64] but at higher energies interactions with the carbon component become increasingly important.

Assuming only single scattering occurs in the scintillator consisting of carbon and hydrogen, the efficiency of the detector produced in a

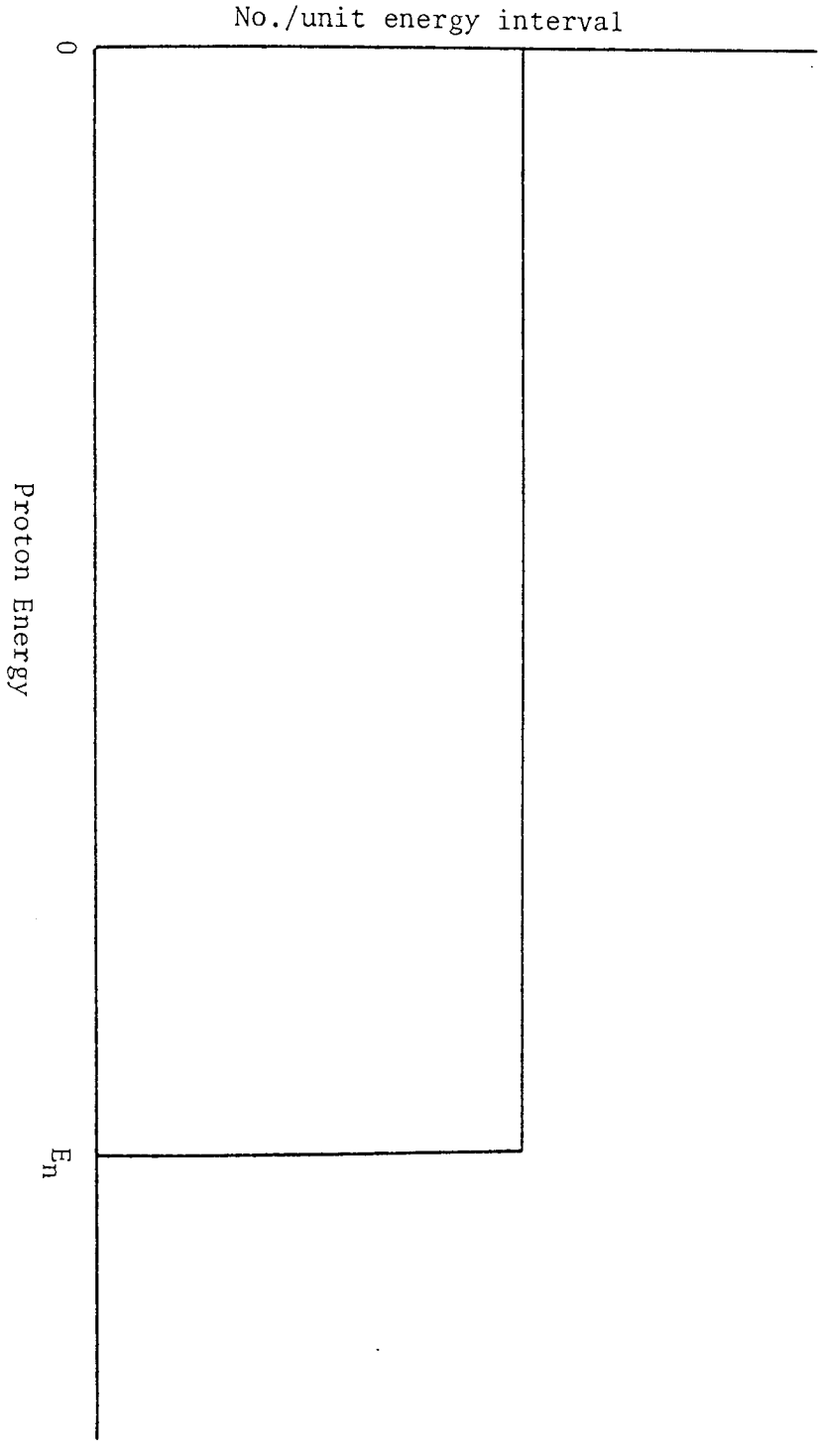

Figure (3.1) Energy distribution of recoil protons

scintillator of length L, is given by [70,72]:

$$\varepsilon_1(E_o,\ L) = \frac{N_1(E_o)}{N_o} = n_H\ \sigma_H\ L\ f(aL) \qquad \ldots\ldots\ (3.12)$$

where $N_1(E_o)$ = number of recoil protons produced

$$f(aL) = [1 - \exp(-aL)]/aL \qquad \ldots\ldots\ (3.13)$$

with $a = n_H\ \sigma_H + n_c\ \sigma_c$

Here n_H = number of hydrogen atoms per unit volume of scintillator

σ_H = neutron-proton scattering cross-section at neutron energy E_o

n_c = number of carbon atoms per unit volume of crystal

and σ_c = neutron carbon cross-section at neutron energy E_o

The parameter f(aL) allows for the attenuation of the neutron beam in passing through the scintillator.

Plots of the elastic scattering cross-section for hydrogen and carbon are shown in figure (3.2) and figure (3.3) respectively.

For NE 102A scintillator, the densities of n_H and n_c are given by the manufacturers as:

$$n_H = 5.25 \times 10^{22} \text{ atoms/cc}$$

and

$$n_c = 4.75 \times 10^{22} \text{ atoms/cc}$$

Applying equation (3.12) to NE 102A detector, the efficiency curve obtained, and it is shown in figure (3.4).

The total neutron-proton scattering cross-section and the (n-p) differential cross-section as a function of neutron energy (in Lab. system) are

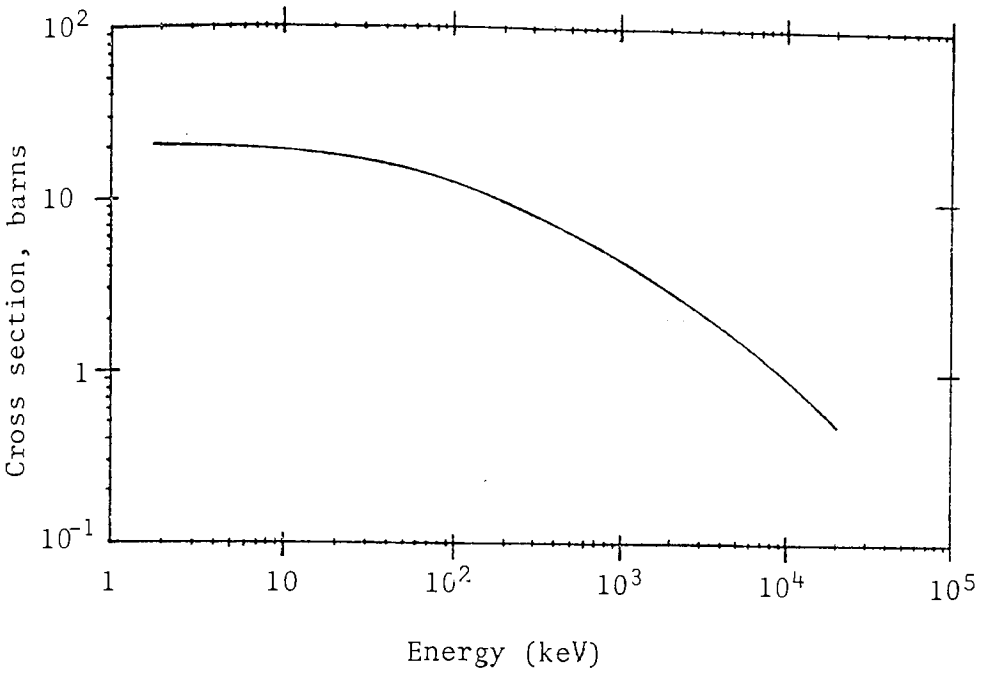

Figure (3.2) Elastic scattering cross-section of Hydrogen [71-72]

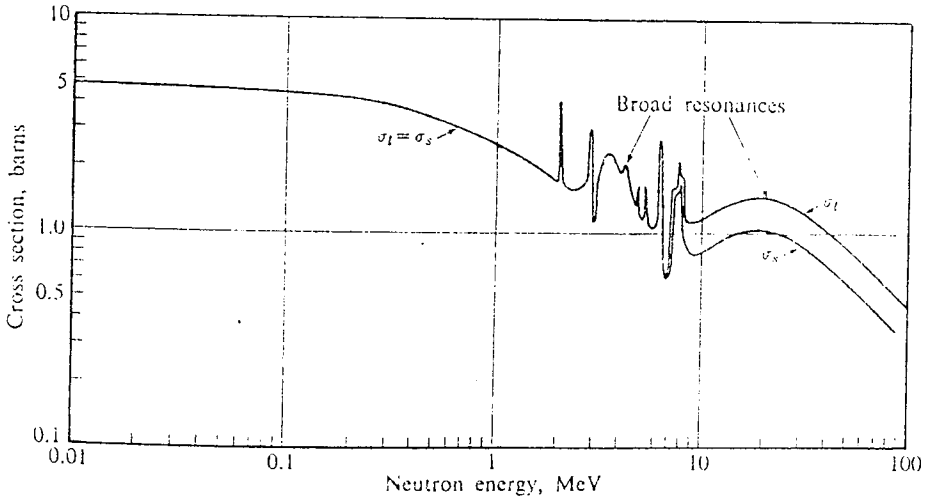

Figure (3.3) The total and elastic scattering cross-section of ^{12}C [3]

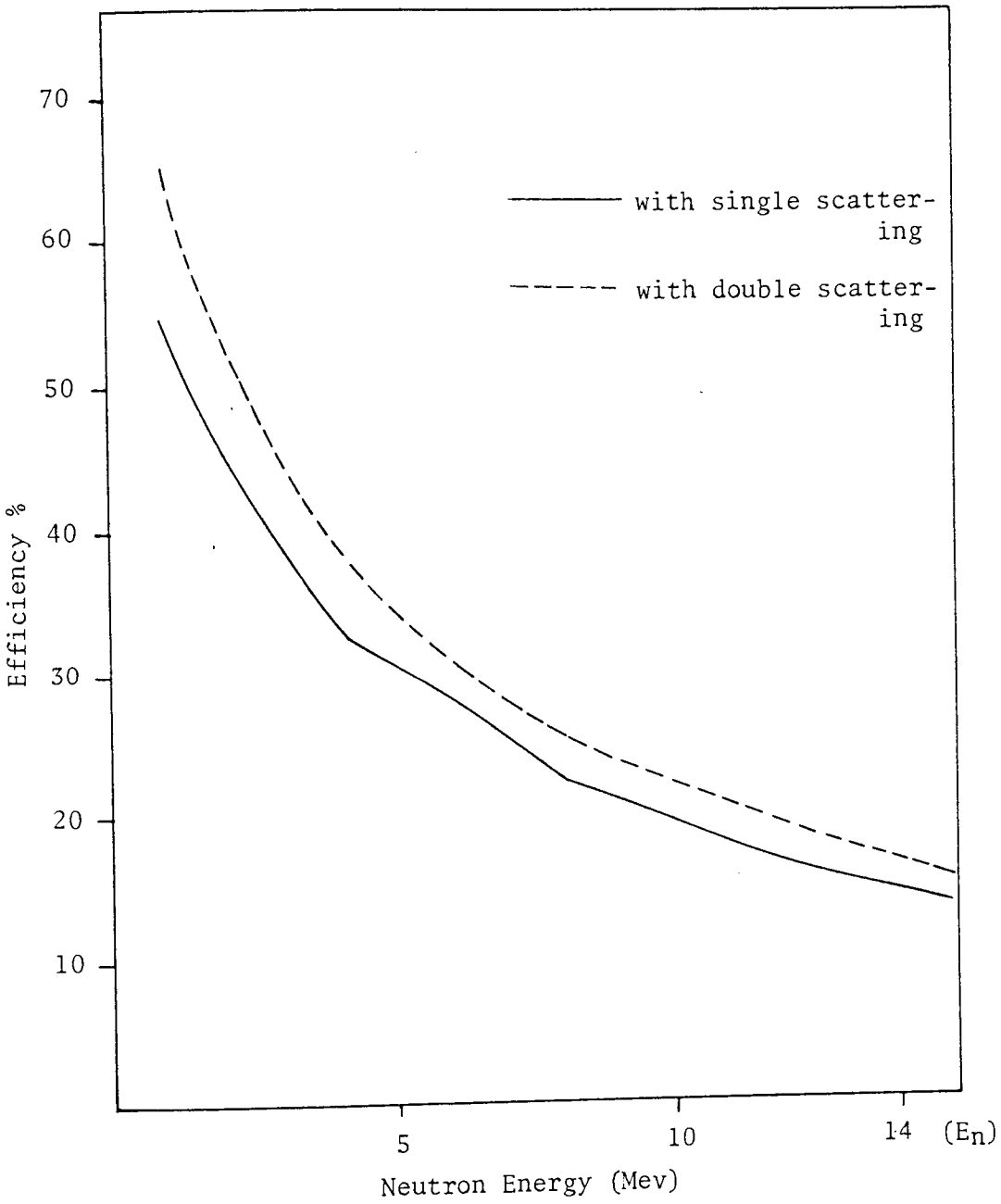

Figure (3.4) Calculated efficiency of NE 102A Scintillator

given by Gammel[73] as follows:

$$\sigma_{(n,p)}(E_n) = 3\pi[1.206\,E_n + (-1.86 + 0.09415\,E_n + 0.0001306\,E_n^2)^2]^{-1} + \pi[1.206\,E_n + (0.4223 + 0.13\,E_n)^2]^{-1} \quad \ldots\ldots (3.14)$$

and,

$$\sigma_{(n,p)}(\theta, E_n) = [\sigma_{(n,p)}(E_n)/4\pi] \cdot [(1 + b\cos^2\theta)/(1 + 1/3b)] \quad \ldots\ldots (3.15)$$

where $\sigma_{(n,p)}(E_n)$ = the (n-p) total cross-section as a function of E_n

$\sigma_{(n,p)}(\theta, E_n)$ = the (n,p) differential cross-section as a function of E_n,

$b = 2\,(E_n/90)^2$

and E_n = the energy of neutrons in Mev

3.6 SCATTERING FROM HYDROGEN AND CARBON

The most probable reaction for a fast neutron incident on a thin plastic scintillator is, single elastic neutron proton scattering. However, with increasing scintillator thickness, more scattering can occur, and the efficiency increases. This introduces a timing uncertainty in the flight times due to the different detection points within the scintillator.

For large detectors, it is possible for an incident neutron to scatter more than once from hydrogen nuclei before escaping from the scintillator. All such events normally occur within a very short period of time compared with the scintillation decay time. Thus double scattering from hydrogen does result in a distortion of the output pulse height spectrum

of the detector.

All organic scintillators contain carbon as well as hydrogen. In the presence of carbon, the scattered neutrons may still undergo a hydrogen scattering after a carbon scattering and before escaping from the scintillator. Because the neutron energy has been decreased in the initial carbon scatter, the incident neutron can lose between 0 and 28% of its energy in a carbon scatter, so the maximum energy of a subsequent recoil proton will vary between 100 and 72 percent of the original energy.

Accurate calculation of the correction for multiple scattering is difficult and requires a Monte Carlo calculation [74-76]. However, the contribution of a second scattering event can be estimated as follows:

The number of neutrons scattered once by carbon in a scintillator of length (L), is given by:

$$N_c(E_o,L) = N_o\, n_c\, \sigma_c\, L(1 - \exp(-aL))/aL \qquad \ldots\ldots (3.16)$$

All the terms are defined in equation (3.13).

The average energy of neutrons by scattered carbon is 0.85 E_n [70,77]. The number of recoil protons by second scattering with hydrogen after travelling a distance x in the scintillator will be:

$$N_{2c} = N_c\, n_H\, \sigma_{H_1}\, x\, (1 - \exp(-a_1 x))/a_1 x \qquad \ldots\ldots (3.17)$$

where σ_{H_1} = the cross-section for average energy of neutron, i.e. $E_1 = 0.85\, E_n$

and a_1 = is the same as "a", for average neutron energy, i.e. $a_1 = a(E_1)$

The total number of recoil protons is $N_1 + N_{2c}$ where N_1 is the same as calculated from equation (3.12) for single scattering only, hence the efficiency will be:

$$\varepsilon_2 = \left(\frac{N_1 + N_{2c}}{N_o}\right) = \varepsilon_1(E_o)\left[1 + \frac{N_{2c}}{N_1}\right] \quad \ldots\ldots (3.18)$$

Swartz et al[70] have obtained good agreement with the experimental results by assuming x = L/2.

Numerical data useful for calculating ε_1 and ε_2 are given in table (3.2).

Applying equation (3.18) and data of table (3.2) the (ε_2) efficiency of NE 102A scintillator was obtained and is shown in figure (3.4) as a dashed line.

Table (3.2)

Values of $n_H \sigma_H$, $n_c \sigma_c$, $n_H \sigma_{H_1}$, ε_2 and ε_1 for NE 102A Scintillator as a Function of Neutron Energy E_n

E_n MeV	$n_H \sigma_H$	$n_c \sigma_c$	$n_H \sigma_{H_1}$	$n_c \sigma_{c_1}$	ε_1%	ε_2%
1	0.2236	0.1221	0.2441	0.1330	53.5	65.2
2	0.1524	0.0807	0.1671	0.0831	45.4	52.9
3	0.1196	0.0618	0.1337	0.0758	39.7	45.1
4	0.0994	0.0912	0.1105	0.1211	32.3	38.6
6	0.0746	0.0489	0.0840	0.0527	28.1	31.5
8	0.0596	0.0689	0.0678	0.3040	22.2	25.1
10	0.0494	0.0546	0.0567	0.0380	19.5	22.3
12	0.0420	0.0594	0.0486	0.0247	16.7	19.3
14	0.0364	0.0636	0.0423	0.0392	14.5	17.0

3.7 RESPONSE OF THE ORGANIC SCINTILLATOR

The fraction of the charged particle energy which is converted into fluorescent energy depends on the particle type and its energy. The photmultiplier output of the detector is often proportional to the luminous output of the detector.

For organic scintillators, the response to electrons is linear for particle energies above about 125 keV [78]. However, the response for protons is always less for equivalent energies and is non-linear in much higher energies. Figure (3.5) shows the scintillation response of plastic NE 102 scintillator.

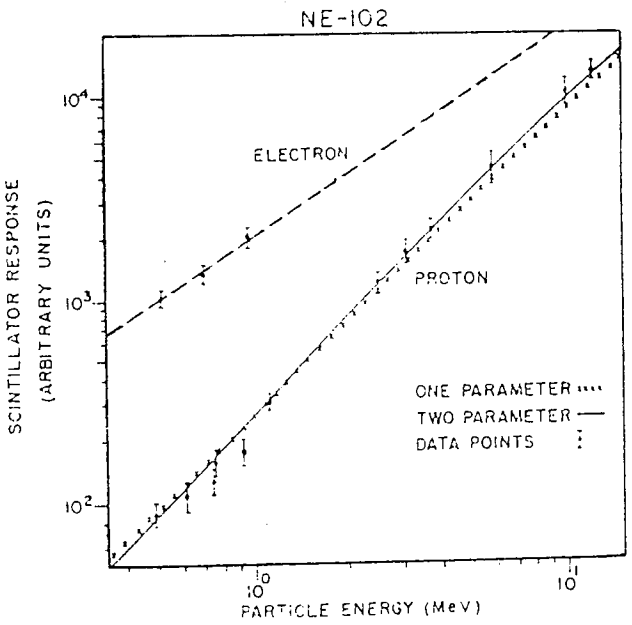

Figure (3.5) Semiempirical fits to electron and proton response data for NE 102 scintillator measured by Smith et al [79]

Birks[63] has derived a formula which has been successful in explaining many of the features of the experimental data for organic scintillators. According to his semi-theoretical formula, the Luminous output of an

organic scintillator for charged particles can be calculated from the equation (3.19):

$$\frac{dL}{dx} = \frac{S\ dE/dx}{1 + KB\ dE/dx} \qquad \ldots\ldots (3.19)$$

where L and x are the Luminous output of the scintillator and path length of the particle in the scintillator respectively.

$\frac{dL}{dx}$ = Luminous output per unit path length,

and $\frac{dE}{dx}$ = specific energy loss for the charged particle,

S and KB being empirical constants, the product KB is treated as an adjustable parameter to fit experimental data for a specific scintillator.

Wright[80] using a different mechanism, suggests that:

$$\frac{dL}{dx} = \frac{c}{\alpha} \ln (1 + \alpha\ dE/dx) \qquad \ldots\ldots (3.20)$$

where c and α are a constant.

Gooding and Pugh[81] have reported measurements on plastic scintillator type NE 102 with the result:

$$\alpha = (0.025 \pm 0.002)(mg/cm^2/Mev) \qquad \ldots\ldots (3.21)$$

Chou[82] modified form of the equation (3.19) with one additional adjustable parameter of dE/dx, i.e.

$$\frac{dL}{dx} = \frac{S(dE/dx)}{1 + KB(dE/dx) + c(dE/dx)^2} \qquad \ldots\ldots (3.22)$$

where c is treated as an empirically fitted parameter. For small values of dE/dx, equation (3.22) approaches equation (3.19). An extensive

analysis of the response of a number of organic scintillators have been carried out by Craun and Smith[83].

In the present calculation, the Birk's formula was used. When excited by fast electrons, dE/dx is very small, then the Birk's formula predicted by

$$(dL/dx)_e = S\ dE/dx \qquad \ldots\ldots (3.23)$$

or, the light output per unit energy loss is a constant.

$$(dL/de)_e = S \qquad \ldots\ldots (3.24)$$

In that case, the light output

$$L \equiv \int_0^E \frac{dL}{dE}\, dE = Se + K' \qquad \ldots\ldots (3.25)$$

is linearly related to the initial particle energy E.

The parameter KB can be calculated as follows:
For an alpha particle, dE/dx is very large, so the equation (3.19) becomes:

$$(dL/dx)_\alpha = S/KB \qquad \ldots\ldots (3.26)$$

From equations (3.23) and (3.26) the value of KB can be written as:

$$KB = (dL/dE)_e/(dL/dx)_\alpha \qquad \ldots\ldots (3.27)$$

To avoid dependence on specific units for the measurement of L in equation (3.19) it is convenient to represent the scintillation output by the variable p = L/S hence equation (3.19) can be written as:

$$dP/dE = S^{-1}\ dL/dE = (1 + KB\ dE/dx)^{-1} \qquad \ldots\ldots (3.28)$$

The units of p and E are the same. For NE 102A Evans and Bellamy [84] and Craun et al[83] have found the value of KB to be: 1.0×10^{-2} (gr cm^{-2} Mev^{-1}) and 1.31×10^{-2} (gr cm^{-2} Mev^{-1}) respectively. However, it has been shown by Evans et al[84], that to obtain the best agreement between theoretical and experimental results KB = 1.0×10^{-2} (gr cm^{-2} Mev^{-1}).

As mentioned before, dE/dx for electrons is small, so dp/dE = 1,

$$\therefore \quad p = E_e \qquad \ldots\ldots (3.29)$$

For protons as dE/dx is large, and cannot be neglected. By integration of equation (3.28), the pulse height for a given proton energy E_p can be obtained.

$$p = \int_0^{E_p} 1/(1 + KB\ dE/dx)\ dE \qquad \ldots\ldots (3.30)$$

As the main constituents of the organic scintillators studied are carbon and hydrogen, the range-energy relationship in the plastic can be taken as that for CH.

Hence,

$$(dE/dx)_{CH} = 0.923(dE/dx)_C + 0.077\ (dE/dx)_H \qquad \ldots\ldots (3.31)$$

Rich and Madey[85] and Craun et al[83] have obtained the specific energy losses of proton in CH and NE 102 scintillator respectively. Gooding et al[81] for energies from 1 to 150 Mev have represented approximately dE/dx for protons by the following relation:

$$dE/dx = 16.94\ x^{-0.448} \qquad \ldots\ldots (3.32)$$

The values of specific energy loss for protons in NE 102A scintillator are shown in Table (3·3).

Using the data of Table (3·3) and KB = 1×10^{-2} (gr cm^{-2} Mev^{-1}) to

Table (3.3)

Response of Plastic Scintillator NE 102A to Proton

E_p Mev	$\frac{dE}{dx}$ [83] Mev cm^2/gr	dp/dE	pulse height p (Mev)
1	238.1	0.296	0.18
2	148.4	0.403	0.54
3	110.3	0.476	0.90
4	88.1	0.532	1.47
5	73.7	0.576	2.03
6	62.5	0.615	2.62
7	55.5	0.643	3.25
8	50.1	0.666	3.91
9	45.3	0.688	4.59
10	41.9	0.705	5.28
11	38.9	0.720	5.99
12	36.3	0.734	6.72
13	34.0	0.746	7.46
14	32.1	0.757	8.21
15	30.3	0.768	8.97

equation (3.28), dP/dE via E_p and the pulse height p as a function of proton energy were calculated for the present detector, giving the curves shown in figure (3.6) and figure (3.7) respectively.

From the energy spectrum of the protons, figure (3.1) the pulse height spectrum was obtained as follows:

Suppose the number of recoil protons with energies between E and E + dE is written as: N(E)dE, and the number of pulses with pulse heights between p and p + dp as: N(p)dp. Since the total area under the two curves must be the same, the two spectra are related by:

$$N(E)dE = N(p)dp \qquad \ldots\ldots (3.33)$$

or $$N(p) = N(E)/(dp/dE)$$

For simplicity, N(E) was taken as one, therefore:

$$N(p) = dE/dp \qquad \ldots\ldots (3.34)$$

Figure (3.8) shows the pulse height spectrum and energy spectrum for 14 Mev neutrons in NE 102A scintillator.

In general, the pulse height spectrum will be distorted as shown with dashed curve in figure (3.8) because of the spread introduced by non-uniform light collection, photoelectron statistics, and fluctuations of photomultiplier output.

However, the total area under the curve should remain unchanged.

3.8 CALCULATION OF DETECTOR EFFICIENCY WITH DISCRIMINATION

In use it is necessary to set a fixed discrimination level to eliminate pulses arising from low energy background neutrons, noise pulses that arise spontaneously in the photomultiplier and the counting system.

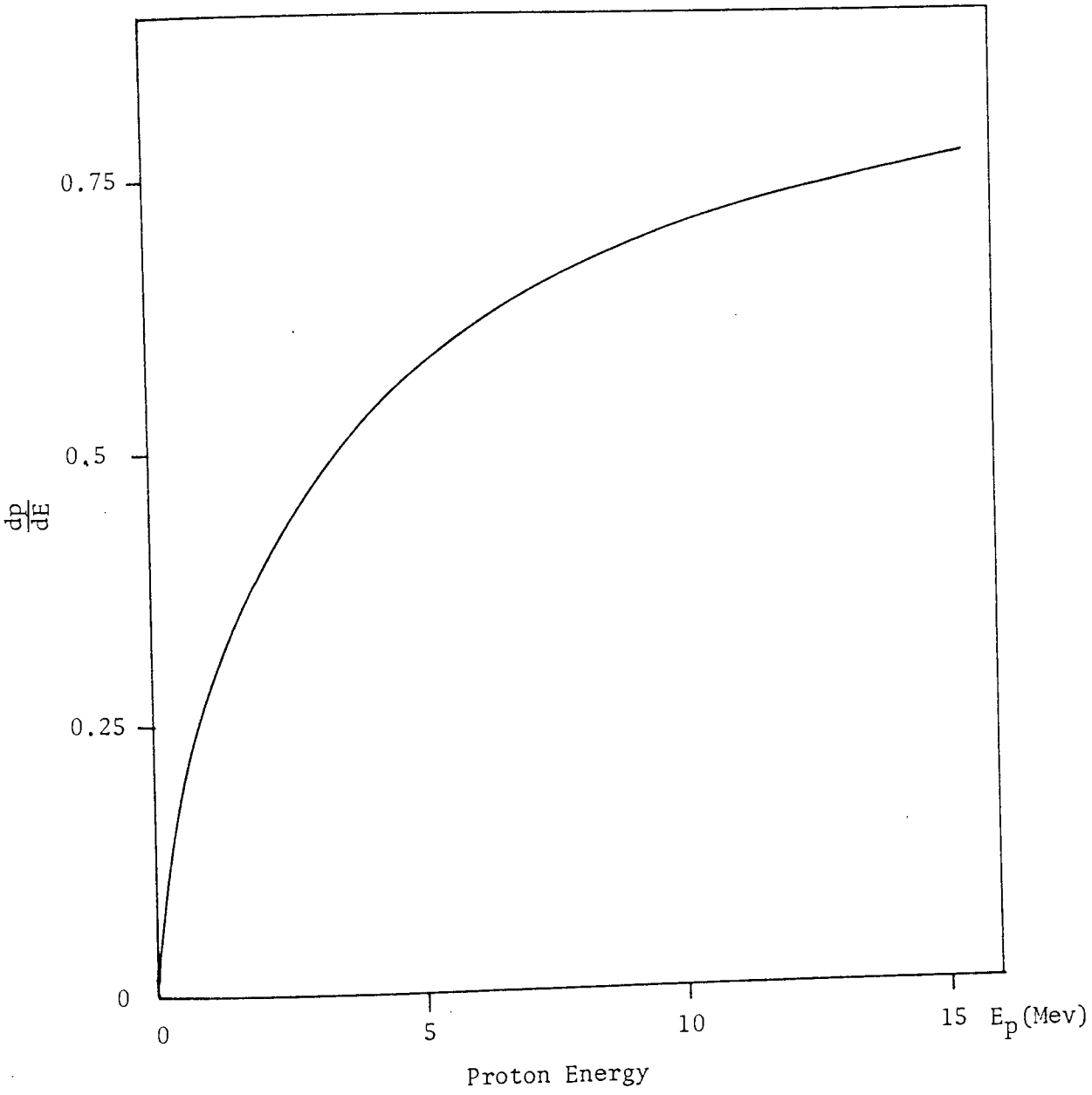

Figure (3.6) Variation of $\frac{dp}{dE}$ via E_p for protons in NE 102A scintillator

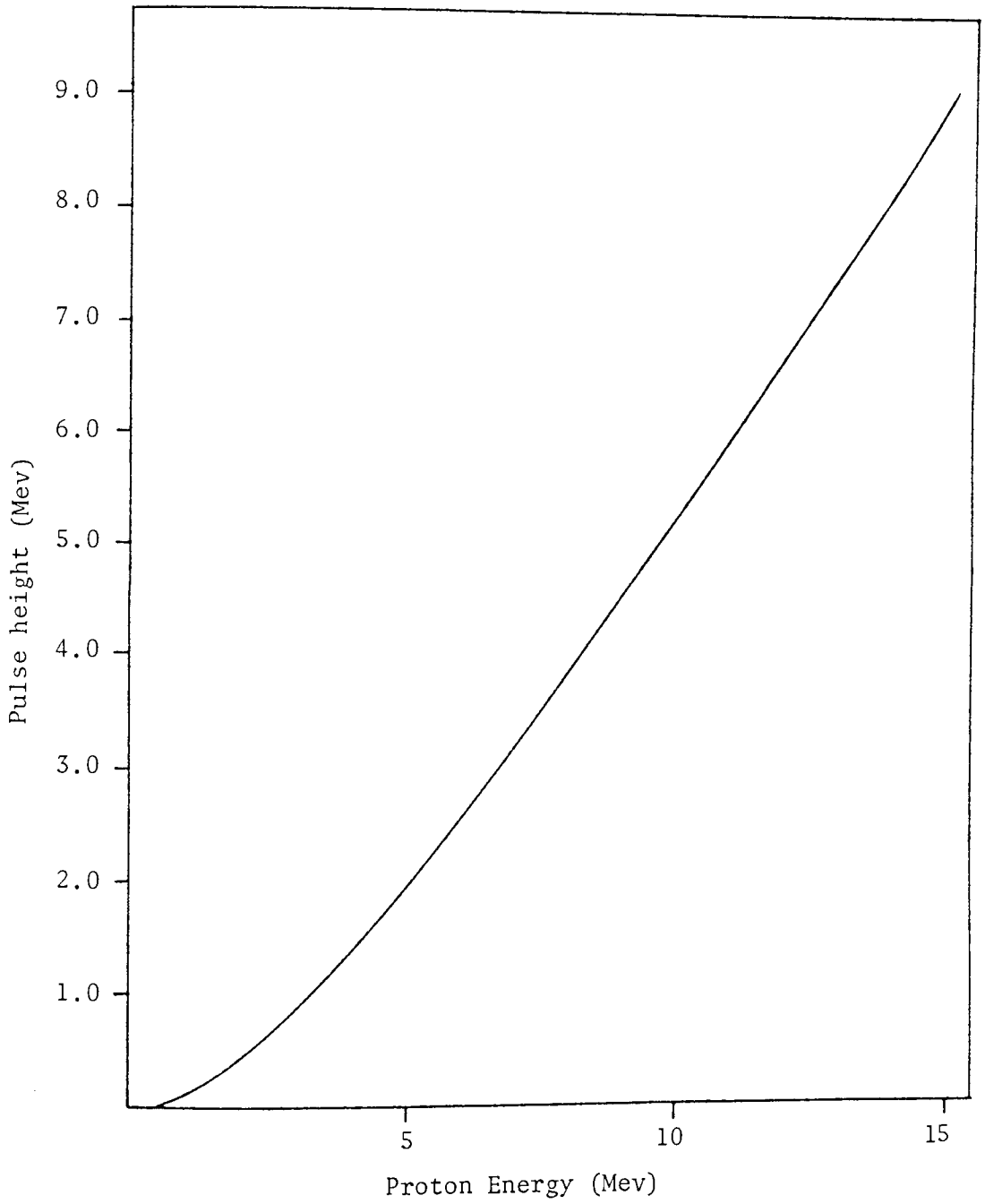

Figure (3.7) Pulse height of protons in NE 102A scintillator

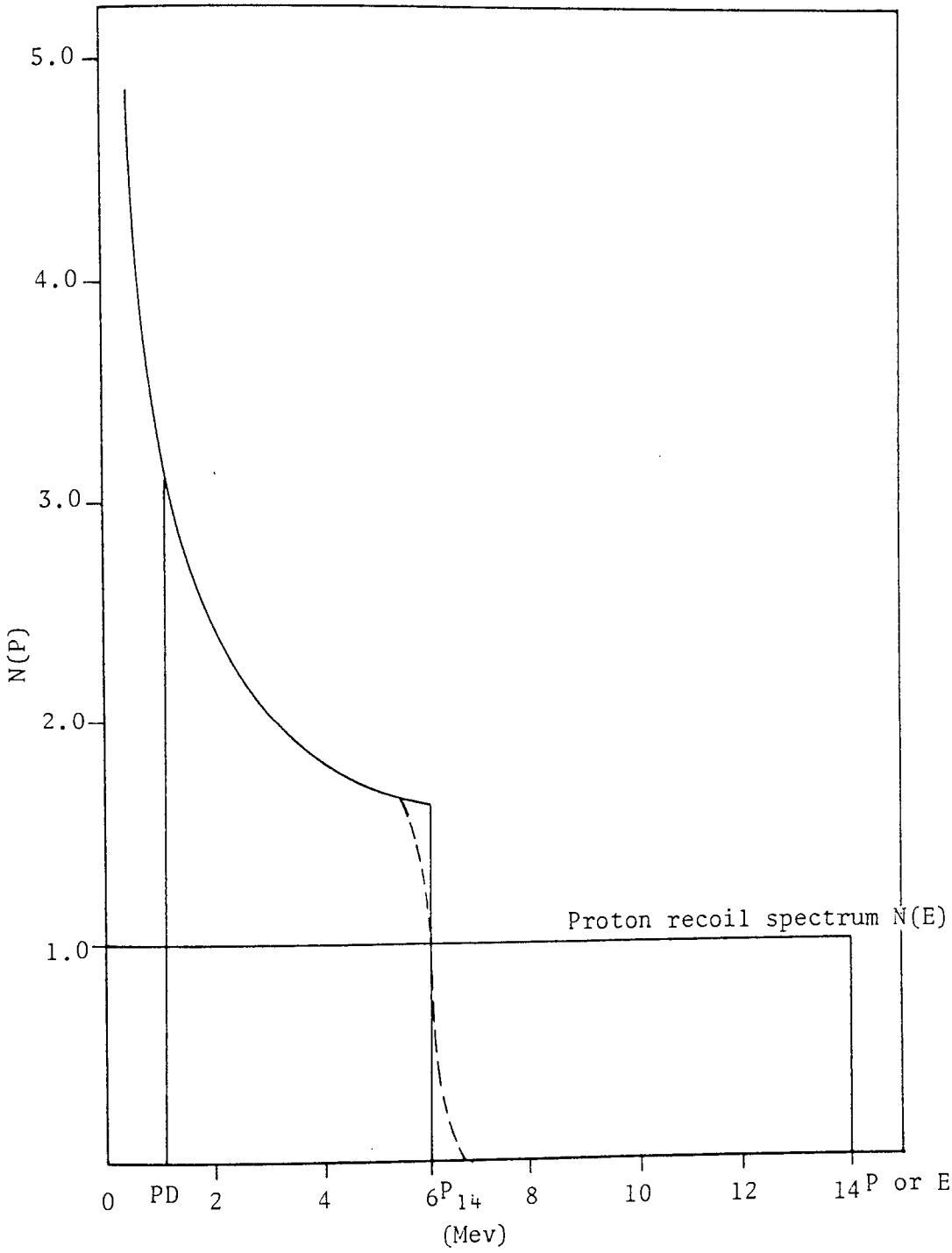

Figure (3.8) Calculated pulse height spectrum by the non-linear response of plastic scintillator (NE 102A)

However, some recoil events will inevitably be eliminated in the discrimination process. Therefore, the scintillator efficiency for 14.0 Mev neutrons will always have a somewhat lower efficiency than the efficiency assuming that all pulses are counted. This is called "zero-bias efficiency".

The detector efficiency with a discriminator designed to reject all pulses of amplitude less than P_D is given by:

$$\varepsilon_{14.0} = \varepsilon_2(14.0) \cdot \frac{(A_{14.0} - A_D)}{A_T} \qquad \ldots\ldots (3.35)$$

where $\varepsilon_2(14.0)$ = the neutron detector efficiency without discrimination for 14.0 Mev neutrons as calculated from equation (3.18)

$(A_{14.0} - A_D)$ = area under pulse height spectrum between P_D (discriminator level) and $P_{14.0}$ (i.e. pulse height due to 14.0 Mev protons)

and A_T = total area under the pulse height spectrum.

From figure (3.8) for neutron energy E Mev the efficiency is given by:

$$\varepsilon(E) = \varepsilon_2(E) \left(\frac{A_E - A_D}{A_T}\right) \cdot \frac{14.0}{E} \qquad \ldots\ldots (3.36)$$

As mentioned in section (3.7), the light output of organic scintillators for electrons is higher per unit energy than for heavy charged particles. The low z-value of the organic scintillators (hydrogen and carbon) results in a very low photo electric cross-section. So most gamma ray interact via compton scattering. Therefore, in a gamma ray spectrum taken with an organic scintillator only the compton edges are distinguishable. The discriminator level has to be fixed with a known pulse height. This can be done by setting the discriminator to reject pulses due to γ-rays from a known specific source.

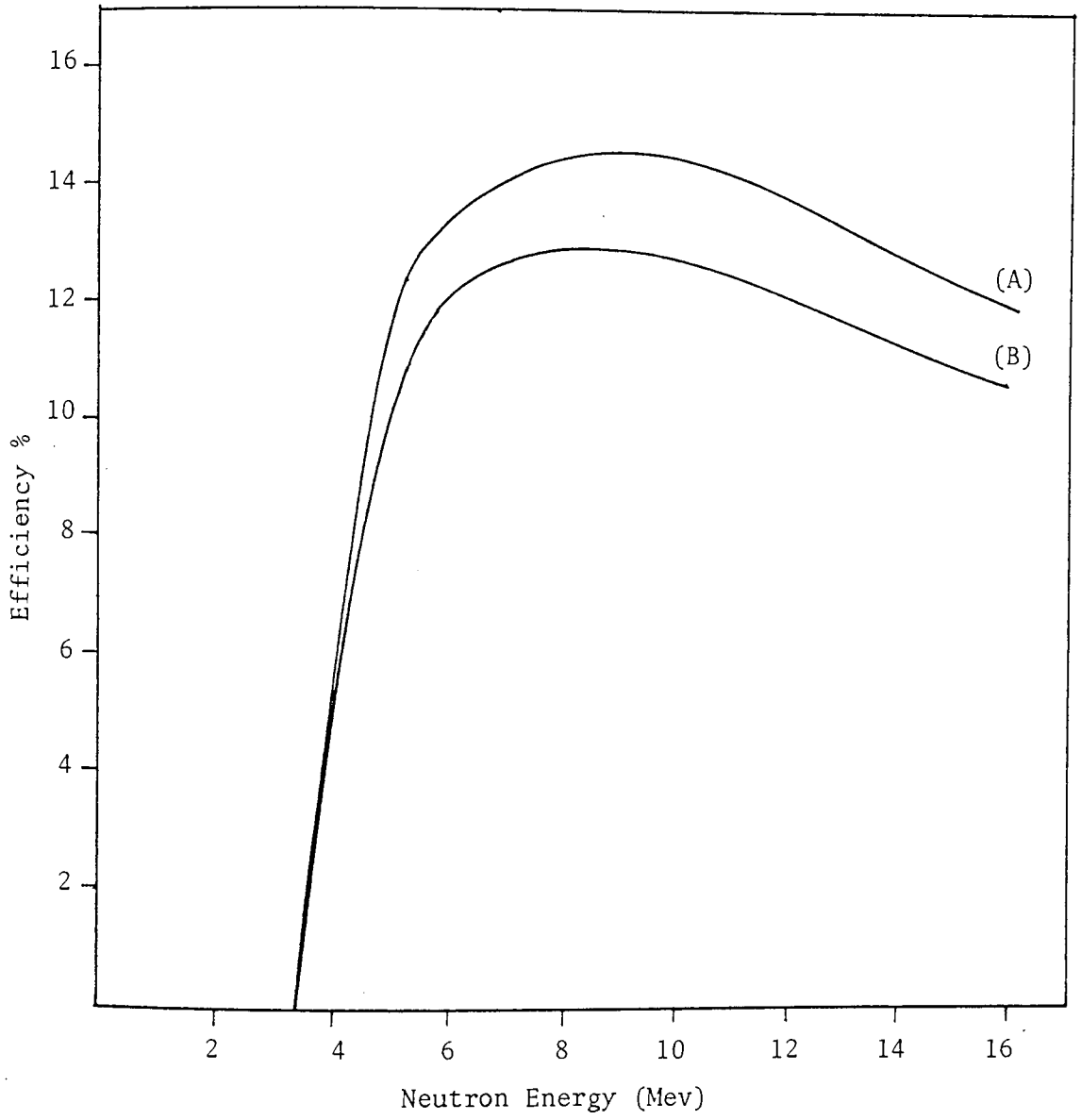

(A) - Including scattering from Carbon and Hydrogen

(B) - No multiple scattering

Figure (3.9) Calculated efficiency of the NE 102A Scintillator with a discriminator level of 3.4 Mev

The γ-ray source used was ^{60}Co which emits two γ-rays at 1.17 Mev and 1.33 Mev. γ-rays interact with the detector and produce compton electrons with energies up to a maximum value given by:

$$E_{max} = (E_o)/(1 + m_oC^2/2E_o) \quad \ldots\ldots (3.37)$$

where E_o = energy of γ-rays in Mev

Applying equation (3.37) to ^{60}Co gamma-ray of energy 1.33 Mev gives the maximum recoil electrons $E_{max.}$ = 1.115 Mev. At this energy the term K_B dE/dx is very small, hence the pulse height due to electrons is given by equation (3.29) i.e.

$$P = E_e \quad \ldots\ldots (3.29)$$

Therefore, a 1.115 Mev electron produces an equivalent proton pulse height of P = 1.115 Mev.

Referring to figure (3.7) a pulse of amplitude P = 1.115 Mev corresponds to a proton energy of 3.4 Mev. As a result using ^{60}Co γ-rays as a reference to set the discriminator level, achieves the rejection of pulses due to neutrons with energies less than 3.4 Mev.

Applying equation (3.36) to figure (3.8), the resulting efficiency curves with the discriminator level were calculated and are shown in figure (3.9)

3.9 SETTING THE NEUTRON DISCRIMINATION LEVEL

In section (3.8) it was shown that, to reject undesired pulses, it was necessary to set the discriminator level with a known gamma-ray source. The discriminator used in the neutron line was the (ORTEC 463) Constant Fraction Discriminator, which is useful for precise timing signals as it eliminates the time walk problem.

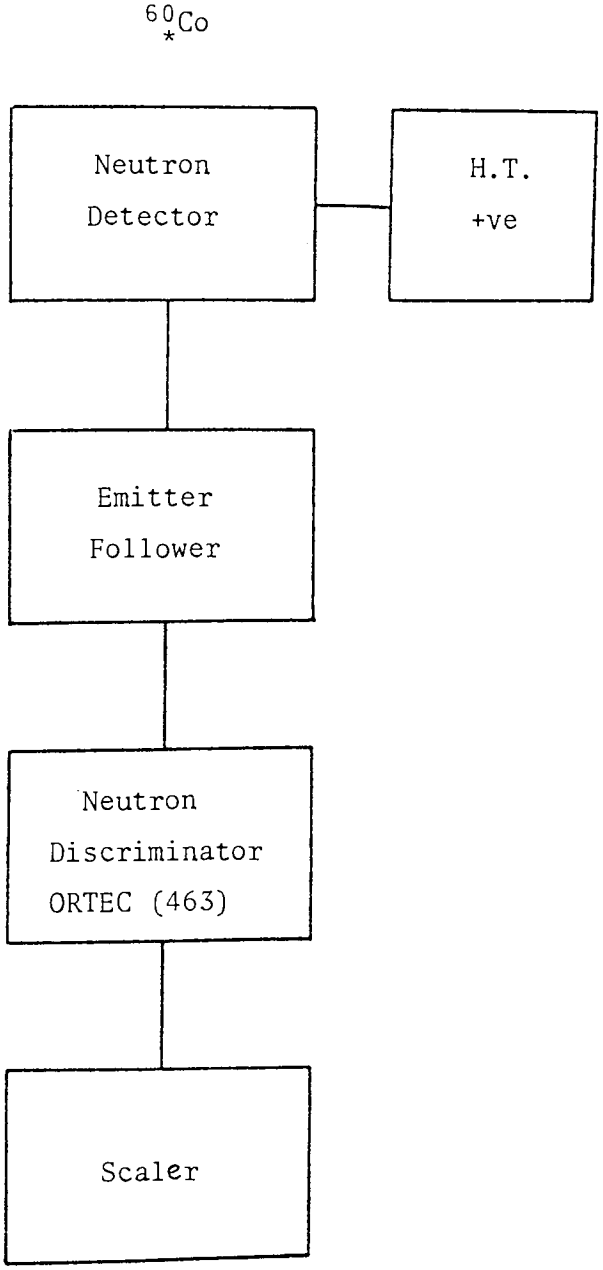

Figure (3.10) Block diagram of the electronics used to set the neutron discriminator level

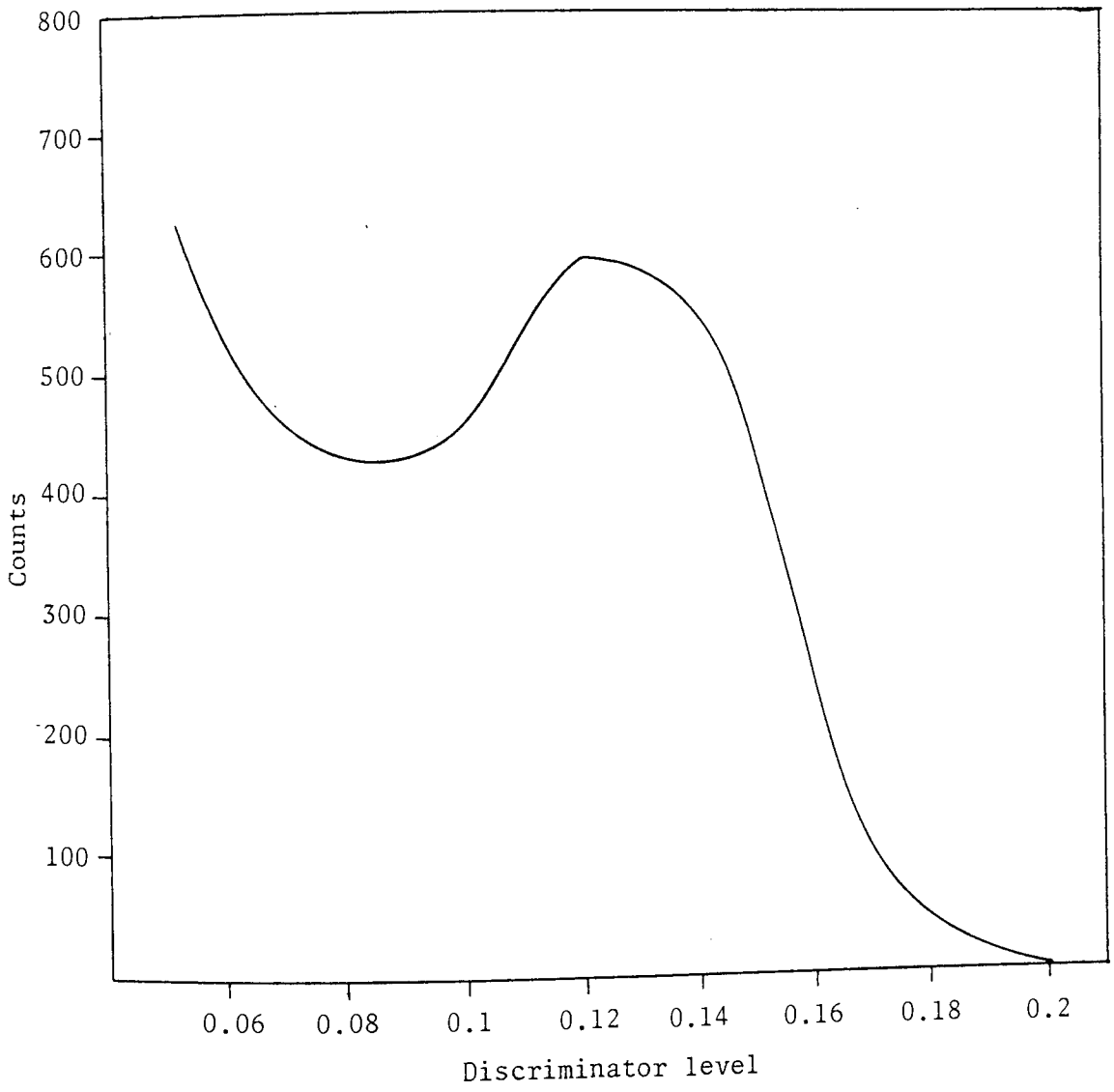

Figure (3.11) Differential compton spectrum for ^{60}Co γ-rays

The experimental arrangement are shown in figure (3.10). The ^{60}Co gamma source was placed in front of the detector, and the count rate was noted as a function of the discriminator level setting. By plotting the difference in the number of counts in successive intervals via that intervals the compton spectrum of ^{60}Co was obtained, and is shown in figure (3.11). Some point on the compton edge should be selected and associated with the maximum energy of a compton recoil electron. Flynn et al [86] have reported in detail the shape of the compton continum, and have suggested a standard procedure, in which the channel number at which the compton edge falls to one-half of its plateau value, is in fact, consistently (4 ± 1)% higher in pulse height than that expected for the energy of the compton edge. Therefore, the compton edge of 1.33 Mev gamma ray was chosen at a point that, the count rate fell to one-half of its peak value. This value was determined as the discriminator level setting for the experiment.

3.10 DETECTION SYSTEM

The use of scintillation counting in radiation detection and spectroscopy would be impossible without suitable devices to convert the weak light output of a scintillation pulse into a corresponding electrical signal. The photomultiplier (PM) tube accomplishes this task without adding a large amount of random noise to the signal.

The construction of the detection system has been reported by Baynham [27] for the detection of fast neutrons. No modifications were found necessary for the detection of neutrons in the present work.

In timing applications, it is important that all photo electrons have as nearly as possible the same transit time from cathode to dynode. In order to minimize the time uncertainties of time-of-flight experiments in the detection process a suitable photomultiplier tube, must have a high

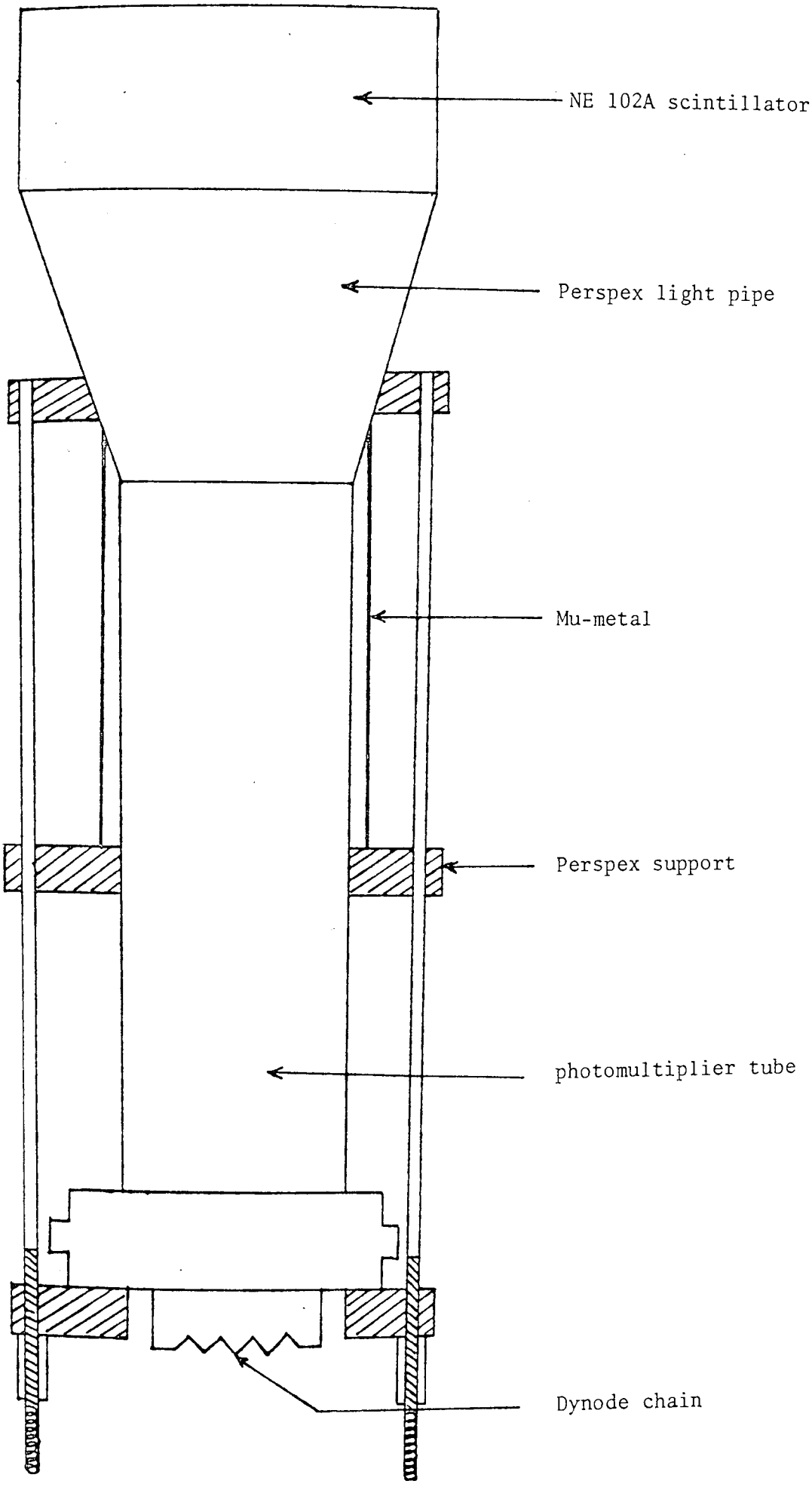

Figure (3.12) The Scintillator Photomultiplier Assembly

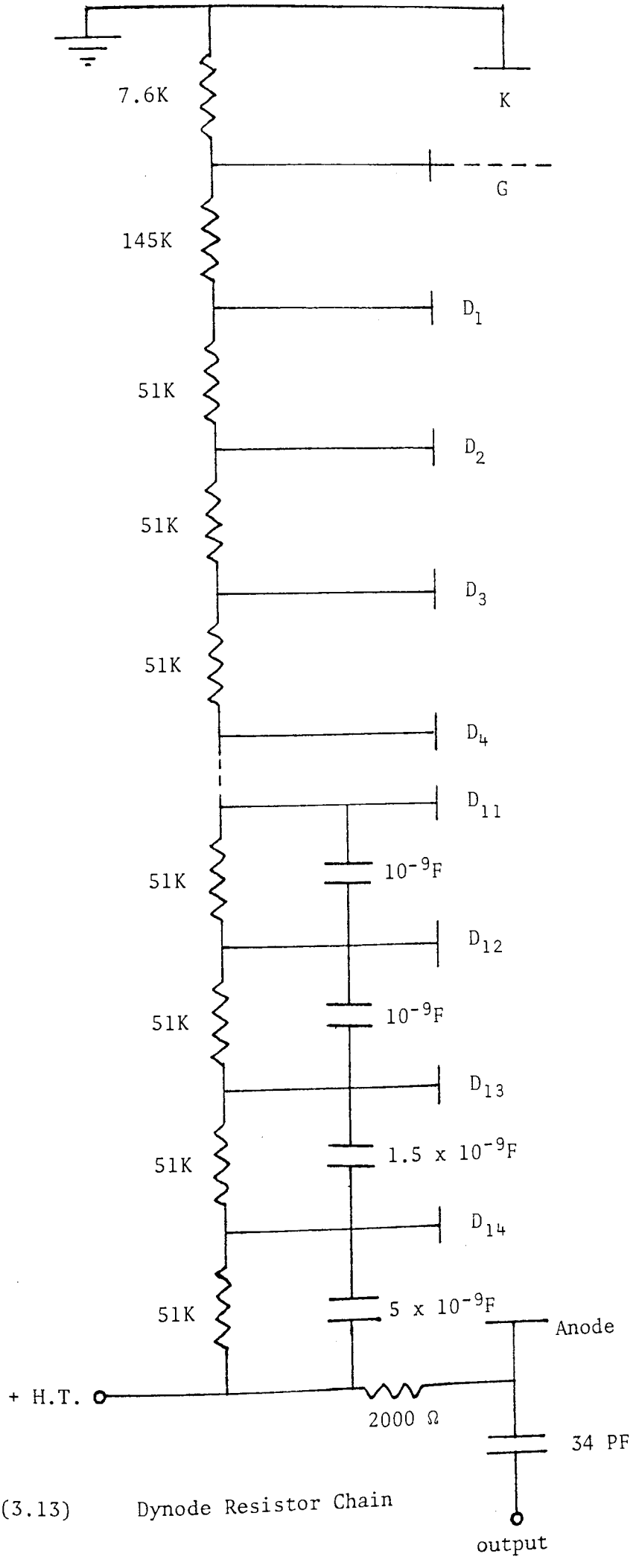

Figure (3.13) Dynode Resistor Chain

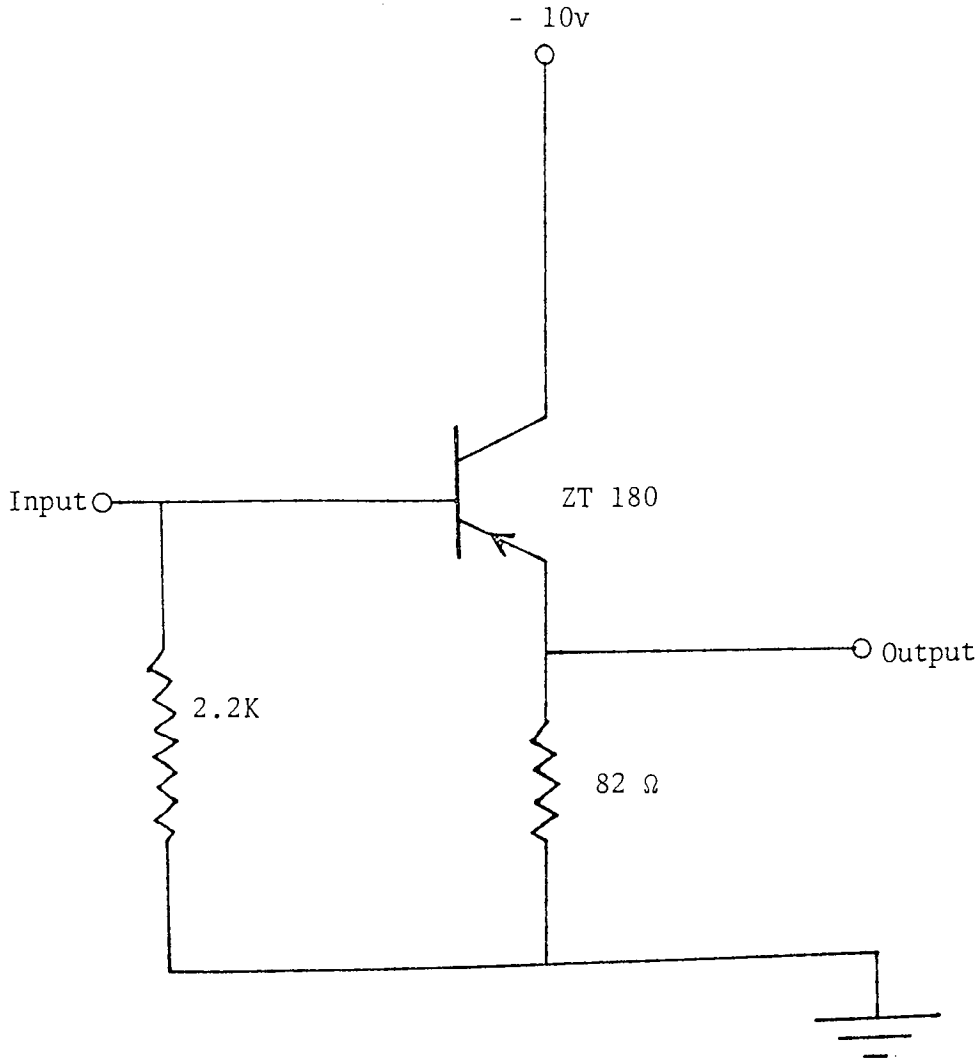

Figure (3.14) Emitter follower circuit

light output, good light transmission and fast transit time. Figure (3.12) shows the scintillator photomultiplier assembly. The 10 cm diameter scintillator was connected to the 5.0 cm diameter photomultiplier tube via a perspex light pipe. The Phillips 56 Avp tube used in the present detector, gave an electron transit time spread of 0.5 n.sec at FWHM, and was adequate for the present work. It is a high gain photomultiplier tube with fourteen stages of amplification which gave a gain of 10^8 when operated at 2 Kv. In order to obtain high gain a dynode resistance chain as in figure (3.13) was used. This supplied the voltages to the dynode stages of the photomultiplier tube. At an operating voltage of 2 Kv the DC, current through the dynode chain was 2.3 mA.

To avoid fluctuations in the dynode potentials especially in the latter stages near to the anode, it was necessary to provide a "stabilizing capacitors", to the stages of the divider string.

Figure (3.13) shows the four capacitors between the last four dynodes. These capacitors supply the current lost from the dynode during the pulse, and is recharged by the divider string current during the period between pulses.

In the present experiment the electronics system was several metres from the experimental area, hence a long coaxial cable was required to connect the neutron detector output to the neutron discriminator.

To avoid reflection in this cable, the anode signals were matched into the cable through an emitter follower, figure (3.14) at the base of photomultiplier.

3.10.1 Magnetic Shielding

The electron optics within a photomultiplier tube are sensitive to magnetic fields, because of the low average energy of the electrons travelling from stage to stage. Connor et al[87] reported that photomultiplier

tubes with a focused dynode structure are especially sensitive to magnetic fields. Even the influence of the earth's magnetic field is sufficient to affect the trajectories of electrons appreciably.

In the present situation, it was necessary to rotate the detector about the sample, therefore it was essential that a magnetic shield be provided to prevent gain shifts of the photomultiplier tube. The most common form consists of a thin cylinder of Mu-metal which fits closely around the outside glass envelope of the photomultiplier tube. The electron trajectories from the cathode to the first dynode are most sensitive to magnetic fields. For most tube designs, this shield must be held at photocathode potential in order to avoid disturbing the electrostatic field between the photocathode, and first dynode. The photomultiplier-tube was placed inside a cylindrical Mu-metal magnetic shield No. 56131 recommended by the manufacturers. The use of Mu-metal shield, besides giving optimum tube gain, gives minimum transit time spread.

3.10.2 The Light Guide

To obtain maximum light collection by the photocathode, care must be taken with the optics of the system. In any scintillator, one would like to collect as much of the light emitted as possible. In practice, however, two effects prevent perfect light collection.

(A) self-absorption within the scintillator

(B) losses at the scintillator surface

The first parameter is important only in a very large scintillator, but the uniformity of light collection normally depends on the conditions which exist at the interface between the scintillator and the container on which it is mounted. Ideally, one would like to couple the scintillator to the photocathode of the photomultiplier tube through a transparent medium of the same index of refraction as the scintillator. As the

scintillator used had a larger diameter than the PM-tube, a light pipe was necessary to make an efficient optical coupling, and to act as a guide for the light from the scintillator, and to spread the light more uniformally over the cathode. More complete discussion of the scintillator mounting and reflection is given by Birks[63]. Keil[88] has also published a useful review of light collection methods.

The surface of the light pipe are highly polished and are often surrounded by a reflective wrapping to reflect back some of the light which would have escaped. Lucite, with an index of refraction 1.49 - 1.51 is the most widely used material.

In the present detector, the conical light guide was 70 mm, from the perspex covering from the scintillator to the photomultiplier tube. The contact between the scintillator and the light pipe was made using NE 580 optical cement which was a refractive index (n = 1.58) close to that of the NE 102A scintillator. Non-drying silicon immersion oil was used as the coupling agent between the scintillator and photmultiplier-tube.

Figure (3.15) shows the complete neutron-detector assembly.

3.11 NEUTRON DETECTOR SHIELDING

In studying the angular distribution of scatterd neutrons it is necessary to shield the detector from the direct neutron beam and background. Since most sources of monoergic neutrons emit neutrons in all directions, the detector will, in general, count many more neutrons which come directly from the source than neutrons which are scattered by the sample.

The purpose of shielding is basically to reduce background effects caused by undesired neutrons and γ-rays scattered from the surrounding materials in the Laboratory.

In time-of-flight experiments, a properly shielded detector provides much better results than the unshielded detector. If one requires a

Figure (3.15) Neutron Detector Assembly

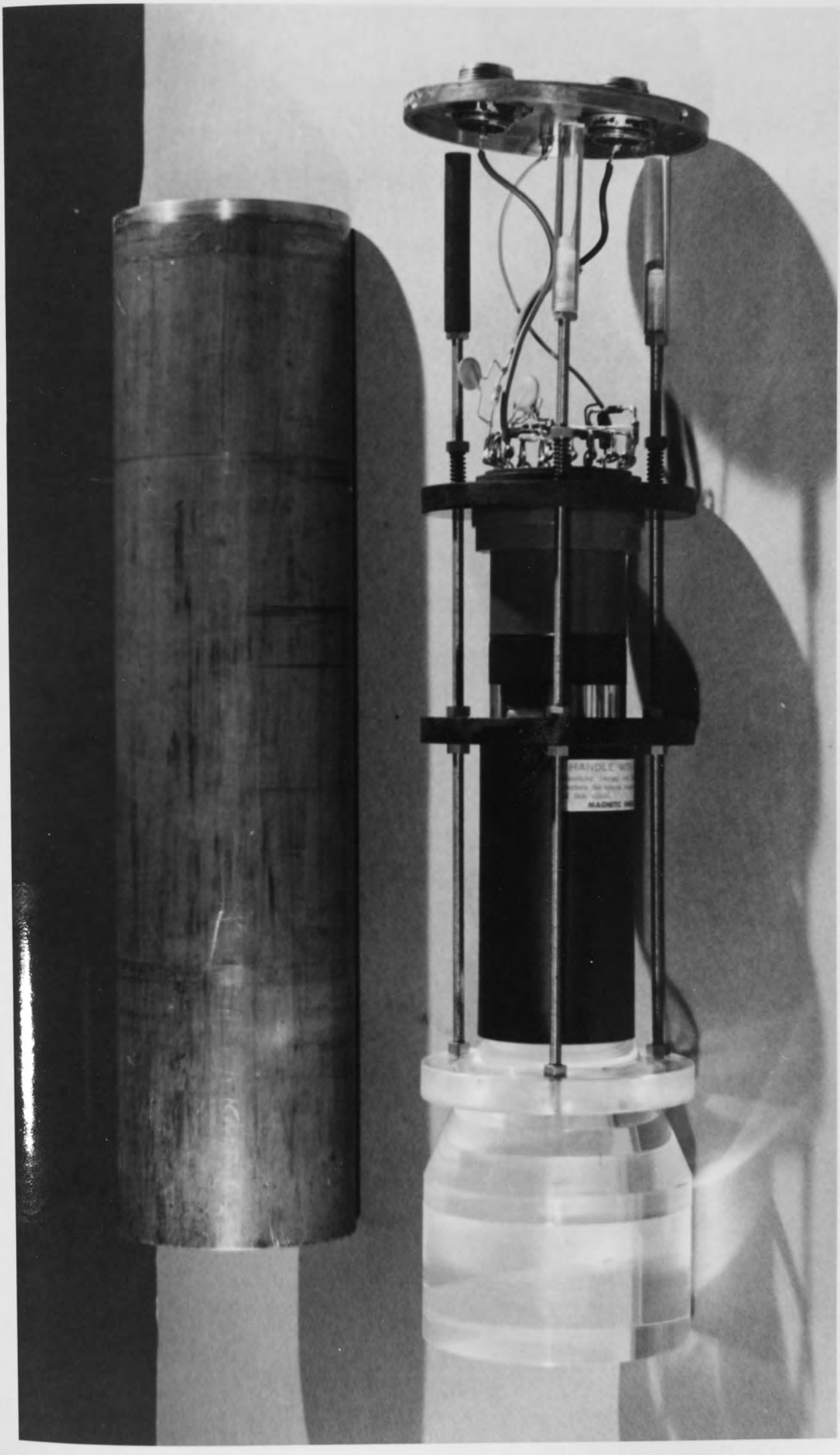

lower background, then one must consider a complete massive shielding around the detector to improve the situation.

Usually two kinds of shielding can be used in the Laboratory:

(1) A massive collimator shielding surrounding the detector

(2) shadow bar shielding

Each of these are discussed in detail in the following sections.

3.11.1 Shielding Materials

In the absence of any background, any scintillation counter must be shielded from light. Sodium iodide crystals are usually canned in a metallic container, and must be hermetically sealed. However, in fast neutron experiments, an effective shield must be used to attenuate fast neutrons without causing activity of the shielding materials, this can be done by: moderating the fast neutrons, absorbing the slow neutrons, and finally absorbing the secondary gamma-rays.

In the present work, both a massive shield and a moveable shadow shield was used. Figure (3.16) shows the neutron-detector shielding mounted on its mobile shield.

The type of shielding materials is influenced by the fact that, neutron attenuation in shielding varies by the ratio:

$$\phi_1/[\phi_o \exp(-\Sigma x)] \qquad \ldots\ldots (3.38)$$

where ϕ_1 = the number of neutrons per unit time scatterd into the detector by the scattering sample

ϕ_o = the number of neutrons per unit time from the source

and $(-\Sigma x)$ = the macroscopic absorption coefficient factor for the shielding material of the thickness x.

Figure (3.16) Neutron detector shielding mounted on its mobile shield

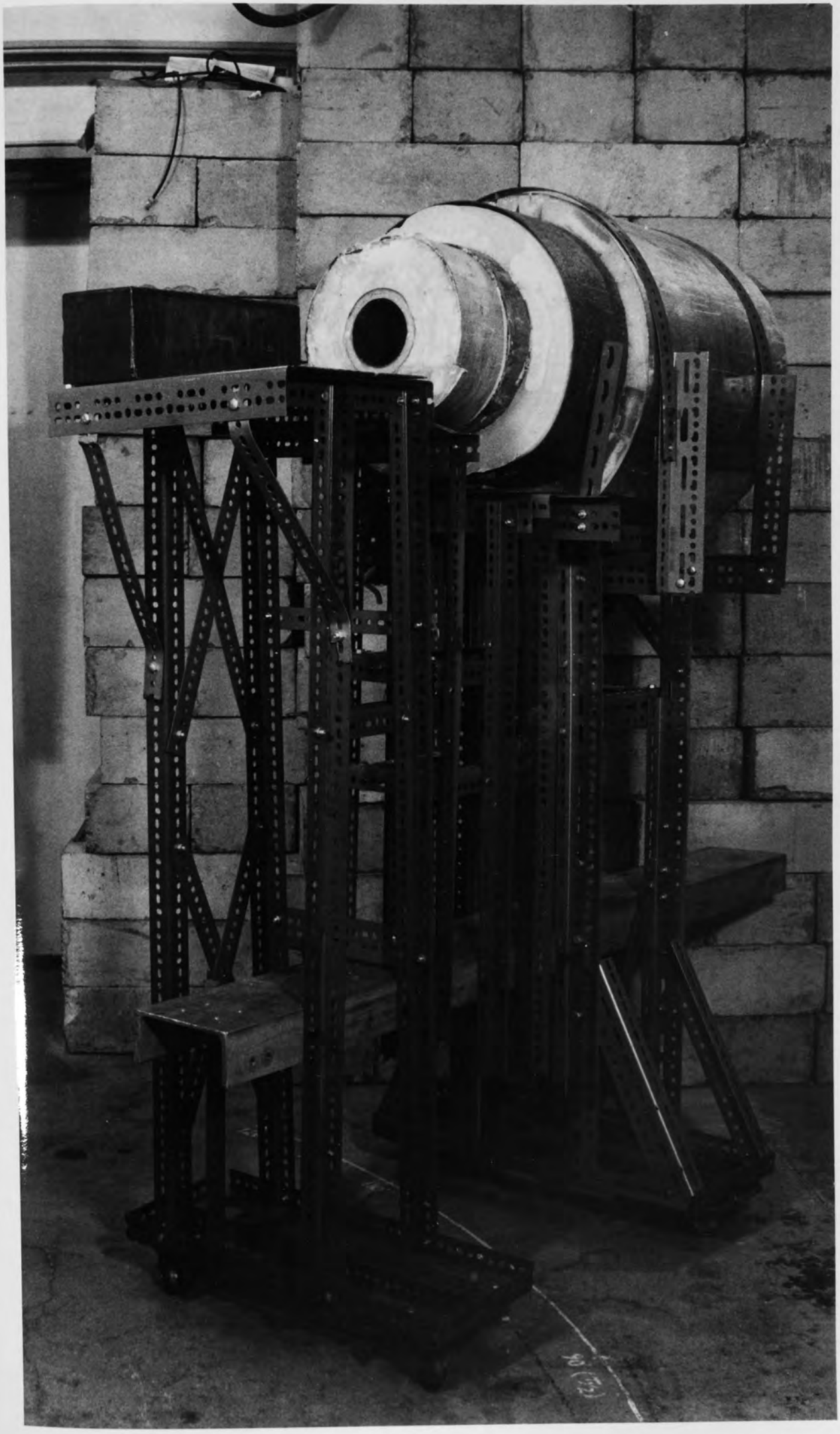

The elastic scattering cross-sections are dominant in light materials containing hydrogen, such as water and paraffin wax, and as the inelastic scattering does not occur with hydrogen, it has a low secondary γ-ray production. For heavy elements the entire elastic cross-section may be neglected. However, non-elastic processes strongly degrade or completely absorb the incident neutrons.

Figure (3.17) shows the variation of the macroscopic cross-section for the total non-elastic cross-sections for heavier elements such as W, Fe, Cu and Pb, while the total elastic cross-sections have been used to calculate Σ for hydrogen. From the same graph, it is shown that for $E_n > 4$ Mev. the maximum Σ will be associated with heavier elements with large cross-sections.

The obvious choice of hydrogenous material is paraffin wax or water. For ease of construction the shield was made from paraffin wax. In this moderating material thermal neutrons captured by hydrogen produce a single γ-ray of 2.23 Mev from the reaction $^{1}_{1}H(n,\gamma)^{2}_{1}H$ with a cross-section of 330 m b •Production of γ-rays via the neutron capture by the hydrogen in the shielding was suppressed by loading the paraffin wax with elements such as ^{6}Li and ^{10}B which has high slow neutron absorption cross-section. Generally, because of constructional reasons both materials are used in the form of a compound, typically Lithium carbonate and boric oxide.

Finally, the innermost part of the shielding should contain a γ-ray absorbing material. In the present work, the Lead γ-ray shield, because of its density and high atomic number, was used. It was 55 mm thick at the side of the detector and had a maximum thickness of 125 mm in front of the detector. The cross-section of the shielding which was used is shown in figure (3.18). The outermost shielding was paraffin wax with 150 mm thickness at the side of the detector, and about 330 mm in front of the detector. The slow neutron absorber of the shield was a 20 mm

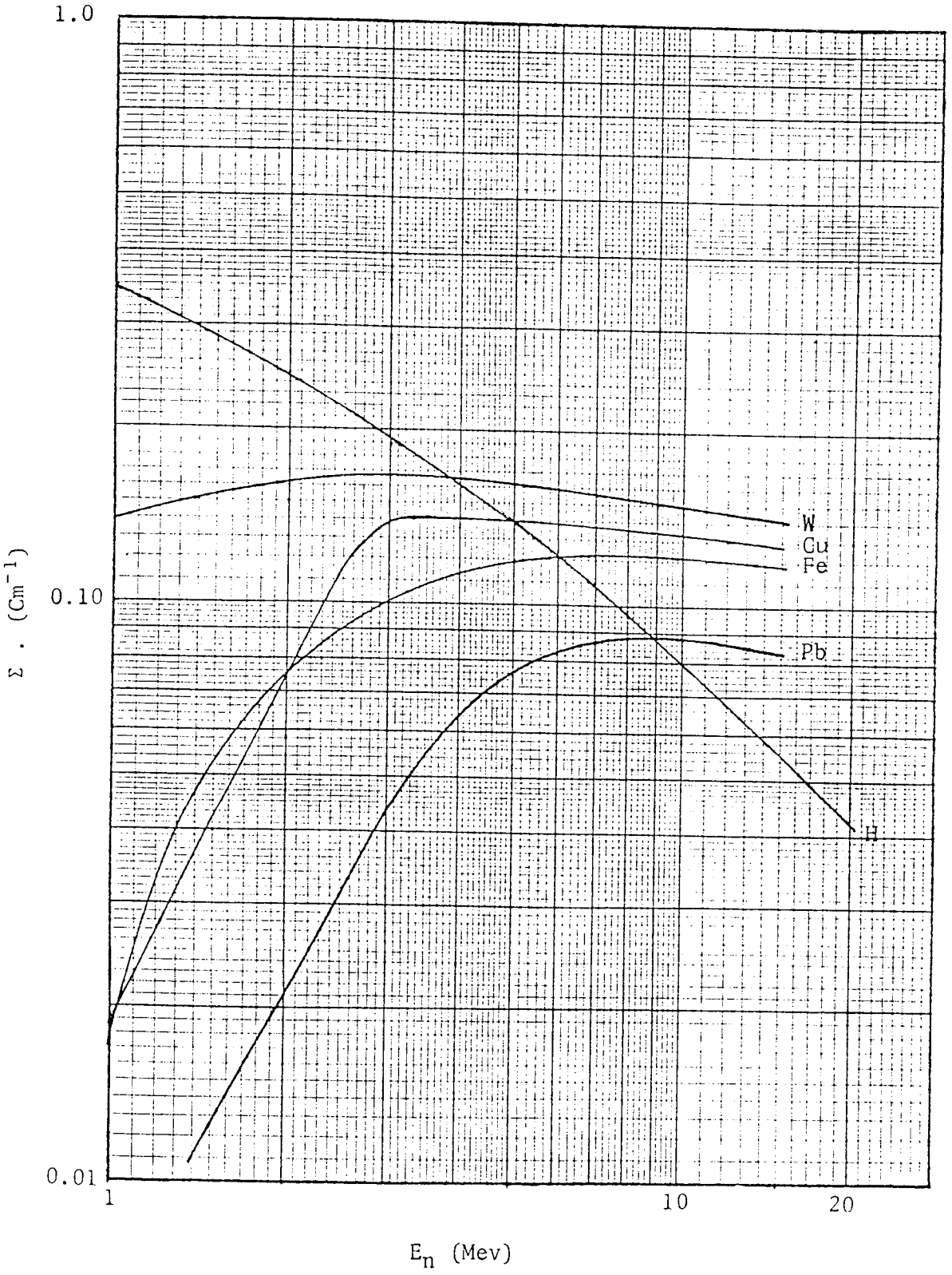

Figure (3.17) Macroscopic non-elastic absorption coefficients for W, Cu, Fe and Pb; and elastic absorption coefficients for H as it is occurs in paraffin wax [90].

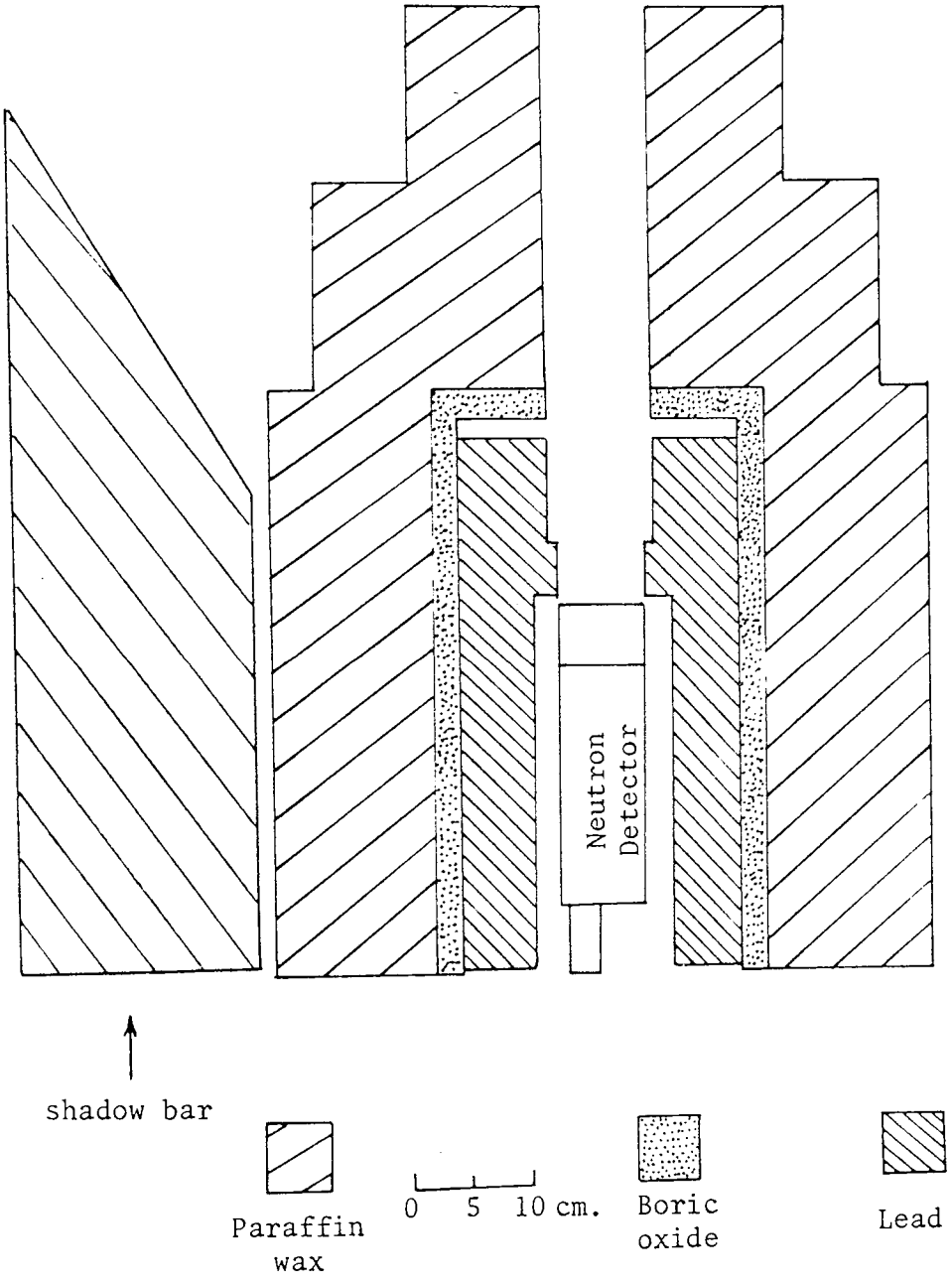

Figure (3.18) Cross-section of the neutron detector shielding and shadow bar

boric oxide powder packed in a double walled cylinder, around the lead and a collimator, which was enough to absorb all thermal neutrons.

3.11.2 Shadow Bar Shielding

Neutron experiments require careful shielding of the detector from the neutron source. This is achieved by interposing a sufficient mass of material directly between source and detector. In the angular distribution measurements, correct location of shadow bar is important. The selection of the appropriate shadow-bar material depends upon space and weight considerations. Some elements such as Fe, W, Cu and paraffin wax can be used as a shadow bar shielding. Hopkins et al[89] and Glasgow et al[90] have discussed the location and materials which are suitable for shadow bar shielding.

In general any shadow bar must be sufficiently massive and long to attenuate the direct neutron beam. It should not intercept neutrons between the neutron source and the scattering sample or detector. The face of shadow shielding closest to the scattering sample should not be viewed by the detector.

In the present work, the shadow bar used was constructed from paraffin wax, as shown in figure (3.18). Using the time-of-flight technique, the efficiency of the shadow bar was measured. The neutron detector was positioned in the direct beam of neutrons and the number of coincidences with and without the shadow bar for a given neutron yield, was recorded. The resultant spectra are shown in figure (3.19)

3.12 THE ALPHA PARTICLE DETECTOR

Two types of detectors, an organic scintillator, or a semi-conductor detector can be used to detect alpha particles from the $T(d,n)^4He$ reaction.

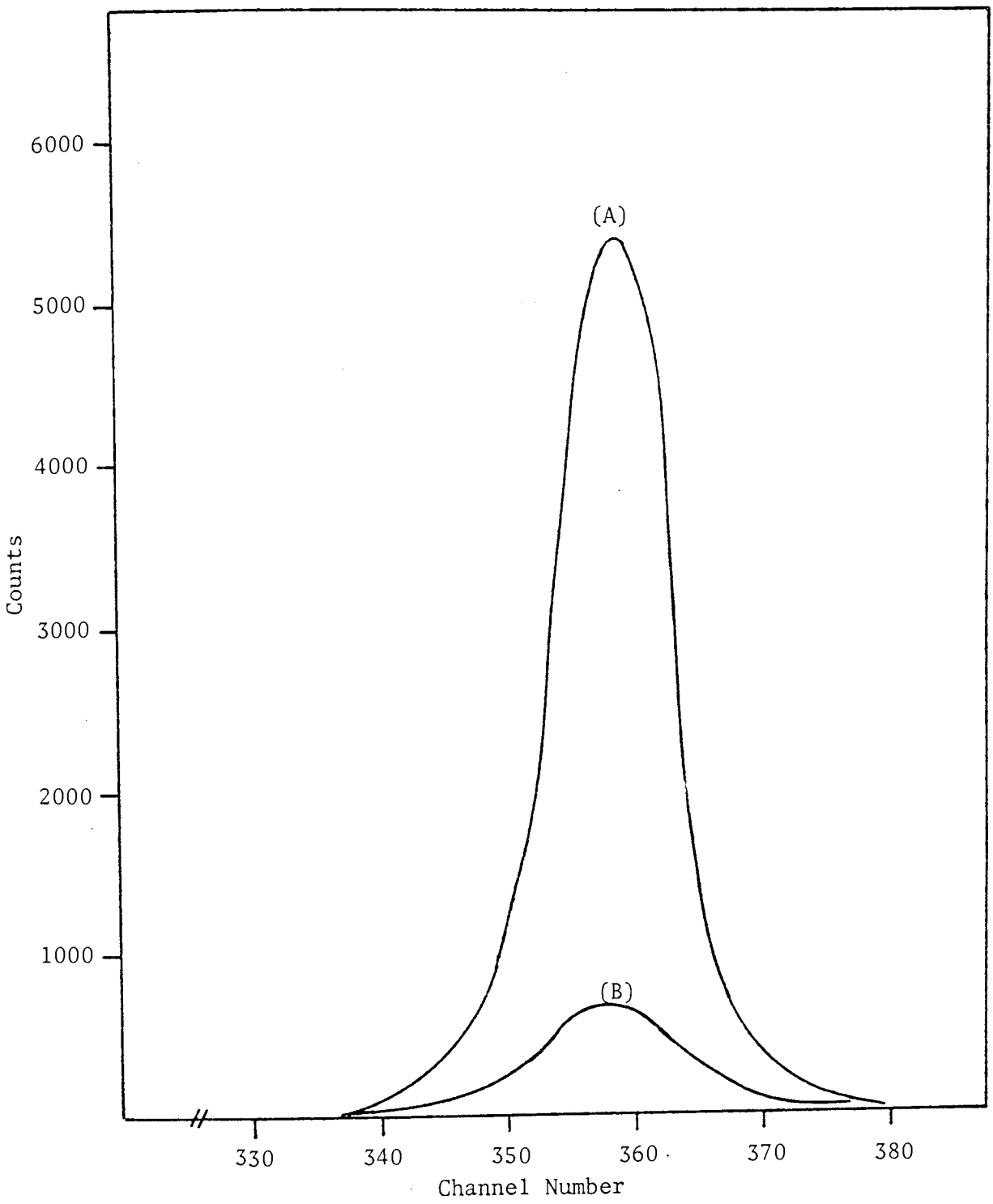

(A) - without shadow bar (B) - with shadow bar

Figure (3.19) The efficiency of shadow bar

A significant advance of organic scintillators in recent years has been the development of thin plastic scintillators led by Muga et al[91-92] with thickness down to 20 μ gr/cm^2. Because of the highly ionizing properties of alpha particles, they can be detected with 100% efficiency with thin scintillator. The energy loss of alpha particles in thin scintillator is discussed by Geissel et al[93]. The alpha particle detector for the present work required the following properties:

(1) Low detection efficiency for neutrons and γ-rays

(2) Excellent detection efficiency for alpha-particles

In comparing the above detectors, the thin plastic scintillator has several advantages:

(A) when it is used with high gain focussed photomultiplier tubes, there is no need to use a pulse amplifier which is required with the semiconductor detectors

(B) it has less sensitivity to radiation damages

(C) it has a faster rise time than the semi-conductor system .

In view of these advantages, an organic scintillator type NE 102A with 0.5 mm thickness and 30 mm square was used to detect alpha-particles. This was used in conjunction with a "Phillips" 56 AVP photomultiplier tube, mounted through a perspex flange of 10 mm thickness which acted as a light pipe and as a vacuum seal for the photomultiplier tube. The scintillator was attached with optical cement type NE 580 to the perspex of the light pipe.

The detector was positioned at 90° with respect to the incident deuteron beam and 90 mm distance from the T-Ti target. The solid angle of the detected alpha particles was defined with a (11 mm x 19 mm) rectangular aperture in the plate. The detector subtended semi-angles of 6 in the

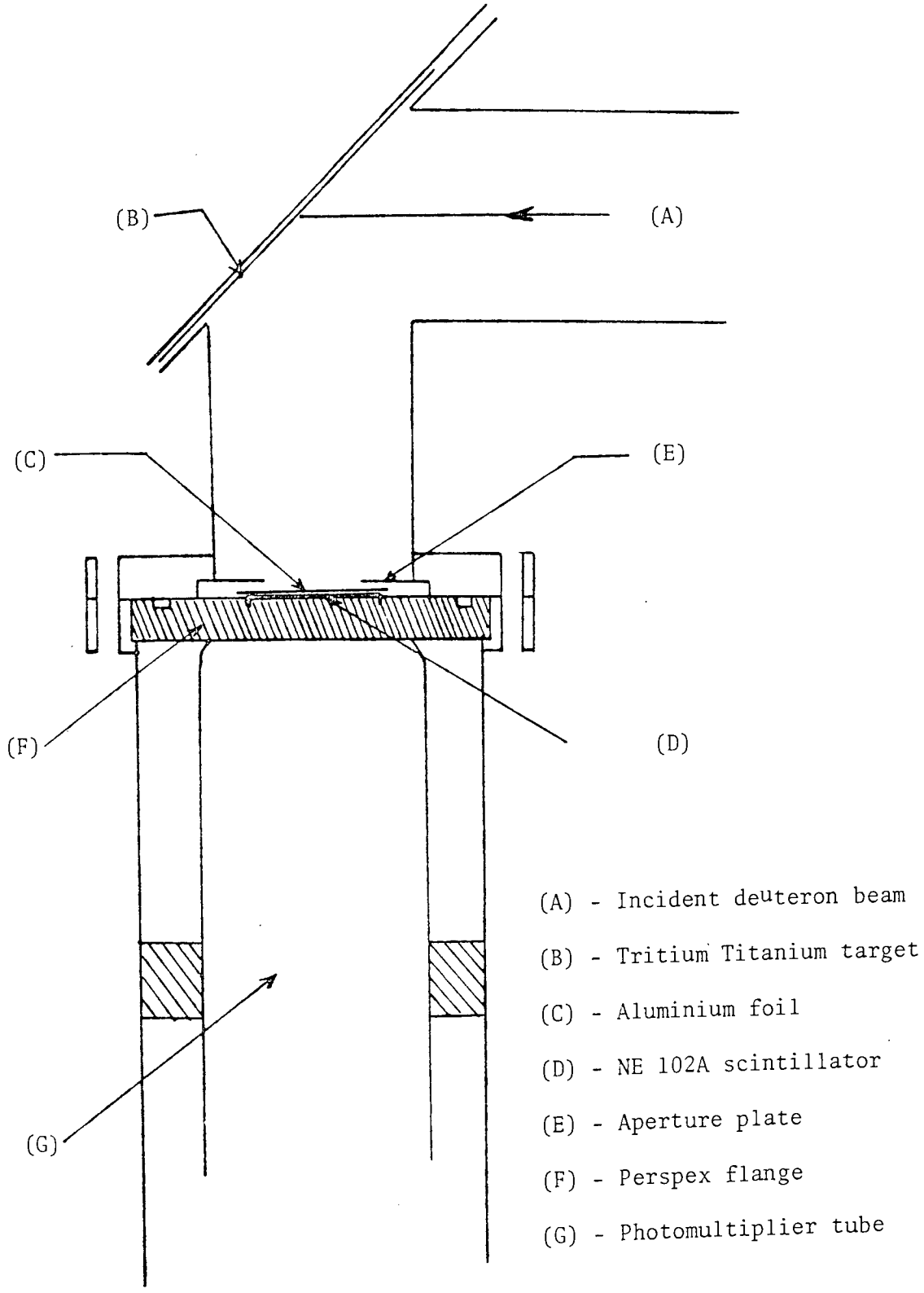

Figure (3.20) The Alpha Particle Detector Assembly

vertical and 3.5° in the horizontal directions. The alpha particle detector arrangement is shown in figure (3.20). The energy of alpha particles emitted at 90° to the deuteron beam was 3.5 Mev (section 2.4). The range of these alpha particles in NE 102A is stated by the manufacturers to be 0.025 mm. Figure (3.21) shows the range of alpha particles in NE 102A plastic scintillator. With the above thickness the alpha particle detection was 100% efficient.

The dynode resistor chain was similar to that used in the neutron detector assembly. The cathode was held at a negative potential, while the anode was held at zero potential. The output pulses were taken from the anode via a 50Ω resistor. Figure (3.22) shows the dynode resistor chain. Since the detector was fixed at 90° with respect to the earth's magnetic field, a Mu-metal shield was not used for the alpha detector.

3.12.1 Alpha Detector Shielding

The alpha detector had to be screened from β-particles and deuterons scattered from the target. The β-particles are produced in the decay of Tritium in the target, i.e.

$$T \rightarrow {}^{3}_{2}He + \bar{\beta} + \bar{\nu} \qquad \ldots\ldots (3.39)$$

with a half-life of 12.3 years. The energy of $\bar{\beta}$ particles released is 18.6 keV and have a maximum range of 0.0022 mm in aluminium [71]. The energy of the scattered deuterons in the alpha detector was less than 140 keV. Using equation (2.25) the range of 200 keV deuterons was found (0.52 mg/cm^2) 0.002 mm in aluminium. Therefore, a thin aluminium foil with 0.0044mm thickness which completely shielded detector from those particles was used. As the range of alpha particles in aluminium is 0.017 mm [49], the alpha particles were able to reach the detector.

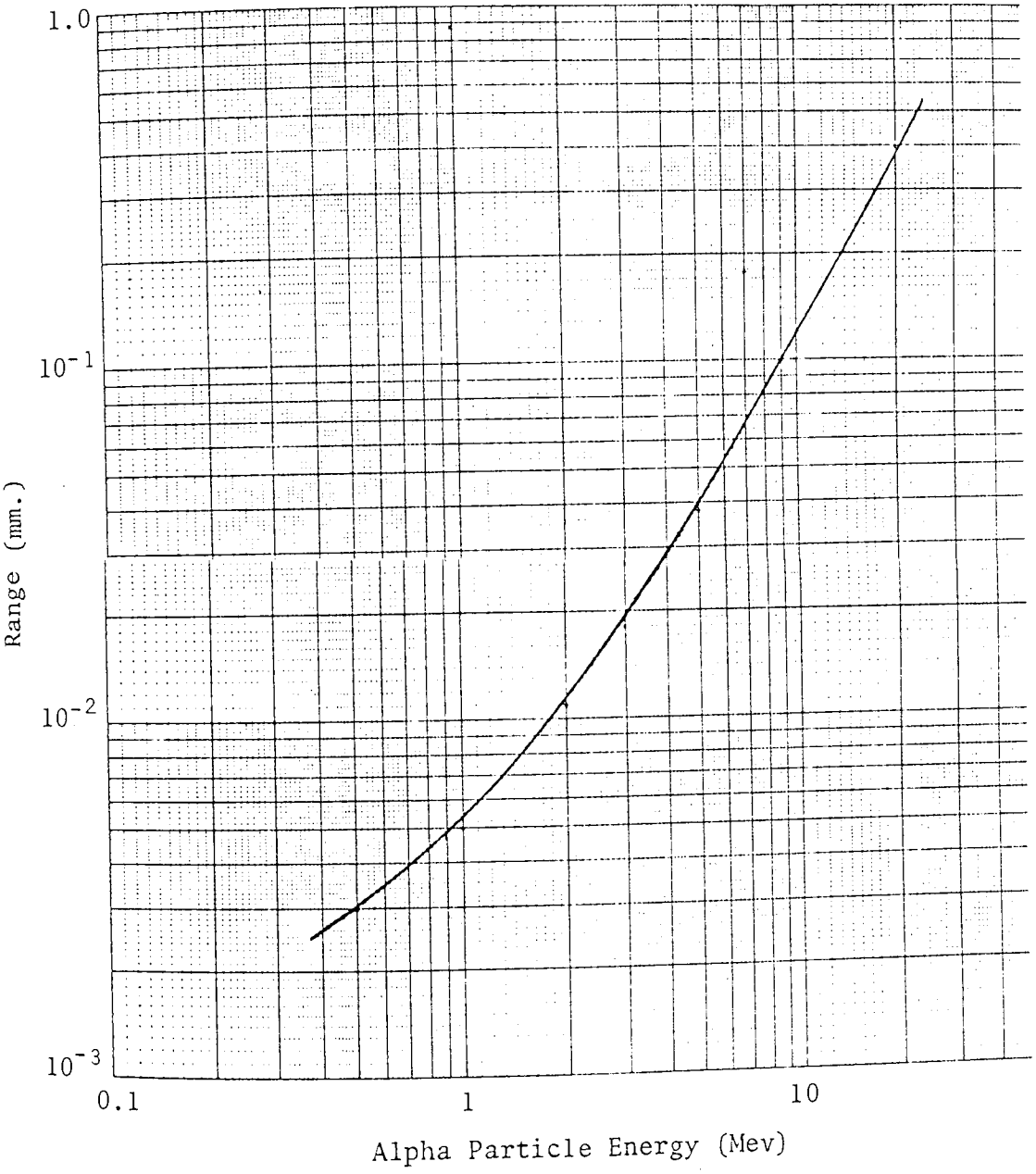

Figure (3.21) Range of alpha particles in Ne 102A [68]

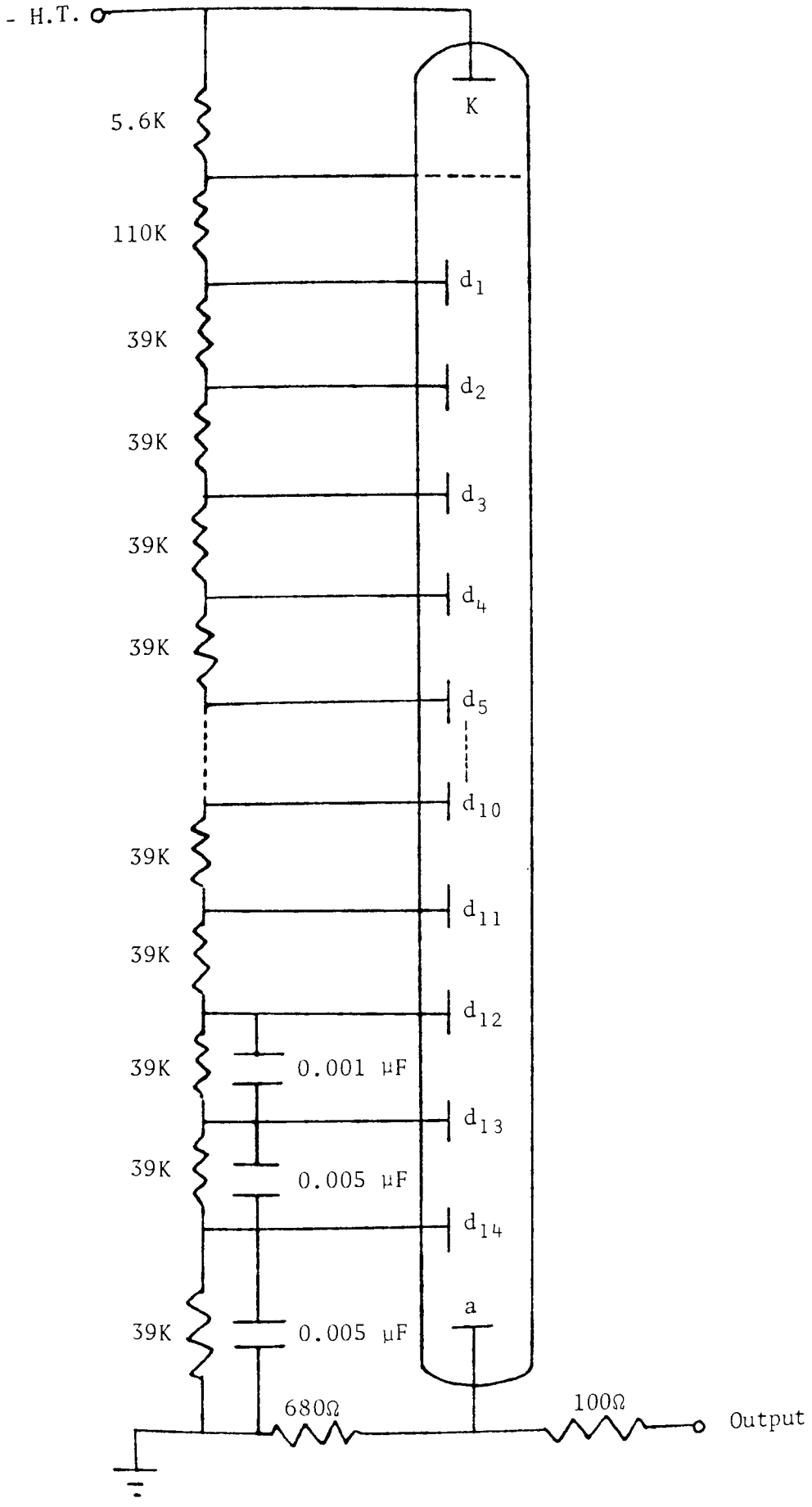

Figure (3.22) The Dynode resistor chain for alpha detector

Figure (3.23) shows the alpha detector scintillator, light pipe, aluminium foil, photomultiplier and aperture plate.

3.12.2 Setting the Alpha Particle Detector Discrimination Level

The alpha-particle pulses were discriminated using a 100 MHz discriminator (ORTEC 436) to remove the low energy background below 3.5 Mev. The experimental arrangement is shown in figure (3.24). Using the linear amplifier (ORTEC 485) the detector output pulse was amplified and then the resulting pulses were gated by the output of the discriminator. As the discriminator level was increased, the linear gate was not opened, hence the lower energy region of the spectrum was removed.

Figure (3.25) shows a pulse height spectrum of the alpha-particles from the $T(d,n)^4He$ reaction.

Figure (3.23) The Alpha Detector photomultiplier, light pipe flange and aperture plate

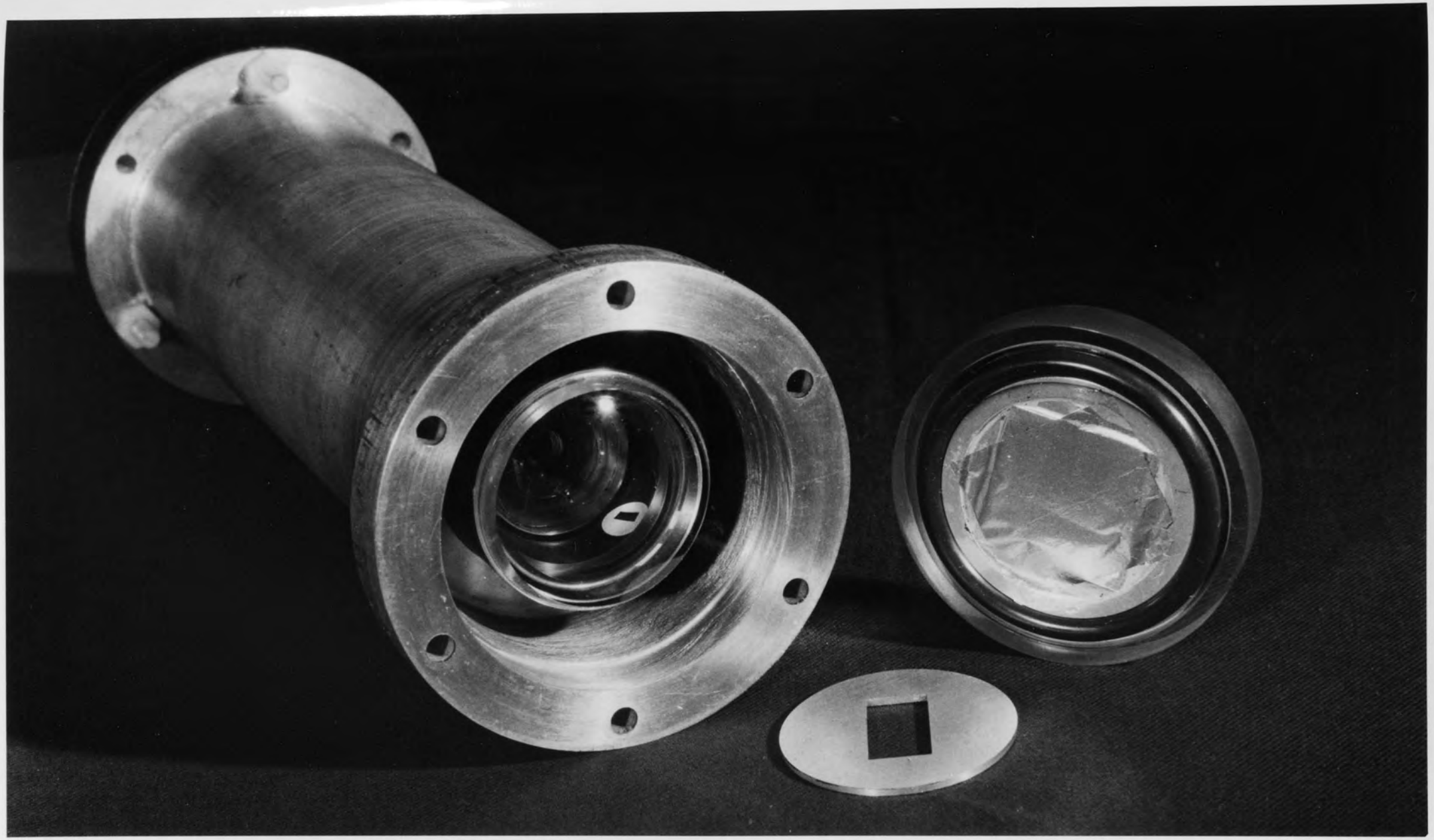

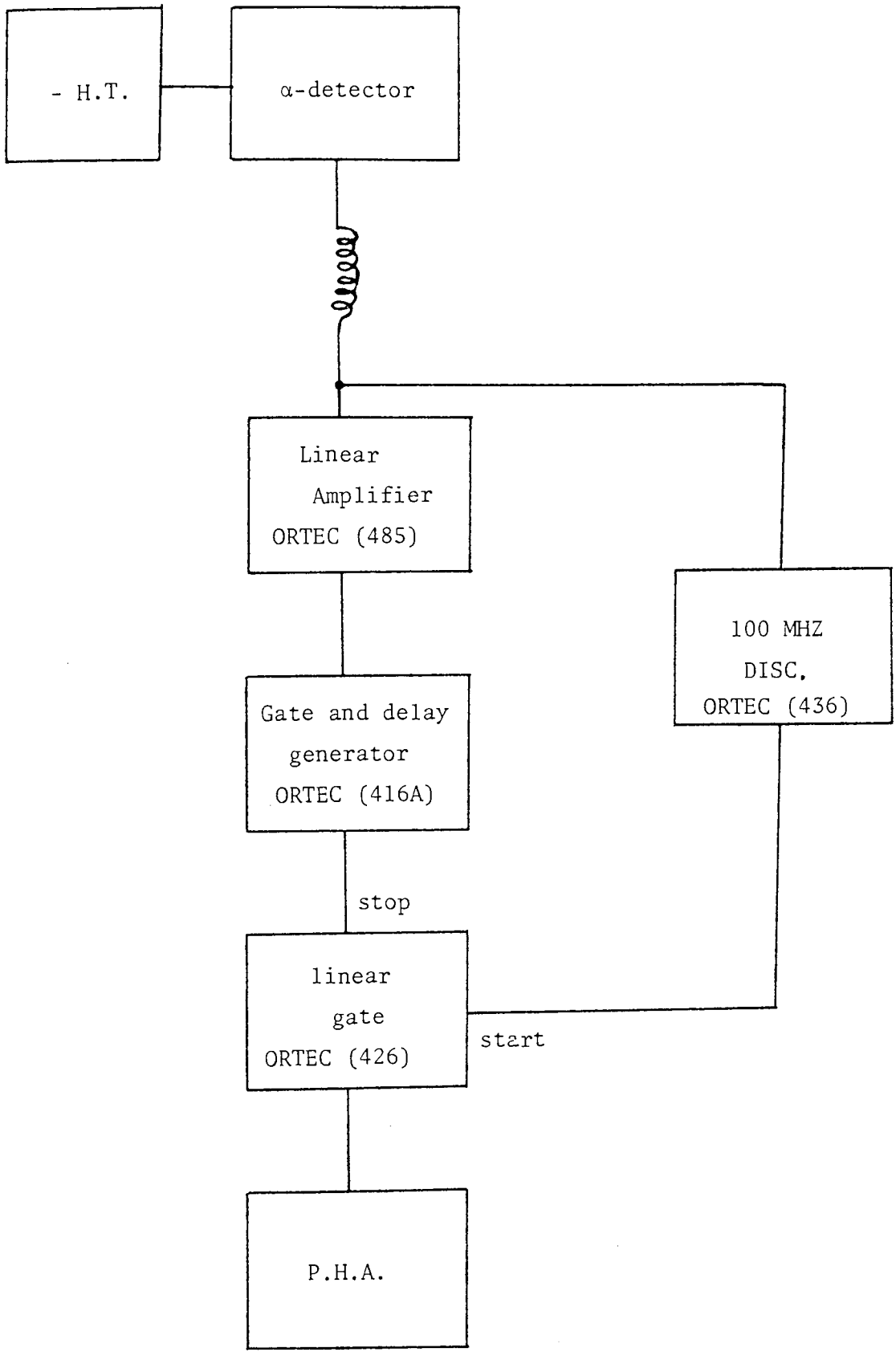

Figure (3.24) Block diagram of the elctronics used for setting the alpha-particle discriminator level.

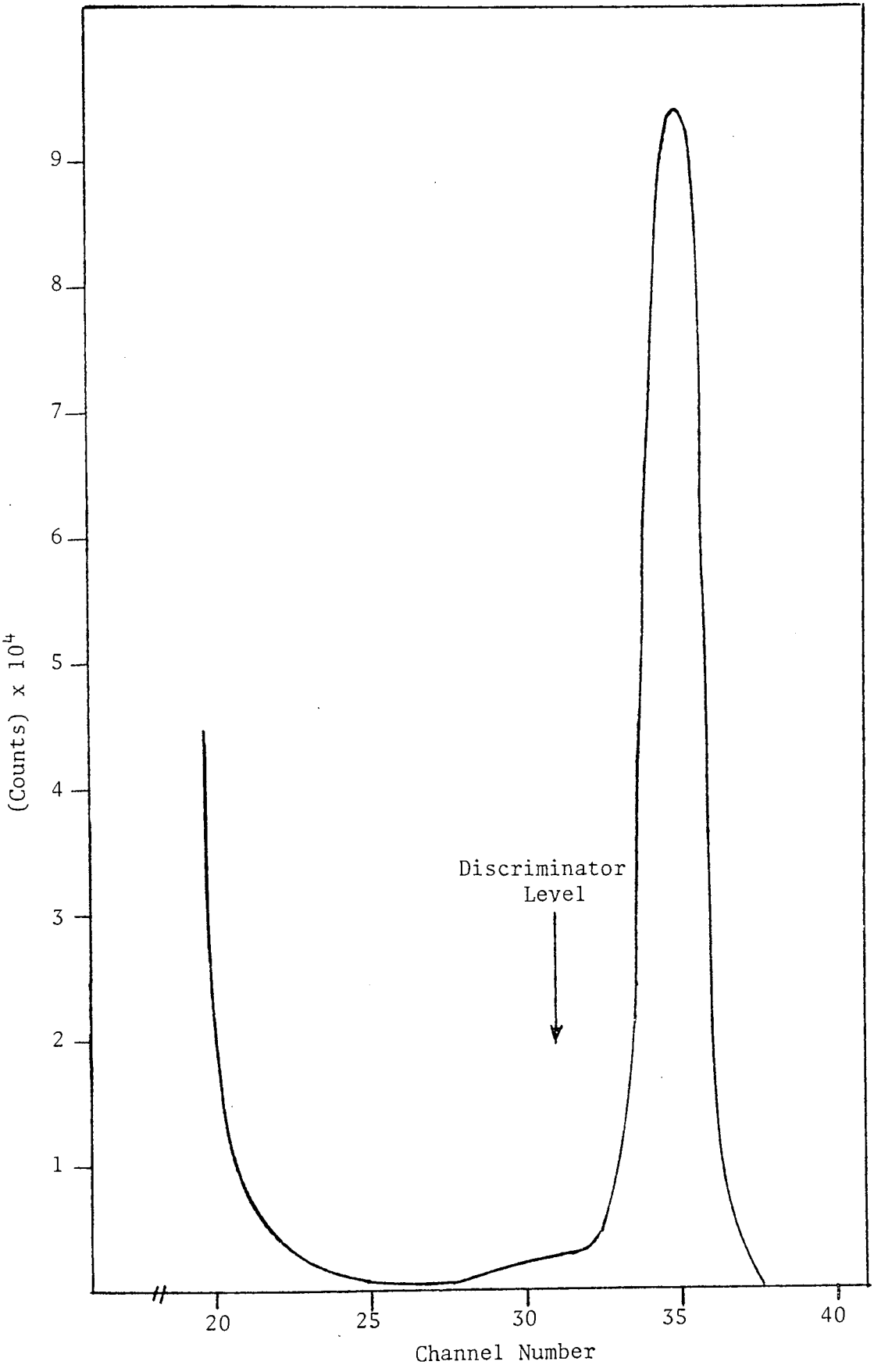

Figure (3.25) Alpha-Particles Pulse Height Spectrum

CHAPTER FOUR

CHAPTER FOUR

ASSOCIATED PARTICLE TIME-OF-FLIGHT SYSTEM FOR THE D(d, n)^{3}He REACTION AT AN INCIDENT DEUTERON ENERGY OF 1 Mev

4.1 INTRODUCTION

The D(d, n)^{3}He reaction has long been used as a source of neutrons in neutron scattering experiments. This exothermic reaction has an appreciable cross-section for deuterons with a bombarding energy of several hundreds of keV. The cross section of this reaction is shown in figure (2.1).

In fast neutron scattering experiments, there is usually a high background count due to scattering of neutrons from the materials in the experimental room. Using the associated particle time of flight technique, many of these background problems have been overcome. As mentioned in section (2.3.2), in this method the detection of the ^{3}He particles can be used to define an associated cone of neutrons. Using the reaction kinematics for a particular deuteron energy and ^{3}He, the direction and energy of the associated neutron can be determined.

In order to determine the neutron flux at the scatterer, the number of ^{3}He particles must be known, hence it is important to be able to resolve the particles produced by the interaction of the deuteron with the deuterons. The most difficult problem is the resolution of ^{3}He particles from the deuterons elastically scattered from the target nuclei.

At low incident deuteron energy (Ed < 300 keV), the range of the ^{3}He is higher than the maximum range of the scattered deuterons, hence an absorber between the detector and target, can be used to remove the scattered deuterons before they reach to the detector. The other charged particles (i.e. protons and Tritons) produced from the competing D(d, p)^{3}H reaction, give no serious problems, due to the higher Q-value (Q = 4.032 Mev) of the reaction. The energy of the protons and Tritons are larger

than the ^3He energy, hence it is possible to produce different pulse heights for the "^3He", "p" and "T" particles respectively.

Various other methods have been applied to resolve the ^3He particles from the elastically scattered deuterons. Okhuysen et al[95] and Dixon et al[96] for Ed = 100 keV used Aluminium foil in front of the charged particles detector, to stop the elastically scattered deuterons. In this case ^3He particles lose some of their energy in the foil, and a poorer ^3He energy resolution resulted. However, for deuteron energies much above 100 keV, a thin foil cannot be used to protect the ^3He detector, since the thickness of foil required to stop the scattered deuterons, will also stop the ^3He particles. Hence at high deuteron beam currents pile up of pulses from the scattered deuterons causes them to mask with the ^3He pulses in the spectrum.

To eliminate the effect of the scattered deuterons, a D_2 gas target may be used with the detector placed at backward angles, since no deuterons are scattered beyond 90°. However, Schuster[97] has shown that above 3.27 Mev bombarding energy, the maximum ^3He angle does not reach 90°. Moreover, a gas target makes it difficult to obtain both good angular resolution and high intensity. Finally, many workers [45, 98-102] have applied electrostatic and magnetic analyzer, to deflect the particles before they strike the detector. Prade et al[100] used an electrostatic analyzer for deuteron energies from (92 - 173) keV, and for neutrons emitted at 50°.Galloway et al[101]adopted the same analyzer for deuteron energies up to 300 keV, and for neutrons emitted around 50°, he resolved the ^3He particles from the other particles. For measurement of the angular distribution of γ-rays from the inelastic scattering of 2.5 Mev neutrons with Iron, Put et al[98] applied an electrostatic analyzer, for an incident deuteron energy of 300 keV, and found that for ^3He detector at about 64° with respect to the incident beam, complete separation between both types of particles is possible. However,the disadvant-

age of this method is that, at higher energies, the longer path length required by the analyzer, causes a larger spread in the time of detection for ^{3}He particles of different energies. In addition these analyzers reduced the count rate capability.

The other method which has been used to reduce the number of scattered deuterons to an acceptable level is the use of a thin deuterated polyethylene target. Because of the small energy loss suffered in these targets by the emitted particles, the full energy of the ^{3}He particle is available. Tripard et al[103] and Schuster[97] using deuteron energies from 2 to 14 Mev respectively, have shown that, by using a thin self-supporting deuterated polyethylene target good results can be obtained. Janicki and Cox[104], using this target, obtained good results for the scattering of 2 - 3 Mev neutrons from ^{40}Ca and ^{32}S. However, the number of scattered deuterons is still sufficiently large to mask the ^{3}He pulses in the detector. By gating the ^{3}He pulses with pulses from a neutron monitor mounted in the associated neutron beam, the ^{3}He pulses can be resolved. To determine the neutron yield accurately, it is usually better to monitor the proton peak produced in the competing $^{2}H(d, p)^{3}H$ reaction, which has high energy and is separated from the low energy groups. By determining the ratio of the cross-section for these two "DD" reactions and relating the proton yield to the ^{3}He yield, the neutron flux can be determined. [105, 106]. The cross-section for these two reactions are given by Blair et al[107] and are shown in figure (4.1).

In the present work, by making a thin deuterated polyethylene target, and using a 1 Mev deuteron energy, the scattering of 3.02 Mev neutrons from an Iron sample was studied. The experimental procedure and electronic systems are discussed in the next sections.

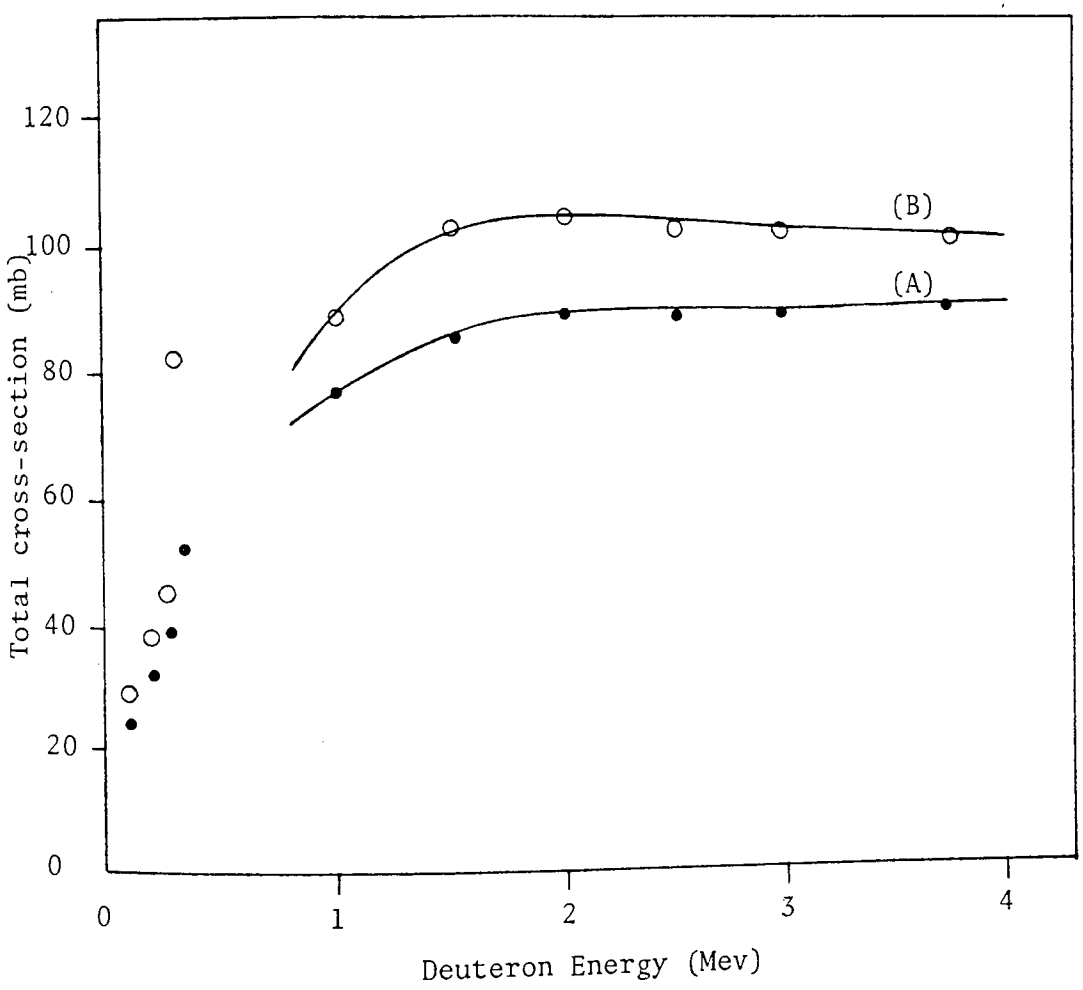

(A) : For D(d, n)^{3}He Reaction (B) : For D(d ,p)^{3}H Reaction

Figure (4.1) Total cross-section for the (DD) reactions for various deuteron energies [107].

4.2 KINEMATICS OF NUCLEAR REACTION

The D(d, n)^{3}He reaction can be used to produce neutrons in the intermediate energy range. For most laboratories this reaction is the only practical source of monoenergetic neutrons of energy between a few Mev and 7 Mev range. In order to detect neutrons and ^{3}He particles, for a particular incident deuteron energy and for a defined neutron angle, the energy and angle for the ^{3}He particles are considered. Using the kinematics of nuclear reaction as discussed in section (2.5) and the relevant equations, the energy E_3, of the neutron emitted at a given angle θ_3 with respect to the incident deuteron direction in the Laboratory system of coordinates and for an incident deuteron energy E_1 can be calculated. The angle of the associated $^3_2$He particle is emitted at an angle θ_4 with respect to the incident deuteron direction was obtained from equation (2.18), and the energy of the $^3_2$He particle was determined from equation (2.9). Figure (4.2) shows the variation of the $^3_2$He angle with neutron angle for various incident deuteron energies. The variation of neutron energy with neutron angle for various incident deuteron energies is shown in figure (4.3), while figure (4.4) shows the variation of $^3_2$He energy with neutron angle for different incident deuteron energies.

In the present system, the neutron production angles were limited to 30°, 75° and 120° to the incident deuteron beam direction. However, in this work, to produce 3 Mev neutrons using an incident 1 Mev deuteron beam, neutrons were detected at 75° to the beam direction. Considering this neutron angle, and calculating the corresponding $^3_2$He angle and energy, the energies of proton and Triton were determined for increasing incident deuteron energies. Using equations (4.1) and (1.12), the energies of the scattered deuteron from deuterium target, and carbon in the target were determined respectively.

For deuteron-deuterium elastic scattering:

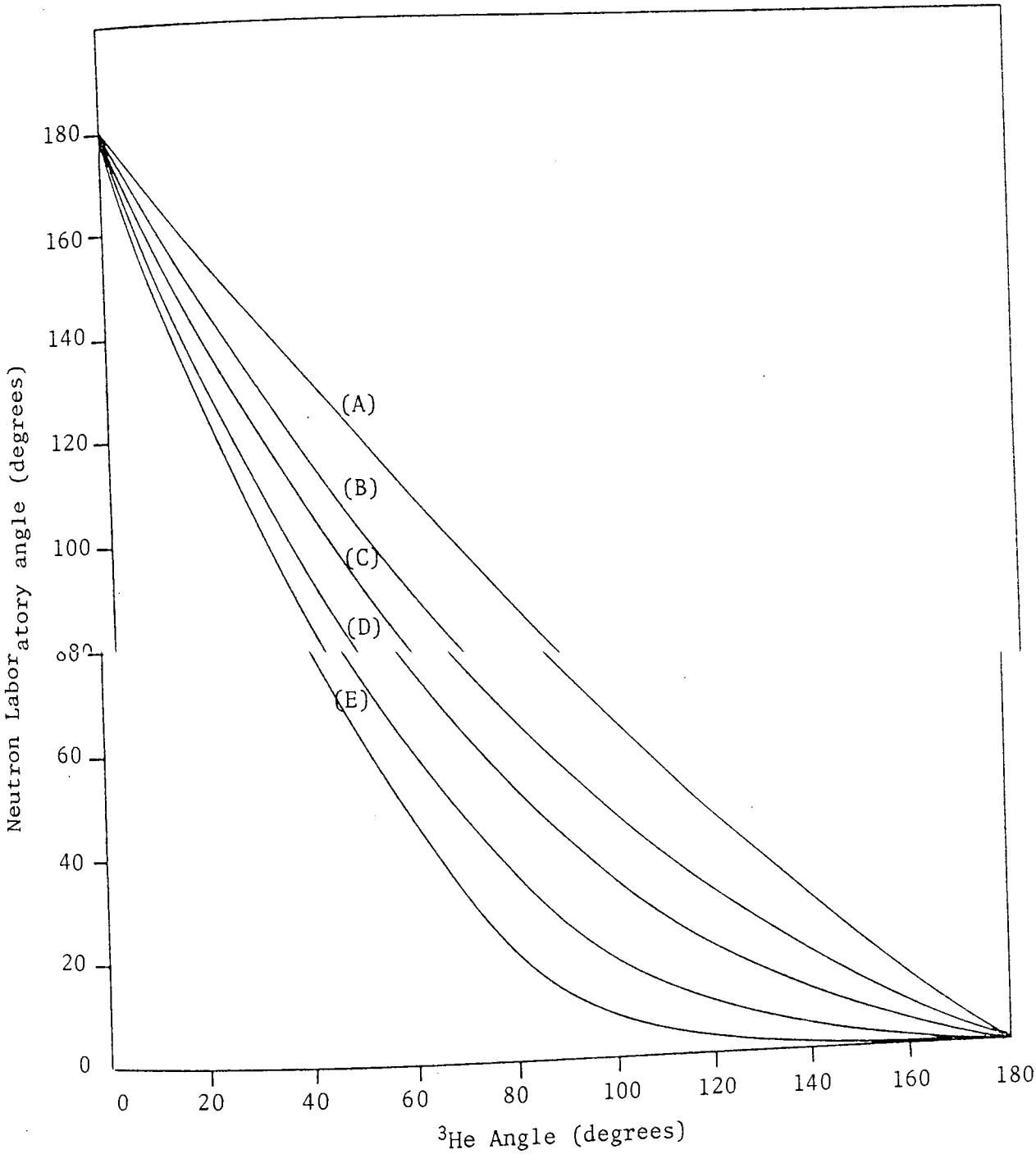

(A) : Ed = 0.1 Mev (C) : Ed = 1 Mev (E) : Ed = 3 Mev

(B) : Ed = 0.5 Mev (D) : Ed = 2 Mev

Figure (4.2) Angle of neutron emission versus the associated ^3He particle angle for different deuteron energies

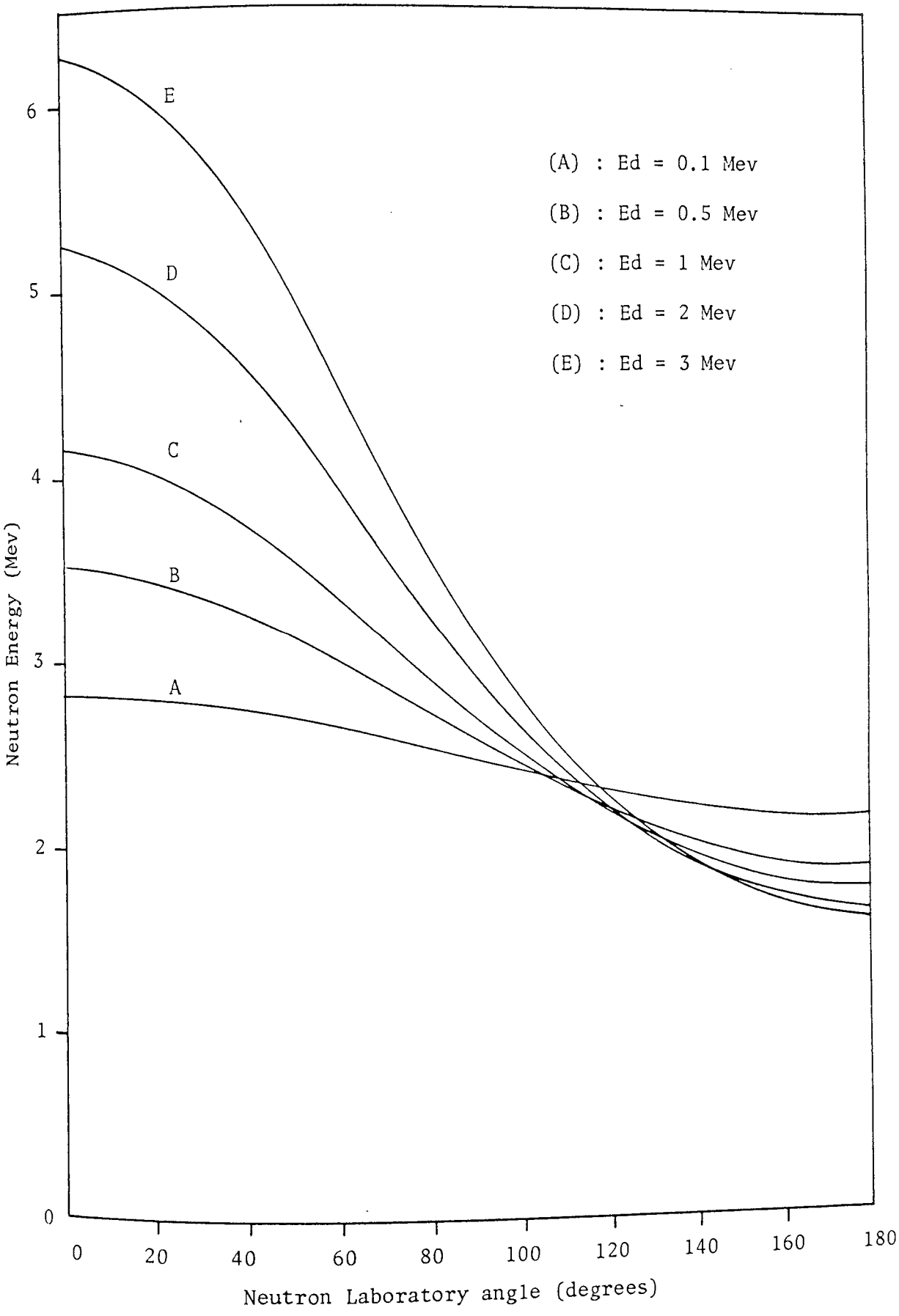

Figure (4.3) Variation of the neutron energy versus angle of emission for deuteron energy 0.1 to 3 Mev in $D(d,n)^3He$ reaction

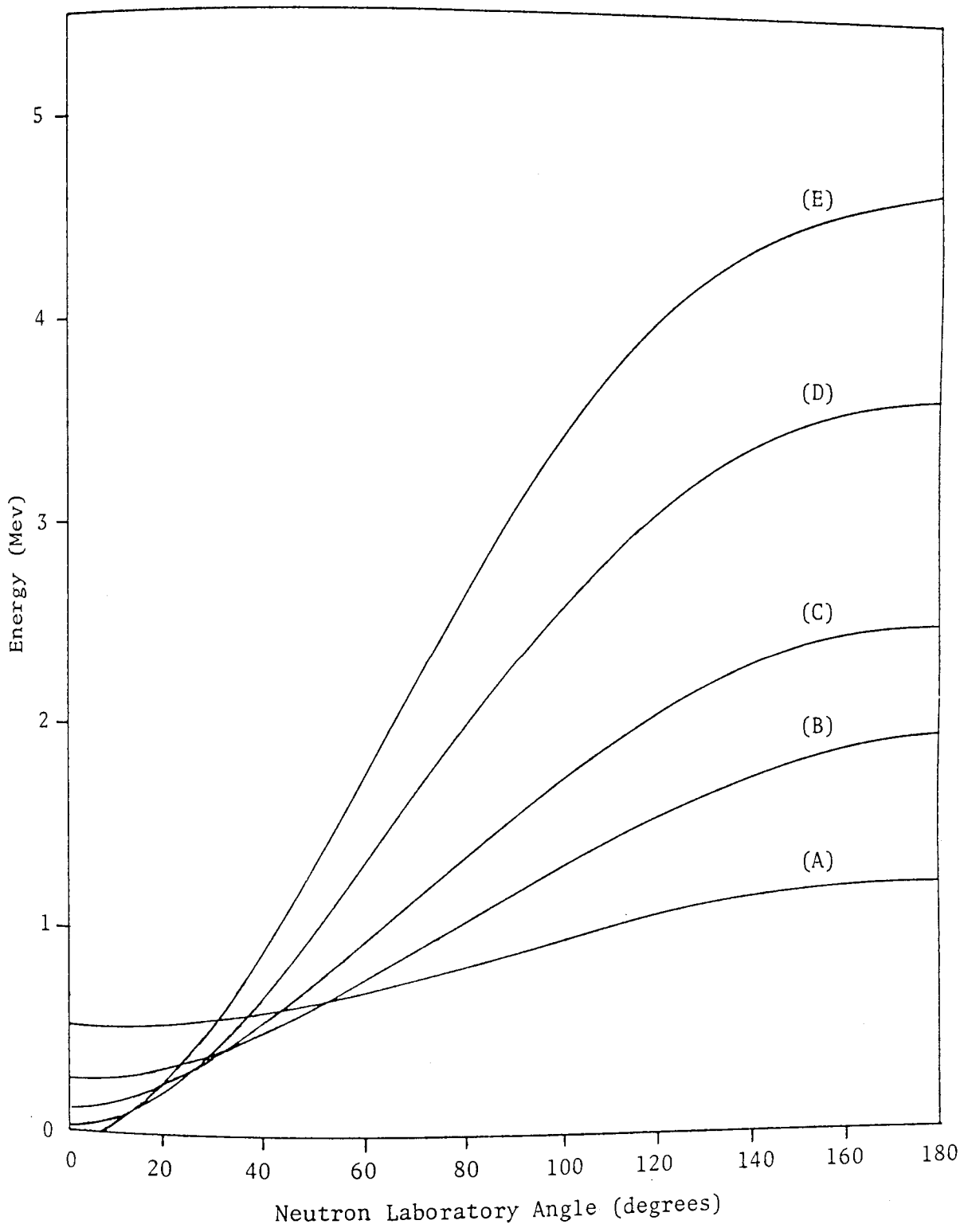

(A) : Ed = 0.1 Mev (C) : Ed = 1 Mev (E) : Ed = 3 Mev

(B) : Ed = 0.5 Mev (D) : Ed = 2 Mev

Figure (4.4) Variation of the ^{3}He particle energy versus angle of neutron emission for various deuteron energies

$$E_1 = E_o \cos^2\theta \qquad \ldots\ldots (4.1)$$

where E_o = the energy of incident deuteron

E_1 = the energy of elastically scattered deuteron from deuterium target

and θ = scattering angle in the Laboratory coordinate system

Figure (4.5) shows the variation of the energies of the emerging particles from the target versus the deuteron energies at $\theta_n = 75°$

4.3 PREPARATION OF THE DEUTERATED POLYETHYLENE TARGET

Deuterated polyethylene is a convenient source of deuterium for target preparation. The target must be thin enough to minimize energy loss and scattering of the emitted $^3_2$He particles. Various method for the preparation of $(C_2\ D_4)_n$ foils have been discussed in the literature [108-113]. Preparation of very thin polyethylene foils with thicknesses between 900 A° and 2500 A° has been reported by White[108] who used vacuum evaporation. However, in this method a large fraction of the evaporated polyethylene is lost in the vacuum chamber. Arnison[109] and Tripard et al[110] used similar method for making thin foils in the thickness range of 1 to 20 mg/cm^2 and 100 µgr/cm^2 respectively. The main difficulty with these targets is their very poor stability in a charged particle beam due to their very low thermal conductivity. Tripard et al[110] found that, by evaporating a thin film of carbon onto the polyethylene, the target stability conductivity was improved.

Bartle et al[111], Bartle[112] and Janicki[113] have discussed a similar technique in which, the $(C_2\ D_4)_n$ is mixed in xylene. The mixture is heated on a hot plate to the boiling temperature of the solution. The solution is then poured onto a glass slide. By immersing the slide

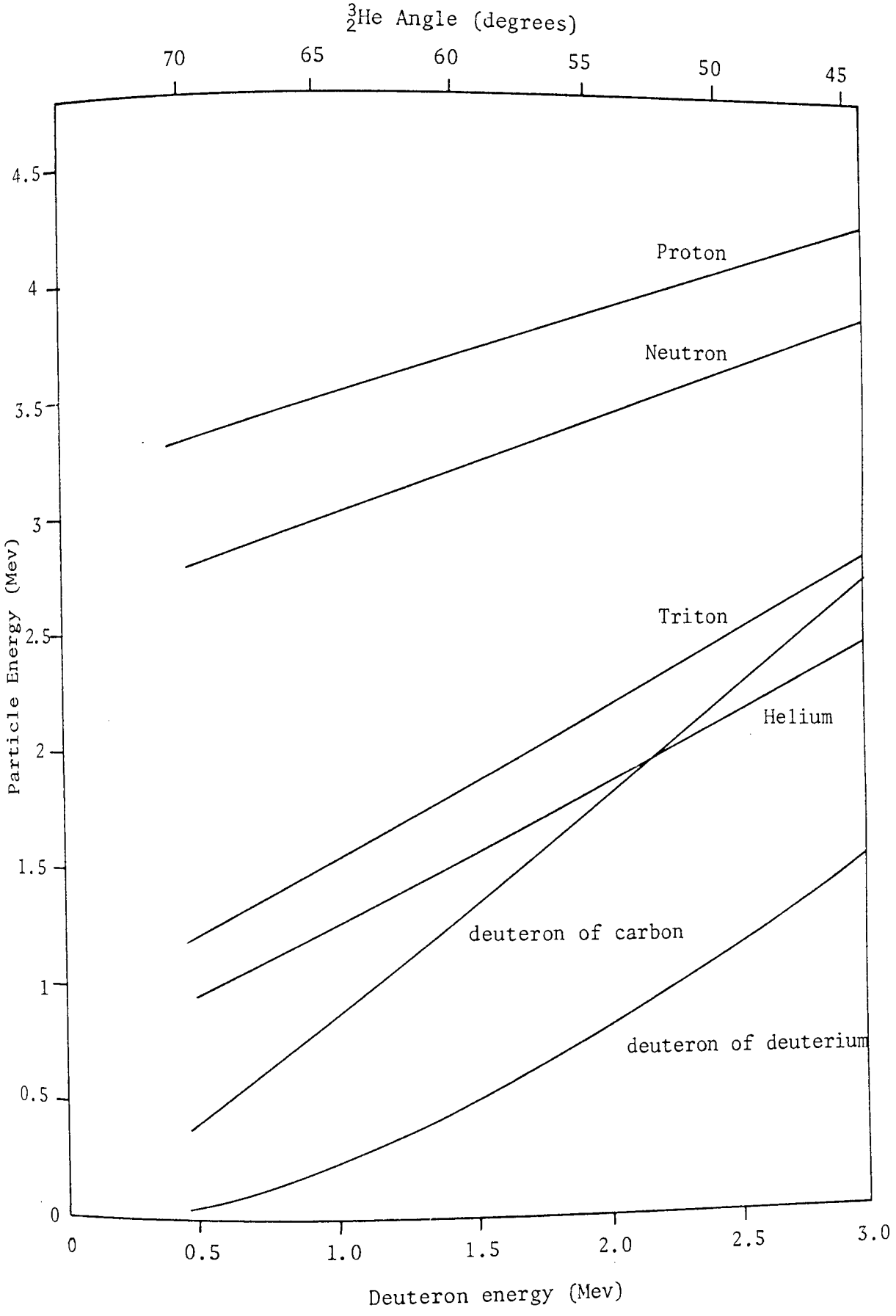

Figure (4.5) Variation of the energy of the charged particles versus various incident deuteron energies produced at 60.2° with respect to the deuteron beam (associated Laboratory neutron angle≈75°)

in water, the films are floated off and can be picked up onto a metal frames. In the present work, this method was used to prepare targets of 2 μm thickness.

A glass slide (5 cm. x 5 cm.) was immersed in the solution of 5 cm^3 of industrial cleaning agent either "TOT" or "TEPOL" and 1.5 litres of distilled water to make the detachment process easier to accomplish, and kept on a hot plate at temperature of about 95°. Then 4 mgr of deuterated polyethylene was added to 5 cm^3 of xylene, the solution was heated to the boiling temperature on the hot plate at approximately 145°C, after about 5 minutes, the deuterated polyethylene was completely dissolved. The solution was allowed to cool down and poured onto the glass slide which was covered in the evaporation stage and kept at 95° for a few minutes. Finally the slide was removed and cooled to room temperature.

To release the film, the slide was immersed in the water surface at about 30° to the surface. Before floating the film off, it was found that it is better to start the floating off procedure by inserting a sharp object at one side of the slide, lifting about 2-3 mm. of the target. The surface tension was used to float the remainder of the film from the slide with no damage to the film. After about 2 hours the film was removed from the glass and floated free on the water surface. The film was fitted onto a stainless steel ring with a centre hole of 2.9 cm. diameter. Normally about 25 targets were made each time. The thickness of each film was determined by twice weighing the dried glass slide which had been pre-coated with the parting agent, and then reweighing the slide after covering it with the deuterated polyethylene target. The average thickness of film was found to be (2 ± 0.5) μm. usually for about 65% of the foils, it was found that, the polyethylene was distributed uniformly.

4.4 TARGET CHAMBER, TARGET ASSEMBLY AND BEAM COLLIMATOR

The cross section of the target chamber used for "DD" reaction is shown in figure (4.6). It was constructed from stainless steel with an internal diameter of 23 cm. . Three ports of 22.5 mm. radius were made at 30°, 75° and 120° to the incident beam on one side of the chamber. The diameter of the tube for the incident beam was 10.2 cm. The area of the target was restricted by a 1 mm. beam collimator made from tantalum. At 45 cm. from the target a 1 cm. diameter aperture in a stainless steel stop was used. The beam collimator was placed 3 cm. distant from the aperture. It was in the form of a disc placed in an annular of aluminium holder, as shown in figure (2.8). The aperture and beam collimator were electrically insulated from the beam line and target chamber.

The rotating target assembly was made from stainless steel, and was mounted at 45° to the direction of the incident beam in the chamber. An RDS rotary drive assembly placed at 30° and was used to drive the target. In the course of this work, the rotary motion drive was changed and a Ferrometic rotary shaft vacuum feed through was used. The target was mounted at the centre of the target assembly. To use the maximum area of the target, it was rotated in a circular mode as well as using a radial scan. The assembly then rotated the annular target ring through 6°, and then the scan would restart. The average life time of a good target was about four hours, and after that, the target was replaced. A copper Faraday cup was mounted in the position of the direct incident beam, behind the target. The beam passed through the target and was monitored by the cup, which was insulated from the chamber. The output was taken out of the vacuum through a vacuum tight insulated connector mounted in the chamber. The maximum current used on the target was 25 nA at 1 Mev incident deuteron beam . At higher currents, the target was damaged and it had to be changed. The neutron cone was restricted by the

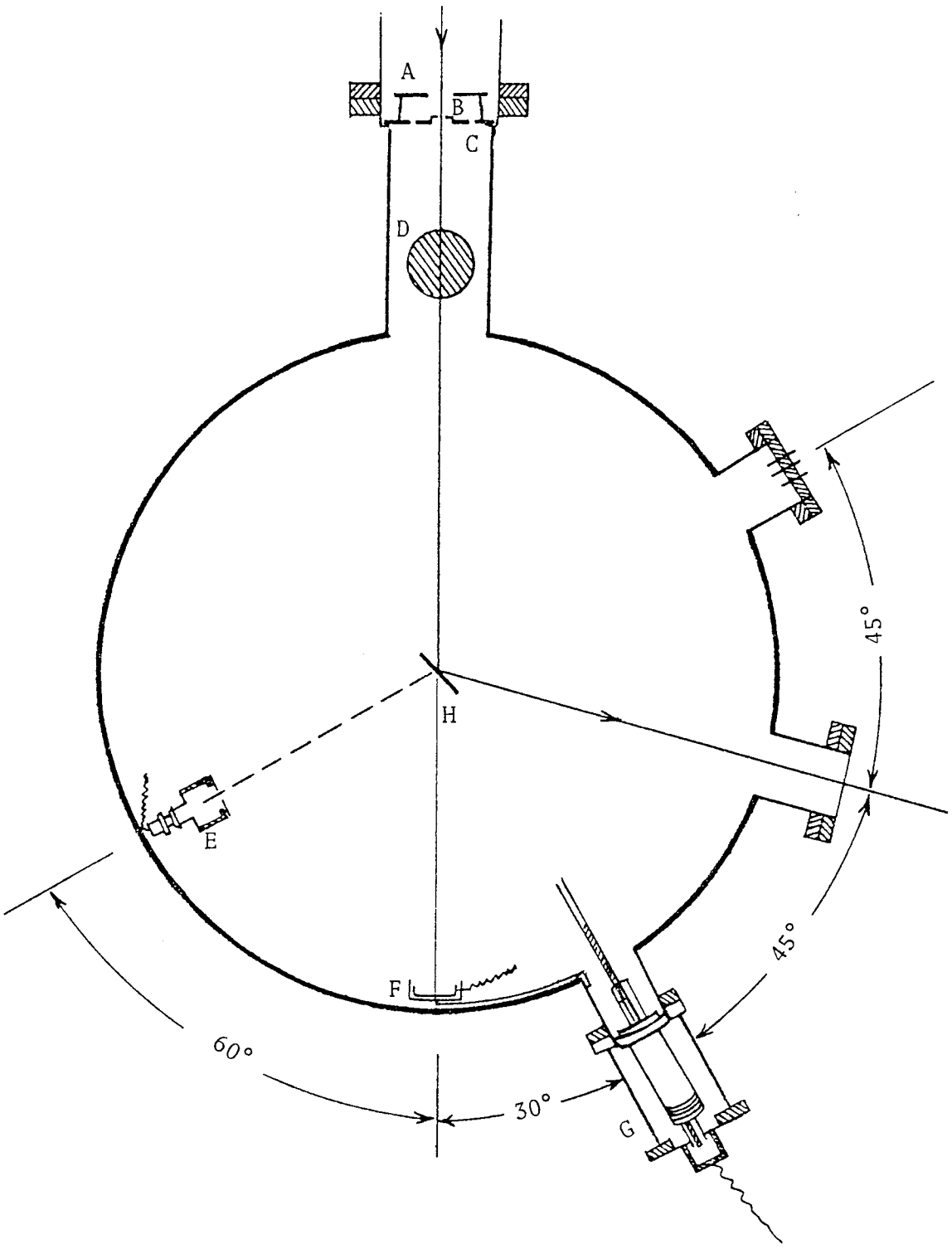

A : Aperture

B : Beam Collimator

C : Aperture Holder

D : Vacuum Port

E : Charged Particle Detector

F : Faraday Cup

G : Target Rotary Drive

H : Target

Figure (4.6) The cross-section of Target Chamber

3.0 mm. diameter aperture of the charged particle detector. The neutron emerged through the one mm. thickness of stainless steel window which was mounted on the 75° port of the chamber. Figure (4.7) shows the internal layout of the target chamber and target assembly.

4.5 CHARGED PARTICLE DETECTION

An ORTEC silicon surface barrier detector was used to detect the charged particles. It has a small size and gives pulses whose height are proportional to the energy lost by the particles in the sensitive region of the detector independenly of the nature of the particles. Also it has a good and constant energy resolution. One of the disadvantages of the surface barrier, is its sensitivity to light. The thin entrance windows are optically transparent and photons striking the detector surface can reach the active volume. In practice, the life of detector is frequently limited by the onset of radiation damage. The present detector had an active area of 300 mm^2 and a sensitive thickness of 100 μm. . The front electrode was gold with a thickness of 42 $\mu gr/cm^2$. A stainless steel collimator with a 3 mm. diameter limited the active area exposed to the charged particles. The detector was placed 5 cm. distant from the deuterated polyethylene target and could be rotated around the target. The output of the detector was taken out via a vacuum tight coupling which was mounted in the chamber, and was connected into an ORTEC 125 charge sensitive preamplifier. The rise time of the output pulse was 20 nsec., and it had a pulse height of 10 mv per Mev deposited. The output pulses of the preamplifier after connection to the electronic system which are discussed in the next section, were analysed on a Pulse Height Analyser. As the distance between the preamplifier and electronic system was about 16 meters, the connecting cable was terminated with a 50 ohm characteristic impedance.

Figure (4.7) Internal Layout of the Target Chamber for the D(d, n)^{3}He Reaction

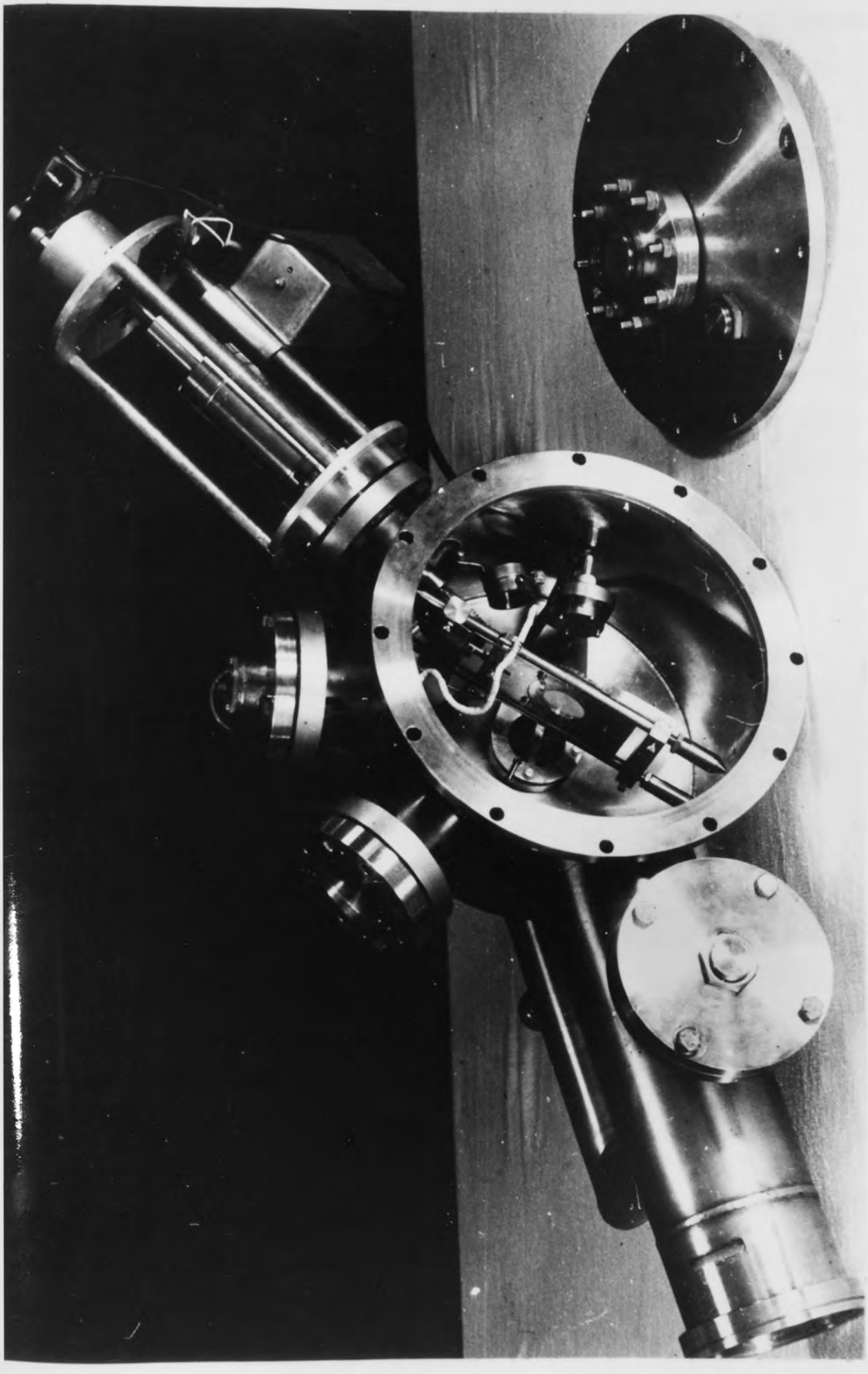

With this geometry the neutron angular spread at 75° central neutron production was ± 7.5°. Due to the 3 mm. collimator, the associated ^{3}He particles for 1 Mev incident deuteron beam energy were detected at 60.2 ± 5°.

4.6 TIME OF FLIGHT ELECTRONICS SYSTEM

As mentioned in section (2.3.2), to measure the neutron flight time, two timing signals are required. These relate to the neutron production and detection. The zero time was obtained by the detection of the associated ^{3}He particle. In the present work, the output pulses of the preamplifier because of their low amplitude were fed to the Timing Filter Amplifier (ORTEC 454) through a coaxial cable. This amplifies the signal but still retains the fast pulse rise time. The Timing Filter Amplifier has a variable gain control which ranged from x 2 to x 200. It was operated on maximum gain, and a fast pulse rise time was obtained. However, the resulting pulses had a very low amplitude and therefore gave poor amplitude resolution between the ^{3}He and deuteron pulses. To overcome this problem a spectroscopic amplifier (CANBERA 1417) was used in conjunction with the Timing Filter Amplifier. The resulting pulses were amplified further by the spectroscopic amplifier. This has a pulse shaping constant for optimum spectrum resolution and minimum amplifier resolving time. Also it has a low noise contribution. It can be used with either positive or negative input pulses and has a variable gain. The gain was adjusted until the ^{3}He, and other pulses were resolved. Either bipolar or unipolar output pulses can be used. In this work, the bipolar output mode was used. Finally, the output of the spectroscopic amplifier was connected to the Timing Single Channel Analyser (ORTEC 420A). This was used to set an electronic window across the ^{3}He peak. The "*start*" input of the Time to Amplitude converter (N.E. 4670) was

derived from the fast negative pulse generated by the timing single channel Analyser. The positive pulse of the timing single channel Analyser was generated at the same time and was connected to the scalar. The Time Converter which was manufactured by Nuclear Enterprises had variable conversion ranges which varied between 0 - 50 ns. to 0 - 200 μsec. In the present system the 1 and 5 μsec. ranges were used to analyse the spectrum on a multichannel pulse height analyser. The "*stop*" input of the time converter was derived from the neutron line. The output pulse from the anode of the neutron detector photomultiplier was connected to the screened coaxial cable through an emitter follower. The resulting output was then fed into a 100 MHZ discriminator (ORTEC 436). This provided two fast negative signals and one positive logic signal. Using a ^{133}Ba gamma ray source, and the same procedure as discussed in section (3.9) the discrimination level was determined. The negative output of the discriminator after being delayed with a Gate and Delay Generator (ORTEC 416A) was fed into the stop of the Time to Amplitude Converter. Finally the output of the Time Converter was displayed on a 1024 Channel Analyser. Figure (4.8) shows the block diagram of time of flight electronics system.

To monitor the neutron yield, the number of protons were counted. To do this, the second output of the preamplifier was amplified by a spectroscopic amplifier (ORTEC 485). Again using a Timing Single Channel Analyser, an electronic window was set across the proton peak, and the positive output pulses of the Timing Single Channel Analyser were counted on a scaler. Using the direct neutron beam at 75°, the time resolution of the spectrometer was obtained. Figure (4.9) shows the time spectrum at this angle. The Full Width at Half Maximum (FWHM) of the spectrometer was (43 ± 2) nsec.. Typical energy spectra are shown in figure (4.10).

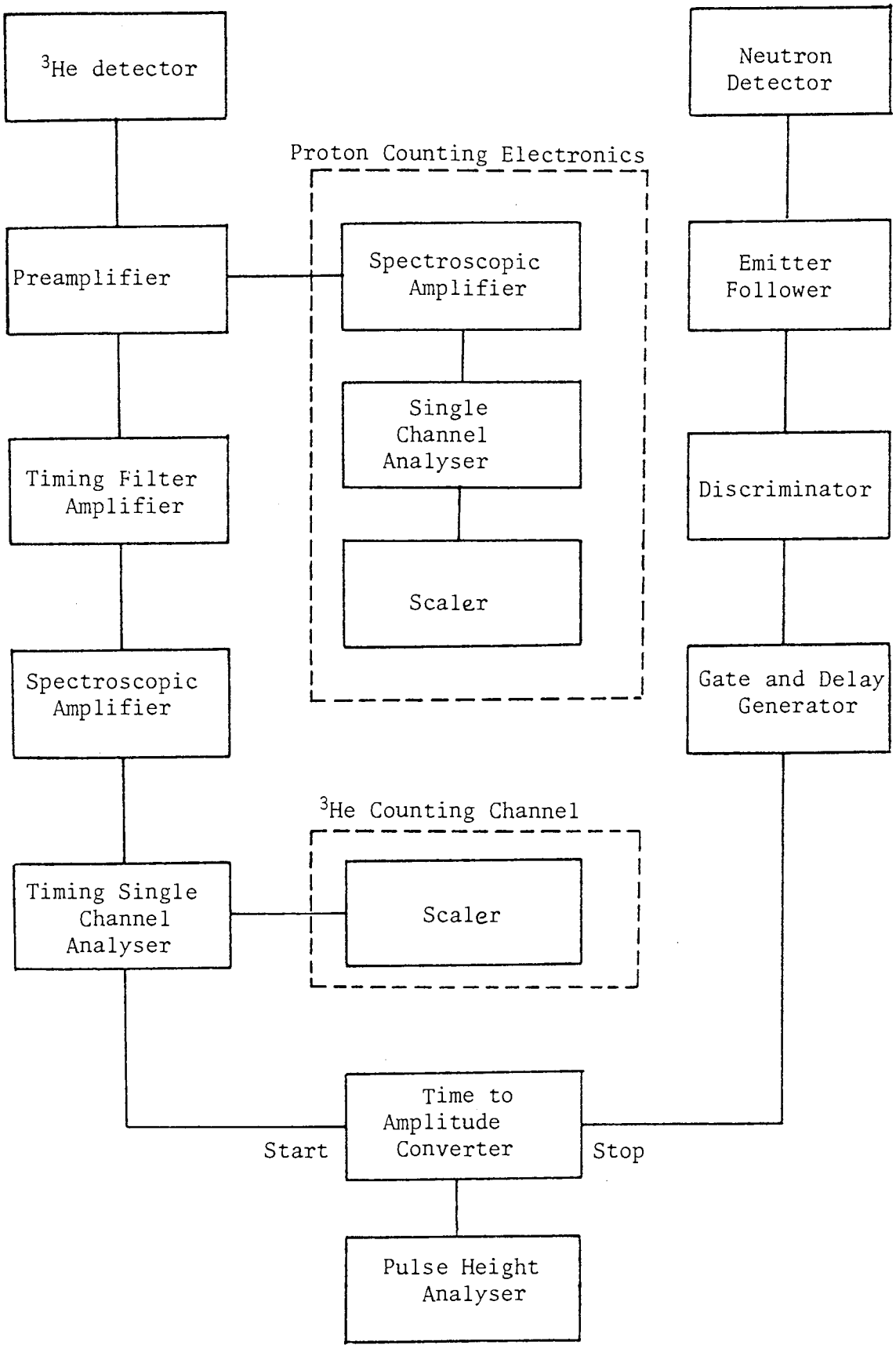

Figure (4.8) Time of Flight Electronics System for $D(d, n)^3He$ Reaction

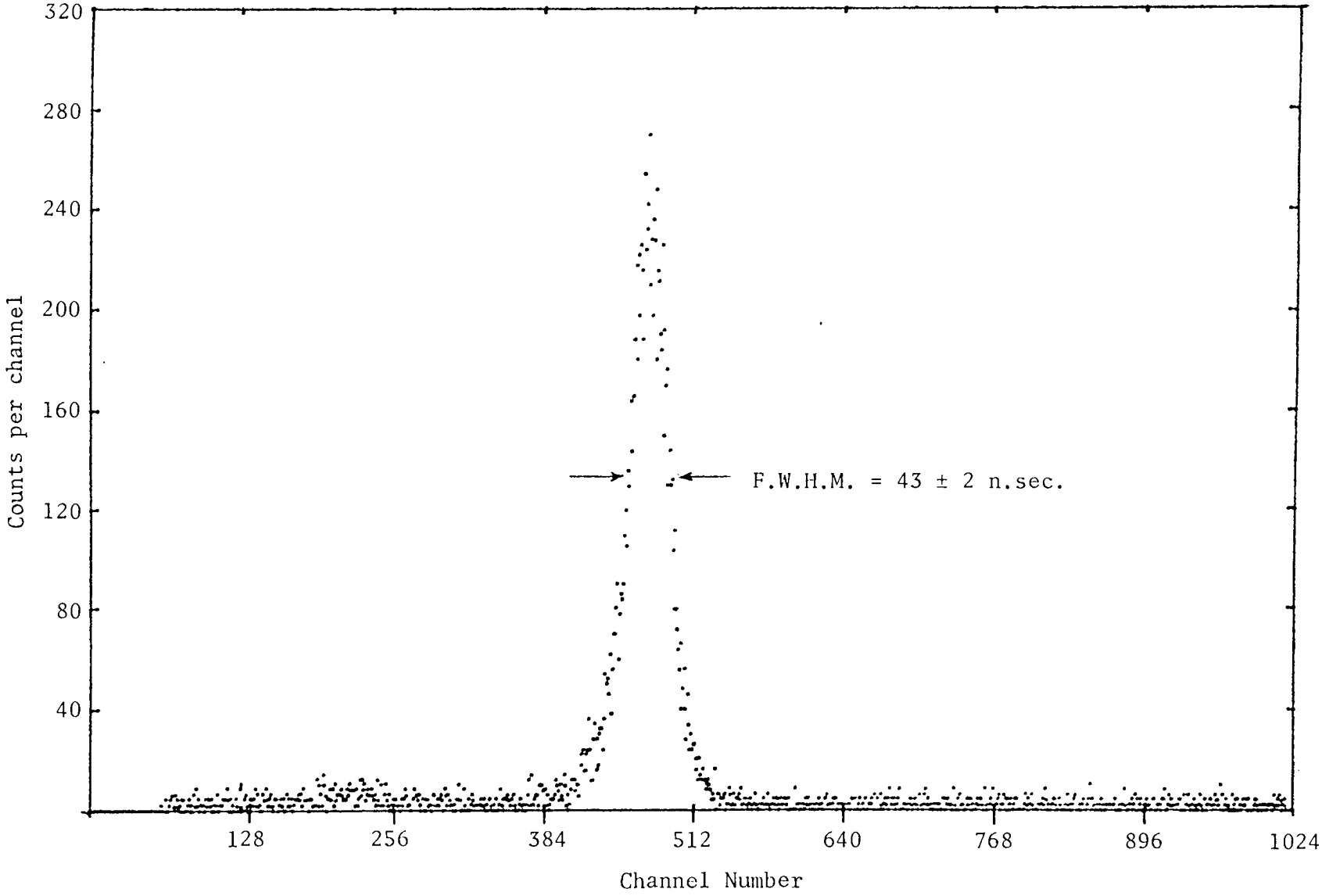

Figure (4.9) Spectrometer Resolution for Neutron Production at 75°

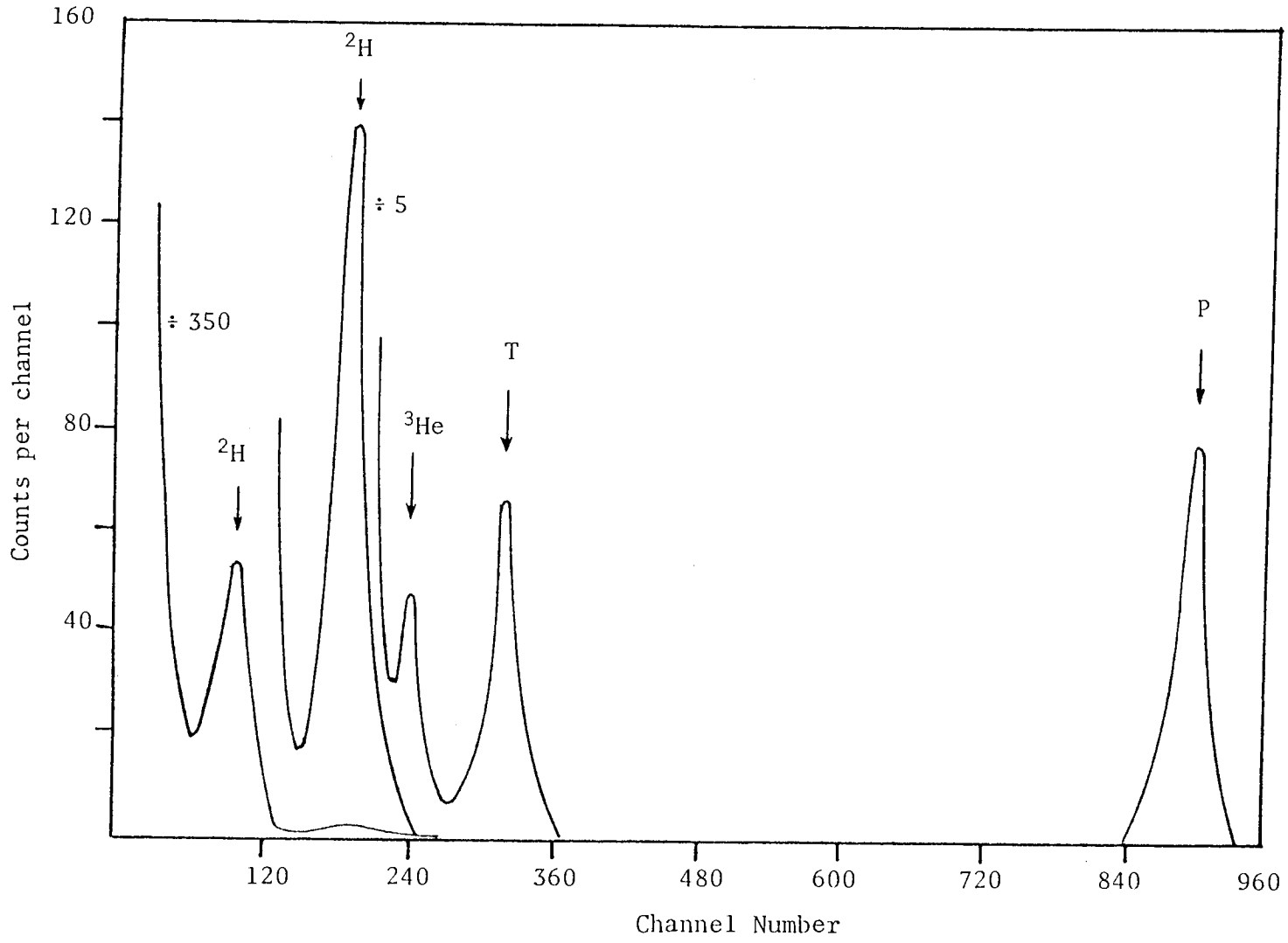

Figure (4.10) Energy Spectrum for Charged Particle Detection at 60.2°

4.7 EXPERIMENTAL PROCEDURE FOR USE WITH THE D(d, n)^{3}He REACTION

A schematic diagram of the apparatus used to detect neutrons from the D(d, n)^{3}He reaction and to measure their flight time after scattering from the Iron samples is shown in figure (5.13). A 20 nA beam of 1 Mev deuterons from the Dynamitron accelerator was allowed to strike the thin rotating deuterated polyethylene target. The resulting reaction yields a 3.02 Mev neutrons at 75° to the incident deuteron beam direction. The neutrons are emitted into the solid angle occupied by the scattering sample. The sample was placed in the neutron cone at 25 cm. from the target. The distance from the sample to the neutron detector was 50 cm. A cylindrical plastic scintillator (NE 102A) of 10 cm. diameter by 5 cm. thicknesses was used to detect the scattered neutrons from the sample. A large shield of paraffin wax and lead protected the neutron detector from the direct beam and neutrons scattered toward the detector from other objects in the room. The neutrons are subsequently scattered from the iron sample, and the time spectrum is recorded at each of some scattering angles. Figure (4.11) shows a typical time spectrum from 4 cm. thick Iron sample at 30°. The F.W.H.M. of the spectrum is (40 ± 2) nsec.

4.8 NEUTRON YIELDS

The yield of neutrons per steradian produced by a deuteron energy interacting in a thin target with the density ρ(gr/cm^3) is given by:

$$Y = \frac{N_d}{\rho} \int_{E_2}^{E_1} \frac{d\sigma/d\omega\ (E)}{dE/dx\ (E)}\ dE \qquad \ldots\ldots\ (4.2)$$

where N_d is the number of deuterium atoms per cm^3 in the target,

dE/dx is the energy loss of the deuteron at an energy E, and

$d\sigma/d\omega$ is the Laboratory differential cross section of the reaction

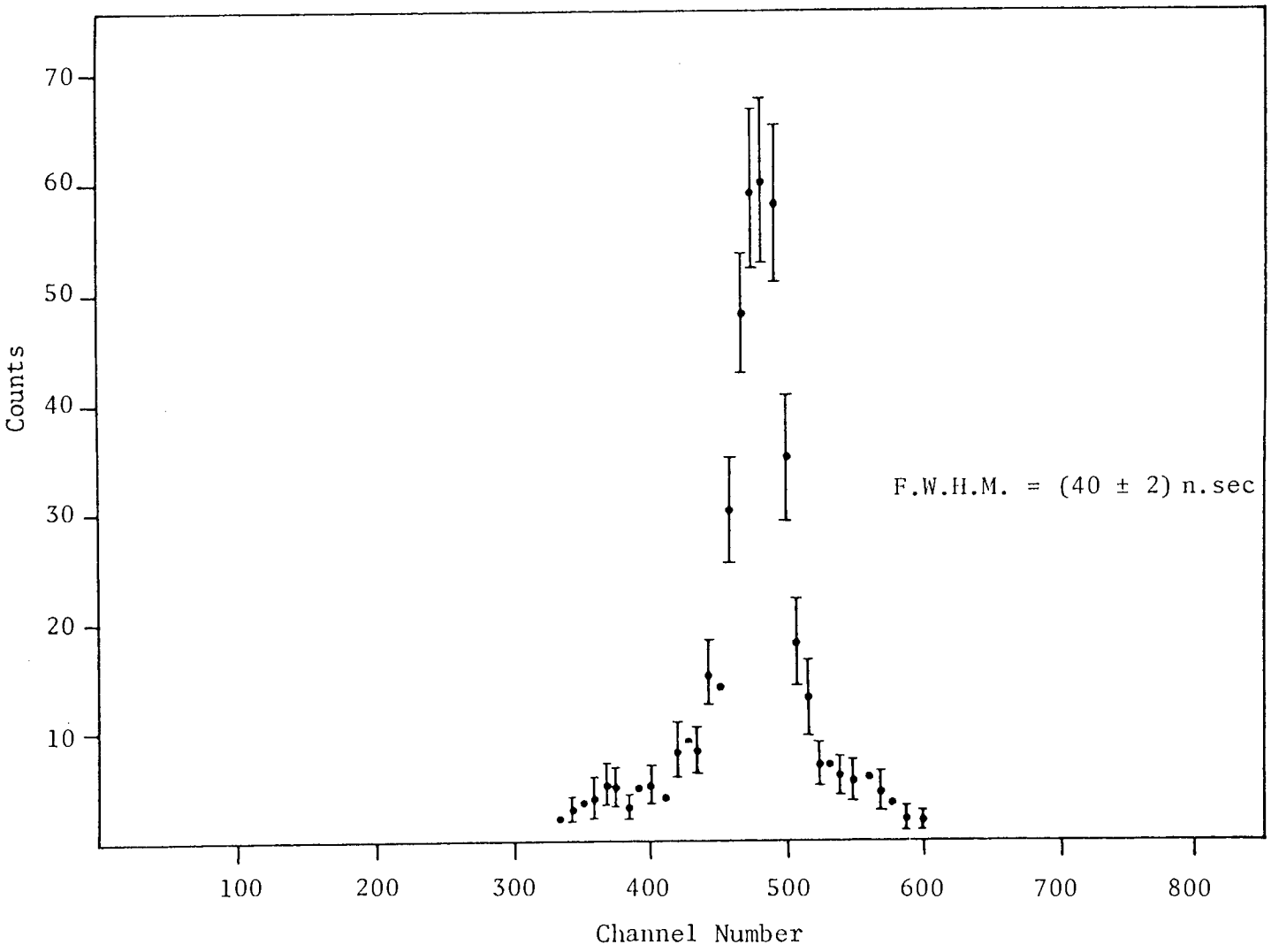

Figure (4.11) Typical Time Spectrum from 4 cm. Thick Iron Sample at 30°

at an energy E in units of barm/steradian.

E_1 and E_2 are the incident and emergent deuteron energies on the thin element of target. In order to calculate the neutron yield, it is necessary to determine the above parameters as a function of deuteron energy.

4.8.1 Differential Cross Section for the D(d, n)^{3}He Reaction

The differential cross-section at an angle ϕ in the centre of mass system can be represented by a Legendre Polynomial:

$$\frac{d\sigma}{d\omega'}\ (E,\ \phi) = \frac{d\sigma}{d\omega'}\ (E,\ 0°)\ .\ \sum_{\ell} A_\ell(E)\ .\ P_\ell(\phi) \qquad \ldots\ldots\ (4.3)$$

where $\frac{d\sigma}{d\omega'}\ (E,\ 0°)$ is the 0° differential centre of mass cross section and can be written as:

$$\frac{d\sigma}{d\omega'}\ (E,\ 0°) = \frac{\sigma_T}{4\pi A_o} \qquad \ldots\ldots\ (4.4)$$

Here σ_T is the total cross section, and $A_\ell\ P_\ell(\phi)$ is the ℓth term of the legendre polynomial. Using equation (2.19) the differential cross-section in the Laboratory system can be found:

$$\frac{d\sigma}{d\omega}\ (E,\ \theta) = \frac{d\sigma}{d\omega'}\ (E,\ \phi)\ .\ \frac{d\omega'}{d\omega} \qquad \ldots\ldots\ (4.5)$$

where $\frac{d\omega'}{d\omega}$ is the anisotropy factor discussed in section (2.4.2), and $\frac{d\sigma}{d\omega}\ (E,\ \theta)$ is the differential cross-section in the Laboratory system. Fowler and Brolley[94] have plotted the Laboratory differential cross-section of the D(d, n)^{3}He reaction at various deuteron bombarding energies. Liskien and Paulsen[60] have tabulated the differential cross-

section of D(d, n)^{3}He and other reactions in the Laboratory system for various deuteron energies. Figure (4.12) shows the differential cross-section in the Laboratory system as a function of deuteron energy for an angle of 75°.

4.8.2 Stopping Power of Deuterons in Deuterated Polyethylene

The target material was deuterated polyethylene, it contained 98% deuteron atoms and 2% consisted of impurity hydrogen atoms bonded to the carbon atoms in the place of deuterium. There was no experimental data available on the rate of energy loss for deuterons up to 1 Mev in deuterated polyethylene target. Rich and Madey[85] have tabulated the stopping power of deuterons for an energy greater than 2 Mev in CD_2 material. However, by applying Bragg's Law the rate of energy loss of deuterons in CD_2 material can be determined as:

$$\left(\frac{dE}{dx}\right)_{CD_2} = \frac{2N_d}{12 + 2N_d + N_H}\left(\frac{dE}{dx}\right)_D + \frac{12}{12 + 2N_d + N_H}\left(\frac{dE}{dx}\right)_C + \frac{N_H}{12 + 2N_d + N_H}\left(\frac{dE}{dx}\right)_H \quad \ldots\ldots (4.6)$$

where N_d and N_H are the number of deuterium and hydrogen atoms per carbon atom.

Assuming 98% deuteration, i.e. 1.96 deuterium atoms per carbon, equation (4.6) becomes:

$$\left(\frac{dE}{dx}\right)_{CD_2} = 0.75188\left(\frac{dE}{dx}\right)_C + 0.00251\left(\frac{dE}{dx}\right)_H + 0.24561\left(\frac{dE}{dx}\right)_D \quad \ldots\ldots (4.7)$$

By using equation (2.25) the energy loss of the deuteron in the material can be determined from the proton data. The average energy loss

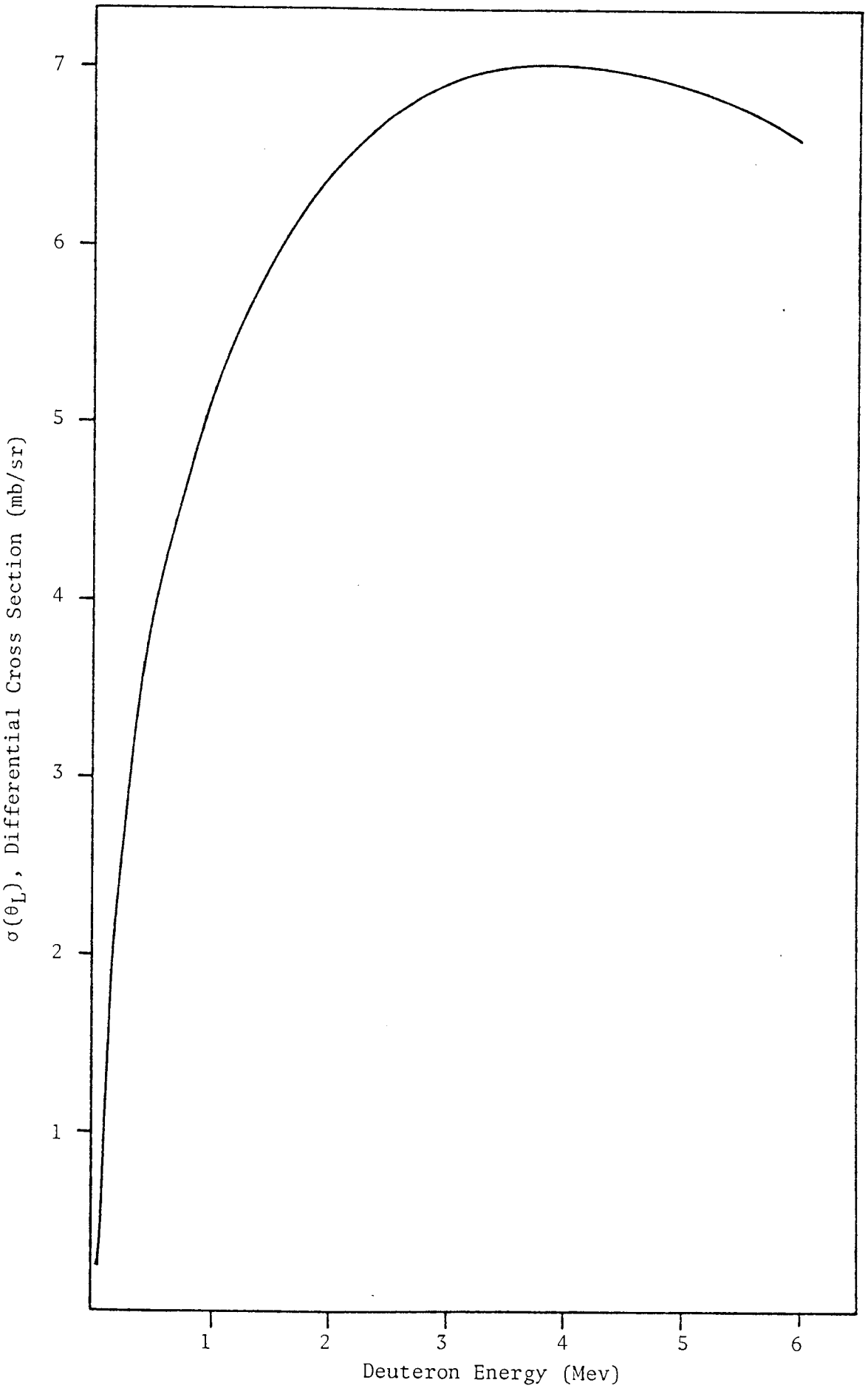

Figure (4.12) Differential Cross Section of D(d, n)^{3}He Reaction for a Neutron Laboratory Angle of 75°

of the deuterons in deuterium in units of keV/mg/cm^2 is equal to one half of the energy loss in hydrogen with the same units. Marion and Young[71] have shown the stopping power of protons in hydrogen, carbon and other elements. However, Anderson and Ziegler[114] have obtained the stopping cross-section of protons in all elements in the range 0.001 Mev < E_p < 100 Mev. The relation between the energy loss $(\frac{dE}{dx})$ in units of (keV/mg / cm^2) and the stopping cross-section "σ" in units of (ev atoms^{-1}cm^2) is:

$$n\sigma = \frac{dE}{dx}$$

where n is the number of constituent nuclei per cm^3. The energy loss values of deuterons in carbon and hydrogen were calculated from the proton data of Anderson and Ziegler[114]. Figure (4.13) shows the deuteron energy loss in carbon, deuterium and hydrogen.

Using equation (4.7) and the data of Table (4.1), the stopping power of deuterons in CD_2 material were obtained. Figure (4.14) shows the rate of energy loss of deuterons in deuterated polyethylene target. Density and the number of nuclei per cm^3 of the deuterated polyethylene target was 1.073 g /cm^3 and 7.93 x 10^{22} atoms per cm^3 respectively [113].

By using the data of table (4.1), figure (4.11) and equation (4.2), the relative yield of neutrons were determined. Figure(4.15) shows the relative neutron yield as a function of deuteron energy for a Laboratory angle of 75°.

4.9 ENERGY LOSS OF CHARGED PARTICLES IN DEUTERATED POLYETHYLENE TARGET

In the previous section, the energy loss of deuterons in a deuterated polyethylene target was determined. To minimize the energy loss of the charged particles after formation inside the target, in emerging from the target, they should traverse the minimum thickness of the target before reaching to the detector. Experimentally, the target was positioned at

Table (4.1)

Energy Loss of Deuterons in Carbon, Hydrogen, Deuterium and CD_2

Deuteron Energy keV	$(dE/dx)_C$ keV/mg / cm^2	$(dE/dx)_H$ keV/mg / cm^2	$(dE/dx)_D$ keV/mg / cm^2	$(dE/dx)_{CD_2}$ keV/mg / cm^2
60	641.28	3498.30	1749.15	920.56
80	696.39	3719.56	1859.78	989.72
120	746.49	3827.20	1913.60	1040.88
160	746.49	3701.62	1850.81	1025.14
200	726.45	3480.36	1740.18	982.34
400	571.14	2392.00	1196.00	729.18
600	465.93	1764.10	882.05	597.85
800	398.79	1405.30	702.60	475.95
1200	315.63	1016.60	508.30	364.71
1600	265.03	813.28	406.62	301.19
2000	228.96	681.72	340.86	257.58
4000	140.78	389.30	194.65	154.63
6000	104.21	279.27	139.64	113.35
8000	83.67	220.06	110.03	90.49
12000	61.12	157.27	78.64	65.67

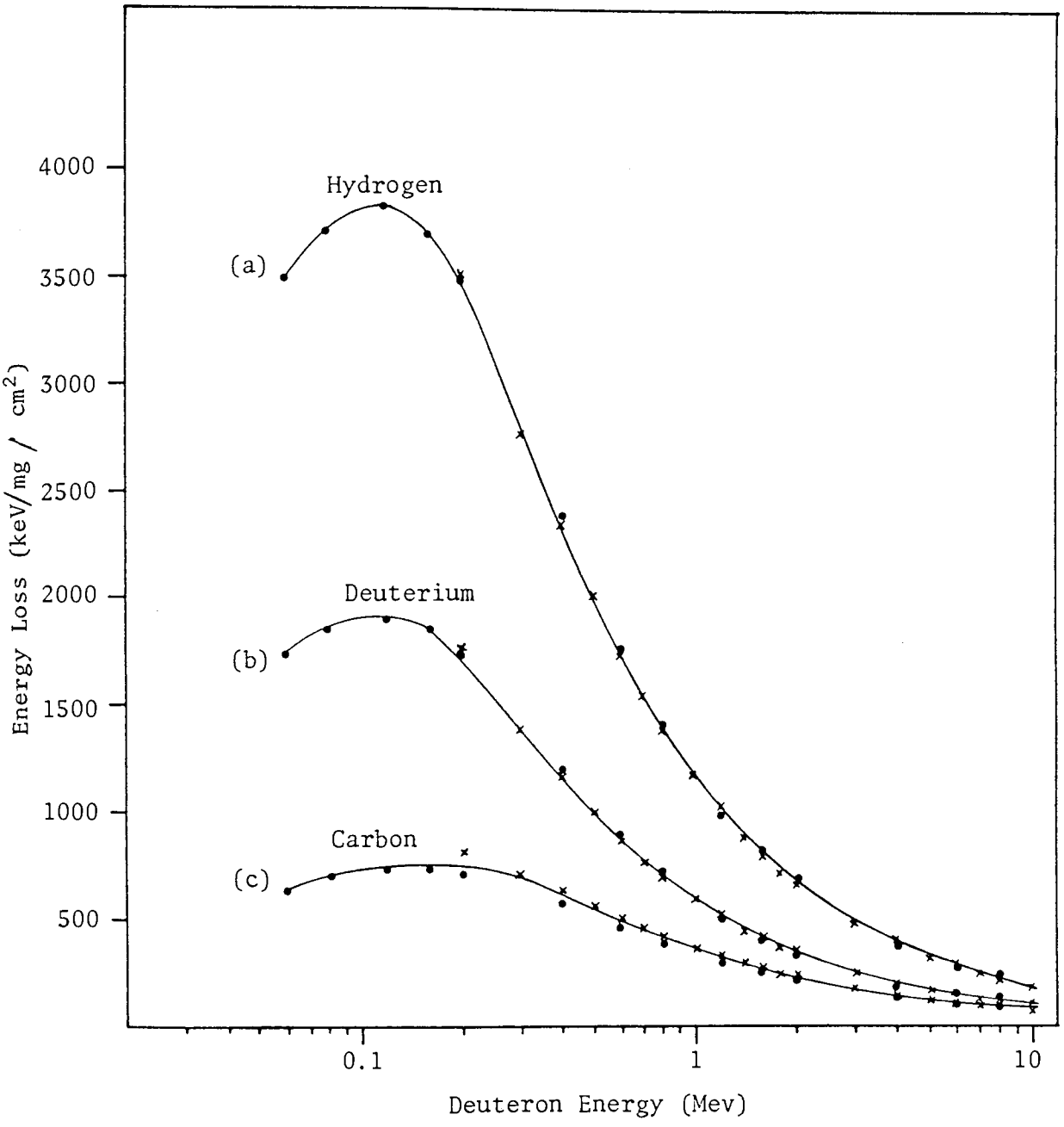

Figure (4.13) Energy Loss of Deuterons in Hydrogen, Deuterium, and Carbon Scaled from Proton Data. References for Experimental Points • [114]; x [71]

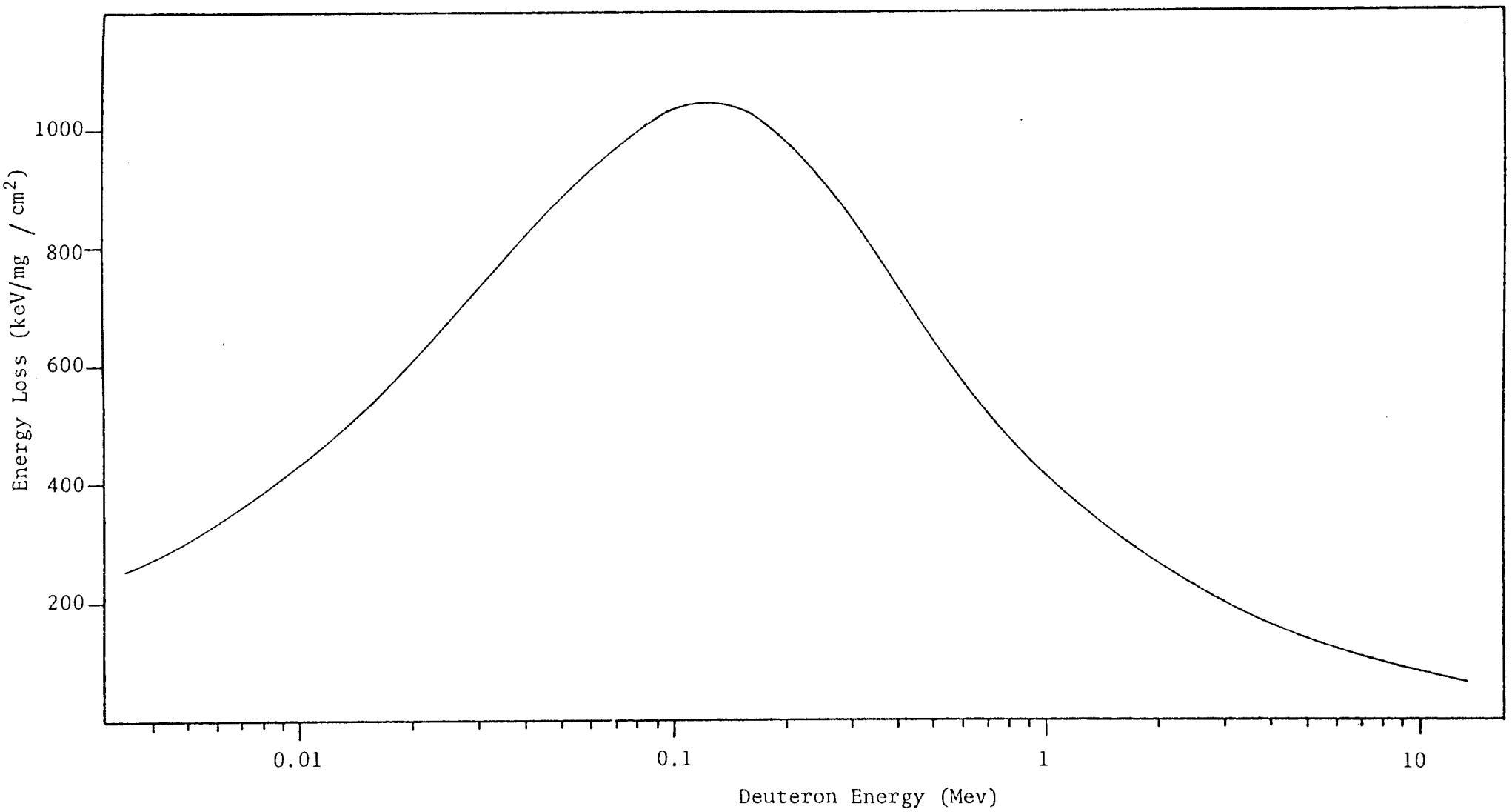

Figure (4.14) Calculated Energy Loss of Deuterons in Deuterated Polyethylene

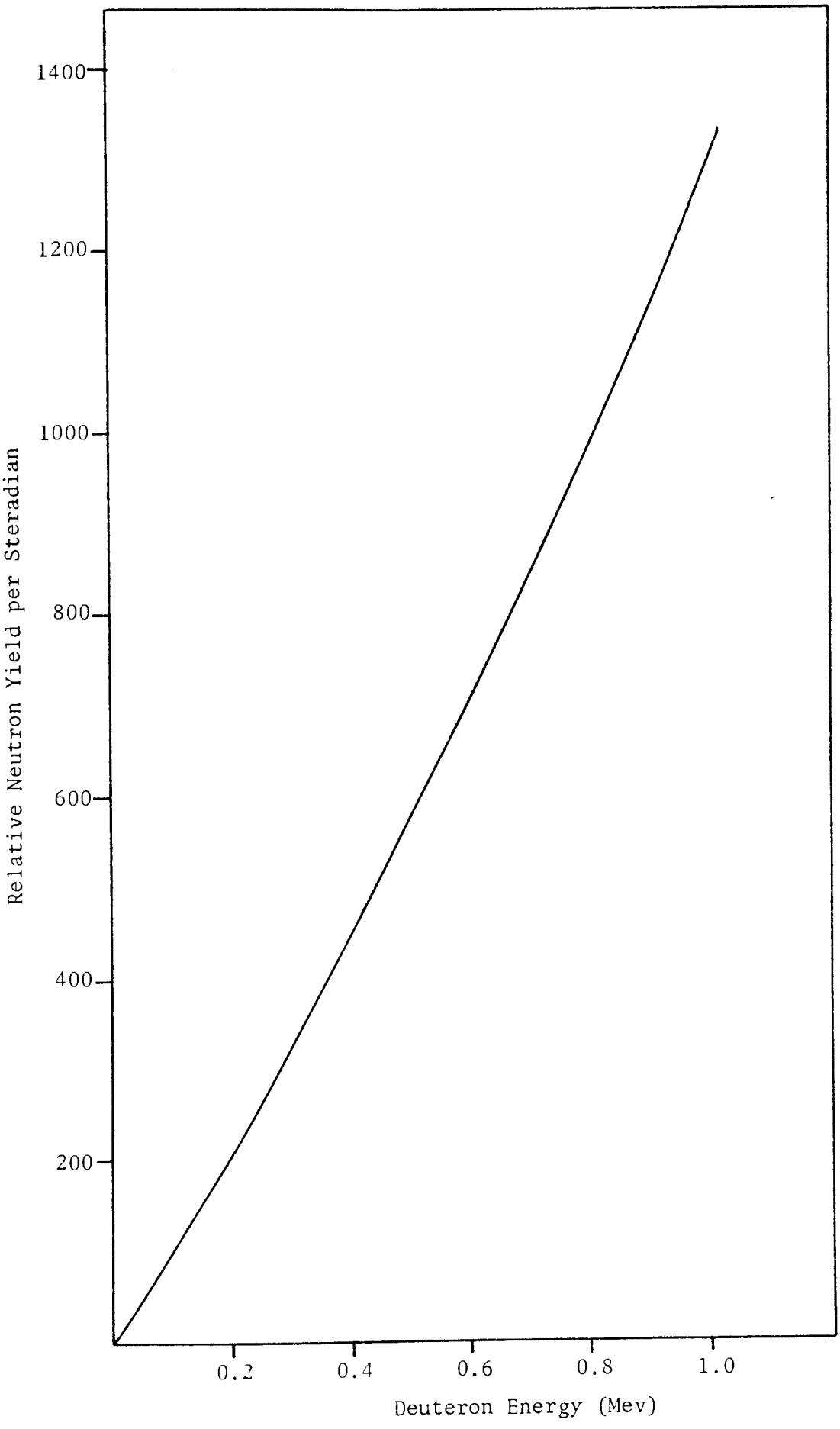

Figure (4.15) The Relative Neutron Yield as a Function of Deuteron Energy for $D(d, n)^3He$ Reaction for a Laboratory Angle of 75°

45° to the incident beam. The target surface was then at 75° with respect to the charged particle detector positioned at 60.2°. By applying the following relations and using the data of table (4.1), the energy loss values of ^3He, p and ^3H were obtained by scaling the deuteron data in the deuterated polyethylene.

For "^3He" particles $\left(\frac{dE}{dx}\right)_{^3He}\left(\frac{3}{2}E\right) = 4\left(\frac{dE}{dx}\right)_D(E)$

For "p" particles $\left(\frac{dE}{dx}\right)_p\left(\frac{1}{2}E\right) = \left(\frac{dE}{dx}\right)_D(E)$ ..... (4.8)

For "T" particles $\left(\frac{dE}{dx}\right)_{^3H}\left(\frac{3}{2}E\right) = \left(\frac{dE}{dx}\right)_D(E)$

Figure (4.16) shows the energy loss of ^3He, p and T in deuterated polyethylene target.

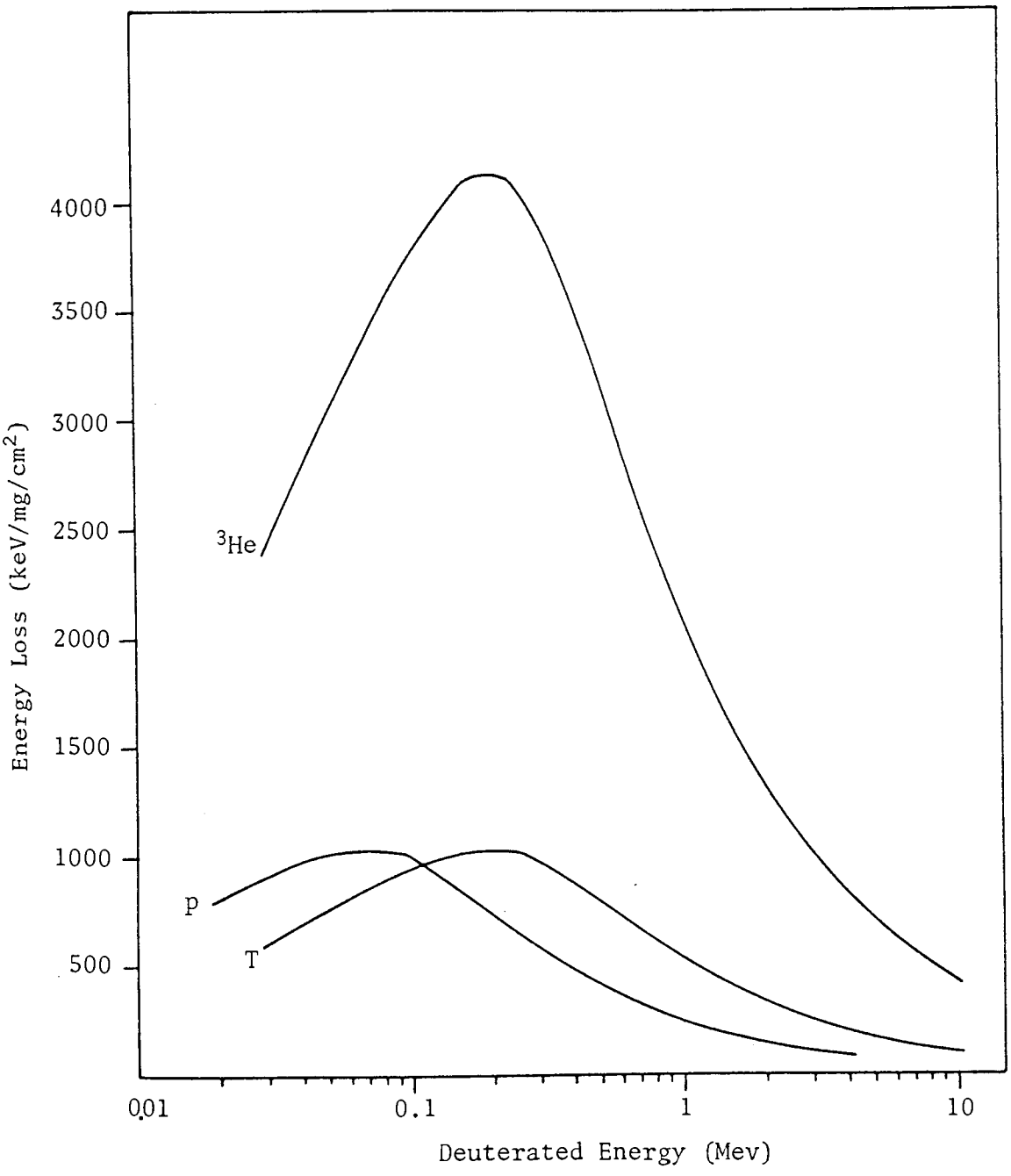

Figure (4.16) Energy Loss of ^{3}He, p and T Particles in Deuterated Polyethylene Target

CHAPTER FIVE

CHAPTER FIVE

DIFFERENTIAL CROSS-SECTION MEASUREMENTS

5.1 THE DIFFERENTIAL CROSS-SECTION

In many nuclear reactions, the product particles are not produced isotropically with respect to the incident beam direction.

To take account of this we define a differential cross-section, denoted by $\sigma(\theta)$. If a particle is scattered in a small solid angle $d\Omega$ at a certain specified angle θ with the incident beam, then the cross-section per unit solid angle is defined as:

$$d\sigma = \sigma(\theta)\, d\Omega \qquad \ldots\ldots (5.1)$$

The quantity $\sigma(\theta)$ is measured in barns or cm^2 per steradian.

The total probability that a neutron will be scattered through any angle is therefore equal to the integral of σ over all solid angle, hence

$$\sigma = \int_{4\pi} \sigma(\theta)\, d\Omega \qquad \ldots\ldots (5.2)$$

If the differential cross-section is independent of azimuth about the incident beam direction then:

$$d\Omega = 2\pi \sin\theta\, d\theta \qquad \ldots\ldots (5.3)$$

and

$$d\sigma = 2\pi\, \sigma(\theta) \sin\theta\, d\theta \qquad \ldots\ldots (5.4)$$

$$\therefore \qquad \sigma = 2\pi \int_0^{\pi} \sigma(\theta) \sin\theta\, d\theta \qquad \ldots\ldots (5.5)$$

The angular distribution $\sigma(\theta_L)$ measured in the Laboratory system, is related to the angular distribution $\sigma(\phi_C)$ in the centre-of-mass system by the relation:

$$\sigma(\phi_C)\ \sin\phi\ d\phi = \sigma(\theta_L)\ \sin\theta\ d\theta \qquad \ldots\ldots (5.6)$$

where the angles θ and ϕ are defined in the Laboratory and centre-of-mass systems respectively.

The present work was concerned with the differential elastic scattering cross-sections for neutrons. For elastic scattering, equation (5.7) can be used to transform the angular distribution from one system to the other [71, 115].

$$\sigma(\theta_L) = \frac{(1 + 2\gamma\ \cos\phi + \gamma^2)^{3/2}}{1 + \gamma\ \cos\phi}\ \sigma(\phi_C) \qquad \ldots\ldots (5.7)$$

where $$\gamma = \frac{M_1}{M_2}$$

Here, M_1 = mass of the incident neutron

and M_2 = mass of the target nuclei

The relation between ϕ which is required for analysis, and θ , which is actually observed, are given by [71]:

$$\phi = \theta + \sin^{-1}(\gamma\ \sin\theta) \qquad \ldots\ldots (5.8)$$

5.2 THE DIFFERENTIAL ELASTIC SCATTERING CROSS-SECTION

Consider a sample of thickness, x, and having n nuclei per unit volume, and scattering of neutron in a small solid angle $d\Omega$ at a certain angle θ to the incident neutron beam direction as shown in figure (5.13).

The total number of elastically scatterd neutrons is given by:

$$N_{el}(\theta) = (\Sigma\phi)\ .\ At.\ .\ \frac{\frac{d\sigma_{el}(\theta)}{d\Omega}}{\sigma_T}\ d\Omega \qquad \ldots\ldots (5.9)$$

where: At. = attenuation of the neutron beam in the sample

$\Sigma\phi$ = total number of incident neutrons on the sample

σ_T = total cross-section for neutrons for the sample under experiment

and $\frac{d\sigma_{el}(\theta)}{d\Omega}$ = differential elastic scattering cross-section for neutrons in a solid angle $d\Omega$-

Equation (5.9) can be written as:

$$N(\theta) = \Sigma\phi \,.\, [1 - \exp(-n\,\sigma_T\,x)] \,.\, \frac{\frac{d\sigma_{el}(\theta)}{d\Omega}}{\sigma_T}\, d\Omega \qquad \ldots\ldots (5.10)$$

As a result, the differential elastic scattering cross-section will be:

$$\frac{d\sigma_{el}(\theta)}{d\Omega} = \frac{N(\theta) \,.\, \sigma_T}{\Sigma\phi \,.\, [1 - \exp(-n\,\sigma_T\,x)] \,.\, \Delta\Omega} \qquad \ldots\ldots (5.11)$$

In the above equation, the neutron detector efficiency $\varepsilon(E_n)$ which is a function of neutron energy should be considered. Hence, equation (5.11) should be written as:

$$\frac{d\sigma_{el}(\theta)}{d\Omega} = \frac{N(\theta) \,.\, \sigma_T}{(\Sigma\phi)[1 - \exp(-n\,\sigma_T\,x)] \,.\, \varepsilon(E_n) \,.\, \Delta\Omega} \qquad \ldots\ldots (5.12)$$

5.3 CORRECTION APPLIED TO THE DIFFERENTIAL CROSS-SECTION MEASUREMENTS

Equation (5.12) is defined as the differential elastic scattering cross-section. However, there are several experimental factors which have to be taken into account. These are discussed in the following sections.

5.3.1 Weighted Sample Thickness

From the neutron beam profile (figure 2.22) it was found that the neutron beam, varies over an angular range of 17°, therefore, the sample thickness varies with the angular range of neutron beam. It was necessary to find the average weighted thickness of sample, to replace the value of x, in equation (5.12).

The weighted average thickness of the sample was determined from the equation:

$$\bar{x} = \frac{\Sigma f_i x_i}{F} \qquad \ldots\ldots (5.13)$$

where $\bar{x}$ = weighted average thickness of the sample

f_i = is the weighting fraction, proportional to the area under the beam profile curve, figure (2.22), in the 1° interval denoted by i.

x_i = sample thickness, depends on ϕ_n, the geometrical dependence is shown in figure (5.1)

and F = total area under the neutron beam profile

The $\bar{x}$ was calculated over one degree interval using the data of figure (2.22). The average thickness of the sample was found as:

$$\bar{x} = x(1.006 \pm 0.001)$$

where, x is the actual thickness of the sample.

5.3.2 Alpha Particle Counts Correction

In the associated particle method, the total number of neutrons incident on the sample is determined from the total number of Alpha Counts. However, the alpha count has to be corrected for background radiation and

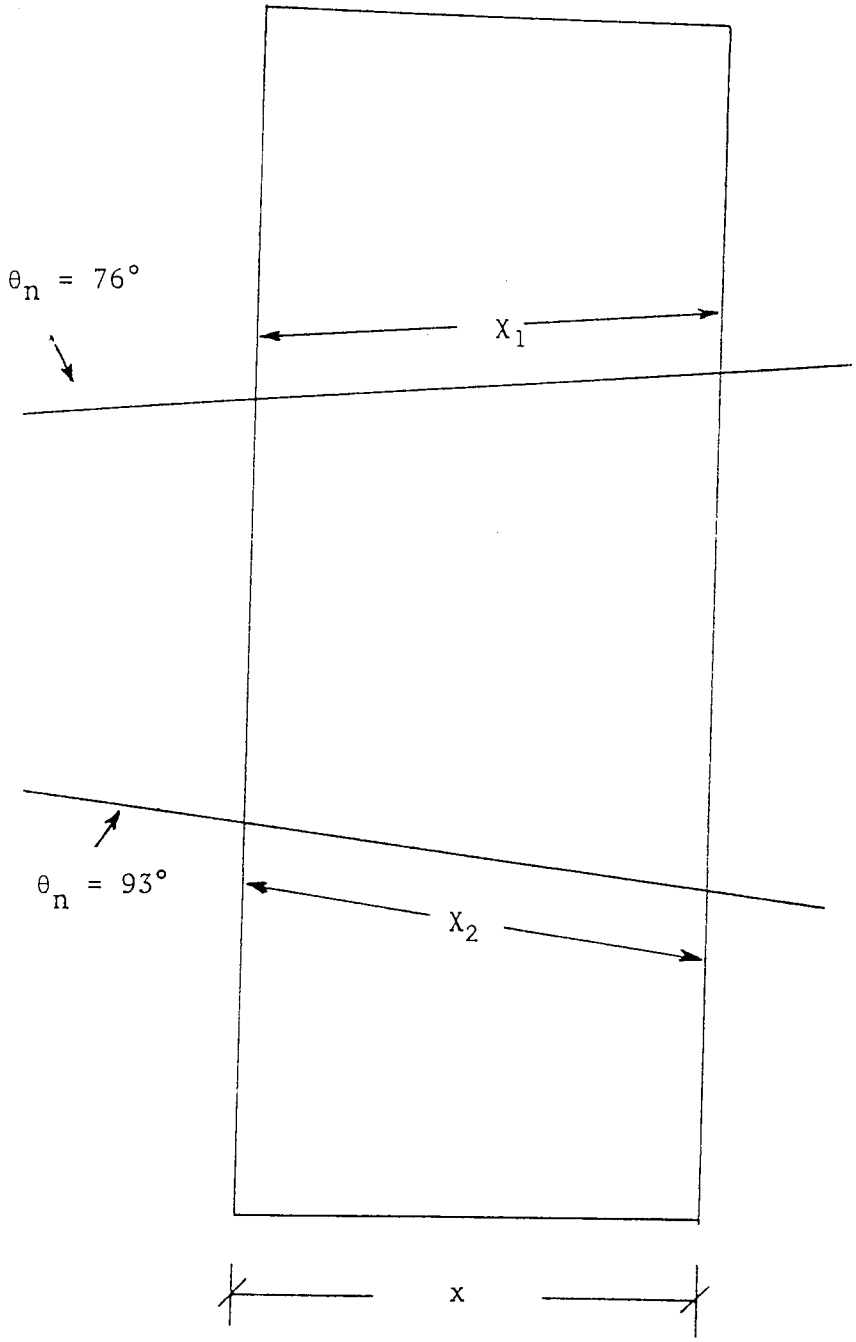

$$\overline{X}_1 = \frac{x}{\cos\theta_n} \qquad 76 < \theta_n < 83$$

$$\overline{X}_2 = \frac{x}{\cos\theta_n} \qquad 83 < \theta_n < 93$$

Figure (5.1) Calculation of the weighted sample thickness $(\overline{x})$

the detection of fast neutrons. These factors have been discussed in detail by Connel[49].

The background radiation in the alpha detector, is due to source neutrons, and radiation from the activated target assembly. This is found by noting the α count rate immediately after switching off the beam, when the accelerator had been running for a long time.

The factor due to the detection of fast neutrons and radiation emitted from the reaction was found by first recording the α counts for various values of target current, then the α-detector aperture plate was replaced by an aluminium plate. The 1 mm thickness of the aluminium plate was sufficient to stop the 3.5 Mev alpha particles [116]. The alpha monitor counts was then monitored for the same target current giving the count rate due to radiation rather than the α, s.

The estimated correction factor due to this background was found as:

$$F_1 = 0.945 \pm 0.005$$

5.3.3 Absorption of Neutrons in the Target Assembly

It was discussed in section (2.1.1.1) that, the target assembly was made from the steel, and was water cooled. With the information on the target holder supplied by the manufacturers, it was noted that the 14 Mev neutrons must be passed through 2.55 mm of steel and 1.3 mm of water. Due to absorption of neutrons in the target assembly, the intensity of the defined incident neutron flux on the sample was reduced. Using the neutron cross-sections for iron and water, the fraction of source neutrons (F_2) escaping from the target can be calculated as:

$$F_2 = \exp - [\Sigma_{Fe}\, x_{Fe} + (\Sigma_H + \Sigma_O)\, x_{water}] \quad \ldots\ldots (5.14)$$

where Σ_{Fe} = the macroscopic cross-section of Iron

Σ_O and Σ_H = the macroscopic cross-section of Oxygen and Hydrogen

x_{Fe} = the thickness of stainless steel of target assembly

x_{water} = the thickness of water

Total cross-section for Iron H and O are shown in table (5.1)

Table (5.1)

Total Cross-section for Iron, Oxygen and Hydrogen with their Thicknesses [49]

Element	$x_{(mm)}$	σ_T (barns)
Iron	2.50 ± 0.03	2.316
Water { Hydrogen	1.30 ± 0.03	0.646
Water { Oxygen		1.523

Using equation (5.14), the factor F_2 was found to be:

$$F_2 = 0.939 \pm 0.007$$

5.3.4 Correction Factor for Scattered Neutrons from the Sample

Suppose a sample of thickness 'T' is placed in the most intense part of neutron beam of intensity ϕ_o, and the detector is placed at an angle θ to the neutron beam direction. If $\phi(x)$ be the intensity of the non-interacted neutrons after penetrating a distance x into the sample, in traversing an additional distance Δx, the intensity of the beam will be decreased by the number of neutrons that have interacted in the thickness Δx. This decrease in intensity is given by:

$$- d\,\phi(x) = n \cdot \sigma_t \cdot \phi(x) \cdot \Delta x \qquad \ldots\ldots (5.15)$$

where n is the number of nuclei per unit volume in the sample. Hence, the fraction of non-interacted beam emerging from the sample is given by:

$$\phi(T) = \phi_o\, e^{- n.\sigma_t.T} \qquad \ldots\ldots (5.16)$$

For neutrons traversing different parts of the thick sample, different values of $\phi(T)$ will be obtained. It is better to keep this correction as small as possible by an appropriate choice of the geometry of the experiment, since it is rarely possible to calculate the correction with any degree of accuracy. In the present work, by drawing the sample detector geometry, and dividing the sample thickness into slices of a half cm. thickness, the path length of the neutron beam travelling in the sample at a specific angle θ was estimated. This was repeated separately for each thickness of sample in the angular range studied.

Finally, the total average scattered neutrons in each sample, at a specific angle θ was found from:

$$C = \frac{\Sigma\, C_i}{N} \qquad \ldots\ldots (5.17)$$

where C_i = the fraction of neutrons scattered at each slice of the sample called (i), and ,

N = the total number of a half cm. thick slice in the sample.

Figure (5.2) illustrates the case where the neutron is scattered from different thicknesses of the sample at an angle θ. It was noted that, at $\theta = 90°$ to the neutron beam direction, all of the neutrons are scattered through the width of the sample, and emerged from the side of the sample.

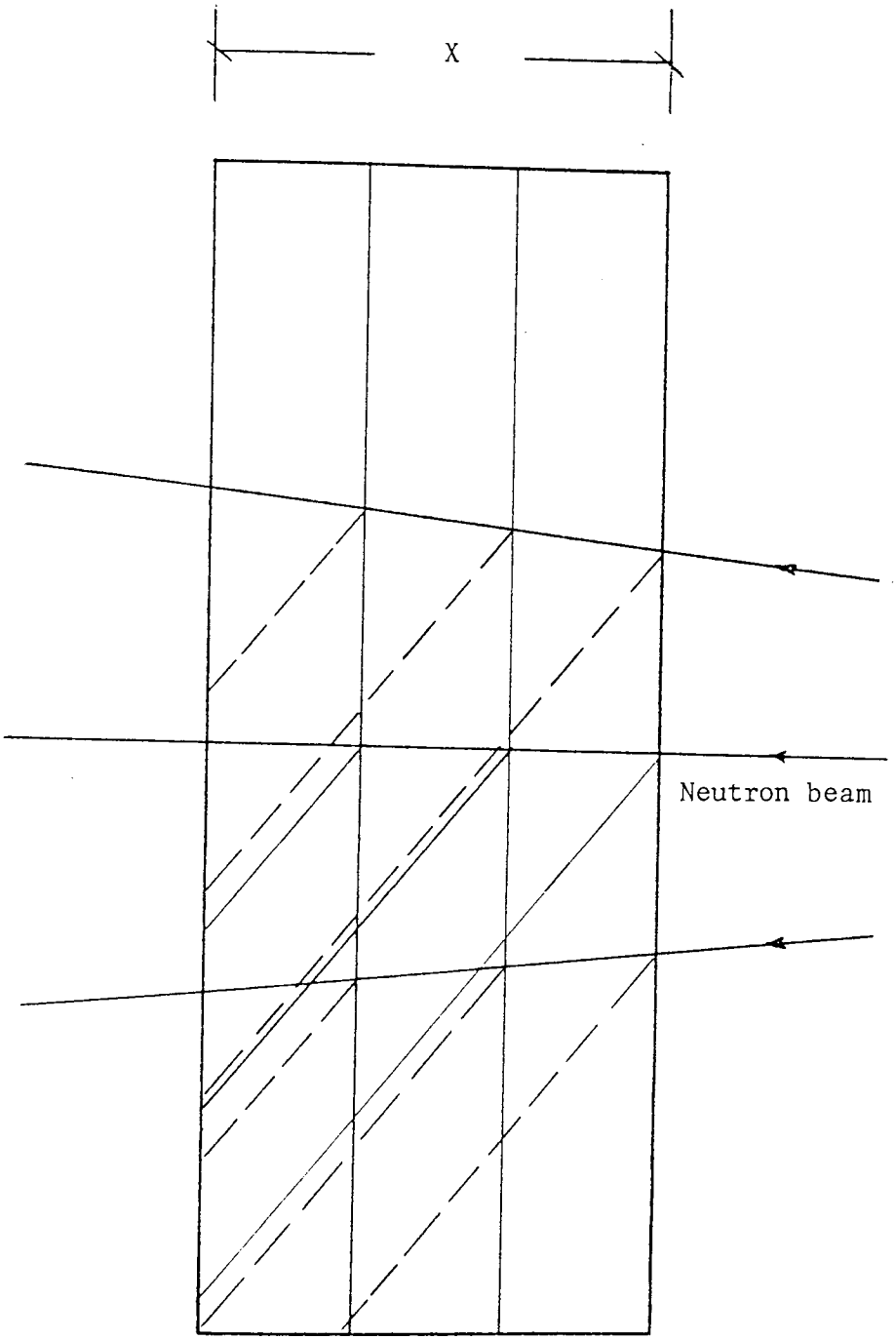

X = sample thickness

Figure (5.2) The Sample Geometry used to Measuring the Path Length of the Scattered Neutrons

5.4 SOLID ANGLE AND CORRECTION FACTOR

In nuclear reaction experiments when absolute differential cross-section are to be determined, it is important to have an exact knowledge of the solid angle subtended by the detector. For a point source, the calculation of the quantities involved is very straightforward and can be obtained from the equation (5.18)

$$\Omega = \frac{A}{R^2} \quad \text{rads} \qquad \ldots\ldots (5.18)$$

where A = area of the detector

and R = distance between sample and detector

However, in case of an extended sample, the following analysis was used.

By drawing the sample geometry and using the defined neutron beam angle, the size of the sample which is radiated by the neutron beam was measured, then the actual area of the sample is radiated by the neutron was projected onto the plane of the detector. Using equation (5.19), the correction factor "G" was determined.

$$G = \frac{A_p}{A_D} = \frac{A_{sample} \times \sin\theta}{A_D} \qquad \ldots\ldots (5.19)$$

where A_p = projected area of the sample

A_D = area of the detector

A_{sample} = area of the sample radiated by the neutron beam

and θ = angle of detector with respect to the position of the sample

5.5 DIFFERENTIAL CROSS-SECTION FORMULA

Applying all the above factors to the equation (5.12), the equation for the differential elastic scattering cross-section was obtained as:

$$\frac{d\sigma_{el}}{d\Omega} = \frac{N(\theta).\sigma_T.G}{(\Sigma\phi).F_1.F_2\ [1 - \exp(-\ n.\sigma_T.\bar{x})]\ C.\Delta\Omega.\varepsilon(E_n)} \quad \ldots\ldots (5.20)$$

where $N(\theta)$ = number of neutron detector counts for elastic peak.

σ_T = total cross-section of neutron for the sample under experiment

n = number of nuclei per unit volume of the sample

$\bar{x}$ = weighted sample thickness

with the other terms as defined previously.

5.6 NEUTRON DETECTOR EFFICIENCY

An important factor in the determination of neutron cross-sections, is the scintillator efficiency used for data acquisition. In the present work the efficiency of the detector was measured in two ways:

(I) The Absolute efficiency at 14 and 14.4 Mev .

(II) The Relative sensitivity, using hydrogenous materials.

5.6.1 Absolute Efficiency Measurement

In the absolute efficiency measurement, the centre part of the detector was positioned at 25 cm from the neutron source. The geometry is arranged so that, the detector lies completely within the neutron cone. Then by knowing the total number of coincidences between the α-particles and the neutron detector, and total number of incident neutrons on the detector, the efficiency was obtained from the relation:

$$\varepsilon(E_n) = \frac{n_C}{n_o} \cdot \frac{d\omega_\alpha}{d\omega_n} \qquad \ldots\ldots (5.21)$$

where n_C = total number of coincidences

n_o = total number of incident neutrons which is defined by the Alpha detector

$d\omega_\alpha$ = solid angle subtended by the α-detector aperture

and $d\omega_n$ = solid angle subtended by the neutron detector at the sample

Using the above relation, the absolute efficiency of detector at 14.0 Mev was found to be:

$$(9.7 \pm 0.1)\%$$

The same procedure was applied with 14.4 Mev neutrons, and the absolute efficiency was determined as:

$$(9.6 \pm 0.1)\%$$

5.6.2 Relative Efficiency Measurement

The relative efficiency of the neutron detector at lower energies than 14.0 Mev can be determined by measuring the yields of scatterd neutrons from hydrogenous materials. If the detector is to be used in a scattering experiment, elastic scattering from hydrogen is the best choice.

Perhaps the greatest deficiency of using hydrogen as a cross-section standard is that, it is not available as a solid sample in the pure state. The hydrogenous materials such as water, or polyethylene (polymerised form of ethylene, $CH_2:CH_2$) can be used. These have a high hydrogen concentration, and are readily available. In the case of

polyethylene, the neutron cross-section of carbon, the other constituent is well-known. Another advantage in using hydrogen for the efficiency measurement is, its small mass, allowing energy ranges to be covered in angular distribution measurements at each incoming energy.

5.6.2.1 Scattering of Neutrons from Polyethylene Sample

To reduce multiple scattering, a thin flat plate of polyethylene was used.

In practice, it was found that, for some angles the inelastically scattered neutron from the 4.43 Mev level in carbon overlapped with the hydrogen elastic peak. To correct for this, a separate run with a graphite scatterer was necessary to determine the background coming from the carbon.

Using equations (5.22) and (5.23) for polyethylene and graphite samples respectively, the thickness of graphite necessary was found as follows:

The number of neutrons scattered from the carbon in polyethylene:

$$N_{C,p} = \Sigma\phi.[1 - \exp - (n_H\,\sigma_{TH} + n_C\,\sigma_{TC}).x_p]\,\frac{n_{Cp}\,\sigma_{TC}}{n_H\,\sigma_{TH} + n_{Cp}\,\sigma_{TC}} \quad \ldots\ldots (5.22)$$

and the number of neutrons scattered from the graphite:

$$N_C = \Sigma\phi[1 - \exp - (n_C \cdot \sigma_{TC} \cdot x_C)] \quad \ldots\ldots (5.23)$$

where $N_{C,p}$ = number of scattered neutrons from carbon in the polyethylene

n_{Cp} = number of carbon atoms per unit volume in polyethylene

n_H = number of hydrogen atoms per unit volume in polyethylene

σ_{TC} = total cross-section of carbon

σ_{TH} = total cross-section of hydrogen

and n_C = number of carbon atoms per unit volume in graphite

Solving equations (5.22) and (5.23), it was found that, for 2 cm thickness of polyethylene, the required graphite sample was 9.4 mm thick allowing direct subtraction of the scattering due to the carbon content of the polyethylene sample.

In order to minimize some of the systematic errors, the detector efficiency was measured with the same geometrical arrangement, and the same collimator and shielding configuration, and at a counting rate similar to those in the main experiment. Because of the problems of shielding the primary neutron source at smaller angles, and the larger energy spread at larger angles, the experiment was carried out between 20° and 50° with respect to the direct neutron beam.

Table (5.2) shows the energy of the scattered neutron for the above angles from hydrogen.

Table (5.2)

Energy of the Scattered Neutron from Hydrogen

θ_{degree}	20	30	40	50
E'_{Mev}	12.36	10.50	8.22	5.78

The sample was placed prependicular to the direct neutron beam. With the same electronics system as discussed in section (2.5), time-of-flight spectra were obtained at 30°, 40° and 50°. Alternative runs were

made with the polyethylene sample in position, and with the graphite sample to correct for the background from the carbon content in polyethylene. Figures (5.3), (5.4) and (5.5) show time spectra at the above angles respectively.

Using equation (5.20) with correction factors, i.e.

$$\varepsilon(E_n) = \frac{N(\theta) \cdot \sigma_T}{(\Sigma\phi).F_1.F_2.\Delta\Omega.[1 - \exp - (n.\sigma_T.\bar{x})].(\frac{d\sigma_L}{d\Omega})_H} \quad \ldots\ldots (5.20)$$

where $(\frac{d\sigma_L}{d\Omega})_H$ = the differential cross-section in the Laboratory system for scattering from hydrogen, and σ_T = the total cross-section for hydrogen. The other parameters are as defined previously. The relative efficiency of the neutron detector was determined.

Figures (5.6) and (5.7) show the differential cross-section of the (n-p) reaction up to 40°, and the total cross-section of hydrogen respectively. At 50° the differential cross-section for (n-p) scattering was obtained by Allred et al[117] and Seagrave[118] as 53 ± 1.5 mb/sr.in the centre-of-mass system. In order to convert $(\frac{d\sigma_{c.o.m.}}{d\Omega})_H$ to the Laboratory system, one simply multiplies by the coefficient of equation (5.7). In the case of neutron-proton scattering, that factor reduces to the equation (5.24), i.e.

$$\sigma(\theta_L) = \frac{(1 + 2\gamma\cos\phi + \gamma^2)^{3/2}}{1 + \gamma\cos\phi}\sigma(\phi_C) \quad \ldots\ldots (5.7)$$

where $\gamma = 1$

$$\therefore \quad \sigma(\theta_L) = 4\cos\theta.\sigma(\phi_C) \quad \ldots\ldots (5.24)$$

where the centre-of-mass angle ϕ which corresponds to a Laboratory angle θ is: $\phi = 2\theta$.

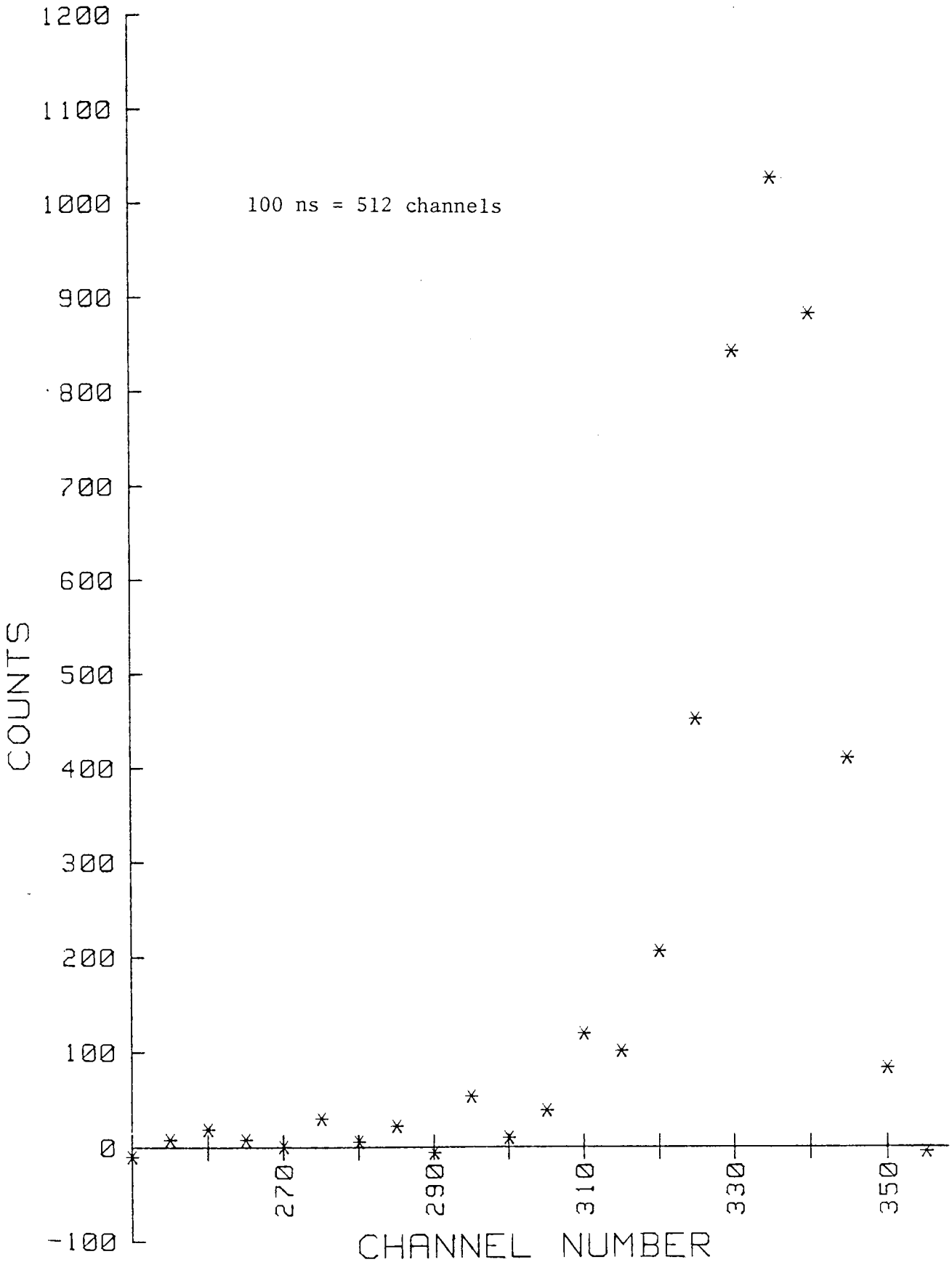

Figure (5.3) Time-of-flight Spectrum for Scattering from Hydrogen in Polyethylene at 30°

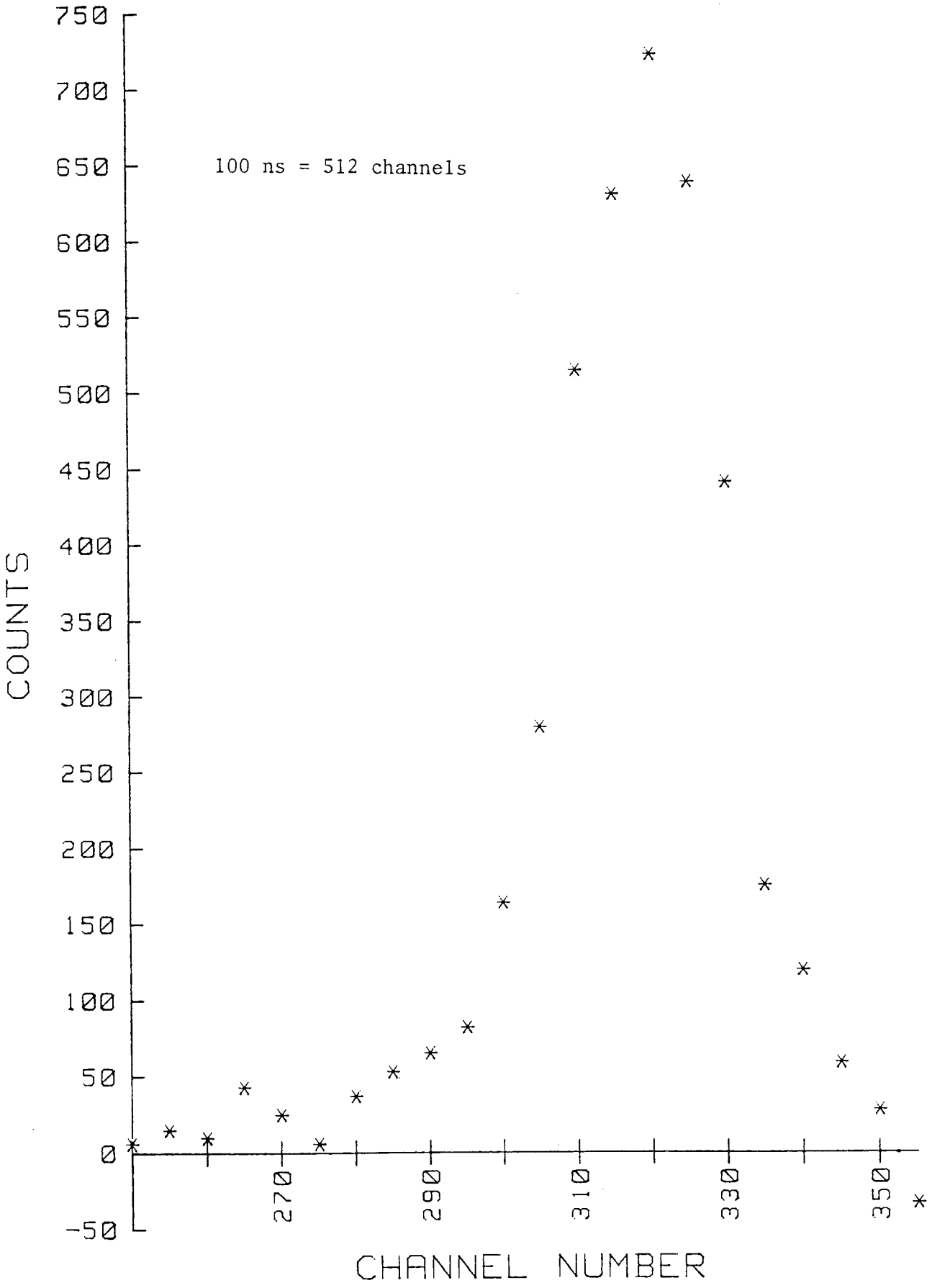

Figure (5.4) Time-of-flight Spectrum for Scattering from Hydrogen in Polyethylene at 40°

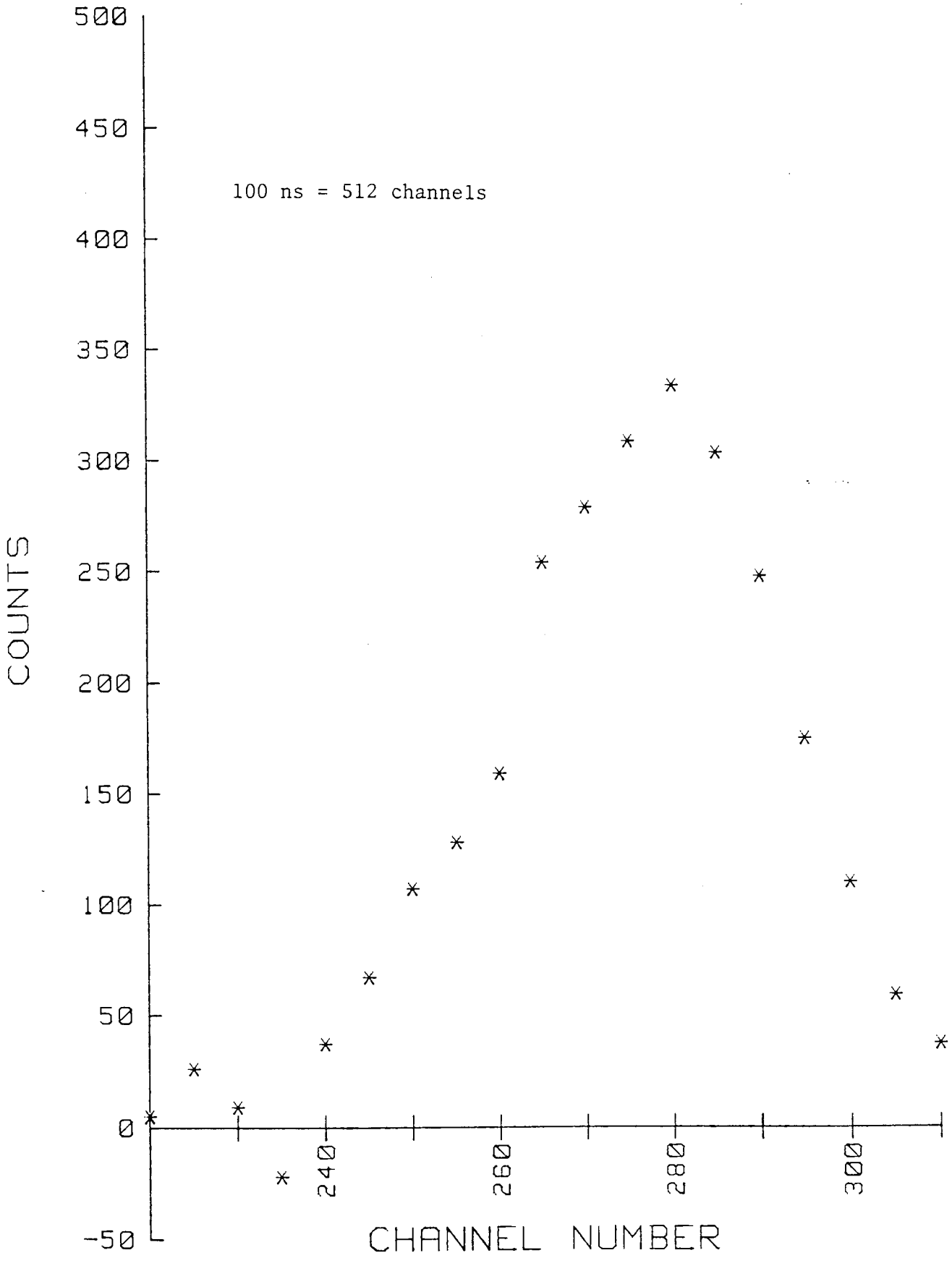

Figure (5.5) Time-of-flight Spectrum for Scattering from Hydrogen in Polyethylene at 50°

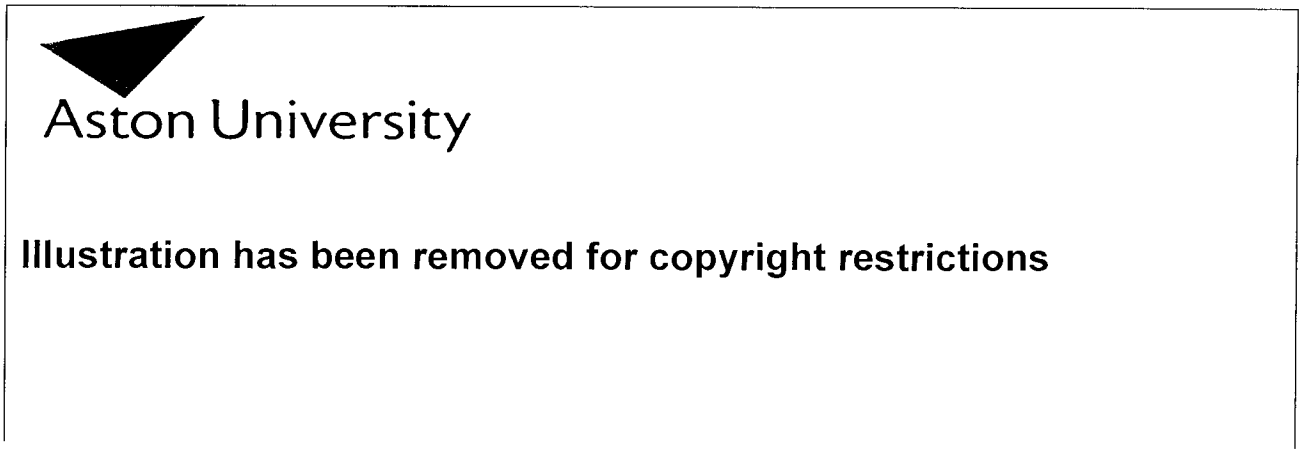

Figure (5.6) (n-p) Differential Cross-section in Laboratory System as a Function of Neutron Energy [94]

Aston University

Illustration has been removed for copyright restrictions

Figure (5.7) Total Cross-section of Hydrogen for Neutrons of Energies Between 1 and 400 Mev [94]

The relative efficiency of the neutron detector determined experimentally as a function of energy with the statistical error is shown in figure (5.8).

The total error of $N(\theta)$ was found as follows:

If A_i counts were added in the ith channel, and B_i the background counts subtracted from the same channel, the error in A_i is given by:

$$(er)_i = (A_i + B_i)^{\frac{1}{2}} \qquad \ldots\ldots (5.25)$$

The total error for a peak was found as $[\Sigma(er)_i^2]^{\frac{1}{2}}$

Table (5.3) shows the error for each term of the equation (5.20).

Table (5.3)

Experimental Errors in each Factor of the Equation (5.20)

Parameter	Estimated error %
Corrected flux: $F_1\ F_2\ \Sigma\phi$	1.0
Hydrogen differential cross section: $(\frac{d\sigma_L}{d\Omega})_H$	4.3
Solid angle: $\Delta\Omega$	1.5
Sample thickness: $\bar{x}$	< 1
Peak counts: $N(\theta)$	$[\Sigma(er)_i^2]^{\frac{1}{2}}$
Attenuation factor	1.3

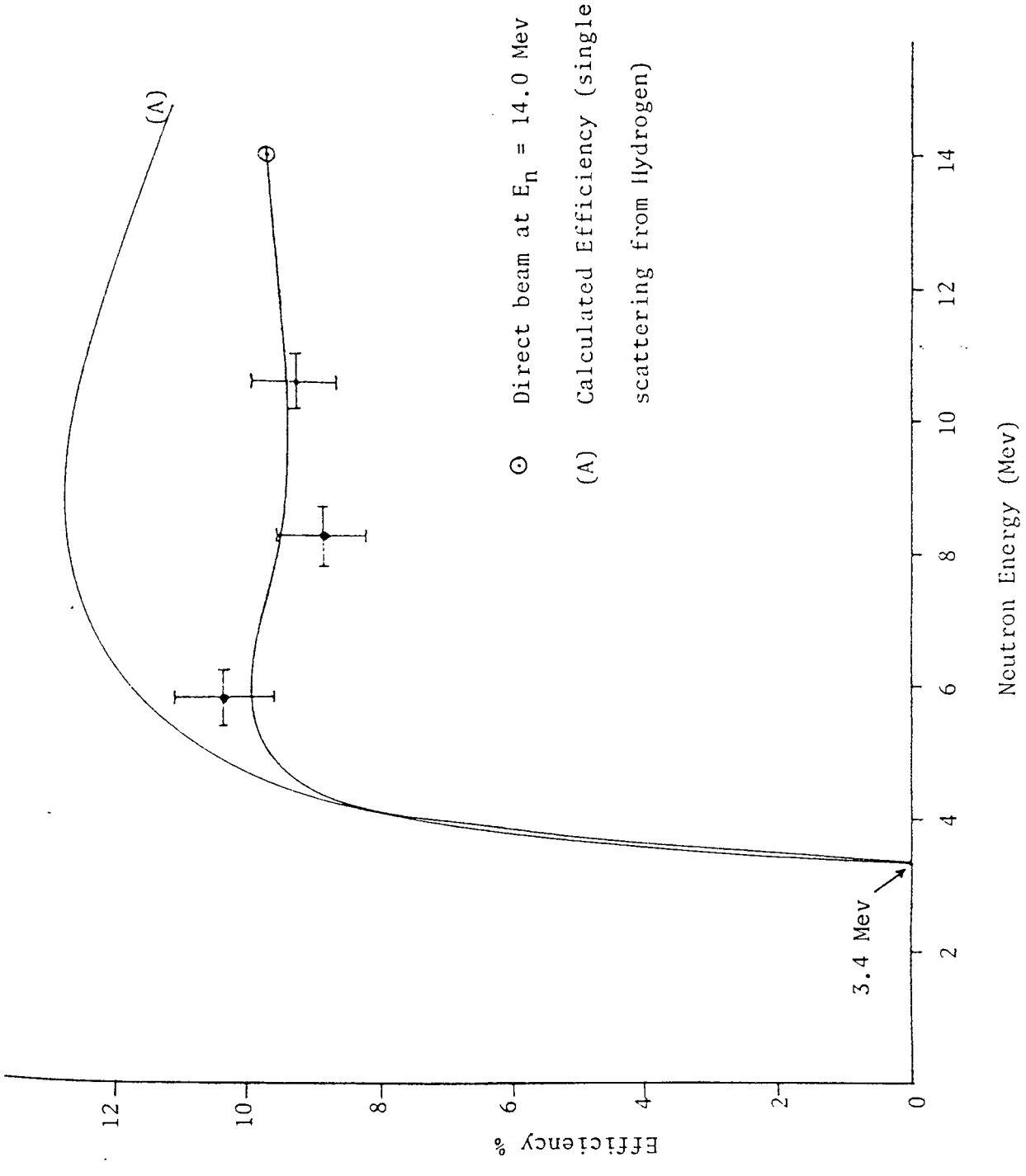

Figure (5.8) Measured Efficiency of the Neutron Detector as a Function of Neutron Energy

5.6.2.2 Scattering of Neutrons from Water

Similar to above procedure, the neutron detector efficiency at 14.4 Mev neutron energy was measured by the scattering of neutrons from the hydrogen in water. In this case, the neutron detector was positioned at 140 cm from the sample. With the same electronic system, time-of-flight spectra were obtained at 30°, 40° and 50° to the neutron direction. At each angle, the experiment was carried out by alternating the dewar filled with water, and with the dewar empty to subtract both the random background, and the background due to scattering from the dewar .

Figures (5.9), (5.10) and (5.11) show the time spectra at 30°, 40° and 50° respectively.

To reduce the error due to the contribution from the oxygen peak on the low energy tail, away from the hydrogen peak, the oxygen and hydrogen peaks were fitted with a normal error distribution programme, and the area of the hydrogen peak was obtained from that programme.

Figure (5.12) shows the relative sensitivity of the neutron detector as a function of neutron energy.

5.7 EXPERIMENTAL PROCEDURE FOR IRON AND CONCRETE SAMPLES

As explained in section 2.1.2 the sample was positioned normal to the direct neutron beam direction, on a stainless steel holder at a distance of 20 cm from the neutron source. It was arranged that, all the neutrons passed through the central area of the sample.

The experimental arrangement is shown in figure (5.13). The neutron detector is shielded by paraffin wax, Lithium carbonate and boric oxide and Lead. A paraffin wax shadow bar is also used to prevent neutrons from the source travelling directly to the detector. The detailed explanation of the shielding materials are given in section 3.11.

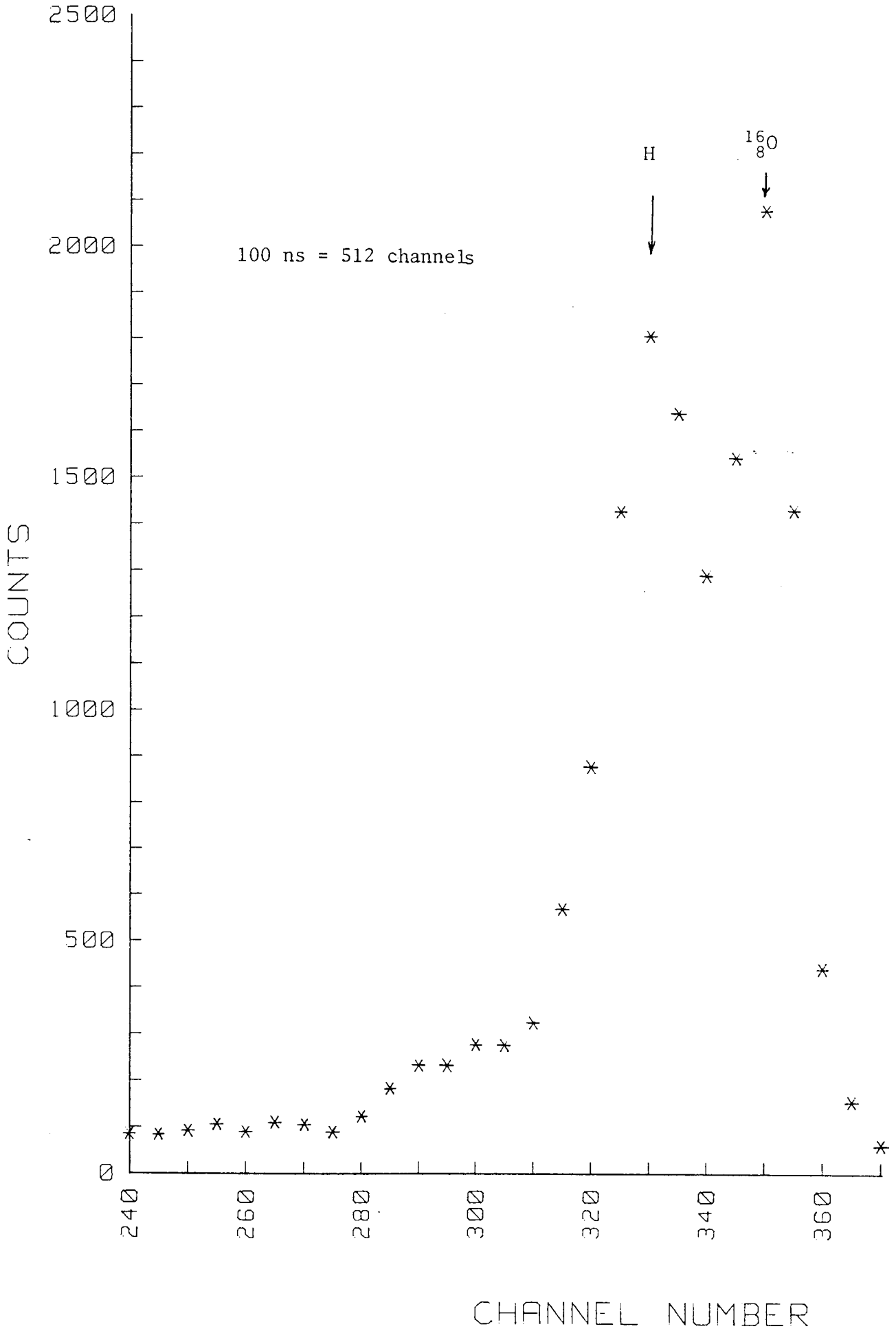

Figure (5.9) Time-of-flight Spectrum for Scattering from Water at 30°

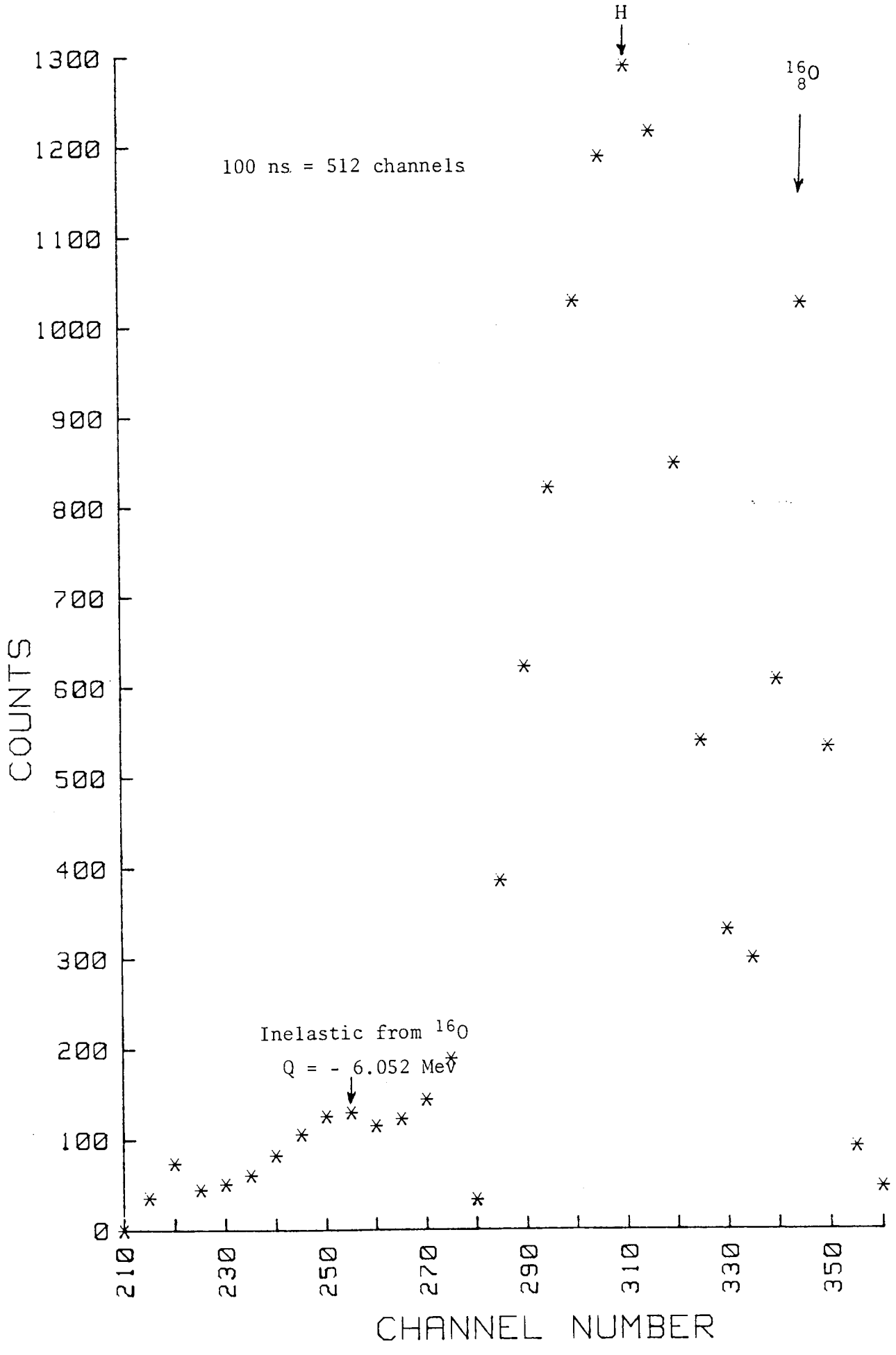

Figure (5.10) Time-of-flight Spectrum for Scattering from Water at 40° in Laboratory System

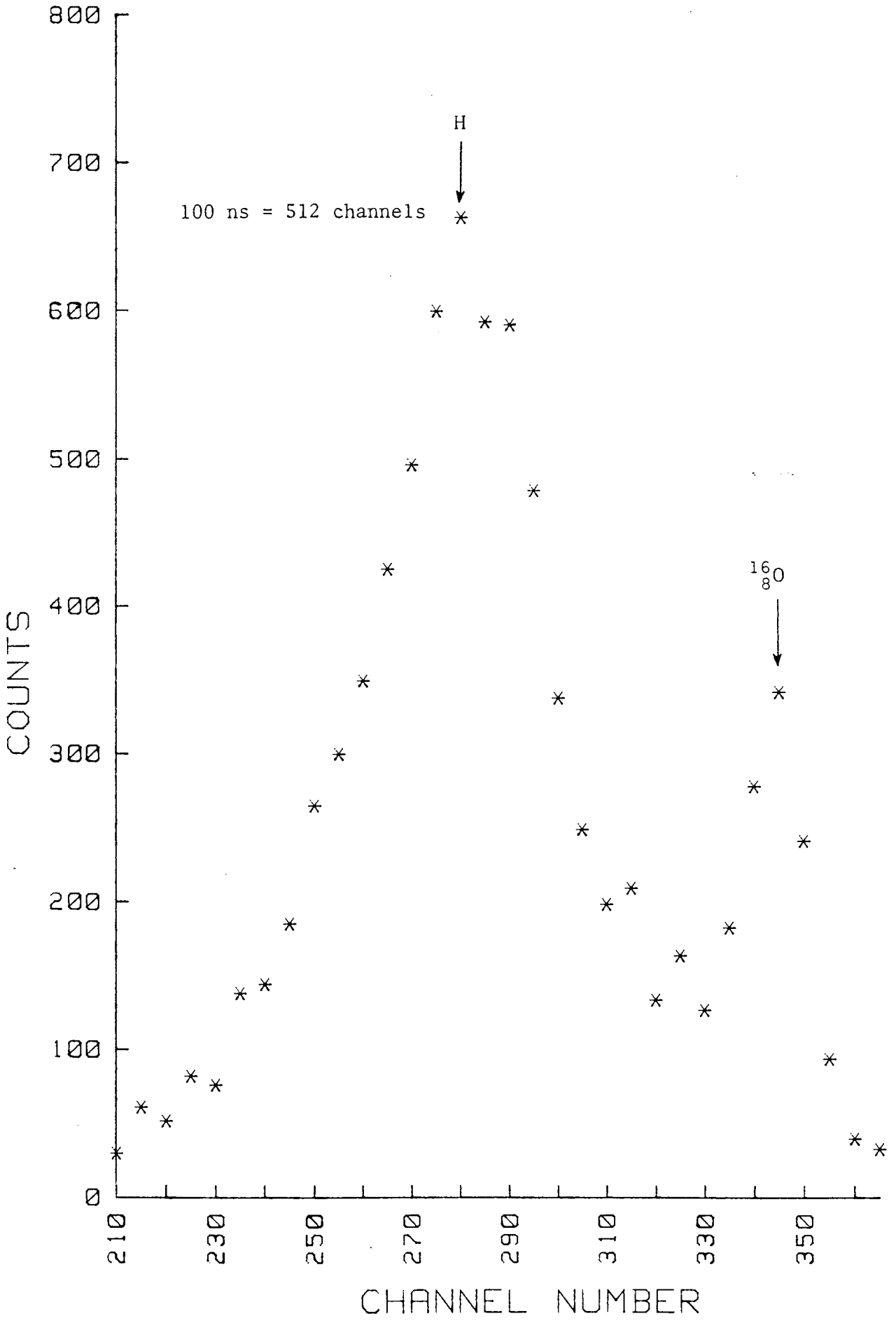

Figure (5.11) Time-of-flight Spectrum for Scattering from Water at 50° in Laboratory System

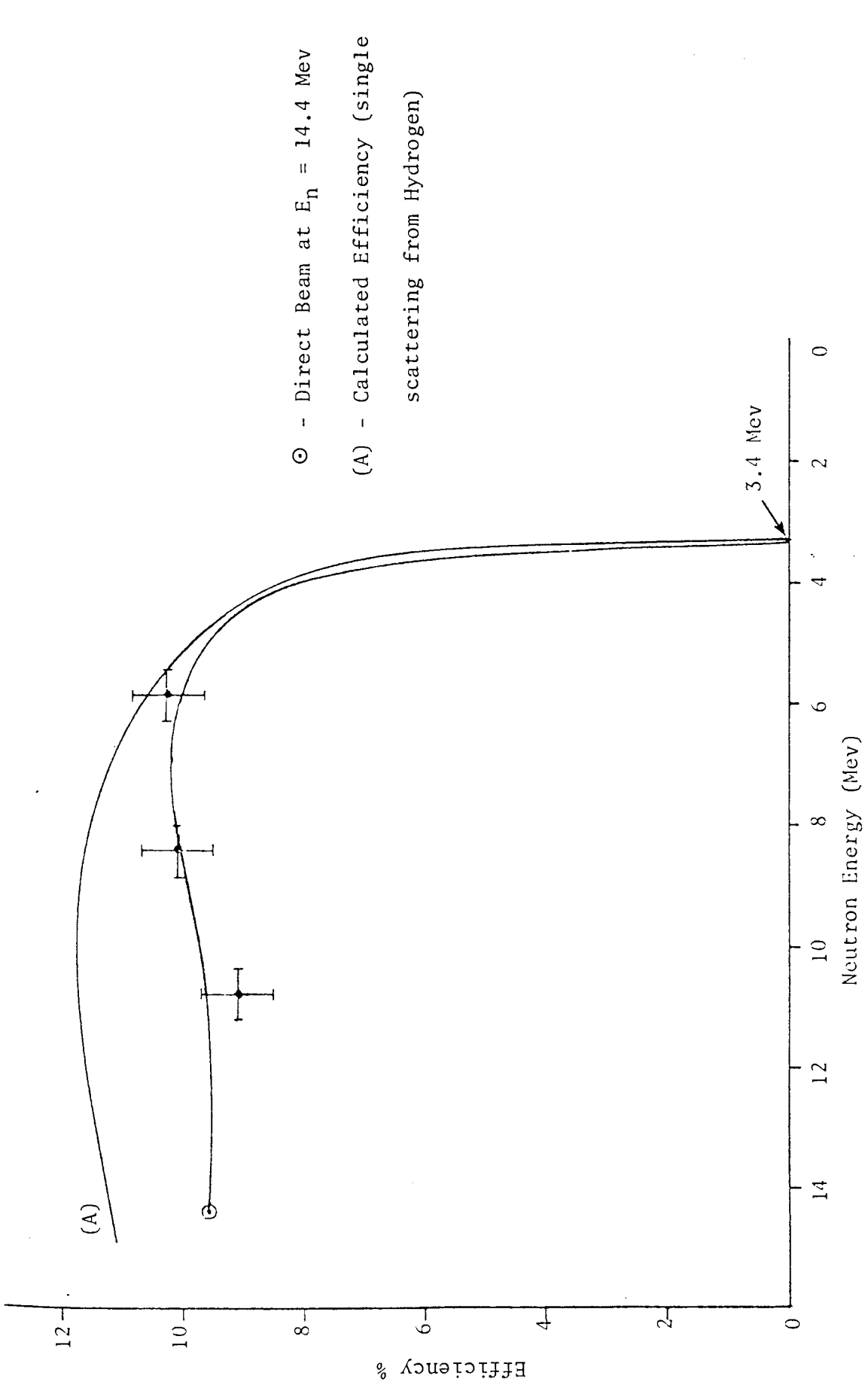

Figure (5.12) Measured Efficiency of the Neutron Detector as a Function of Neutron Energy

Prior to each measurement, the electronic system was switched on, and the machin run for 30 minutes to allow the system to stabilize, and to allow the activity of the target assembly to reach a steady state.

To obtain the spectrum for each sample data was accumulated with the pulse-height Analyser in the "ADD" mode for a fixed number of α-counts.

To subtract background radiation, the sample is removed and pulse-height Analyser was set in the "SUB" mode, and experiment repeated for the same number of alpha counts. Finally the net pulse height spectrum was obtained.

5.8 IRON DIFFERENTIAL CROSS-SECTION MEASUREMENTS

5.8.1 Iron Samples

Iron consists of different isotopes. The most abundant isotope of iron is $^{56}_{26}Fe$, (91.57%), with the other naturally occuring iosopes of iron being $^{54}_{26}Fe$, $^{57}_{26}Fe$ and $^{58}_{26}Fe$ with isotopic abundances of 5.84%, 2.17% and 0.33% respectively. The other materials such as nickel, carbon and oxygen are present in iron but in small quantities.

In this work, four different thicknesses of iron samples were examined, the size of thin sample of iron was 14.0 cm x 14.0 cm with 2 cm thickness, while the length and width of the other three samples were:

(A) 14.0 cm x 14.0 cm

(B) 20.0 cm x 17.0 cm

(C) 20.0 cm x 17.0 cm

but with thicknesses of 4.0 cm, 6.0 cm and 8.0 cm corresponding to 0.87, 1.30 and 1.73 mean free paths respectively at E_n = 14 Mev.

The energy level diagram of $^{56}_{26}Fe$ is shown in figure (5.14)

14.4 Mev neutrons are produced using the Dynamitron accelerator,

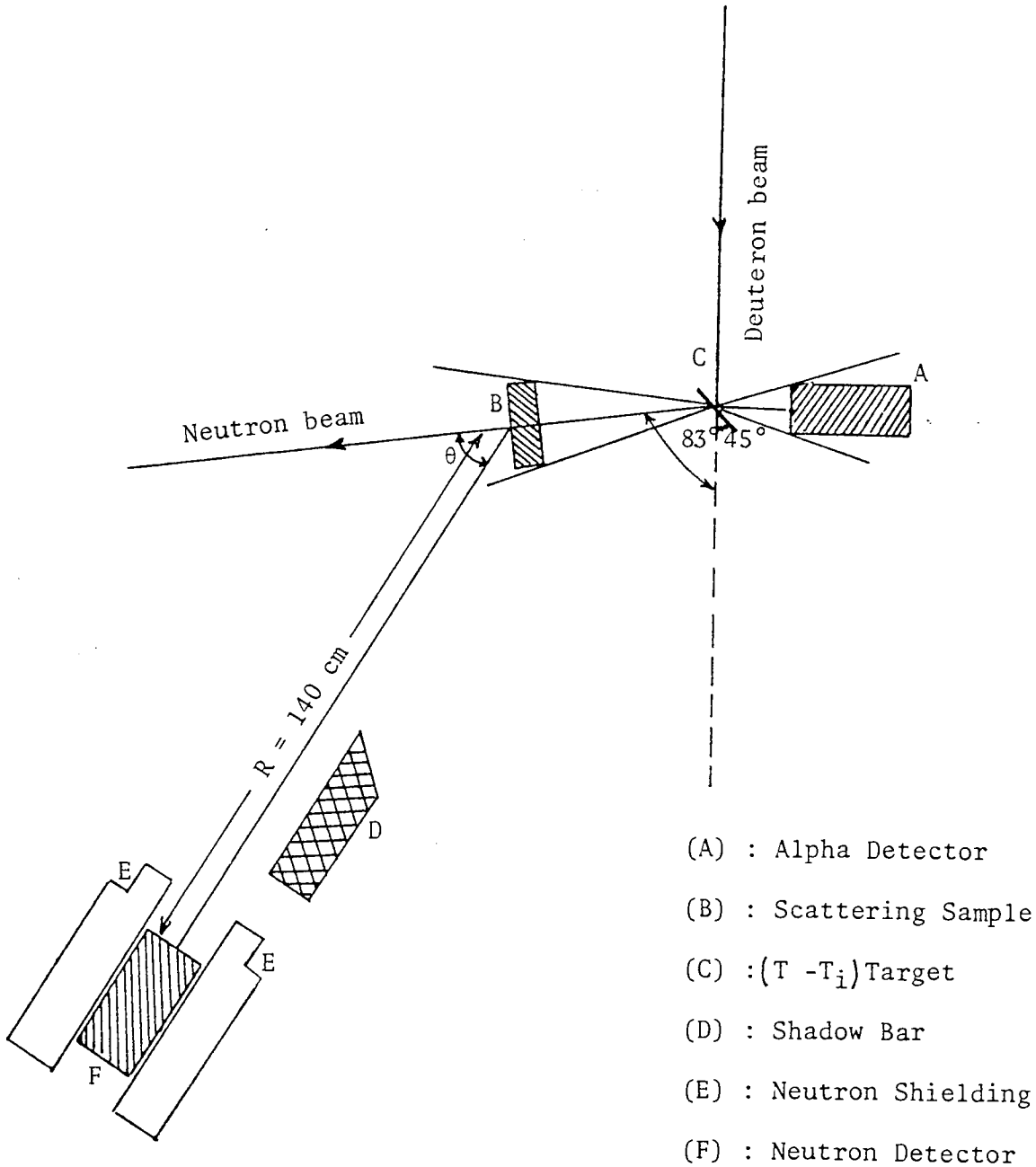

Figure (5.13) Neutron Detector with Shielding and Scattering Sample (not to scale)

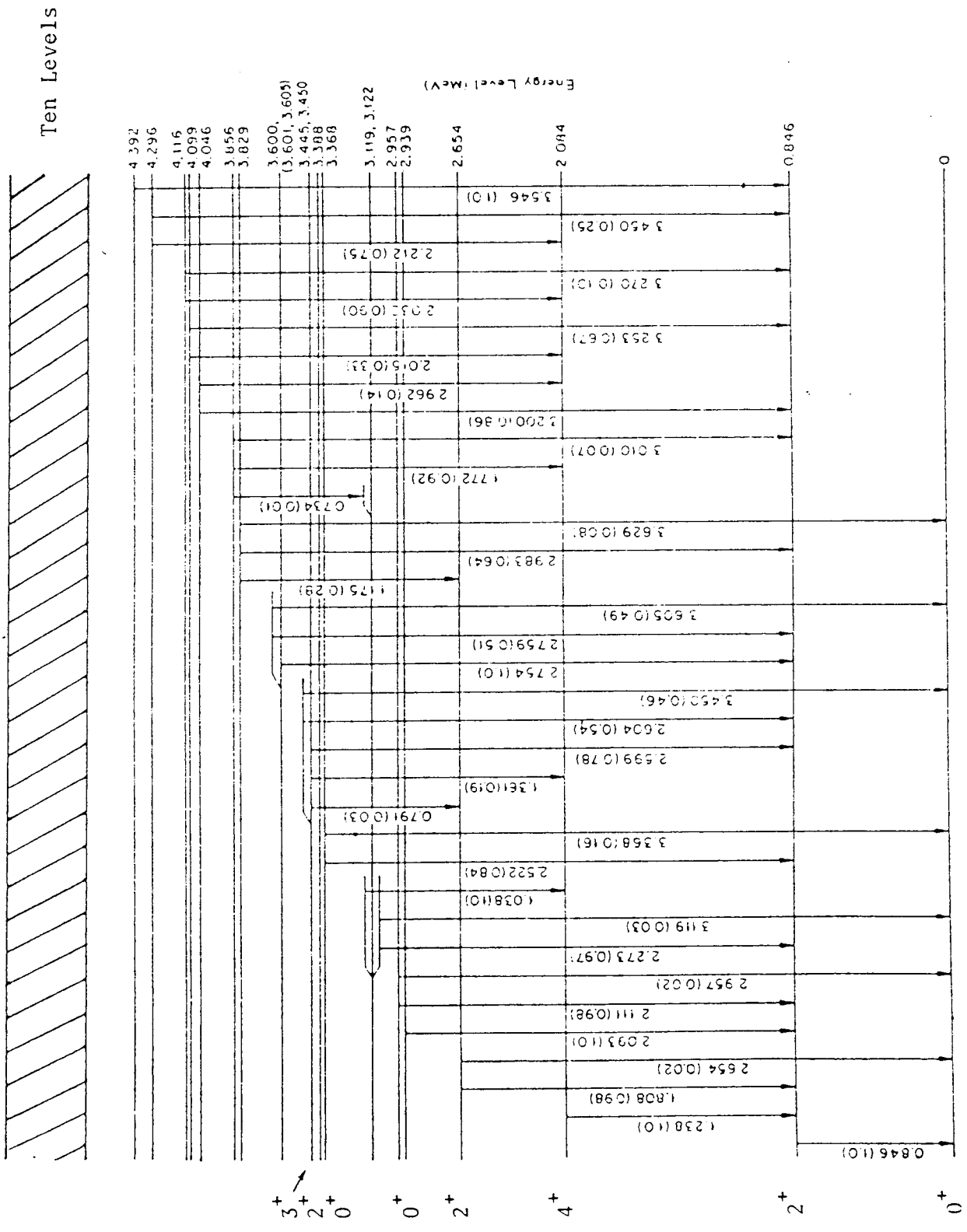

Figure (5.14) Energy Level Diagram of $^{56}_{26}Fe$ and Branching Ratio of Some Levels [119 - 120]

with a 900 keV mass III deuteron beam. For this energy only three different thicknesses of iron samples i.e. 2 cm, 6.0 cm and 8.0 cm were examined.

5.8.2 Time of Flight Spectra

Using the electronic system discussed in section 2.5 the time spectra from the iron samples at E = 14 Mev were measured at 25°, 45°, 65° and 85° to the neutron beam direction. The time spectrum for the thin sample was also measured at 90°. Typical time spectra are shown in figures (5.15) and (5.16) corresponding to Laboratory angles of 25° and 45° respectively.

In the case of 14.4 Mev neutrons using the Dynamitron accelerator, the time spectra from the thin sample was measured at 30°, 50°, 70°, 80° and 90°, but for other thicknesses of iron the time spectra were determined at 30°, 50°, 70° and 90° only. Typical time spectra are shown in figures (5.17), (5.18) and (5.19) corresponding to the Laboratory angles of 30°, 70° and 80° respectively.

Using the Gaussian shape of the elastic peak, it was possible to "strip off" the contribution from the elastically scattered neutrons. By using this technique, the effect of the inelastically scattered neutrons was therefore eliminated. A normal error curve was then fitted to the elastic peak from which the area was obtained.

5.8.3 Experimental Results for Iron

A: E_n = 14.0 Mev

Using equation (5.20) the differential elastic scattering cross-section of $^{56}_{26}Fe$ was evaluated. The number of neutrons, $N(\theta)$ scattered elastically at angle θ was obtained using the normal error curve programme. The errors indicated in the differential cross-section were

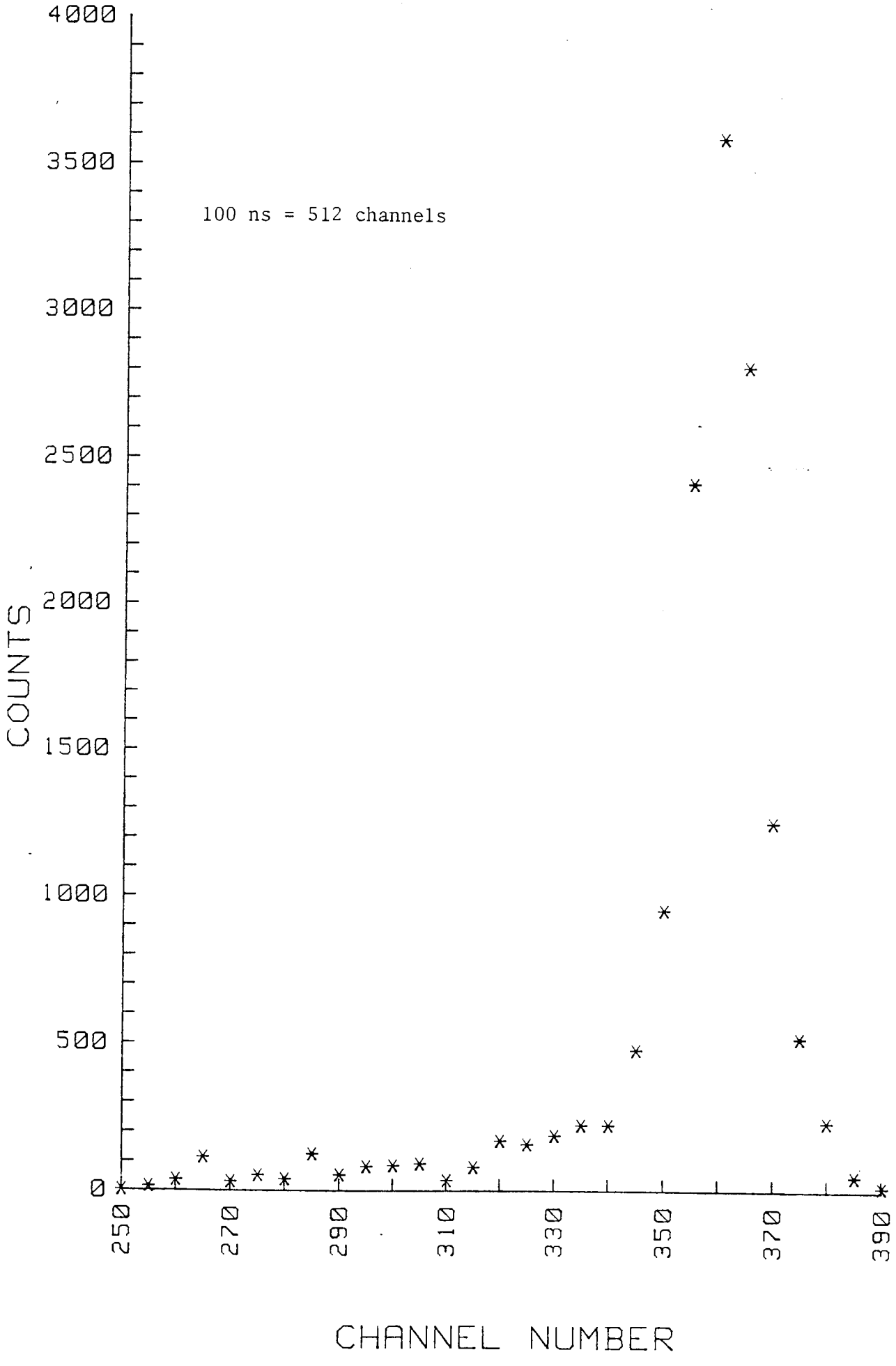

Figure (5.15) Time-of-flight Spectrum for Scattering in 4 cm Thick Iron at 25°

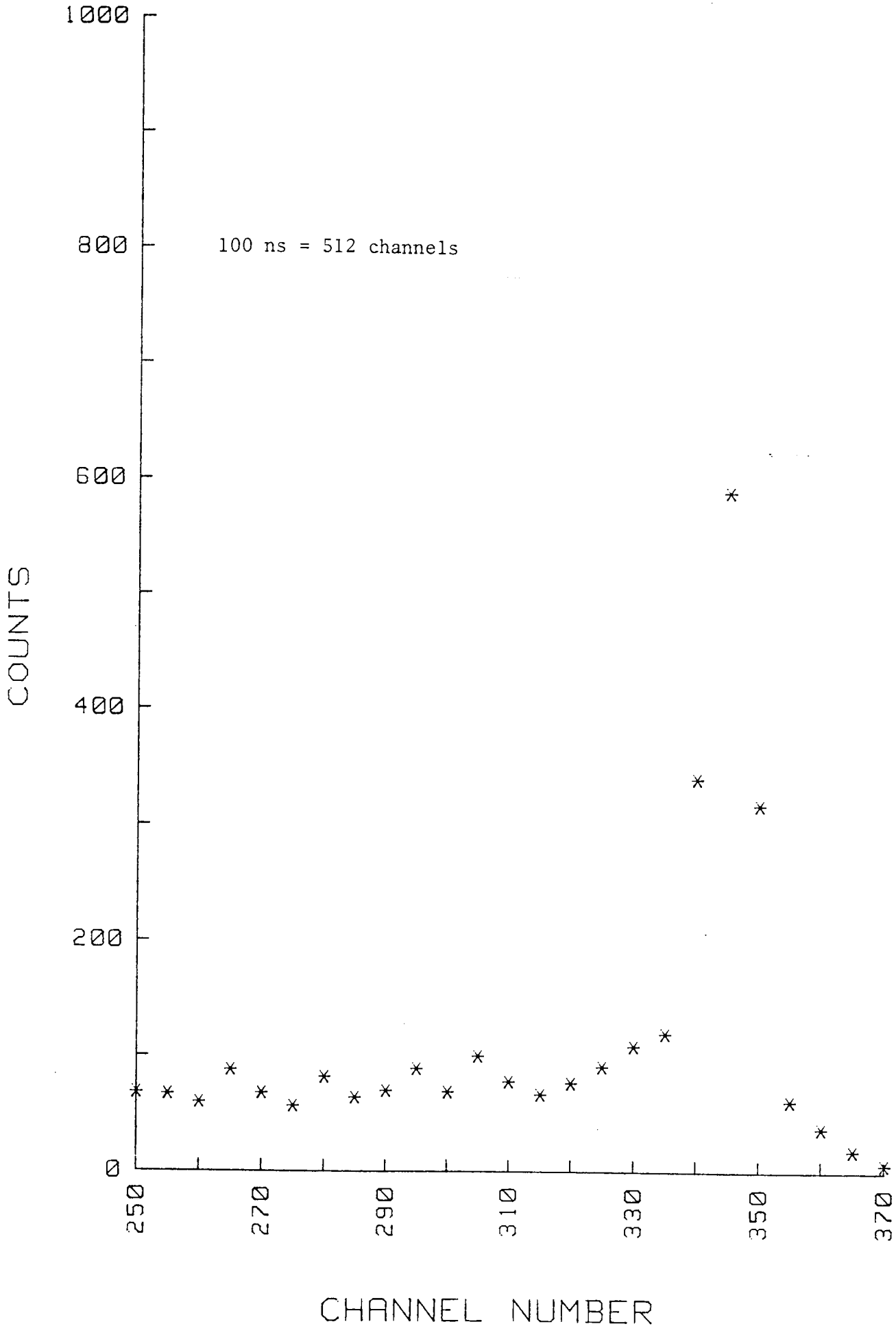

Figure (5.16) Time Spectrum for Scattering in 2 cm Thick Iron at45°

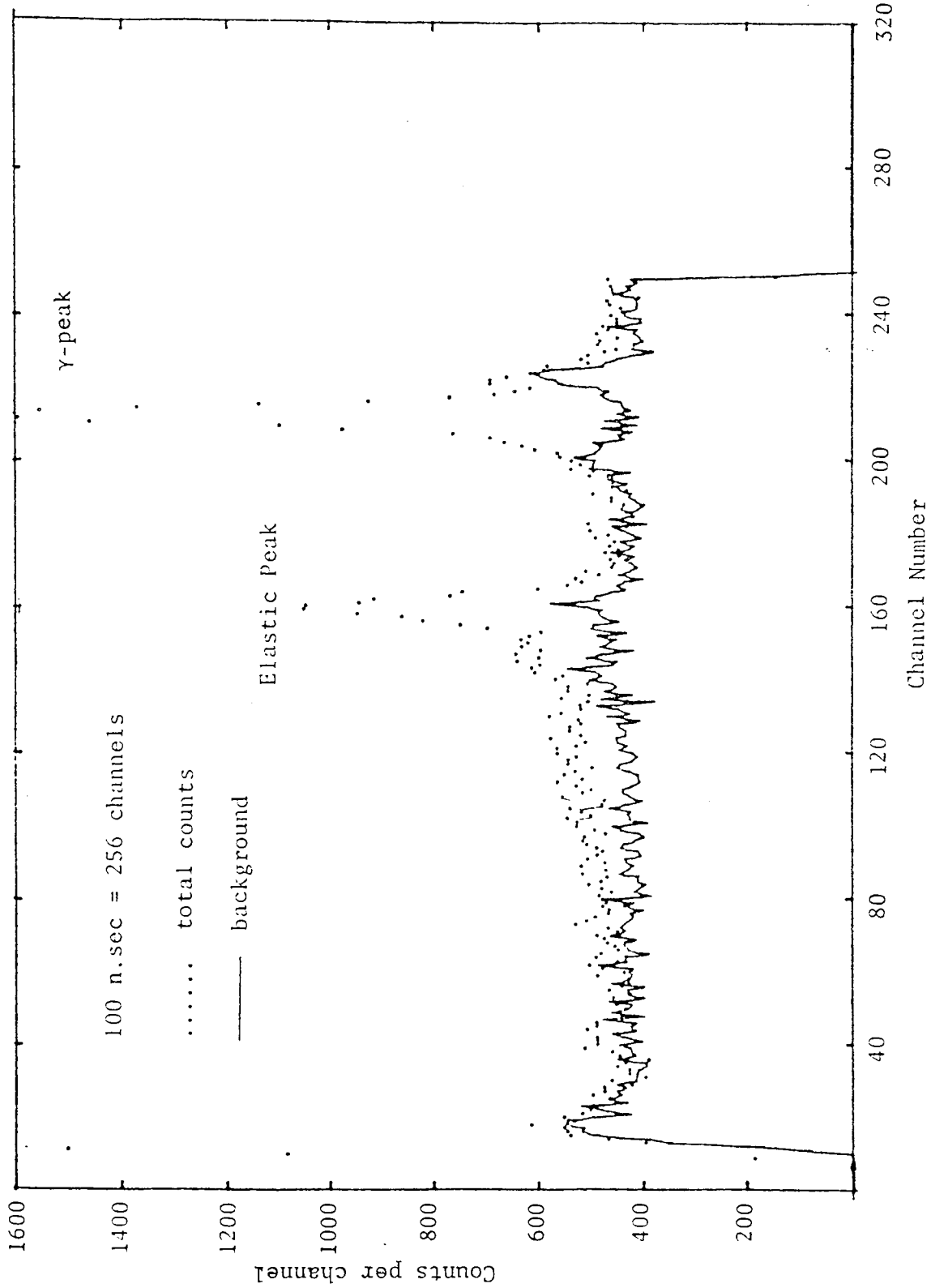

Figure (5.17) Time Spectrum for Scattering in 8 cm Thick Iron at 30°

(E_n = 14.4 Mev)

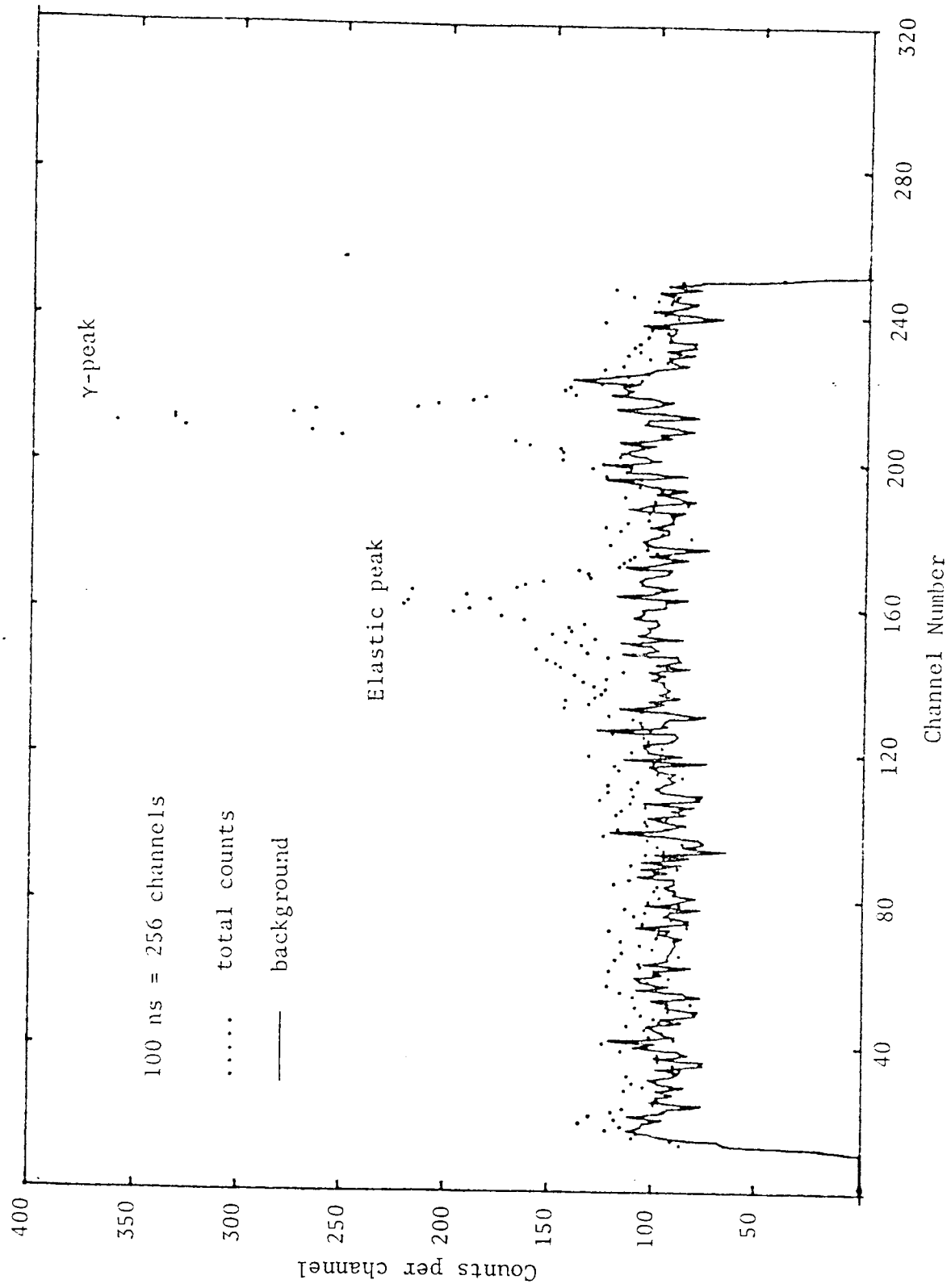

Figure (5.18) Time Spectrum for Scattering in 6 cm Thick Iron at 70°

(E_n = 14.4 Mev)

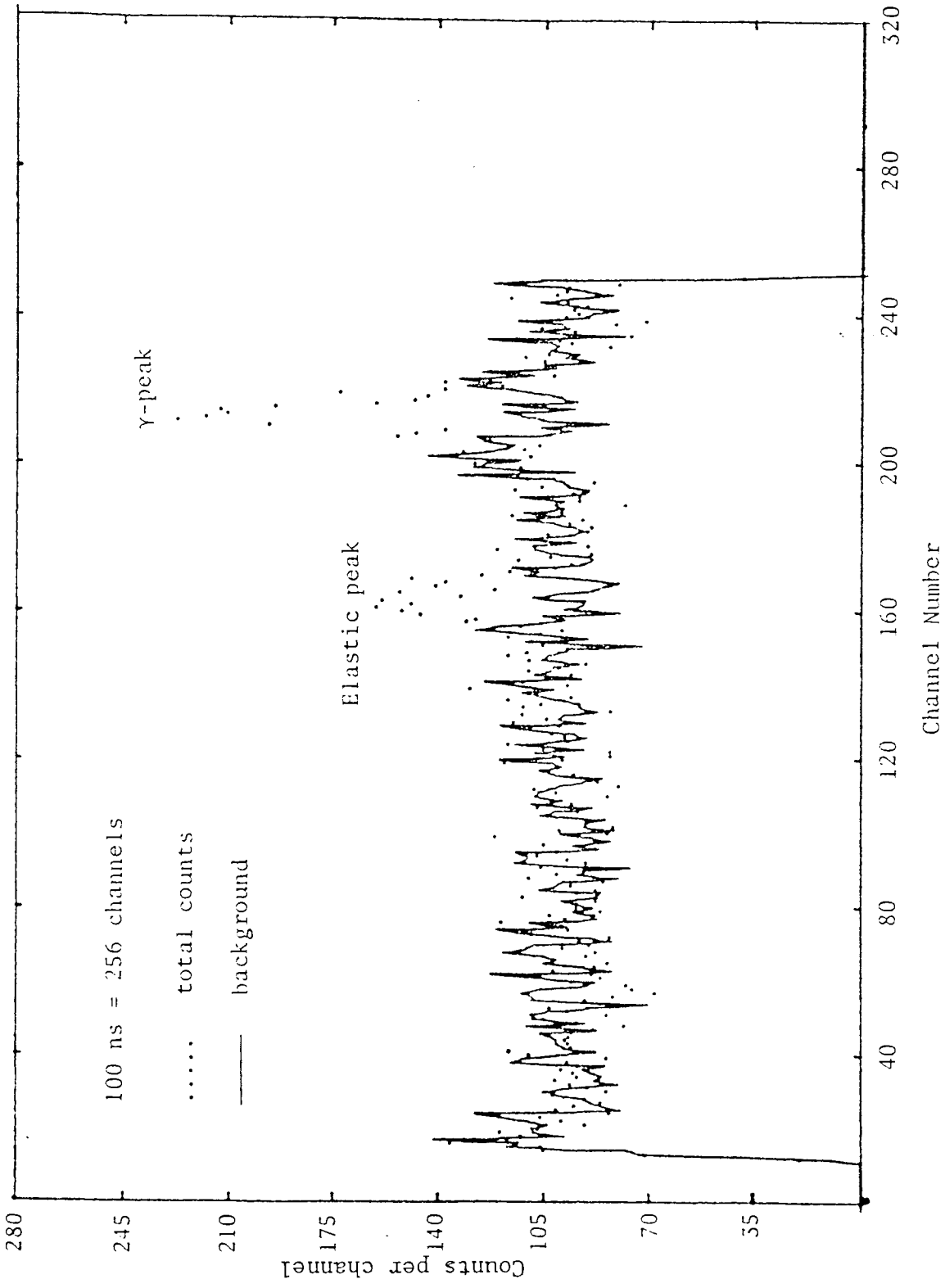

Figure (5.19) Time Spectrum for Scattering in 2 cm Thick Iron at 80° . (E_n = 14.4 Mev)

obtained by the error in each term of the equation (5.20), to give the total experimental error. The average experimental error in each parameter of the equation (5.20) is given in Table (5.5).

The results of the differential elastic scattering cross-section for all thicknesses of Iron with corresponding errors are shown in Table (5.4).

In Table (5.6) the results of the angular distribution of the thin iron sample, together with the results of other published data are presented.

The data reported by Yuasa[12] using a disk-shaped scatterer was between 70° and 170°.

For cylindrical geometry, the data of the angular distribution of iron and other elements reported by Elliot[15] extended angles between 5° and 55°. This data was less reliable at large angles.

The results obtained for the thin sample are in good agreement within the experimental error with those obtained by Coon et al[121] except for 45°.

In order to compare the results of the angular distribution with the optical model and other published data, it was necessary to transfer the differential elastic scattering cross-sections to the centre-of-mass system. This was done, using equations (5.7) and (5.8).

Figure (5.20) compares the measurements of the differential elastic scattering cross-section from the thin iron sample at 14 Mev neutron energy with other published data. The angular distribution of elastically scattered neutrons from the iron samples are shown in figure (5.21).

B: E_n = 14.4 Mev

The differential elastic scattering cross-section for iron samples at 14.4 Mev neutrons were determined, using the same technique with the Dynamitron.

Table (5.4)

$^{56}_{26}Fe$ Differential Cross-section for Elastic Scattering of 14.0 Mev Neutrons (in mb/Sr.)

Scattering angle (θ) degree	Centre-of-mass angle (ϕ) degree	x = 2 cm λ = 0.433 (mfp.)	x = 4 cm λ = 0.866 (mfp.)	x = 6 cm λ = 1.298 (mfp.)	x = 8 cm λ = 1.731 (mfp.)
25°	25.44°	368.5 ± 30.1	374.6 ± 30.9	376.2 ± 33.6	420.6 ± 36.9
45°	45.73°	75.3 ± 6.4	80.6 ± 6.8	95.7 ± 8.3	102.7 ± 9.2
65°	65.94°	27.8 ± 2.6	34.6 ± 3.1	38.2 ± 3.5	39.6 ± 3.7
85°	86.03°	23.3 ± 2.3	24.7 ± 2.3	28.8 ± 2.7	40.2 ± 3.7
90°	91.03°	21.1 ± 2.1	-	-	-

Table (5.5)

Experimental Errors in the Calculation of the Differential Elastic Scattering Cross-section of the Iron Samples

Factor	Estimated error %
$\Sigma\phi \cdot F_1 \cdot F_2$	1
$N(\theta)$	$[\Sigma (er)_i^2]^{\frac{1}{2}}$
$\Delta\Omega$	1.5
C	2
$\varepsilon(E_n)$	6.5
attenuation factor	1 4
$\bar{x}$	< 1

The results of the angular distribution of 14.4 Mev neutrons for three different thicknesses of iron samples are shown in Table (5.7).

There is only one published set of data at 14.5 Mev neutron energy by Coon et al[16], using cylindrical shell geometry. Table (5.8) shows the results of Coon et al and of this work for the thin iron sample (x = 2 cm). The results of this work for some angles are again higher than that of Coon et al[16].

The discrepancy of the present data with the data of Coon et al[16], is possibly due to an overcorrection for the inelastic contribution.

Secondly, the energy of neutron at "0 geometry" carried out by Coon et al varied between 14.9 Mev to 14.2 Mev and at scattering angles from

Table (5.6)

Comparison of the Differential Elastic Scattering Cross-section

from Iron for 14.0 Mev Neutrons
($d\sigma/d\Omega'$ in mb/sr.)

Scattering angle (θ) degree	Centre-of-mass angle (ϕ) degree	Present Work	J.O. Elliot data [15]	Yuasa data [12]	Coon et al data [121]	Wilmore et al data (Theoretical values) [13]	Bjorklund et al data (Theoretical) [14]
25°	25.44	368.5 ± 30.1	510.0 ± 63.0	-	367.9	760	600
30°	30.52	-	268.0 ± 95.0	-	162.4	341	≈ 310
35°	35.59	-	101.0 ± 18.0	-	61.2	110	122
40°	40.67	-	43.7 ± 16.0	-	38.9	52	60
45°	45.73	75.3 ± 6.4	41.48 ± 3.5	-	50.7	46	47.5
50°	50.79	-	56.0 ± 3.0	-	51.8	40	≈ 43
55°	55.85	-	42.22 ± 1.5	-	43.1	30	35
60°	60.90	-	-	-	18.7	15	22.9
65°	65.94	27.8 ± 2.6	-	-	19.7	6.6	8.5
70°	70.97	-	-	12.6 ± 4.2	8.7	9	6

Table (5.6) contd.

Scattering angle (θ) degree	Centre-of-mass angle (ϕ) degree	Present Work	J.O. Elliot data [15]	Yuasa data [12]	Coon et al data [121]	Wilmore et al data (Theoretical values) [13]	Bjorklund et al data (Theoretical) [14]
75°	75.95	-	-	-	13.9	18.7	10
80°	81.02	-	-	17.0 ± 3.2	19.4	26.6	18
85°	86.03	23.3 ± 2.3	-	-	23.4	30.0	24
90°	91.03	21.1 ± 2.1	-	24.7 ± 4.5	26.8	29.0	27

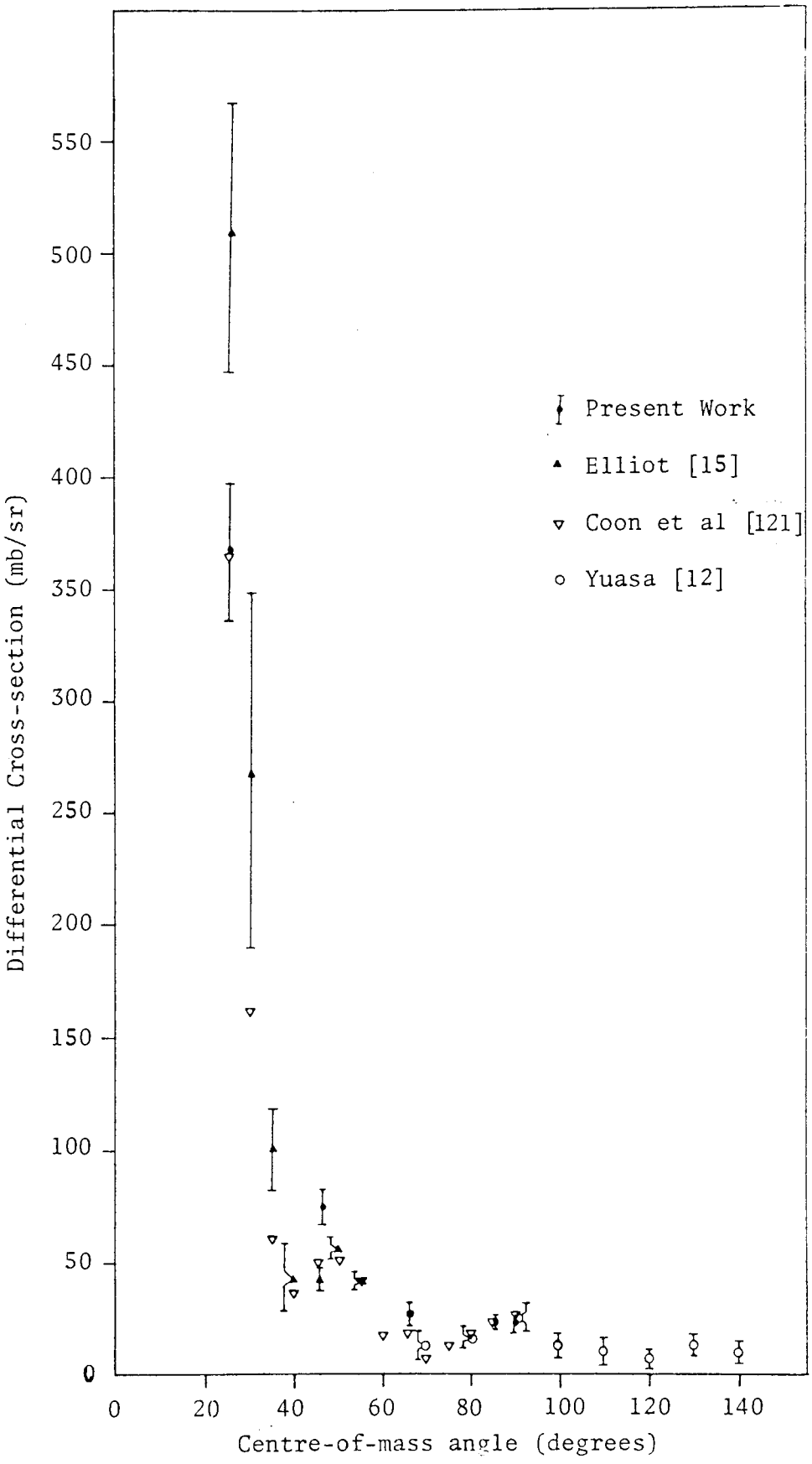

Figure (5.20) Comparison of the Differential Elastic Scattering Cross-section from Iron for 14.0 Mev Neutrons

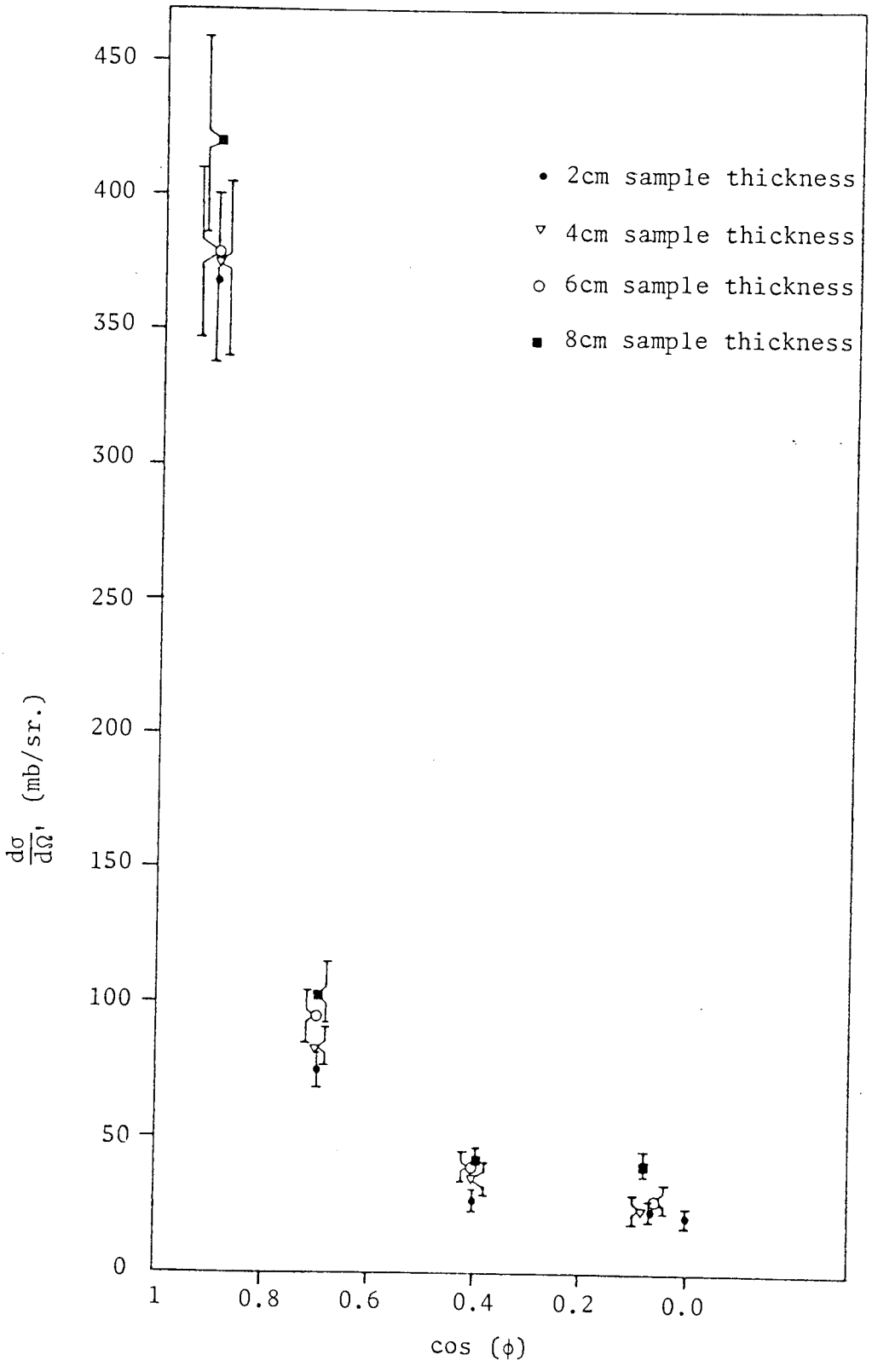

Figure (5.21) The Angular Distribution of Elastically Scattered Neutrons from Iron Samples

5° to 150° whereas in this work, the energy varied between 14.4 to 13.8 Mev at scattering angles between 0° to 90°.

Thirdly, the lowest energy of the recoiling protons whose pulses are recorded by Coon et al was 9 Mev, but in the present work it was 3.4 Mev.

The angular distributions for the thin iron sample, and the data of Coon et al[16] are shown in figure (5.22).

The angular distribution of elastically scattered neutrons from iron for different thicknesses are shown in figure (5.23).

Table (5.7)

$^{56}_{26}$Fe Differential Cross-section for Elastic Scattering of 14.4 Mev Neutrons

$(\frac{d\sigma}{d\Omega})$ (mb/sr.)

Scattering angle (θ) degree	Centre-of-mass angle (ϕ) degree	x = 2 cm. λ = 0.426 (mfp)	x = 6 cm. λ = 1.278 (mfp)	x = 8 cm. λ = 1.704 (mfp)
30	30.52	170.3 ± 15.7	175.1 ± 16.1	185.1 ± 17.2
50	50.79	64.6 ± 7.8	94.6 ± 9.6	112.3 ± 11.4
70	70.97	34.7 ± 6.0	68.5 ± 6.8	87.0 ± 9.4
80	81.02	36.9 ± 5.9	-	-
90	91.03	26.9 ± 4.3	29.1 ± 4.8	33.1 ± 4.5

Table (5.8)

Comparison of the Measurements of the Differential Elastic Scattering Cross-section from Iron for 14.4 Mev Neutrons

Scattering angle (θ) degree	Centre-of-mass angle (ϕ) degree	Present Work $\frac{d\sigma}{d\Omega}$ (mb/sr.)	Coon et al data $E_n \simeq 14.5$ Mev $\frac{d\sigma}{d\Omega}$ (mb/sr.) [16]
30	30.52	170.3 ± 15.7	183
40	40.67	-	≃ 44
50	50.79	64.6 ± 7.8	50
60	60.89	-	≃ 30
70	70.97	34.7 ± 6.0	9
80	81.02	36.9 ± 5.9	≃ 23
90	91.03	26.9 ± 4.3	28
100	101.02	-	16
110	110.97	-	8.5
120	120.90	-	9

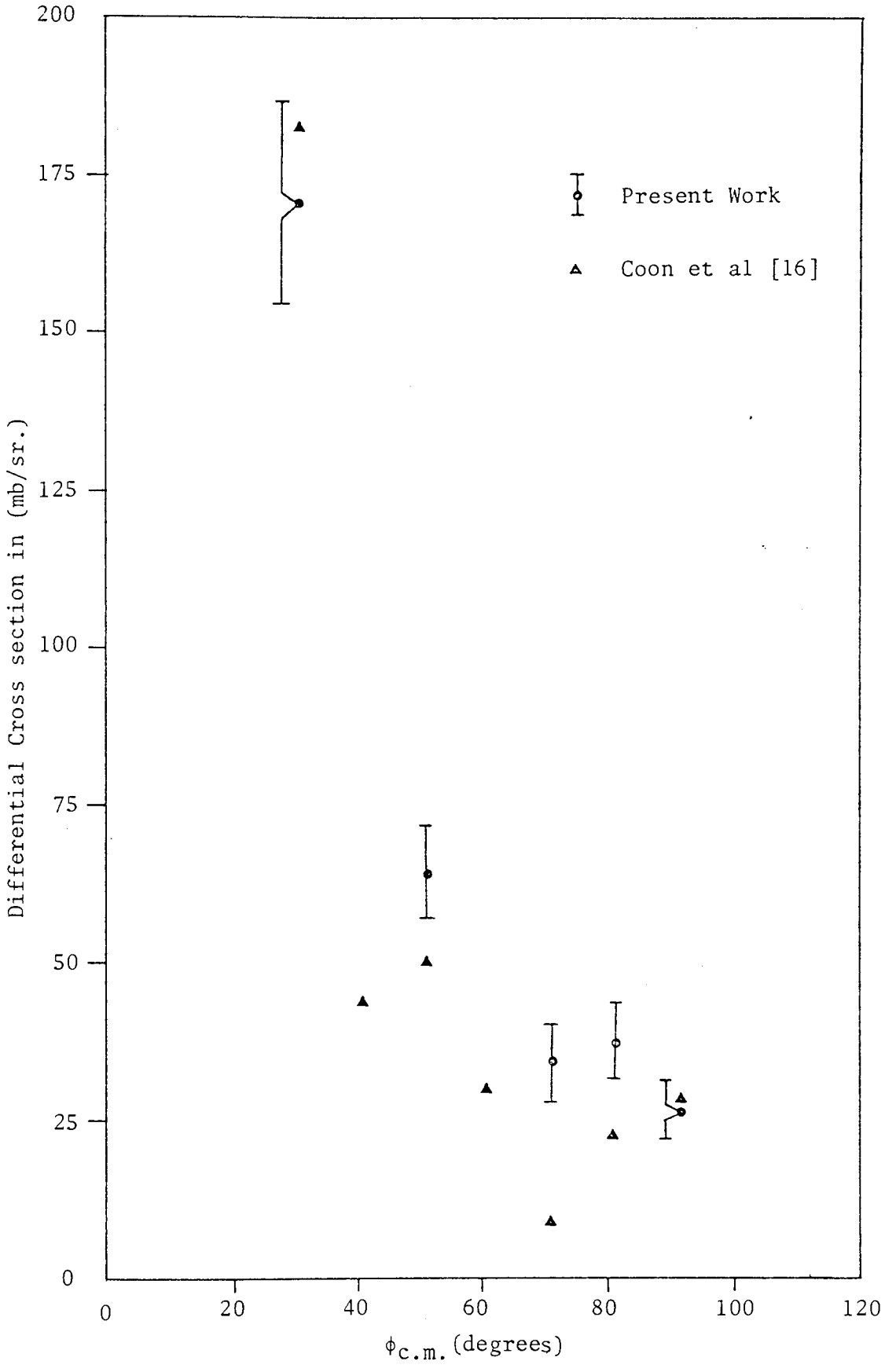

Figure (5.22) Comparison of the Measurements of the Differential Elastic Scattering Cross-section from $^{56}_{26}Fe$ for 14.4 Mev Neutrons

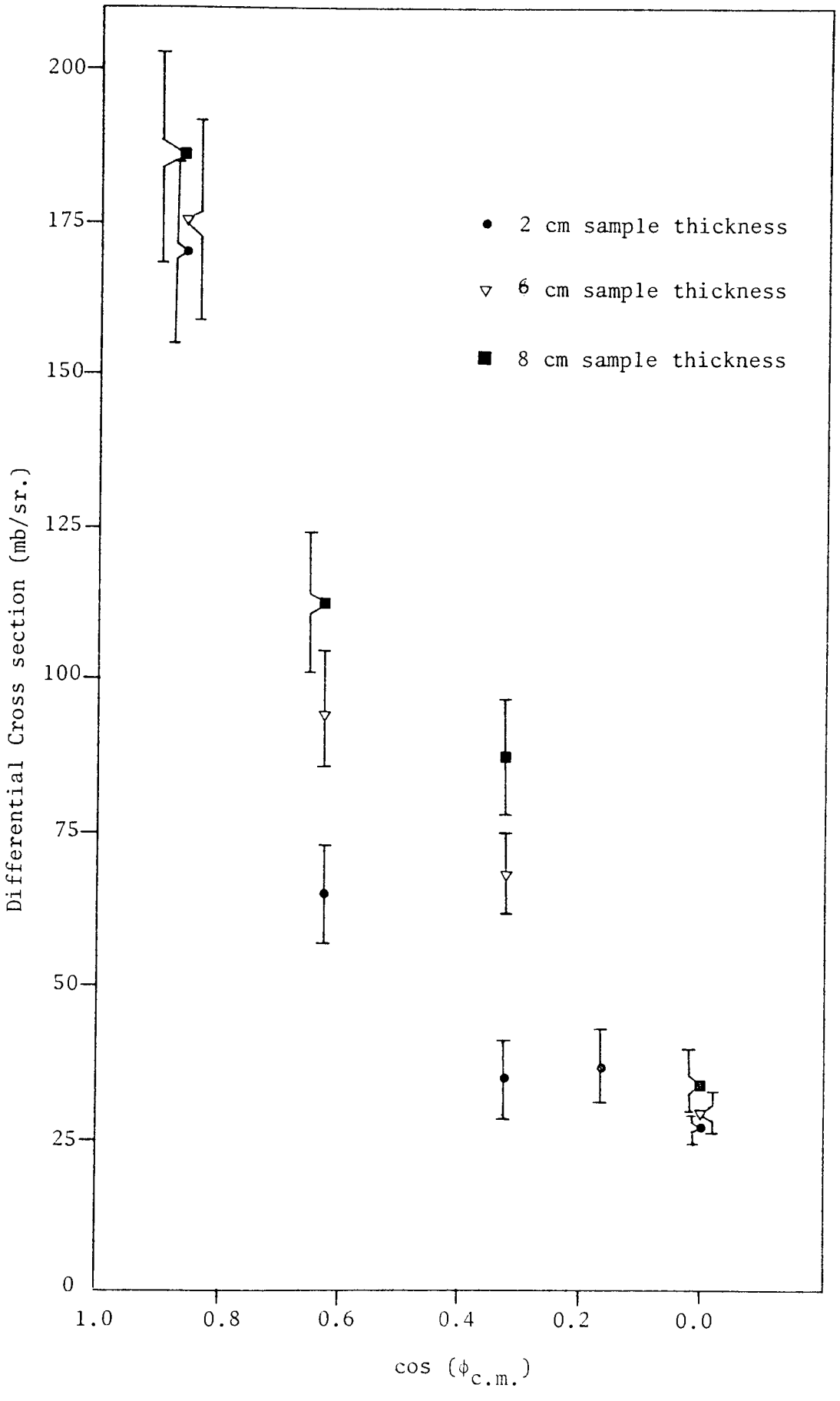

Figure (5.23) The Angular distribution of elastically scattered neutrons from Iron with different thicknesses

5.8.4 Results of the Differential Cross-section for the Thick Iron Samples

The experimental results of the differential elastic scattering cross-section for the four different Iron samples of thickness 2, 4, 6 and 8 cm. are given in table (5.4). It can be seen that, the elastic scattering cross-section for all samples at a specific angle, are almost the same within the statistical errors. From equation (5.20), it is seen that, as the sample thickness increases, the attenutation, and the reaction rate increase. The result of these variation effects the result of the differential elastic scattering cross-section.

The variation of the cross-section with sample thickness was fitted to the following equation:

$$\left(\frac{d\sigma}{d\Omega}\right)_x = \left(\frac{d\sigma}{d\Omega}\right)_o \cdot \exp(\alpha.X) \qquad \ldots\ldots (5.26)$$

where $\left(\frac{d\sigma}{d\Omega}\right)_x$ = the measured differential cross-section

$\left(\frac{d\sigma}{d\Omega}\right)_o$ = the differential cross-section as the sample thickness approaches zero.

α = constant parameter, obtained from the experimental results,

and X = sample thickness in units of mean free path.

Taking logarithm of the equation (5.26), the variation of the differential cross-section via sample thickness was obtained as:

$$\log_e (\text{X-section})_x = \log_e (\text{X-section})_o + \alpha.X \qquad \ldots\ldots (5.27)$$

This is the equation of a straight line, using the least squares method, the constant α for iron results was determined as:

$$\alpha_{Iron} = 0.26 \pm 0.11 \quad \text{/mean free path}$$

Applying equation (5.27) for 14.4 Mev neutrons on Iron results, other constant β was obtained as:

$$\beta_{Iron} = 0.36 \pm 0.13 \quad \text{/mean free path}$$

The variation with thickness of the differential elastic scattering cross-section for 14 and 14.4 Mev neutrons from Iron samples are shown in figures (5.29) and (5.30) respectively.

5.9 CONCRETE DIFFERENTIAL CROSS-SECTION MEASUREMENTS

5.9.1 Elemental Composition of Concrete

Concrete is a mixture of cement, sand, gravel (principally SiO_2) and water. The usual cement is Portlant cement, which consists of a mixture of hydrated calcium silicate and other oxides. The composition of Portland cement is shown in Table (5.9) after Hood et al[122].

Table (5.9)

Composition of Portland Cement [122]

Element	Wt.%	Vol.%
Ca O	63	59.2
$Si\ O_2$	23	29.6
$Al_2\ O_2$	8	6.2
$Fe_2\ O_3$	4	2.4
Mg O	2	2.6

Concrete varies widely according to the mix and raw materials used. Typical mixing proportions and percentages of materials in normal concrete are given in table (5.10) [123, 124].

Table (5.10)

Typical Composition of Ordinary (Portland) Concrete [123, 124]

Material	Vol.%	Wt.%
Portland Cement	12.1	8.2
Sand	24.3	28.7
Gravel	48.6	56.4
Water	15.0	6.7

The density of the present concrete was found to be:

$$\rho = 2.47 \pm 0.06 \text{ g /cm}^3$$

Apart from this it is identical to ordinary concrete type 5 (i.e. 5 - Harwell concrete with density $\rho = 2.5$ g /cm^3).

In order to calculate the differential elastic scattering cross-section, the elemental composition of concrete is needed, concrete contains of different elements. The elemental composition of typical ordinary concrete is shown in table (5.11).

Table (5.12) shows the elemental composition in terms of gram of element/cm^3 of concrete.

Table (5.11)

Elemental Composition of Ordinary Concrete

Element	Wt.% [126]	Atomic % [125]
H	0.85	15.13
O	50.64	55.72
C	-	3.14
S	0.12	-
Na	1.66	1.34
Mg	0.23	1.76
Al	4.44	3.24
Si	30.49	14.87
K	1.87	0.45
Ca	8.03	3.60
Fe	1.19	0.62

Table (5.12)

Elemental Densities of Ordinary Concrete Type

(5-Harwell Concrete) [126]

Element	Concrete composition in (g of element/cm^3 of concrete)
O	1.231
H	0.022
C	0.008
Na	0.029
Mg	0.002
Al	0.131
Si	0.630
S	0.0037
Ca	0.242
K	0.025
Fe	0.045
Ni	0.122
Ti	0.017

The relationship between total macroscopic cross-section and microscopic cross-section is:

$$\Sigma_t = N \sigma_t \qquad \ldots\ldots (5.28)$$

where N = number of nuclei/cc of material

Σ_t = total macroscopic cross-section

and σ_t = total microscopic cross-section

The total macroscopic cross-section of concrete, for transmission of 14.0 Mev neutrons through different thickness was determined experimentally, number of nuclei/cc for normal concrete was obtained from published data [20,125], and was corrected for the present density of concrete. Figure (5.24) shows a plot of the total macroscopic cross-section of ordinary concrete as a function of neutron energy after Jaeger et al[126].

Figure (5.24) Total macroscopic neutron cross-sections for ordinary concrete [126]

5.9.2 Time of Flight Spectra

Using the same experimental procedure and electronics system as discussed in sections (5.7) and (2.5), the time-of-flight spectra from five different thicknesses of concrete samples at 35°, 55°, 75° and 85° with 14 Mev of neutron energy were obtained.

The size of the thin sample of concrete was 23.1 cm x 15.1 cm with 5 cm thickness, while the size of the other four samples were the same length and width, but with thicknesses of 7.6 cm, 12.7 cm, 17.8 cm and 25.4 cm corresponding to 0.687, 1.144, 1.602 and 2.288 mean free paths respectively.

For each measurement, the sample was positioned at 20 cm from the target. The detector to sample distance was again 140 cm.

Typical time spectra are shown in figures (5.25), (5.26) and (5.27) corresponding to the Laboratory angles of 35°, 55° and 85° respectively.

5.9.3 Results of the Differential Elastic Scattering Cross-sections for 14 Mev Neutrons

The differential elastic scattering cross-sections of concrete were calculated using the equation (5.20).

Applying the same procedure discussed in section (5.8.3) for iron, the number of elastically scattered neutrons, i.e. $N(\theta)$ was obtained using the normal error curve programme.

Table (5.13) shows the results of the differential elastic scattering cross-section for concrete samples with corresponding errors. The errors indicated in the above table, were obtained by the error in each term of the equation (5.20), to give the total experimental errors. Table (5.14) shows the experimental errors in each factor of the equation (5.20).

In the published literature, no data were found with which to compare

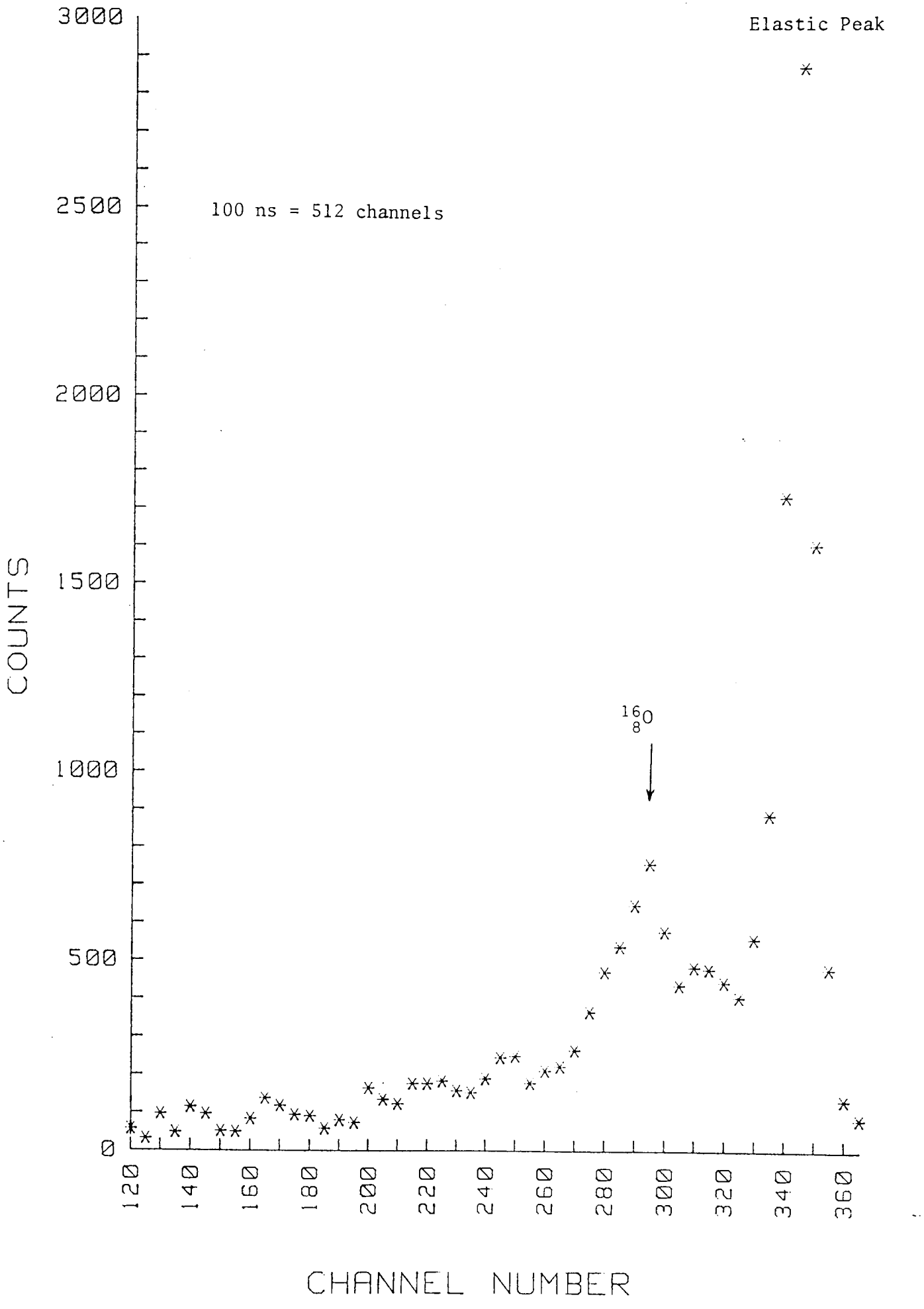

Figure (5.25) Time Spectrum for Scattering in 12.6 cm Thick Concrete at 35°

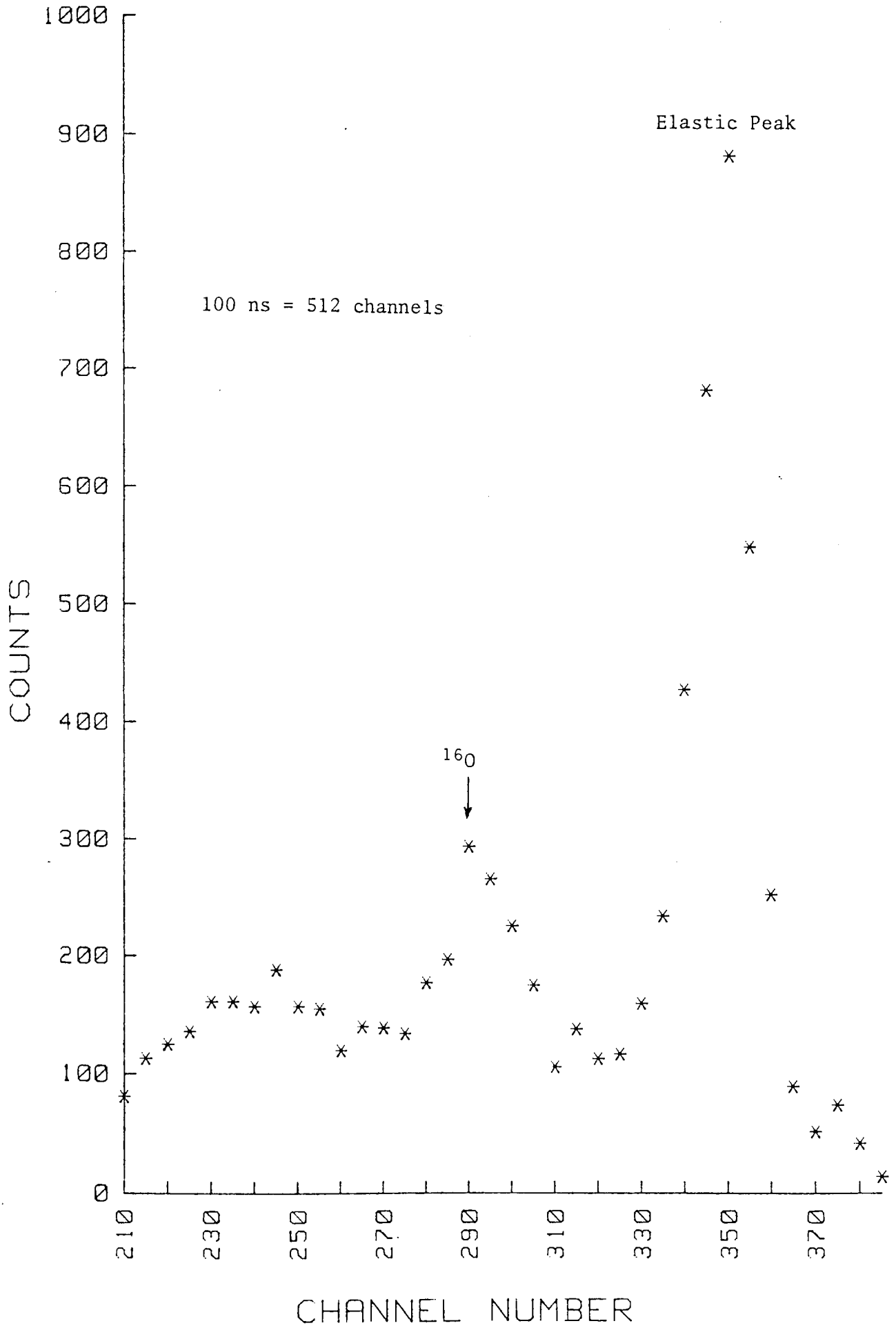

Figure (5.26) Time Spectrum for Scattering in 5 cm Thick Concrete at 55°

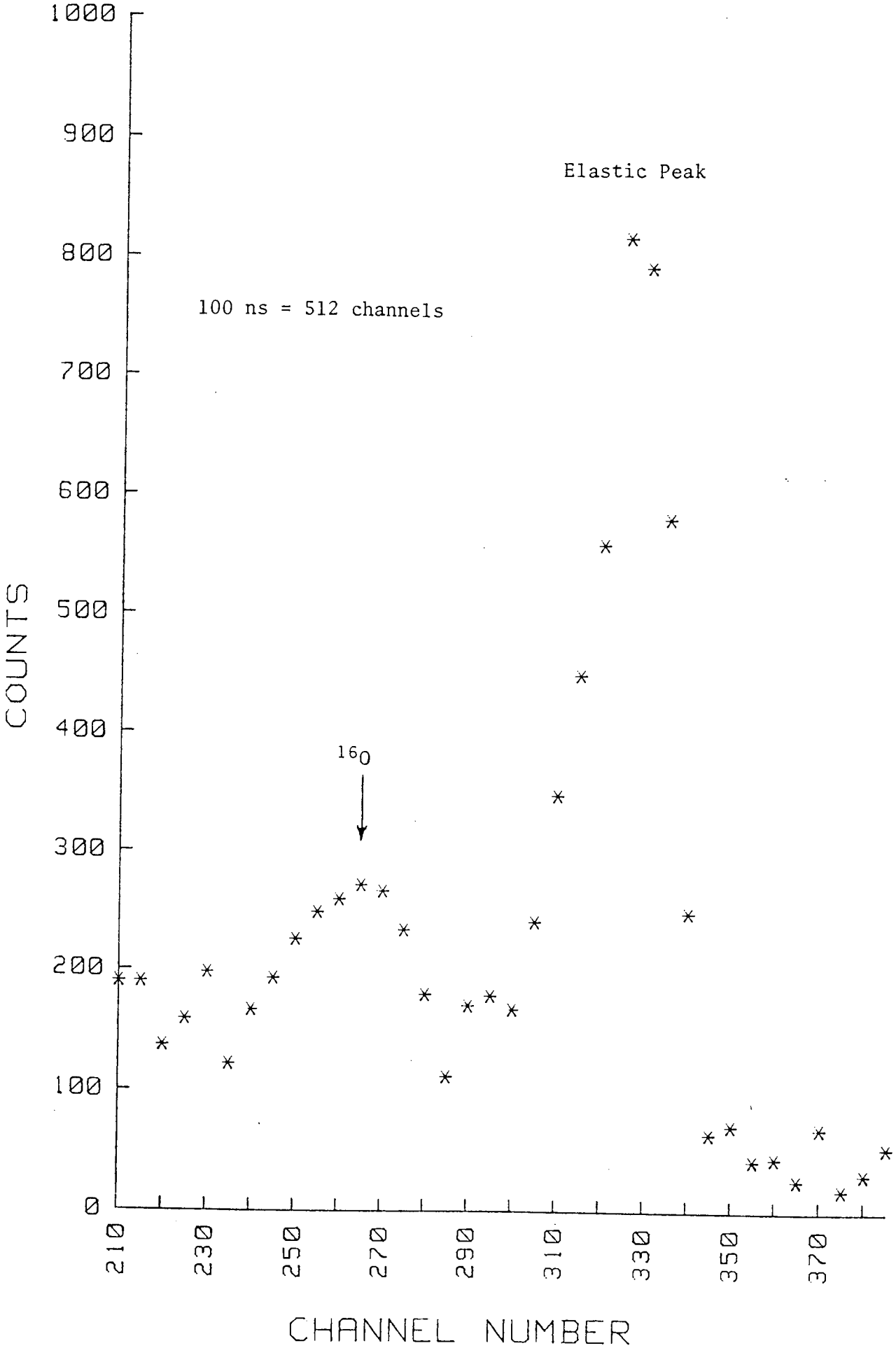

Figure (5.27) Time Spectrum for Scattering in 25.4 cm Thick Concrete at 85°

Table (5.13)

Concrete Differential Cross-section for Elastic

Scattering of 14.0 Mev Neutrons

Scattering angle (θ) degree	Sample thickness (x) cm.	Mean free path (λ)	Geometry factor (G)	$(\frac{d\sigma}{d\Omega})$ with Error (mb/sr.)
35.00	5.00	0.458	1.000	154.6 ± 13.1
35.00	7.62	0.687	1.000	128.9 ± 10.5
35.00	12.70	1.144	1.000	144.7 ± 12.2
35.00	17.78	1.602	1.000	159.9 ± 14.3
35.00	25.40	2.288	1.274	169.9 ± 16.3
55.00	5.00	0.458	1.000	65.9 ± 5.7
55.00	7.62	0.687	1.000	51.2 ± 4.3
55.00	12.70	1.144	1.000	58.4 ± 5.0
55.00	17.78	1.602	1.126	68.2 ± 6.3
55.00	25.40	2.288	1.820	112.2 ± 10.7
75.00	5.00	0.458	1.000	46.9 ± 4.1
75.00	7.62	0.687	1.000	45.9 ± 3.8
75.00	12.70	1.144	1.000	47.9 ± 4.1
75.00	17.78	1.602	1.327	58.7 ± 5.2
75.00	25.40	2.288	2.146	104.1 ± 10.0
80.00	5.00	0.458	1.000	47.6 ± 4.2
85.00	5.00	0.458	1.000	29.3 ± 2.6
85.00	7.62	0.687	1.000	35.1 ± 2.9
85.00	12.70	1.144	1.000	49.4 ± 4.3
85.00	17.78	1.602	1.369	56.8 ± 5.0
85.00	25.40	2.288	2.213	101.3 ± 9.7

the present results. However, using the published cross-sections for the four major constituent elements of concrete, i.e. Oxygen, Hydrogen, Silicon and Aluminium, theoretical differential elastic scattering cross-sections of concrete were calculated, and compared with the experimental results. This is discussed in chapter 6.

The angular distributions of elastically scattered neutrons from concrete samples are shown in figure (5.28).

5.9.4 The Variation of Measured Cross-section with the Sample Thickness in Concrete

The variation of the differential elastic-scattering cross-section of concrete for five different thicknesses which are shown in table (5.13) were analysed as discussed in section (5.8.4) for Iron.

Using equation (5.27) i.e.:

$$\log_e \left(\frac{d\sigma(\theta)}{d\Omega}\right)_x = \log_e \left(\frac{d\sigma(\theta)}{d\Omega}\right)_o + \alpha.X \qquad \ldots\ldots (5.27)$$

and applying least squares method, the constant α for concrete results was determined as:

$$\alpha_{concrete} = 0.38 \pm 0.14 \quad \text{/mean free path}$$

It is explained in section (5.8.4) that, the constant α for 14 and 14.4 Mev neutrons for Iron results were determined as:

for 14 Mev: $\alpha_{Iron} = 0.25 \pm 0.11$ /mean free path

and for 14.4 Mev: $\beta_{Iron} = 0.36 \pm 0.13$ /mean free path

Then by combining all the above three constants, a Universal Constant K was determined as:

$$K_{Univ.} = 0.33 \pm 0.20 \text{ /mean free path}$$

The variation with the thickness of the differential elastic scattering cross-section for 14 and 14.4 Mev neutrons from Iron samples are shown in figure (5.29) and figure (5.30) respectively. In each case, the dashed and solid lines represent a least squares fit according to equation (5.27), using the Universal Constant ($K_{univ.} = 0.33$) and Iron constant respectively.

Figure (5.31) shows the variation of measured cross-section with the sample thickness (in terms of mean free path) for concrete in the angular range studied.

Table (5.14)

Experimental Errors in the Calculation of the Differential Elastic Scattering Cross-sections of the Concrete Samples

Factor	Estimated error %
$F_1 . F_2 . \Sigma\phi$	1
$N(\theta)$	$[\Sigma\ (er)_i^2]^{\frac{1}{2}}$
$\Delta\Omega . G$	2.5
C	2
$\varepsilon(E_n)$	6.5
Attenuation factor	1.4
$\bar{x}$	< 1

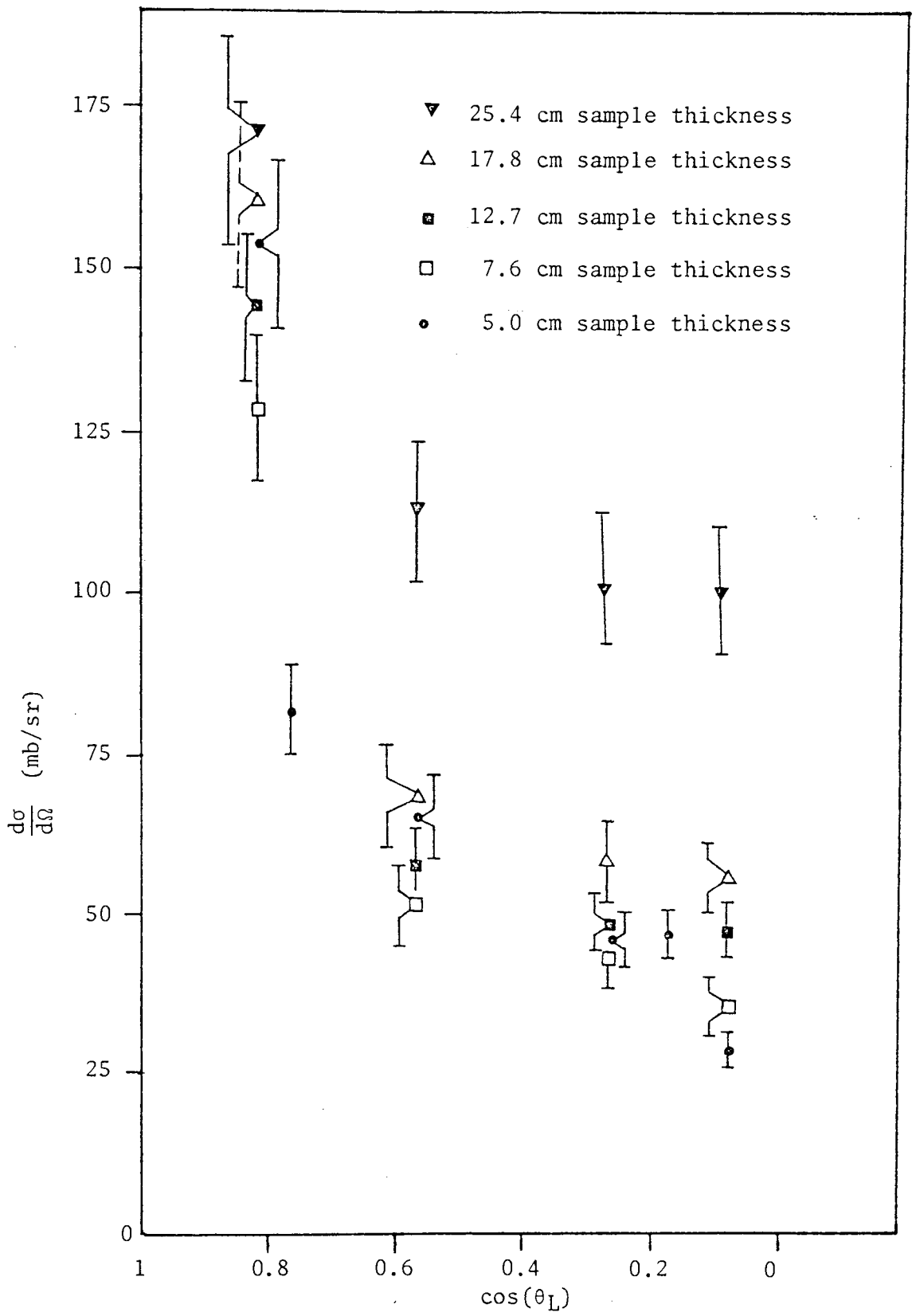

Figure (5.28) Differential Cross-section for Elastic Scattering in Concrete

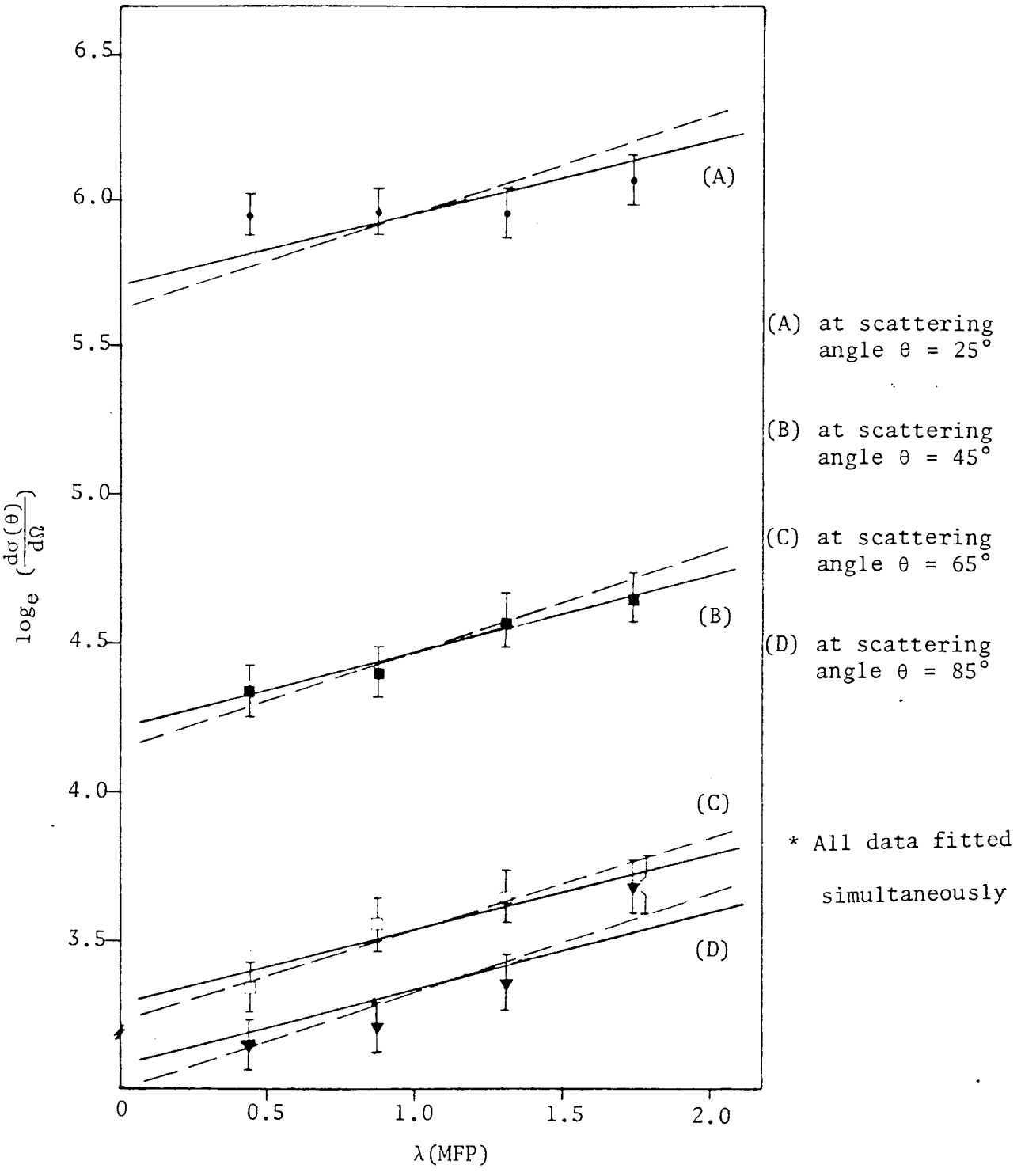

Figure (5.29) The variation of the measured differential elastic scattering cross-section from Iron samples with sample thickness for 14 Mev neutrons. The lines represent least squares fit, using $\alpha_{Iron} = 0.26$ (solid line), and the universal constant $K_{univ.} = 0.33$ (dashed line)

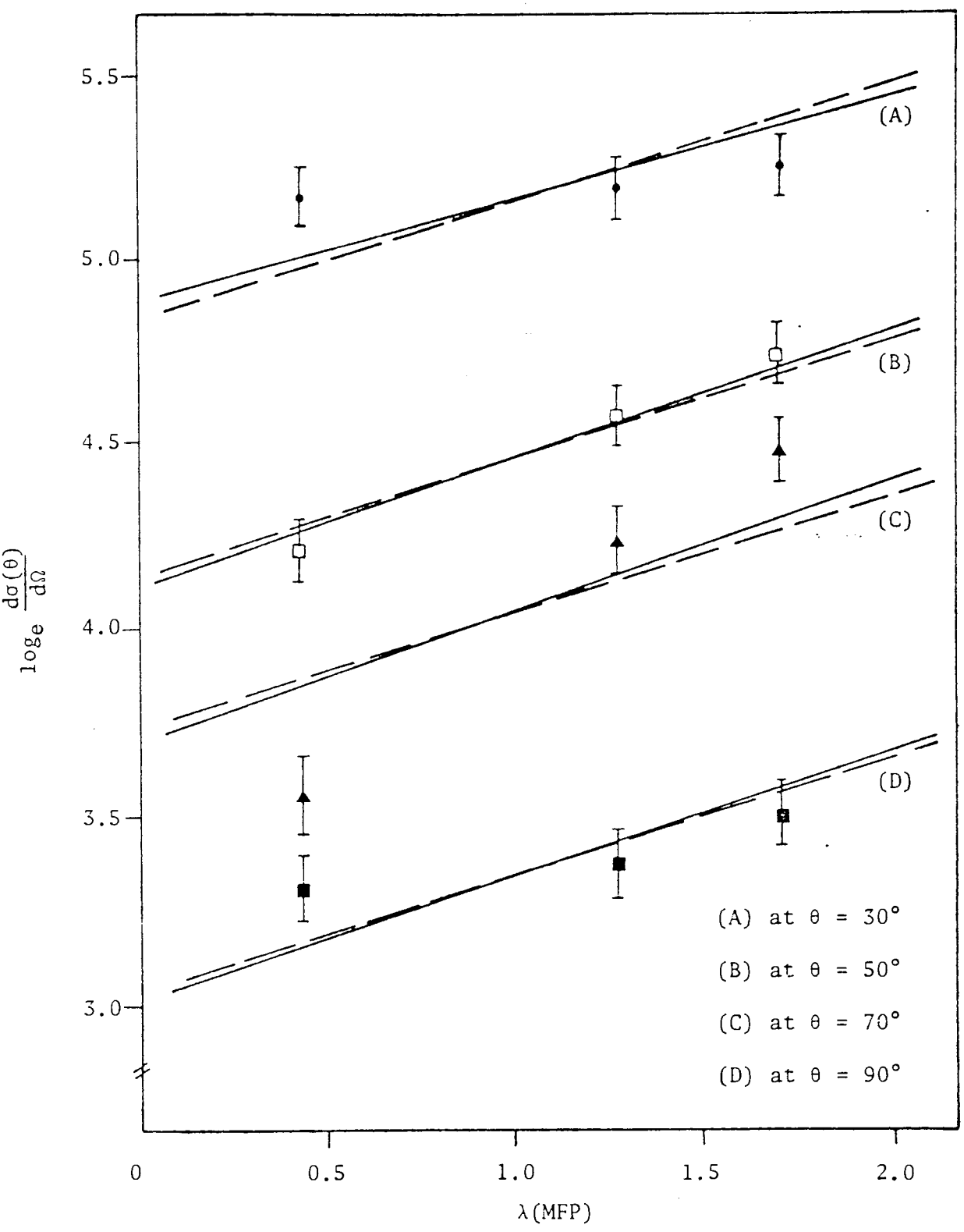

Figure (5.30) The variation of the measured differential elastic scattering cross-section from Iron samples with sample thickness for 14.4 Mev neutrons. The lines represent least squares fit, using $\beta_{Iron} = 0.36$ (solid line) and the universal constant $K_{univ} = 0.33$ (dashed line)

* All data fitted simultaneously

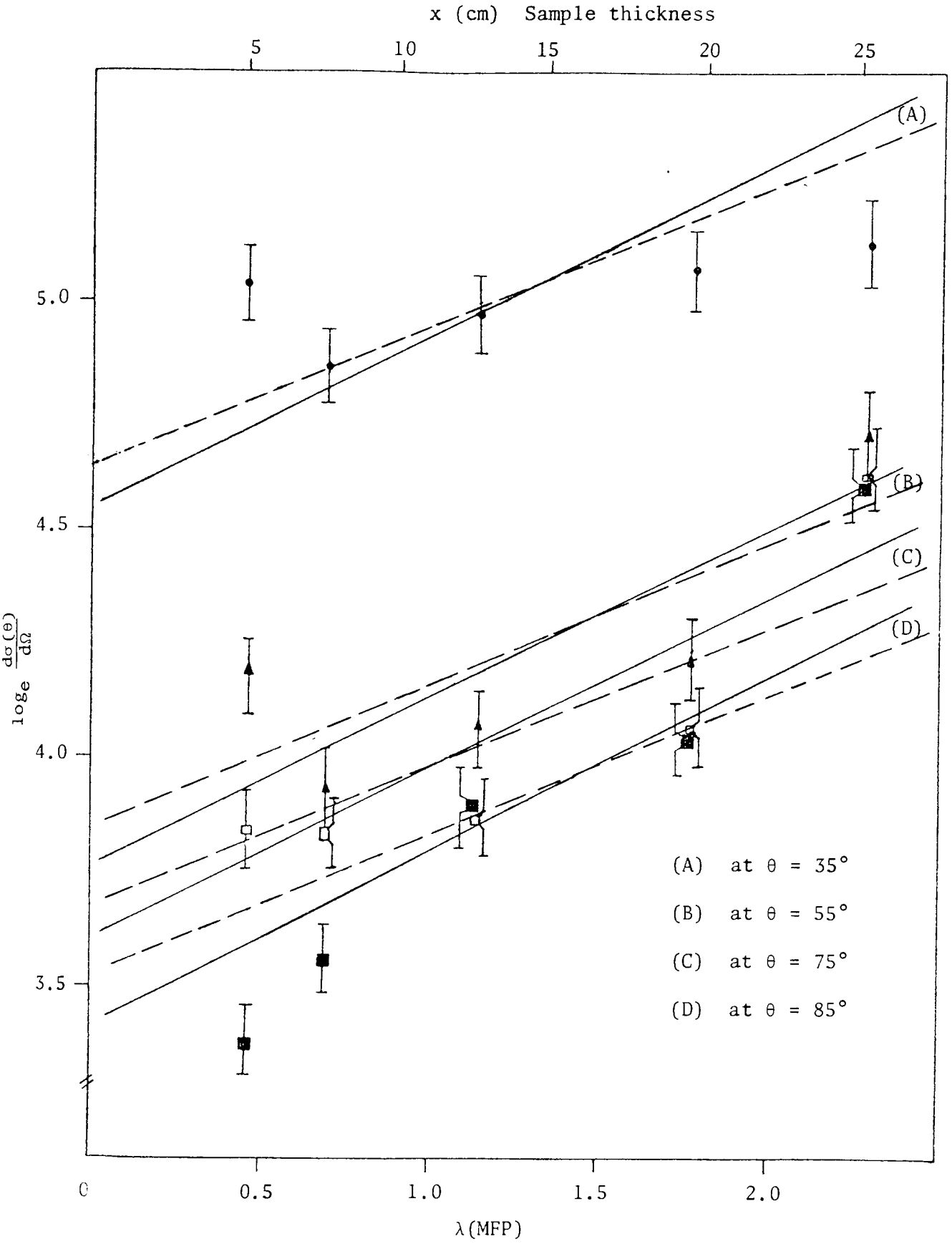

Figure (5.31) The variation of the measured differential cross-section from concrete samples with sample thickness at various angles. The lines represent least squares fit, using $\alpha_{concrete}$ (solid line), and the (K = 0.33) universal constants (dashed line)

* All data fitted simultaneously

CHAPTER SIX

CHAPTER SIX

COMPARISON OF THE RESULTS WITH THEORY

6.1 OPTICAL MODEL ANALYSIS

The elastic scattering of neutrons by medium and heavy nuclei has been analysed successfully using the optical model. The knowledge of the optical potential together with the formation of the optical model, enables both elastic scattering and other reactions to be analysed. In all cases it gives a unique total cross-section. Many features of the nucleus which can thus be deduced from the optical model are in agreement with those derived from other approaches.

The optical model of the nucleus aims at describing in simple phenomenological terms the nuclear interaction of nucleon (proton or neutron) with a nucleus. The scattering is described by a complex valued central potential V(r) for the spin-independent part of the interaction, and a spin-orbit potential for that part of the interaction depending on the spin of the nucleon.

The use of a complex central potential was first proposed by Fernbach et al[7] for the case of nucleons of high incident energy (E > 10 Mev). It was later shown by Feshbach, Porter and Weisskopf[127] that the same type of potential with suitably modified parameters could be used with considerable success at low energies.

When interpreting a given set of experimental data by means of the optical model, it is necessary to fit two total cross-sections. The total cross-section, σ_e, for elastic scattering and the total cross-section, σ_a, for all other processes, and in addition two functions of the scattering angle θ, the angular distribution $d\sigma/d\Omega$ of elastically scattered particles, and the polarization P.

The most extensive analysis of the neutron scattering is due to Perey and Buck[128] who used a non-local potential. They found that the data on neutron scattering from 1 to 25 Mev could be fitted by a non-local potential. An equivalent overall local potential has been obtained by Wilmore and Hodgson[13] with different parameters.

In this model, the potential is a complex form with a real part representing the elastic scattering process and an imaginary term taking all absorbing processes into account. If the incident particle has spin, and the interaction between it and the target nucleus has a spin-dependent component, then its state of polarization may be changed in the interaction. Usually, the incident beam is unpolarized, and the spin-dependent interaction can polarize the scattered particles. Such processes may be brought within the scope of the optical model by assuming a suitable spin-dependent term in the optical potential. An attempt to provide a potential that accounts for all the neutron data from 1 to aroung 200 Mev has been made by Engelbrecht and Fiedeldey[129]. To cover such a range of energies they assumed that it is necessary to allow the imaginary part of the potential to vary continuously from the surface form at low energies to the volume form at high energies.

A comprehensive analysis of a wide range of proton and neutron data for energies less than 50 Mev and nuclei with $A > 40$ has been made by Becchetti and Greenlees[24]. They utilized differential cross-sections, reaction cross-sections, and total cross-sections, and obtained excellent overall fits with a wide range of different assumptions, concerning the dependence of the parameters on A and E. The optical model parameters are discussed in detail in the section (6.3).

The optical model analysis in the present work was performed using the computer search code RAROMP (Regular And Reformulated Optical Model Programme)[130]. The programme was run at the Rutherford High Energy Laboratory, via the link line from the University of Birmingham.

6.2 THE OPTICAL POTENTIAL FORMS

The optical potential $U_{OPT}(r)$, used is a combination of *Woods-Saxon* volume, and surface derivative forms with:

$$U_{OPT}(r) = U_R(r) + iW_I(r) + U_{SO}(r) \quad \ldots\ldots (6.1)$$

where $U_R(r)$ = Real central potential and its form is taken as:

$$U_R(r) = - v_R \, f\,(r, R_R, a_R) \quad \ldots\ldots (6.2)$$

The form factor f(r, R, a) is characterized by a radius parameter R_R, and a surface-diffuseness parameter, a, that is a measure of the distance over which the potential falls from the maximum value to zero. Its form is taken to be that of *Woods-Saxon* type [8], and it can be represented by:

$$f(r, R, a) = [1 + \exp(\frac{r - R_R}{a_R})]^{-1} \quad \ldots\ldots (6.3)$$

In fact the shape-elastic scattering can be obtained with the real part of the optical potential. The second term of the potential, i.e. $i\,W_{Ima.}(r)$, which is Imaginary potential, is responsible for the absorption process contains, surface, W(d) and volume W(v), absorption potential, and is given by the following relation:

$$i\,W_{Ima.}(r) = - W(v)\, f\,(r, R_I', a_I') + W(d).4a_I \frac{d}{dr} f\,(r, R_I, a_I) \quad \ldots\ldots (6.4)$$

where $f\,(r, R, a) = [1 + \exp(\frac{r - R}{a})]^{-1}$ $\quad \ldots\ldots (6.5)$

W(v) = Imaginary volume potential and has the same potential form

as the real central potential. It is responsible for absorption within the nuclear volume.

W(d) = the potential which is responsible for absorption taking place near the nuclear surface, and has a *Woods-Saxon* derivative form.

Finally if the incident particle has a spin, then the interaction between it and the target nucleus has a spin-dependent component. In the case of scattering, the form of the spin-dependent term is allowed to be complex. Physically this corresponds to the possibility of preferential absorption of particles with a particular spin orientation. The spin-orbit potential, $U_{SO}(r)$ is given by the usual *Thomas* form:

$$U_{SO}(r) = -(V_{SO} + i\,W_{SO})\left(\frac{\hbar}{m_\pi c}\right)^2 \frac{1}{r}\frac{d}{dr} f(r, R_S, a_S)\hat{L}\,.\hat{\sigma} \qquad \ldots\ldots (6.6)$$

$$\text{where,}\quad f(r, R_S, a_S) = \left[1 + \exp\left(\frac{r - R_S}{a_S}\right)\right]^{-1} \qquad \ldots\ldots (6.7)$$

and the coefficient $\left(\frac{\hbar}{m_\pi c}\right)^2 \simeq 2$ is the square of half the pion Compton wavelength which is applied to keep the dimensions of spin orbit potential correct. Here $\hbar = \frac{h}{2\pi}$, c is the velocity of the light and m_π is the pion mass. In equation (6.6) $\hat{L}\,.\hat{\sigma}$ is the scalar product of the intrinsic and orbital angular momentum operators. In the case of particles with spin ½, like protons and neutrons, the spin angular momentum can couple to the orbital angular momentum to give two possible values of the total angular momentum as:

$$J = \ell \pm \tfrac{1}{2}$$

Usually the Imaginary part of spin orbital potential, i.e. W_{SO} taken to be zero [131]. This assumption is used in the present analysis.

Greenlees, Pyle and Tange[131] have suggested that, when data for a range of elements at one neutron energy are analysed, it is usual to use

a set of "average" geometry parameters by assuming the radii R_R, R_I, R_I' and R_{SO} vary as $A^{1/3}$. The advantage of such procedures is in the comparison of more data interims of a limited number of parameters and in exhibiting trends in the strength parameters. In the above equations an $A^{1/3}$ variation was initially assumed for all the radii, i.e.

$$\begin{aligned} R_R &= r_R A^{1/3} \\ R_{SO} &= r_{SO} A^{1/3} \\ R_I' &= r_I' A^{1/3} \\ R_I &= r_I A^{1/3} \end{aligned} \qquad \ldots\ldots (6.8)$$

The strength and geometry of the optical potential is thus determined by the parameters V_R, r_R, a_R, V_{SO}, r_{SO}, a_{SO}, W_v, r_I', a_I' and W_d, r_I, a_I.

6.3 OPTICAL MODEL PARAMETERS

Accurate neutron scattering measurements provide data for a detailed study of the properties of the nuclear optical model. The usual method of analysis is to assume a suitable potential and a set of parameters, calculate the cross-section numerically and then iterate the calculation. Systematic variation of the parameters constitutes a search of the best values.

In the present analysis, the optical model parameters of Becchetti and Greenlees [24] were used as initial values to predict theoretical differential cross-section values for concrete and Iron.

The parameters of Becchetti and Greenlees [24] were as follows:

$$(V_R) \quad : \quad V_R = 56.3 - 0.32\,E - 24.0\,\left(\frac{N - Z}{A}\right) \qquad \ldots\ldots (6.9)$$

$$(R_R) \quad : \quad r_R = 1.17 \qquad \ldots\ldots (6.10)$$

(A_R) : $a_R = 0.75$ ..... (6.11)

$(W_{(V)})$: $W_V = 0.22\ E - 1.56$, or zero whichever is greater ..... (6.12)

(R_V) : $r_V = 1.26$ ..... (6.13)

(A_V) : $a_V = 0.58$ ..... (6.14)

(W_S) : $W_d = 13.0 - 0.25\ E - 12(\frac{N - Z}{A})$ or zero, whichever is greater ..... (6.15)

(R_D) : $r_d = 1.26$ ..... (6.16)

(A_D) : $a_d = 0.58$ ..... (6.17)

(V_S) : $v_s = 6.20$ ..... (6.18)

(R_S) : $r_s = 1.01$ ..... (6.19)

(A_S) : $a_s = 0.75$ ..... (6.20)

When all the potential strengths are in Mev, and the geometrical parameters are in femtometers (fm.) and E is the incident neutron energy in Laboratory system in Mev. Using the above equations and the optical potential defined by equation (6.1) it is possible by adjustment of the parameters, to obtain a good fit over all elastic scattering data.

The presence of a fairly strong absorptive component in the optical potential has the consequence that the elastic scattering is sensitive mainly to the potentials in the surface region. Greenlees et al[24] have shown that below 20 Mev incident energy the data can be satisfactorily represented using only pure surface form for the Imaginary potential.

Perry[132] in analysing proton data at energies between 9 and 22 Mev, used $W_V = 0$ and obtained reasonable agreement with the differential cross-section data. Rosen et al[133] analysed data in the energy range 7-22 Mev,

with similar parameter restrictions, and obtained reasonable agreement. At higher energy data, the parameters restrictions imposed by Perry[132], and by Rosen et al[133] have been removed.

More restriction of the parameters can be considered. As the calculated cross-section at forward angles, does not change with the spin orbit potential V_{SO}, as the values of the spin orbit terms can be taken as constant. However, Perry[132] has found that, it modifies the cross-section at backward angles.

In the present work, this value (i.e. V_{SO}) was kept constant. However, the effect of the volume term in combination with surface term of the imaginery potential was examined.

6.4 FITTING PROCEDURE

It is always necessary to compare the calculated angular distributions with experimental data. It is convenient to incorporate facilities for doing this into the computer programme to find the quantity of χ^2. In fact the aim of the fitting procedures is, to obtain good numerical values for the parameters of the optical model which gives the best fit of the prediction to the experimental data.

χ^2 is defined as:

$$\chi^2/\text{point} = N^{-1}\sum_{1}^{N}\left[\frac{\sigma_T(\phi_i) - \sigma_{Ex}(\phi_i)}{\Delta\sigma_{Ex}(\phi_i)}\right] \quad \ldots\ldots (6.21)$$

where, $\sigma_{Ex}(\phi_i)$ = the measured experimental differential cross-section in the centre-of-mass system

$\Delta\sigma_{Ex}(\phi_i)$ = the error corresponding to the measured differential cross-section,

and $\sigma_T(\phi_i)$ = the theoretical predicted cross-section.

Obviously the lower values of χ^2 give the better fit. If the experimental cross-sections are determined with detectors of large angular acceptance, then it is better to introduce experimental averaging into the measured quantities. In such a situation, the theoretical quantities should be averaged over the experimental angular acceptance before making the χ^2 comparison. In the present work due to the finite angular-resolution of the neutron detector, the theoretical quantities were averaged using equation (6.22) over the experimental angular resolution.

$$\bar{\sigma}(\phi) = \int_{-\Delta\phi}^{\Delta\phi} \sigma(\phi)d\phi \qquad \ldots\ldots (6.22)$$

where $\pm \Delta\phi$ is the experimental angular resolution.

6.5 OPTICAL MODEL ANALYSIS OF THE $^{56}_{26}Fe$ CROSS-SECTIONS

A: E_n = 14 Mev

An initial comparison was made between the experimental data and the theoretical prediction of the optical model using the parameters of Becchetti and Greenlees[24], are shown in equations (6.9) to (6.20). The values of the potentials at 14 Mev neutron energy were found to be:

$$\begin{aligned} V_R &= 50.1011 \text{ Mev}, \\ W_D &= 8.6406 \text{ Mev}, \quad \text{and} \\ W_V &= 1.52 \text{ Mev} \end{aligned} \qquad \ldots\ldots (6.23)$$

Using the above potentials, and other geometry parameters a fit was obtained which is shown in figure (6.1). The agreement of the experimental data with theoretical values was no more thus adequate. It was found that, to obtain good agreement, the parameters of Becchetti et al needed to be

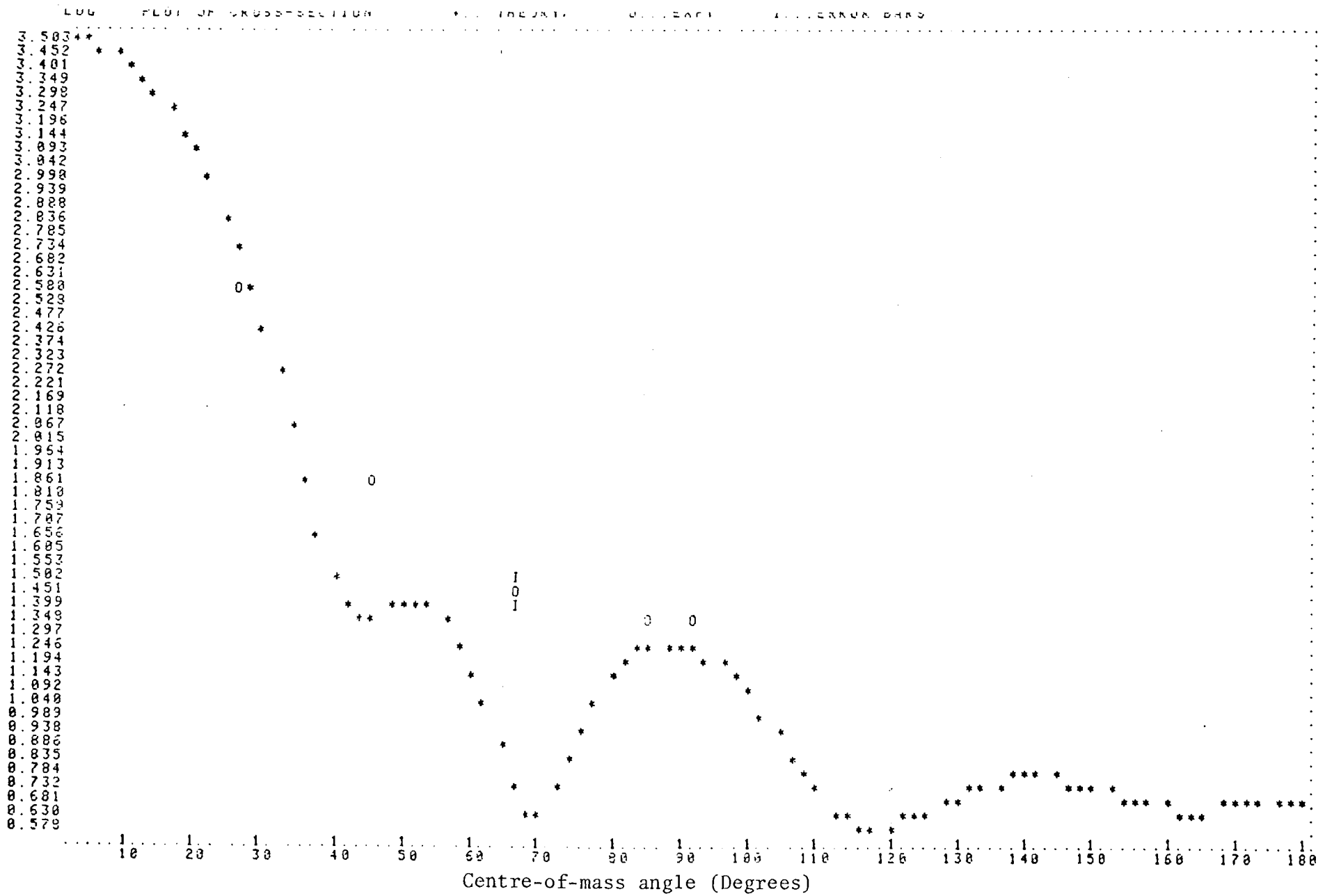

Figure (6.1) with Becchetti and Greenlees parameters[24]

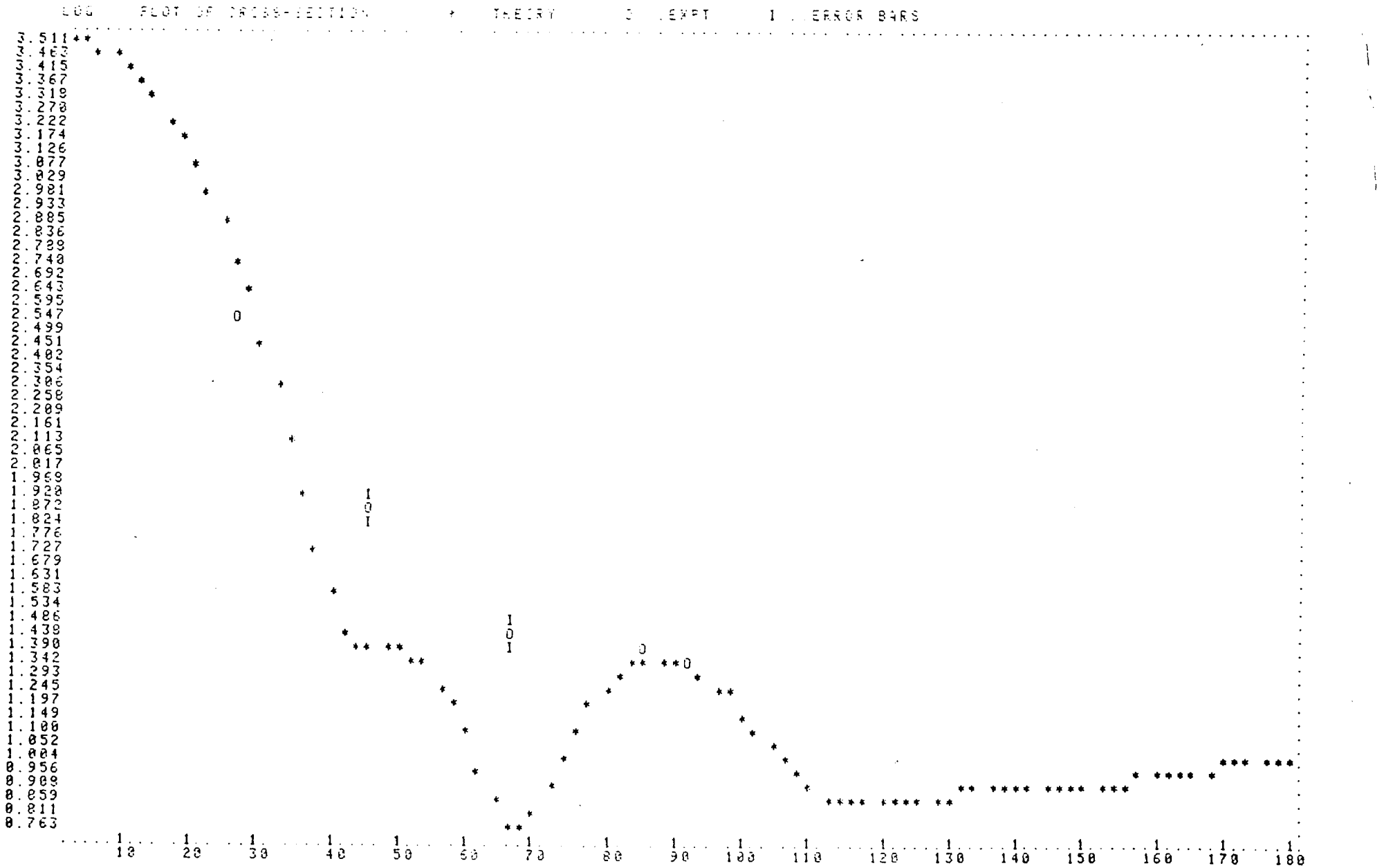

Figure (6.2) W_D, W_V, R_D, (6)

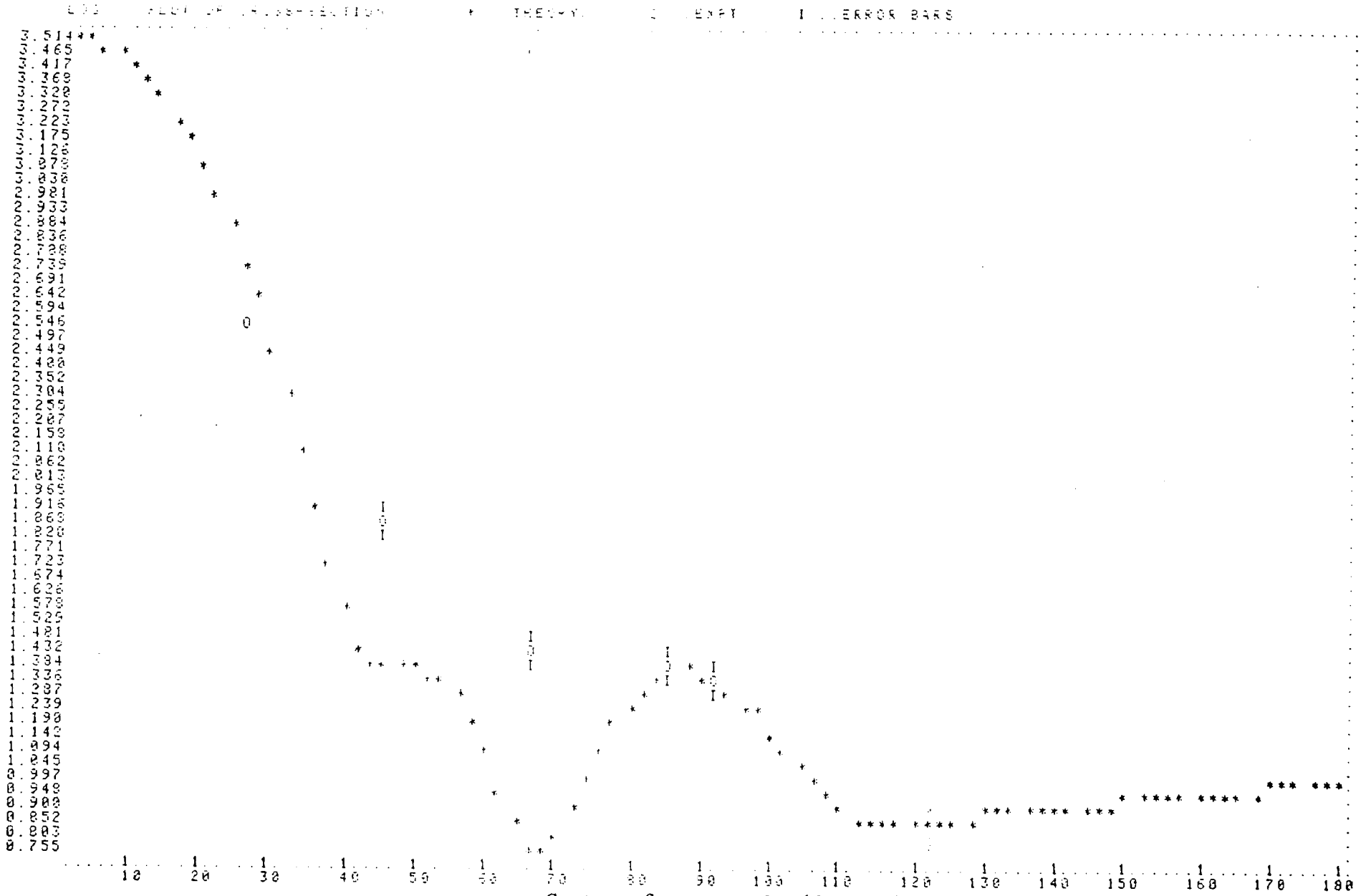

Figure (6·3) W_D, A_D, R_V, A_V, (6)

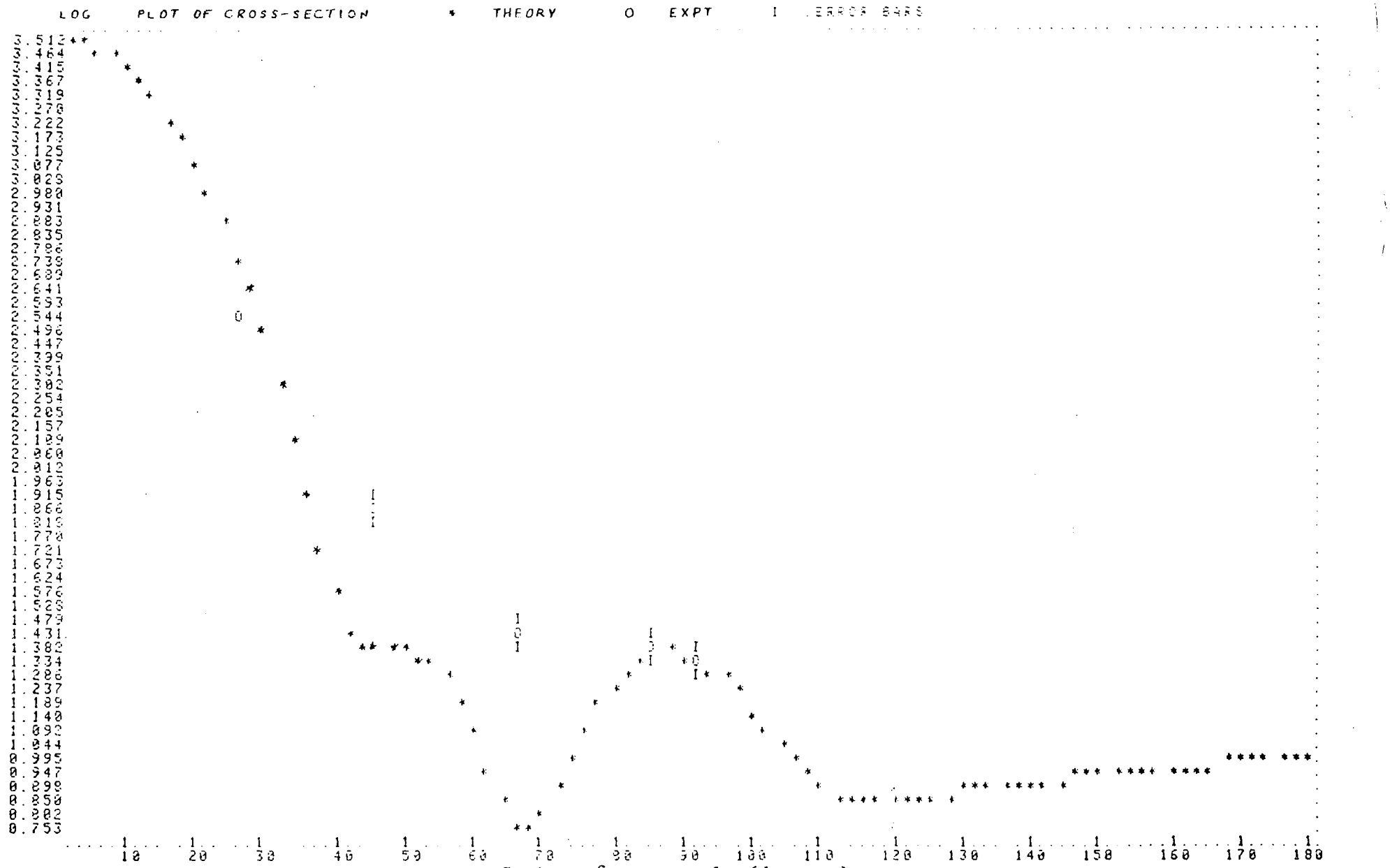

Figure (6.4) W_D, A_D, R_D, W_V, A_V, R_V (6)

changed. Initially it was attempted to find the optimum values of the volume and surface potential by searching W_D, W_V, (6) and the other parameters were kept constant. The χ^2 per point was high, and the agreement was not good . Using the optimum values of W_V and W_D from the previous search, three searches: W_D, W_V, R_D, (6) - W_D, A_D, R_V, A_V, (6) and W_D, A_D, R_D, W_V, A_V, R_V, (6) were executed. The real potential and its geometry parameters were kept constant. The fits obtained are shown in figures (6.2), (6.3) and (6.4) respectively.

Finally the real potential was optimised using the values of W_D and W_V from the previous search as:

$$W_D = 8.3520 \text{ Mev, and } W_V = 0.3517 \text{ Mev} \quad \ldots\ldots (6.24)$$

a search of V_R, W_D, R_D, (6) was executed, the results after 5 iterations was good, and χ^2 per point was 0.35. The fit obtained is shown in figure (6.5).

The next stage of the analysis, was to investigate the effect of all potentials. Using the Becchetti et al[24] parameters, a search of V_R, W_D, W_V, (6) was executed. The optimum values of the potentials were found to be:

$$\begin{aligned} V_R &= 49.0749 \text{ Mev}, \\ W_D &= 9.7959 \text{ Mev}, \\ W_V &= 0.5043 \text{ Mev} \end{aligned} \quad \ldots\ldots (6.25)$$

Finally using the above values, six iterations were made to search: V_R, W_D, R_D, (6). The other geometry parameters were kept constant. The agreement obtained was good, and χ^2 per point was 0.34. The theoretical prediction for the angular distribution to the experimental data is shown in figure (6.6). Some authors [132,133,137,14] suggested that, for neutron energies less than 20 Mev, it is not necessary to include a volume poten-

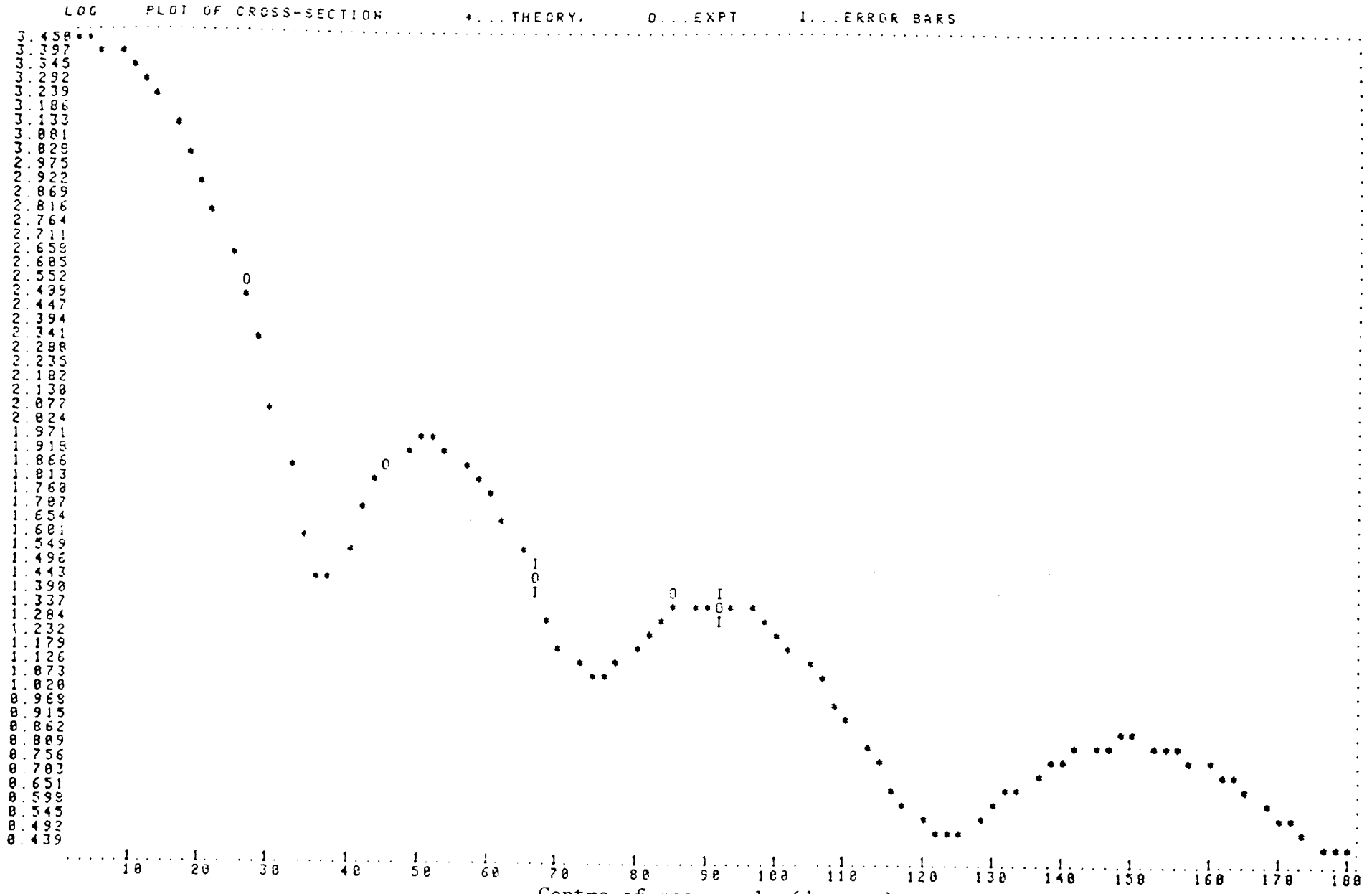

W_V = 0.3517 Mev; W_D = 7.5362 Mev; V_R = 40.5752 Mev; R_D = 1.3619

Figure (6.5) V_R, W_D, R_D, (6)

V_R = 40.5034 Mev; W_D = 7.3667 Mev; R_D = 1.3666

Figure (6.6) V_R, W_D, R_D, (6)

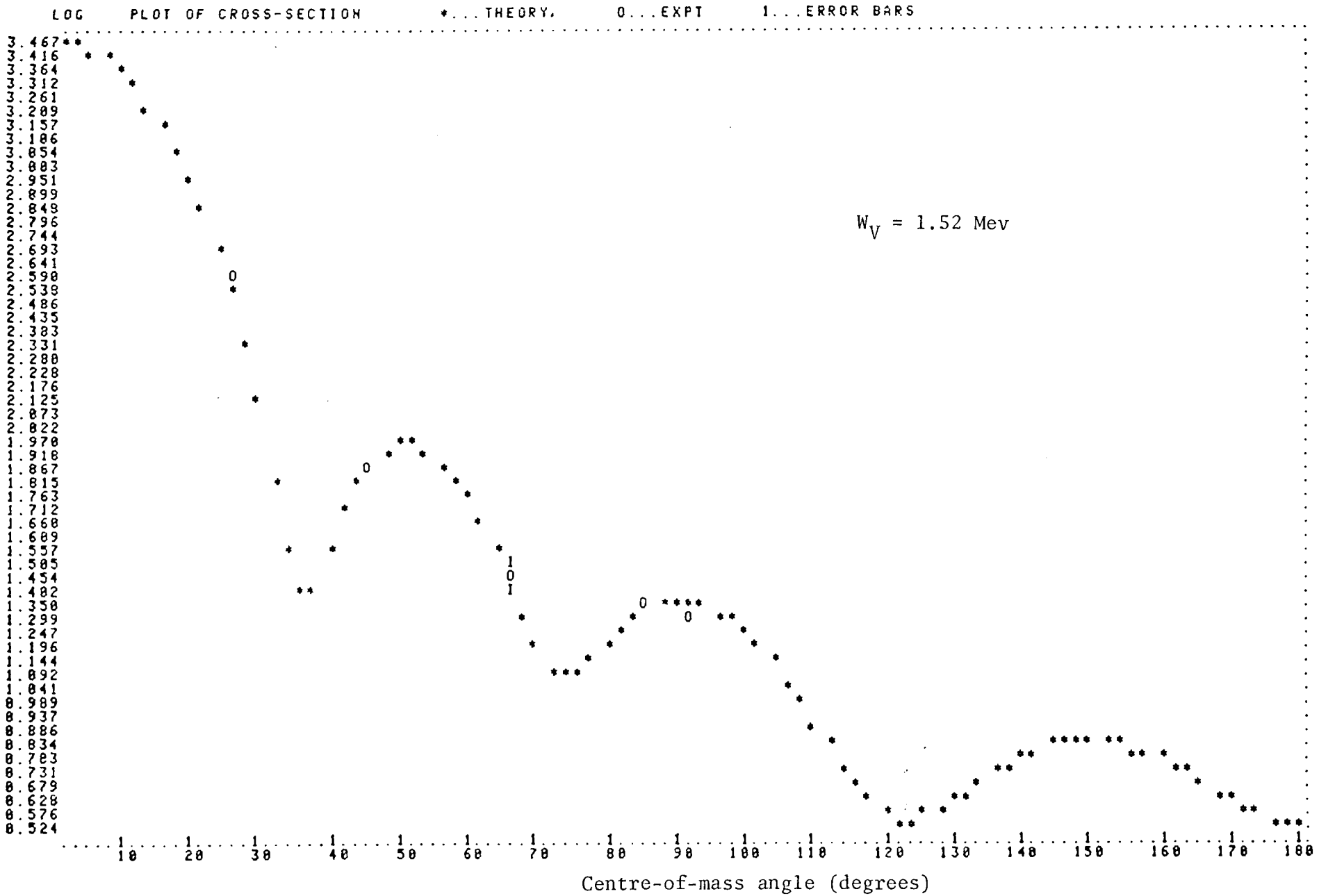

Figure (6.7) V_R, W_D, R_D, (6)

tial term. However in this work the effect varying it was studied. Again the search V_R, W_D, R_D, (6) was executed, the fit was a further improvement and χ^2 per point was found as 0.29.

The fit obtained is shown in figure (6.7).

Table (6.1)

Optical Model Parameters Used to Fit Iron Elastic Scattering Cross-section for 14 Mev Neutrons

Parameter	Present Work Data
V_R (Mev)	40.0320
R_R (fm.)	1.17
A_R (fm.)	0.75
W_D (Mev)	6.2407
R_D (fm.)	1.4017
A_D (fm.)	0.58
W_V (Mev)	1.52
R_V (fm.)	1.26
A_V (fm.)	0.58
V_{SO}(Mev)	6.20
R_S (fm.)	1.01
A_S (fm.)	0.75
χ^2/point	< 0.3

The optimum optical model parameters obtained to fit the iron differential elastic scattering cross-section for 14 Mev neutron energy, are given in

table (6.1)

B: E_n = 14.4 Mev

The procedure for the analysis of the iron differential cross-section for 14.4 Mev neutron energy was the same as that for 14.0 Mev. The values of the three potentials using the Becchetti and Greenlees[24] parameters were:

$$\begin{aligned} V_R &= 49.9763 \text{ Mev} \\ W_V &= 1.6060 \text{ Mev} \\ W_D &= 8.5430 \text{ Mev} \end{aligned} \qquad \ldots\ldots (6.26)$$

An initial comparison was made between the experimental data and the theoretical predictions of the optical model. The agreement was again poor. At the values as with 14 Mev all the goemetrical parameters were kept constant, given by Becchetti et al[24] subsequently the three potentials were optimized by searching: V_R, W_D, W_V, (6). The optimum values were found to be:

$$\begin{aligned} V_R &= 49.4626 \text{ Mev} \\ W_D &= 9.0907 \text{ Mev} \\ W_V &= 0.7587 \text{ Mev} \end{aligned} \qquad \ldots\ldots (6.27)$$

The fit obtained is shown in figure (6.8). The χ^2 per point was high.

At the next stage, the optimum values of the potentials were used from the equation (6.27) and the following searches were executed:

V_R, W_D, R_D, (6) - V_R, A_R, W_D, A_D, (6) and V_R, A_R, W_D, R_D, A_D, (8).

The χ^2/point for the above searches was 0.76, 0.72 and 0.1 respectively.

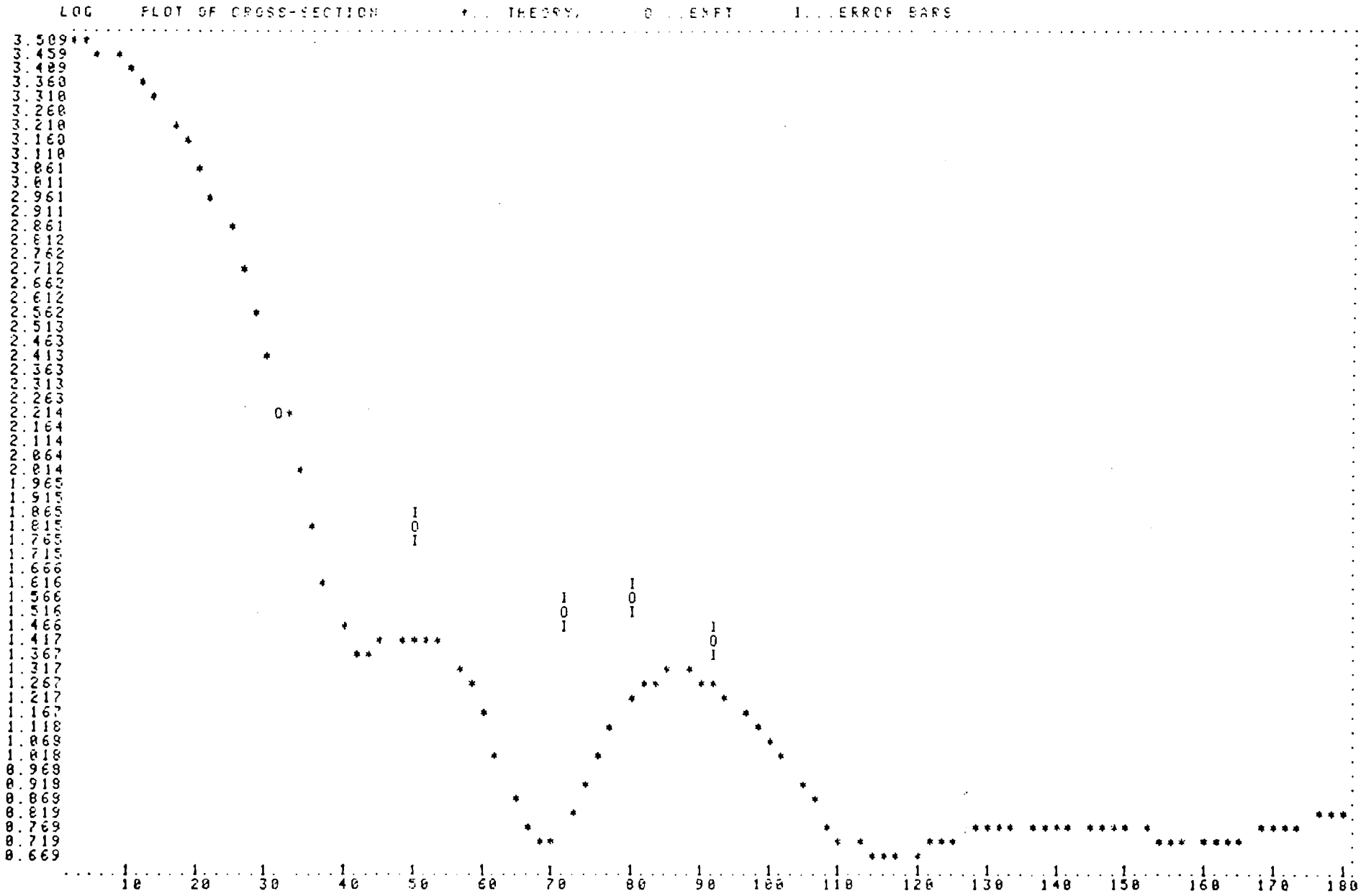

Figure (6·8) V_R, W_D, W_V, (6)

The agreement of the experimental data and theoretically predicted cross-section was good. The fits obtained are shown in figures (6.9), (6.10) and (6.11) respectively.

Table (6.2) shows the optimum optical model parameters used to fit the iron differential elastic scattering cross-section for 14.4 Mev neutron energy.

Table (6.2)

Optical Model Parameters Used to Fit Iron Elastic Scattering Cross-section for 14.4 Mev Neutrons

Parameter	Data
V_R (Mev)	49.6274
R_R (fm.)	1.17
A_R (fm.)	0.3637
W_D (Mev)	2.6245
R_D (fm.)	1.9211
A_D (fm.)	0.5852
W_V (Mev)	0.7580
R_V (fm.)	1.2600
A_V (fm.)	0.5800
V_S (Mev)	6.2000
R_S (fm.)	1.0100
A_S (fm.)	0.7500
χ^2/point	0.1

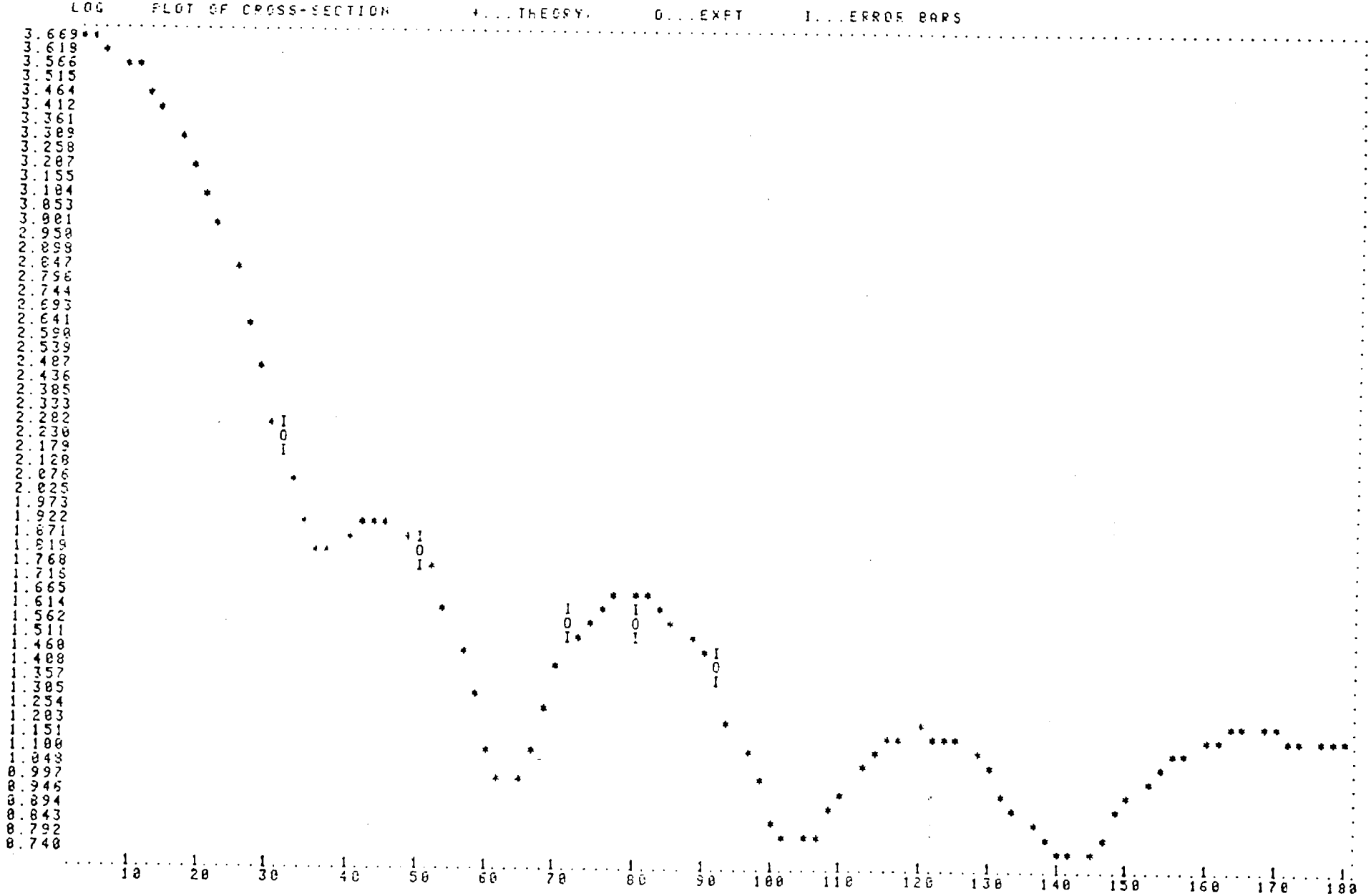

Centre-of-mass angle (degrees)

Figure (6·9) V_R, W_D, R_D, (6)

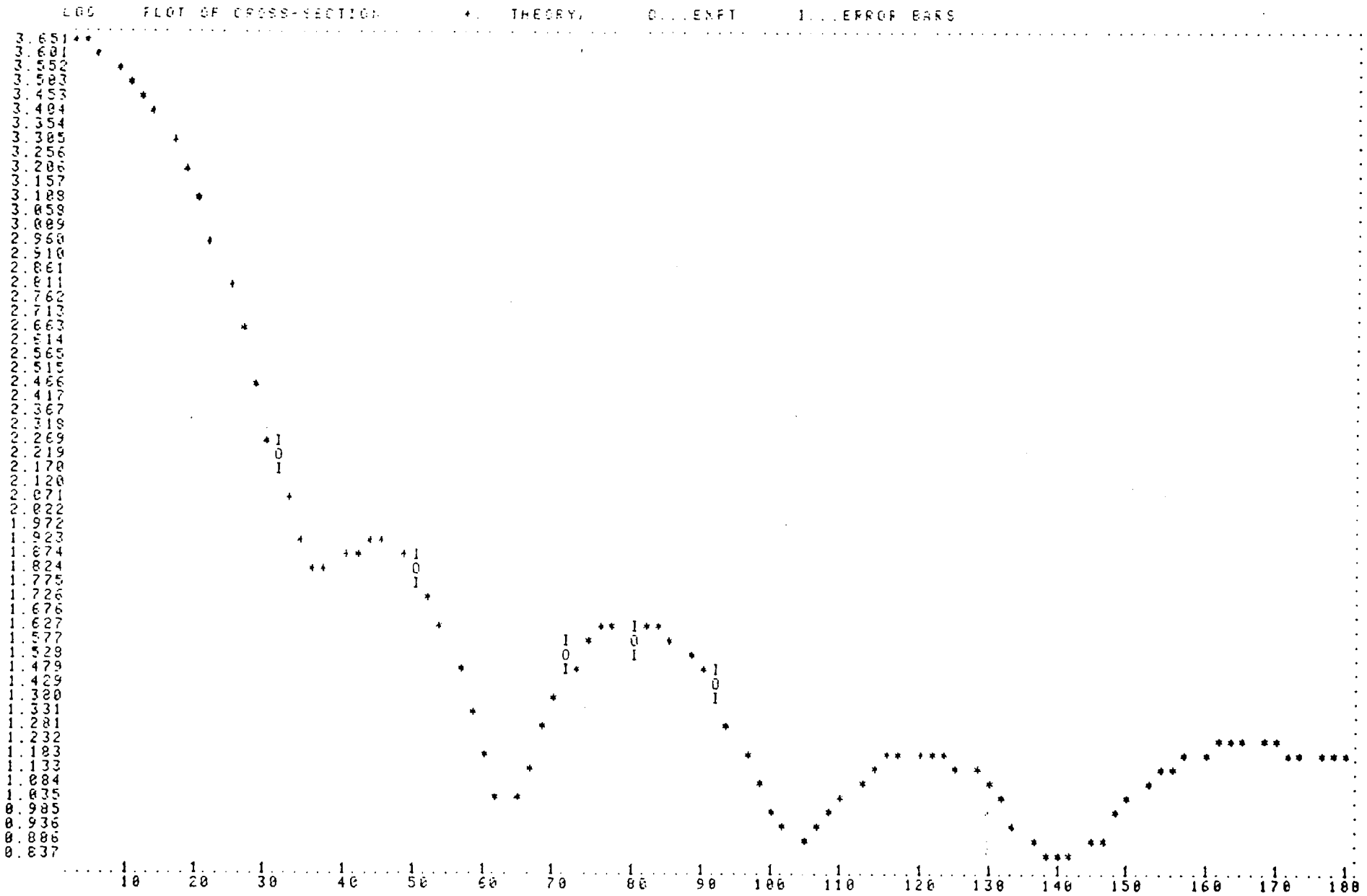

Centre-of-mass angle (degrees)

Figure (6.10) V_R, A_R, W_D, A_D, (6)

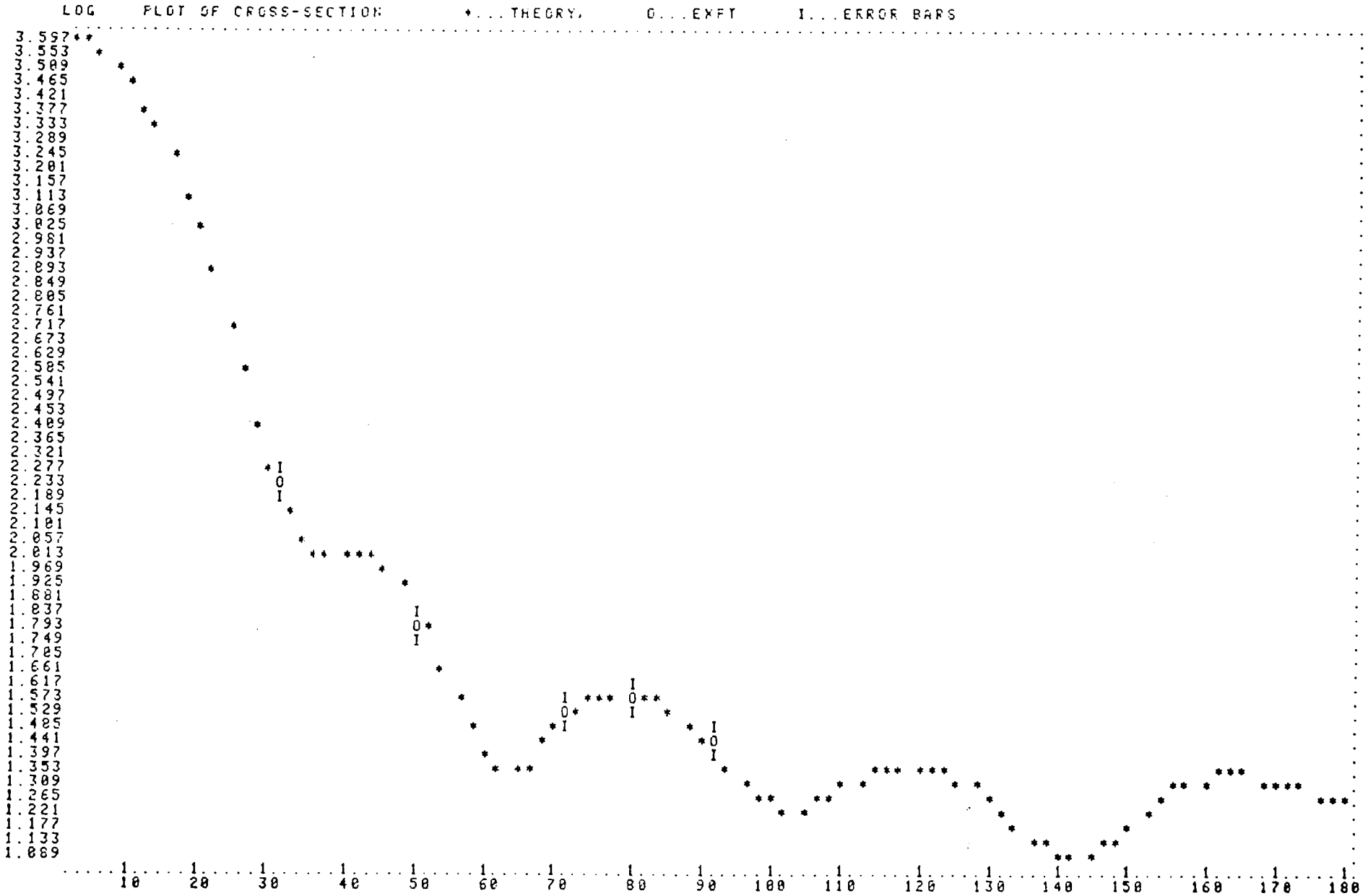

Figure (6·11) V_R, A_R, W_D, R_D, A_D, (6)

6.6 CALCULATION OF THE NUMBER OF NEUTRONS SCATTERED FROM THE IRON SAMPLES BASED ON THE CONTINUOUS SLOWING DOWN MODEL

The experimental results for the thin sample of iron were compared with the predictions of the optical model. In the case of thick samples, however a semi-analytical model based on the continuous slowing down model was adopted. Calculation of the actual neutron energy distribution is complex, but using the *"Fermi Age Theory"* the neutron energy distribution can be found. In this model it is assumed that the moderator consists of a single nucleide, is infinite in extent, and is non-absorbing. It is also assumed that:

(1) The neutron slows down continuously not in discrete steps as in reality and ξ the *"logarithmic energy decrement"* is small.

(2) Scattering is isotropic in the centre-of-mass system.

(3) The diffusion theory is valid at all energies.

(4) Fast neutrons are produced uniformly throughout the medium, and the properties of the medium are uniform.

This model is not expected to be valid for light or heavy water as a moderator, since the above assumptions are violated.

To determine the slowing down density, it is necessary to write the Fermi Age equation as: [3,134].

$$- \frac{D(E)}{\xi(E)\ \Sigma_s(E)\ E}\ \nabla^2 q\ (r,\ E) = \frac{\partial\ q(r,\ E)}{\partial E} \qquad \ldots\ldots\ (6.28)$$

where $\xi(E)$ = the logarithmic energy decrement per collision,

$q(r, E)$ = the slowing down density with energy E at the point r.

$\Sigma_s\ (E)$ = the macrocopic scattering cross-section at energy E

and $D(E)$ = diffusion coefficient.

Equation (6.28) can be written in a simple form by introducing a new variable $\tau(E)$ defined by the integral:

$$\tau(E) = \int_{E_o}^{E} \frac{D(E)}{\xi(E)\Sigma_s(E)\ E}\, dE \qquad \ldots\ldots (6.29)$$

where E_o is the energy of the source neutrons. Upon making the transformation, whereby the variable E is replaced by τ, equation (6.28) reduces to:

$$\nabla^2 q(r, \tau) = \frac{\partial\ q(r,\tau)}{\partial \tau} \qquad \text{for } r \neq 0 \qquad \ldots\ldots (6.30)$$

This equation is known as the "*Fermi-Age Equation*", and $\tau(E)$ is called the "*Fermi-Age*", which has dimensions of (length)^2. During the slowing down process, τ increases as a function of the time, during which the neutron moves a distance dx from the position of its production.

Equation (6.30) represents the spatial distribution of the slowing down density in a non-absorbing medium.

Normally the Fermi-Age equation is solved by applying the following boundary conditions:

(1) Since $\tau = 0$ corresponds to the source energy, then $q(r, 0)$ will be equal to the neutron source at any location r.

(2) At the extrapolated boundary of the system, the slowing down density should be zero, i.e. $q(\chi, \tau) = 0$ for any value of τ.

Applying these boundary conditions, and separating the variables:

$$q(r, \tau) = F(r) \,.\, T(\tau) \qquad \ldots\ldots (6.31)$$

and supposing that the source is located in (Z - Y) plane, the general solution of the equation (6.30) will be:

$$q(x, \tau) \propto F(x) \cdot \exp(-B^2 \tau(E)) \quad \ldots\ldots (6.32)$$

where B is a constant value.

The slowing down density for a plane source infinite in extent in the y and z directions, and placed at x = 0 emitting s neutrons per unit area per second is:

$$q(x, \tau) = \frac{s}{(4\pi\tau)^{\frac{1}{2}}} \cdot \exp(-x^2/4\tau) \quad \ldots\ldots (6.33)$$

Geraseva and Vavilov [135] using equation (6.34) have calculated the Fermi-Age (τ) for Iron between 2 Mev and 1.46 eV as: $\tau = 743$ cm^2.

$$\tau = \frac{1}{6} \cdot \frac{\int_0^\infty Ar^4 \, dr}{\int_0^\infty Ar^2 \, dr} \quad \ldots\ldots (6.34)$$

Applying equation (6.29) and assuming, D(E), $\xi(E)$ and $\Sigma_s(E)$ are constants, equation (6.35) is obtained as:

$$\tau = K \ln\left(\frac{E_o}{E}\right) \quad \ldots\ldots (6.35)$$

However, although the elastic scattering cross-section of Iron from 0.5 Mev to 6 Mev is approximately constant, thereafter, the cross-section decreases as the energy increases [142], hence assuming $D(E) \simeq \frac{1}{3\Sigma_s(E)}$, equation (6.35) can be written as:

$$\tau_1 = \frac{K_1}{\sigma^2(E)} \ln\left(\frac{E_o}{E}\right) \quad \ldots\ldots (6.36)$$

Using $\tau = 743$ cm^2 and the cross-sections data, the constant values K and K_1 are obtained from equations (6.35) and (6.36) respectively.

In this work, the sample was divided into 0.5 cm. slices, and using equations (6.33) and (6.35) the slowing down density for neutron energies

between 14 Mev and 0.1 Mev was determined for each slice. The sum of the $q(x, \tau)$ after normalization gave the total number of neutrons which had slowed down past the energy E in the sample.

By measuring the path length of the neutron from each slice of the sample, the total number of neutrons of a given energy incident onto the detector was determined from the equation:

$$P(\theta) = \frac{\Sigma q(x, \tau).C.\Delta\Omega.\varepsilon(E_n).[1 - \exp - (\Sigma_t.x)].\frac{d\sigma(\theta)}{d\Omega}}{\sigma_t \cdot G} \quad \ldots\ldots (6.37)$$

where $\Sigma q(x, \tau)$ = the total number of neutrons from all the slices of the sample slowed down to a given energy from a source energy of 14 Mev,

and $C = \exp - (\Sigma_t.Y(I))$ where $Y(I)$ is the path length of the neutron in each slice of the sample, the other parameters are defined in chapter five.

In the next stage of the analysis, using the above procedure and the Fermi-Age τ_1, the slowing down density $q_1(x,\tau_1)$ and finally $P_1(\theta)$ were determined.

The variation of $P_1(\theta)$ and $P(\theta)$ with $\cos\theta$ (where θ is the detection angle) for the iron samples are shown in figures (6.12) through to (6.15) as solid and dashed lines respectively.

The same procedure was used for a neutron source energy of 14.4 Mev for Iron samples, and the variation of $P_1(\theta)$ and $P(\theta)$ versus $\cos\theta$ are shown in figures (6.16), (6.17) and (6.18).

6.7 OPTICAL MODEL ANALYSIS OF THE CONCRETE CROSS-SECTIONS

As discussed in section (5.9.1) concrete consists of different elements. However, from the published data [20,138], only the number of

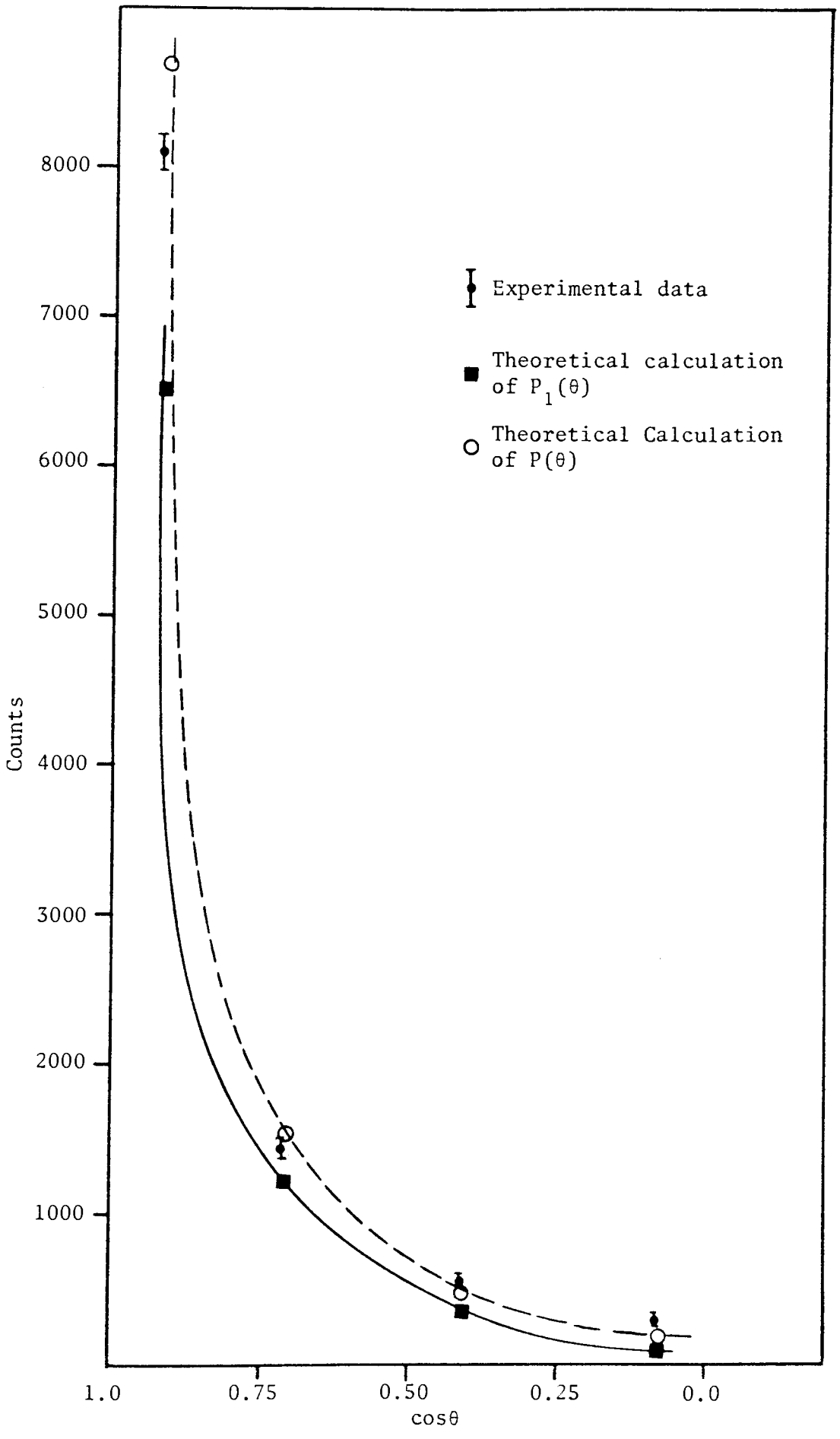

Figure (6.12) Comparison of the Experimental Measurement and Theoretical Calculation of the Number of Neutrons Scattered from 2 cm. Thick Iron Sample (E_n = 14 Mev)

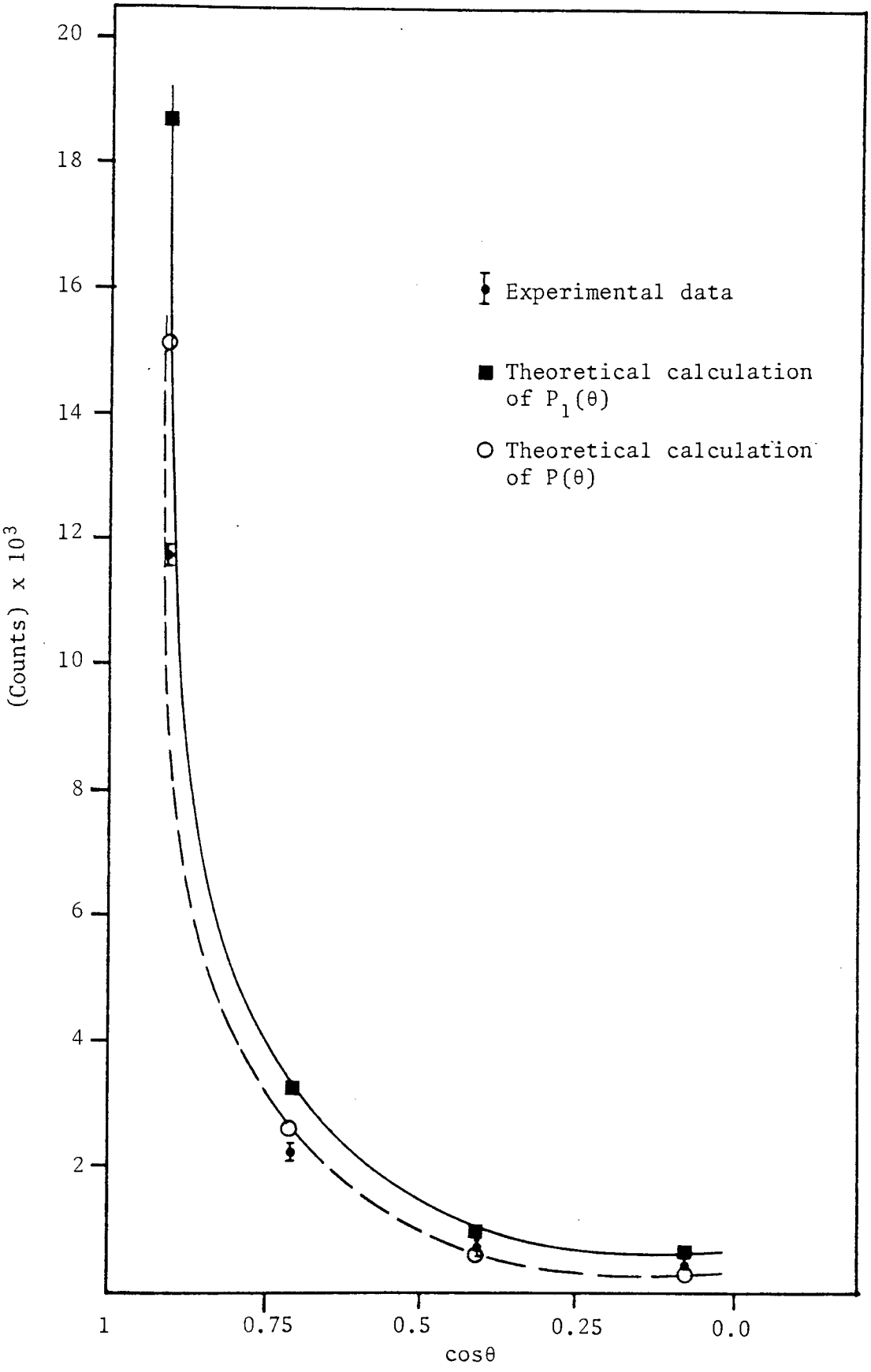

Figure (6.13) Comparison of the Experimental Measurement and Theoretical Calculation of the Number of Neutrons Scattered from 4 cm. Thick Iron Sample (E_n = 14 Mev)

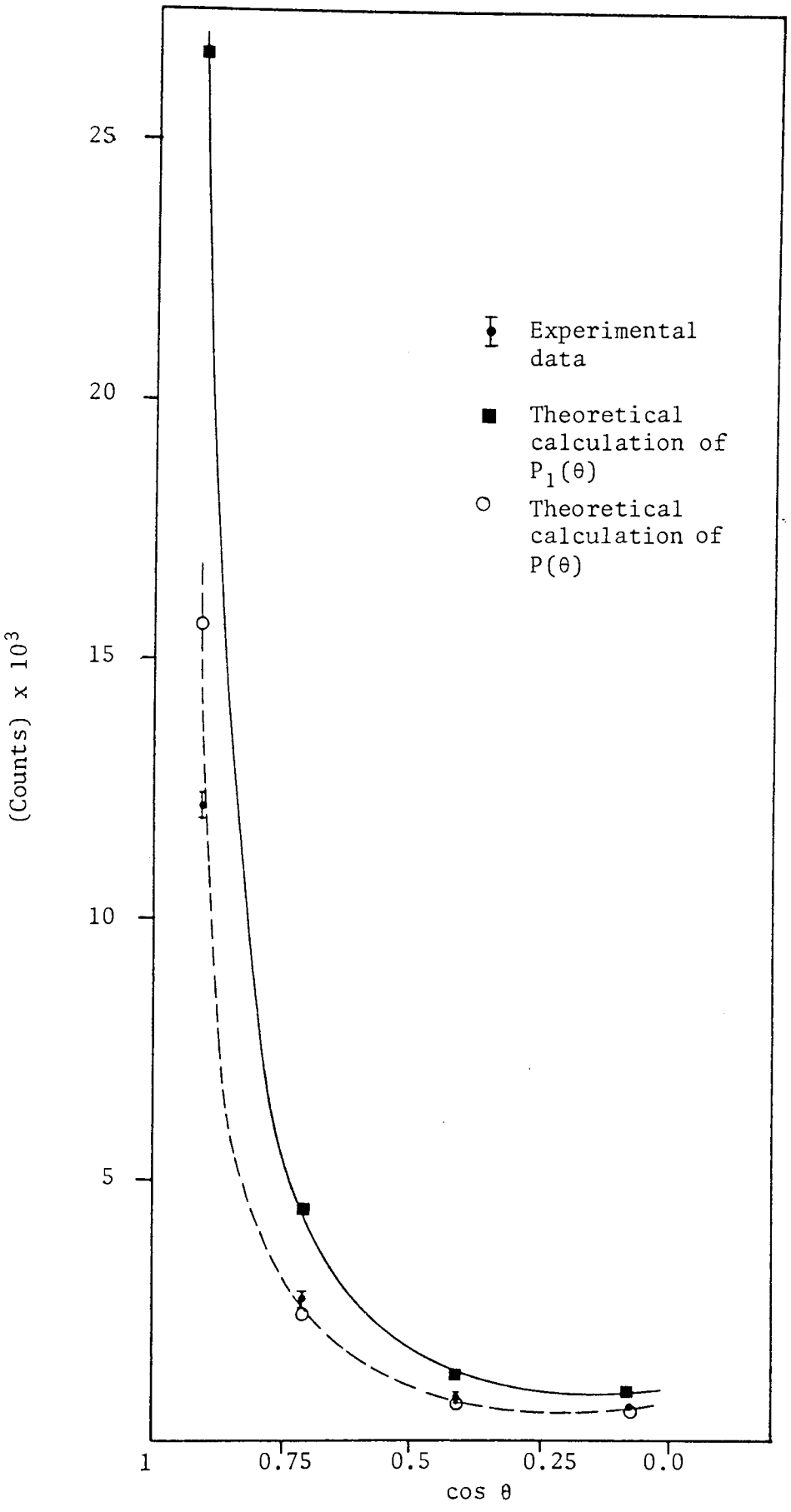

Figure (6.14) Comparison of the Experimental Data and Theoretical Calculation of the Number of Neutrons Scattered from 6 cm. Thick Iron Sample (E_n = 14 Mev)

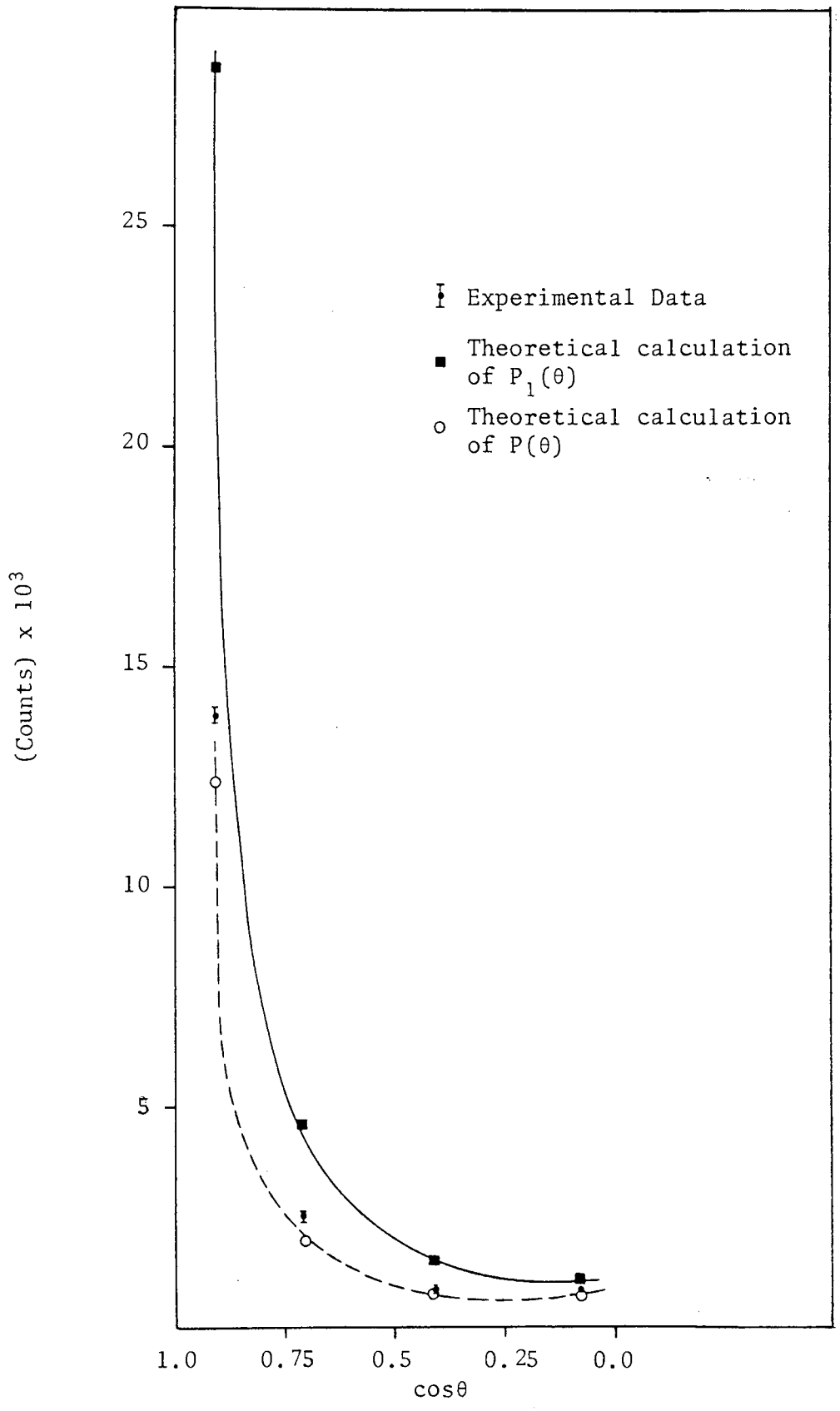

Figure (6.15) Comparison of the Experimental Measurement and Theoretical Calculation of the Number of Neutrons Scattered from 8 cm. Thick Iron Sample (E_n = 14 Mev)

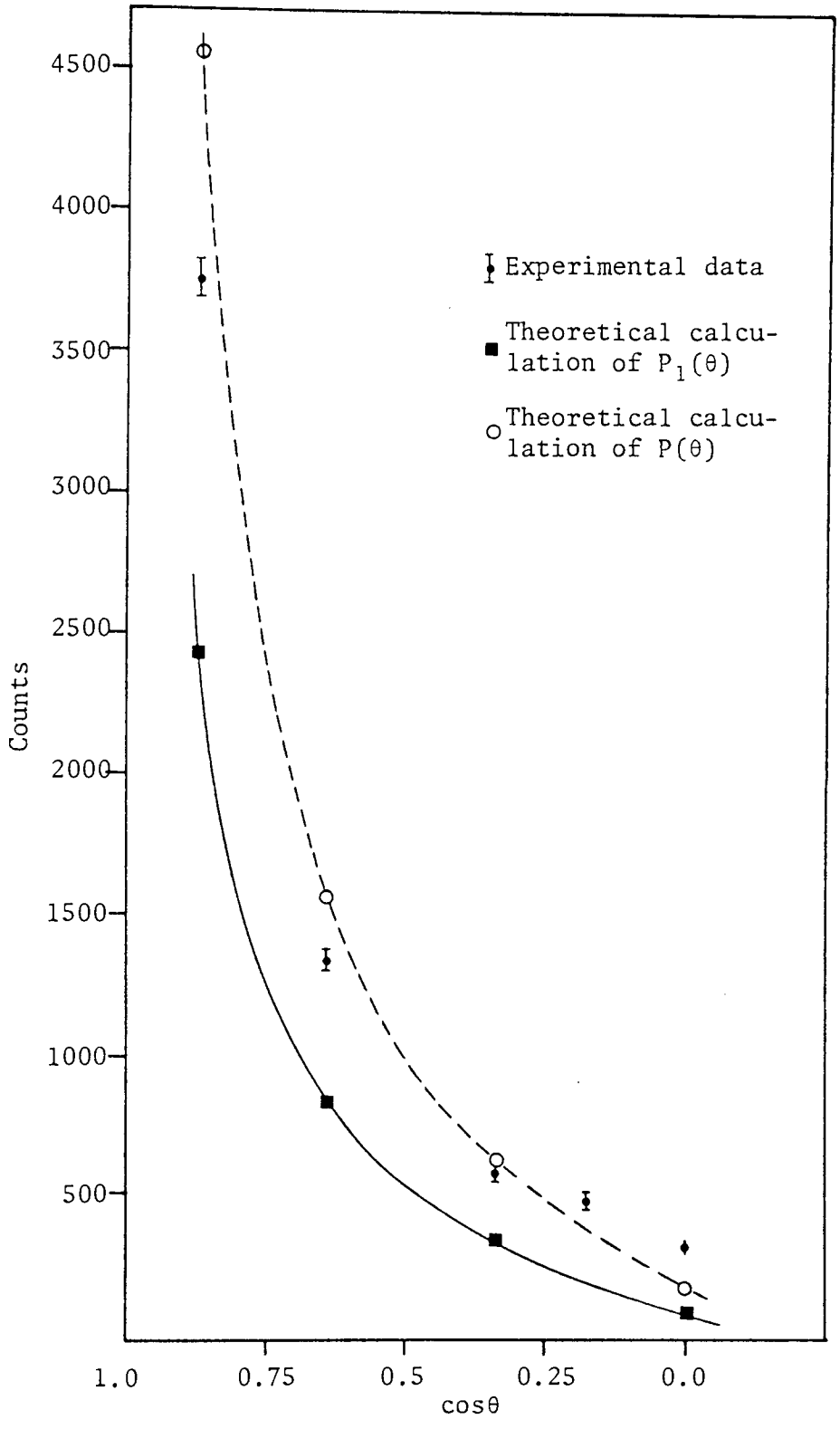

Figure (6.16) Comparison of the Experimental Measurement and Theoretical Calculation of the Number of Neutrons Scattered from 2cm. Thick Iron Sample (E_n = 14.4 Mev)

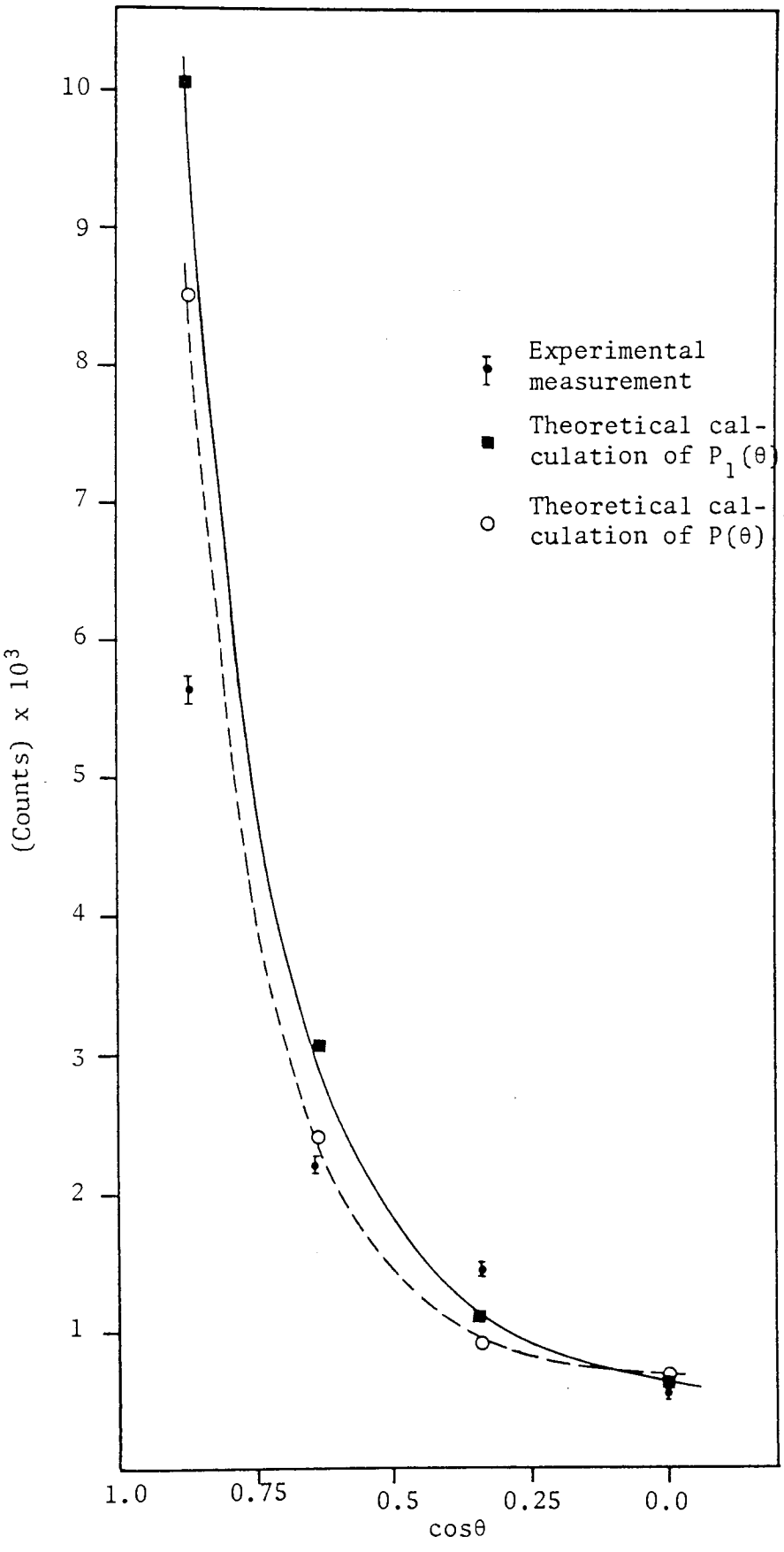

Figure (6.17) Comparison of the Experimental Measurement and Theoretical Calculation of the Number of Neutrons Scattered from 6cm. Thick Iron Sample (E_n = 14.4 Mev)

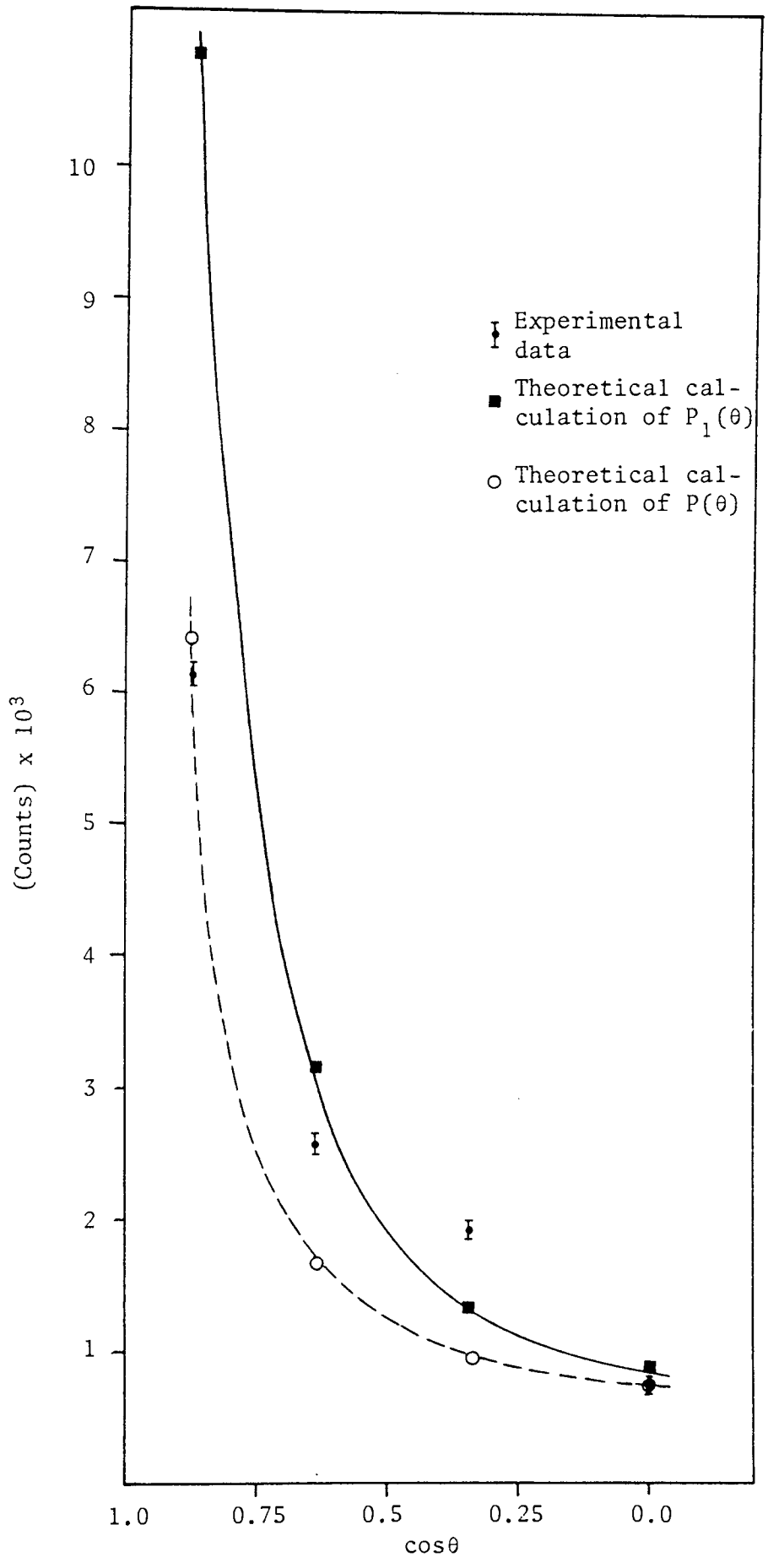

Figure (6.18) Comparison of the Experimental Measurement and Theoretical Calculation of the Number of Neutrons Scattered from 8 cm. Thick Iron Sample (E_n = 14.4 Mev)

nuclei per unit volume of four elements, i.e. Oxygen, Hydrogen, Silicon and Aluminium were available. However, as the atomic percentage of these elements accounted for most of the constituents, only these elements were taken into account in the calculation of the differential elastic scattering cross-section of concrete.

Using equations (6.9), (6.10) and (6.11), the values of the three potentials were found, are shown in table (6.3).

Table (6.3)

Values of Potentials V_R, W_D and W_V Using the Becchetti and Greenlees[24] Parameters

Elements	V_R	W_D	W_V
	[All in (Mev)]		
$^{16}_{8}O$	51.8200	9.5000	1.5200
$^{28}_{14}Si$	51.8200	9.5000	1.5200
$^{27}_{13}Al$	50.9305	9.4629	1.5200

Using the above potentials, and the other geometry parameters of Becchetti and Greenlees[24], the optical model fits for O, Si and Al were obtained are shown in figures (6.19) through to (6.21). The differential cross-section of Hydrogen has been determined by Seagrave[118] as 53 ± 1.5 mb/sr. in the centre of mass system, and by Fowler and Brolley[94] as shown in figure (5.6). Applying equation (5.7) viz:

$$\sigma(\theta_L) = \frac{(1 + 2\gamma \cos\phi + \gamma^2)^{3/2}}{1 + \gamma \cos\phi} \sigma(\phi_C) \qquad \ldots\ldots (5.7)$$

Centre-of-mass angle (degrees)

Figure (6.19) The Optical Model Fit for $^{16}_{8}O$

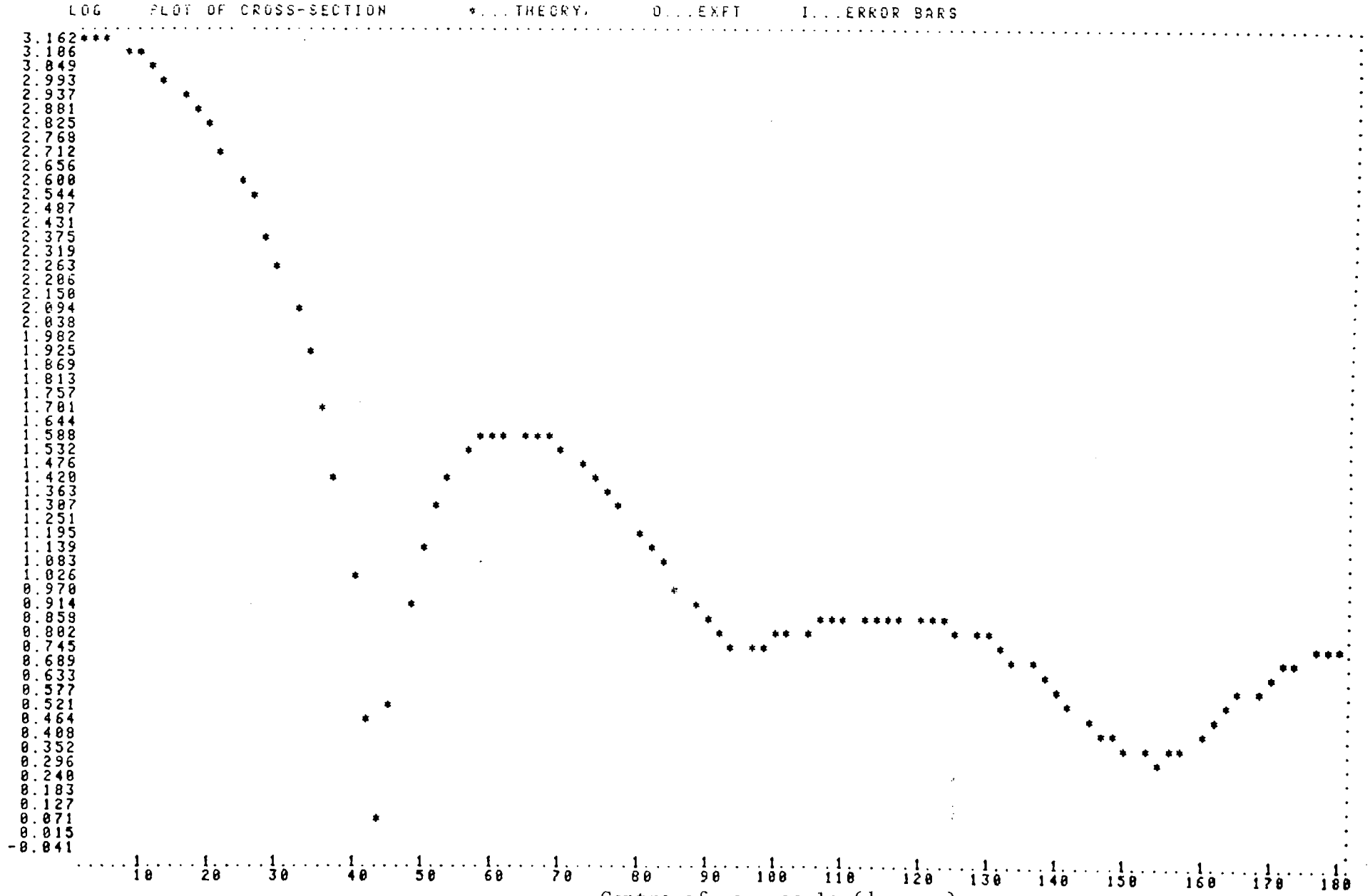

Figure (6.20) The Optical Model Fit for $^{27}_{13}Al$

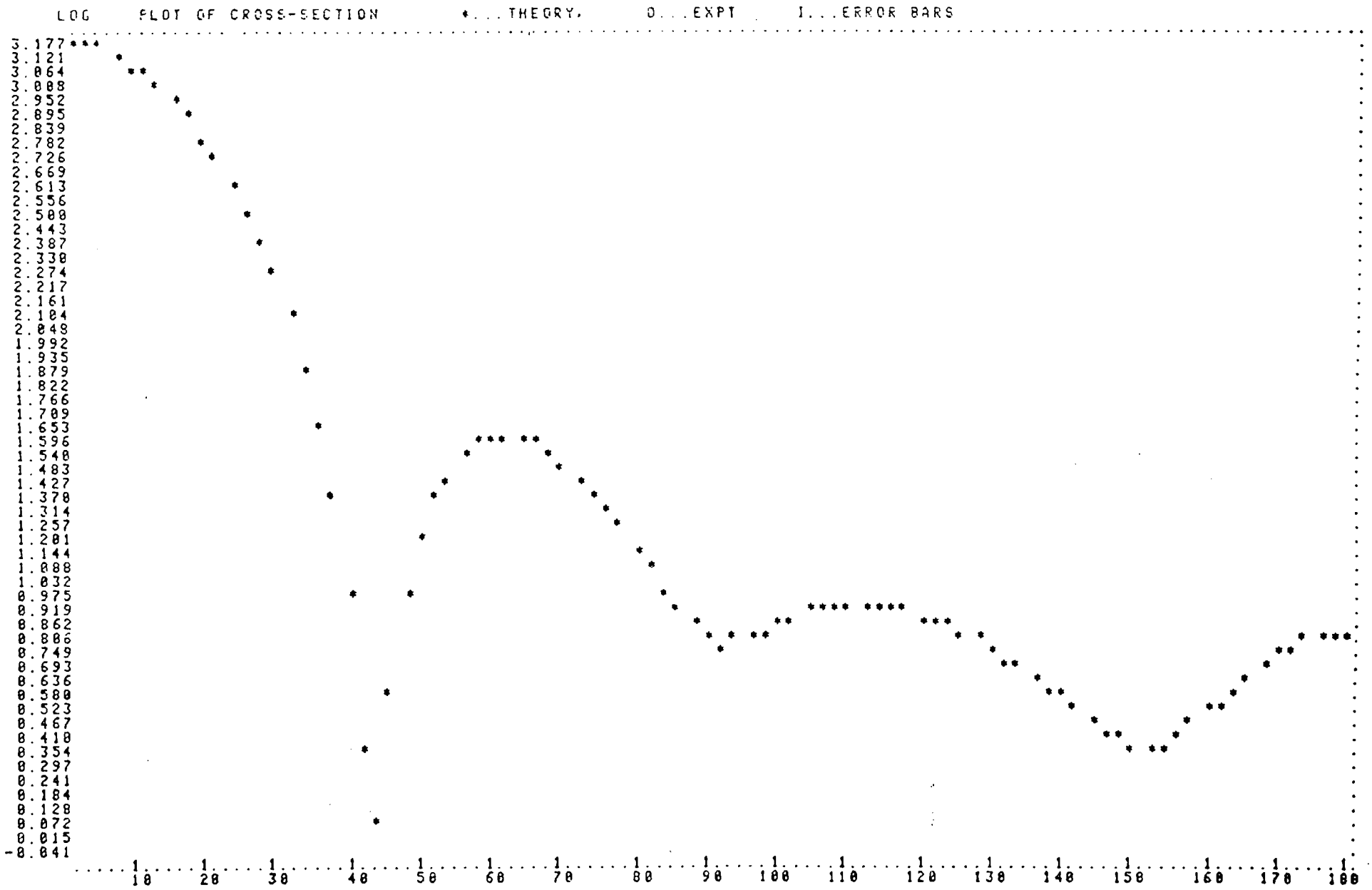

Figure (6·21) The Optical Model Fit for $^{28}_{14}Si$

and assuming the published atomic percentages of each element in concrete and using figures (6.19), (6.20) and (6.21) the theoretically predicted differential cross-sections of a 5 cm. thick concrete sample after normalization were determined. Figure (6.22) shows the comparison of the theoretically predicted and experimentally determined cross-sections. However, the agreement was poor, and it would appear that, the parameters of Becchetti et al are not suitable for fitting the concrete differential cross-sections.

In the next stage of the analysis, it was attempted to reduce the potentials of the three elements, i.e. (O), (Al) and (Si) by 10 per cent from the Becchetti et al[24] parameters in order to optimize the fit. The potentials were found for three elements are shown in table (6.4).

Table (6.4)

Values of the Potentials V_R, W_D and W_V
by 10% Reduction

Elements	V_R	W_D	W_V
	[All in (Mev)]		
$^{16}_{8}O$	46.6380	8.5500	1.368
$^{28}_{14}Si$	46.6380	8.5500	1.368
$^{27}_{13}Al$	45.8375	8.5166	1.368

Using the same procedure as explained above, the theoretically predicted cross-sections were determined. Table (6.5) shows the comparison of the experimentally determined and the theoretically calculated values. This produced an improved fit shown in figure (6.22) as a dashed line.

However, the agreement was not very good.

Finally, the Imaginary Volume potential was assumed to be zero, the real and the surface potentials were reduced by 25 per cent from the Becchetti et al[24] parameters, the result was better than the previous calculation, but in general some of the experimental points were higher than the theoretical calculation. The results are shown in figure (6.22) as a solid line.

Table (6·5)

Comparison of the Experimental Results and Theoretical Calculation of the Differential Elastic Scattering Cross-section for 5 cm. Thick Concrete Sample for 14 Mev Neutron Energy

Angle (θ) degree	Experimental data mb/sr.	with Becchetti and Greenlees parameter [24] mb/sr.	with 10% reduction of potentials mb/sr.	W_V = 0 and 25% reduction of V_R and W_D mb/sr.
25	-	349.4	391.9	505.5
35	154.6 ± 13.1	111.5	136.8	205.5
45	-	37.4	47.7	76.8
55	65.9 ± 5.7	37.8	40.0	46.8
65	-	41.4	42.2	42.6
75	46.8 ± 4.1	31.6	33.1	34.0
80	-	24.4	25.8	27.3
85	29.2 ± 2.6	16.8	18.1	20.0
90	-	10.4	11.0	12.9

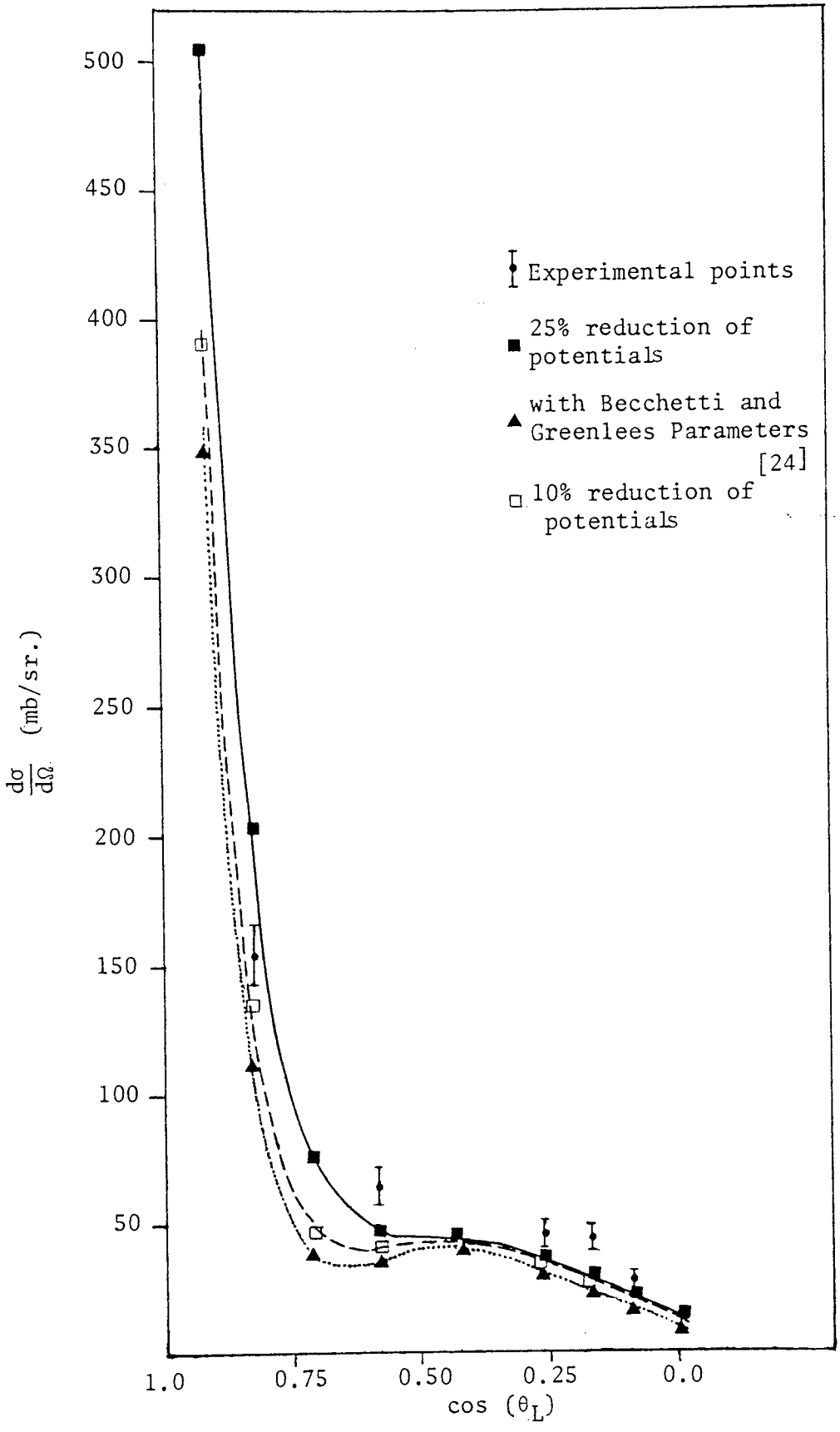

Figure (6.22) Comparison of the Experimental Data and Theoretical Calculation of the Differential Elastic Scattering Cross-section for 5 cm. Thick Concrete Sample

6.8 CALCULATION OF THE NUMBER OF NEUTRONS SCATTERED FROM THE CONCRETE SAMPLES BASED ON THE CONTINUOUS SLOWING DOWN MODEL

For the concrete sample the Fermi Age (τ) has been determined by Grimeland and Dönvold[136] using the equation (6.34) as: $\tau = (444 \pm 11)$ cm^2 for the concrete of the density: $\rho = 2.057$ g /cm^3

In this work, the density of the concrete was $\rho = 2.47 \pm 0.06$ g /cm^3 hence using equation (6.38): [11]

$$\tau(\rho) = \tau(\rho_o)\left(\frac{\rho_o}{\rho}\right)^2 \qquad \ldots\ldots (6.38)$$

where $\tau(\rho_o)$ = the Fermi Age of the sample with the density of ρ_o

and $\tau(\rho)$ = the Fermi Age of the sample with the density of ρ.

For the concrete samples, equation (6.35) was applied to determine the constant K for $\tau = 444$ cm^2 .

In the present work, the large scattering sample was divided into slices of rectangular shape having thicknesses of 1.25 cm., using the same procedure as discussed in the section (6.6) and equation (6.37), the total number of the scattered neutrons from the sample, incident onto the detector was determined. Figures (6.23) through to (6.27) show the total number of scattered neutrons predicted by the continuous slowing down model and those determined experimentally from the measured time spectra.

In the next stage of the analysis, the differential elastic scattering cross-sections of the four main elements in concrete, i.e. H, Si, Al and O were obtained from the published data [118,139-141].

Table (6.6) shows the cross-sections of these four elements, and the calculated effective cross-section of the concrete sample. Using equation (6.37) and data of the table (6.6), the total number of scattered neutrons from the sample was determined. The results are shown in figures (6.23) through to (6.27) as a dashed line.

The discrepancy in the data is mostly due to the presence of hydrogen and other light elements in the concrete, since the Fermi-Age does not hold for these elements, and also due to the error in the published values of the differential cross-sections of four elements. However, the shape of the spectra has the correct form.

Table (6.6)

Comparison of the Measurement and Calculated Differential Elastic Scattering

Cross-section of 5 cm. Thick Concrete Sample for 14.0 Mev Neutrons

Angle (θ) degree	$\frac{d\sigma(\theta L)}{d\Omega}$ of (O) [141] mb/sr.	$\frac{d\sigma(\theta L)}{d\Omega}$ of (Si) [140] mb/sr.	$\frac{d\sigma(\theta L)}{d\Omega}$ of (Al) [139] mb/sr.	$\frac{d\sigma(\theta L)}{d\Omega}$ of (H) [118] mb/sr.	Calculated $\frac{d\sigma(\theta L)}{d\Omega}$ of concrete mb/sr.	Experimental values of $\frac{d\sigma(\theta L)}{d\Omega}$ mb/sr.
35	163.4	254.2	59.4	173.7	176.6	154.6 ± 13.1
55	35.4	12.6	55.3	121.6	46.9	65.9 ± 5.7
75	43.8	57.5	42.8	54.9	47.9	46.9 ± 4.1
85	39.4	17.3	19.1	18.5	31.4	29.3 ± 2.6

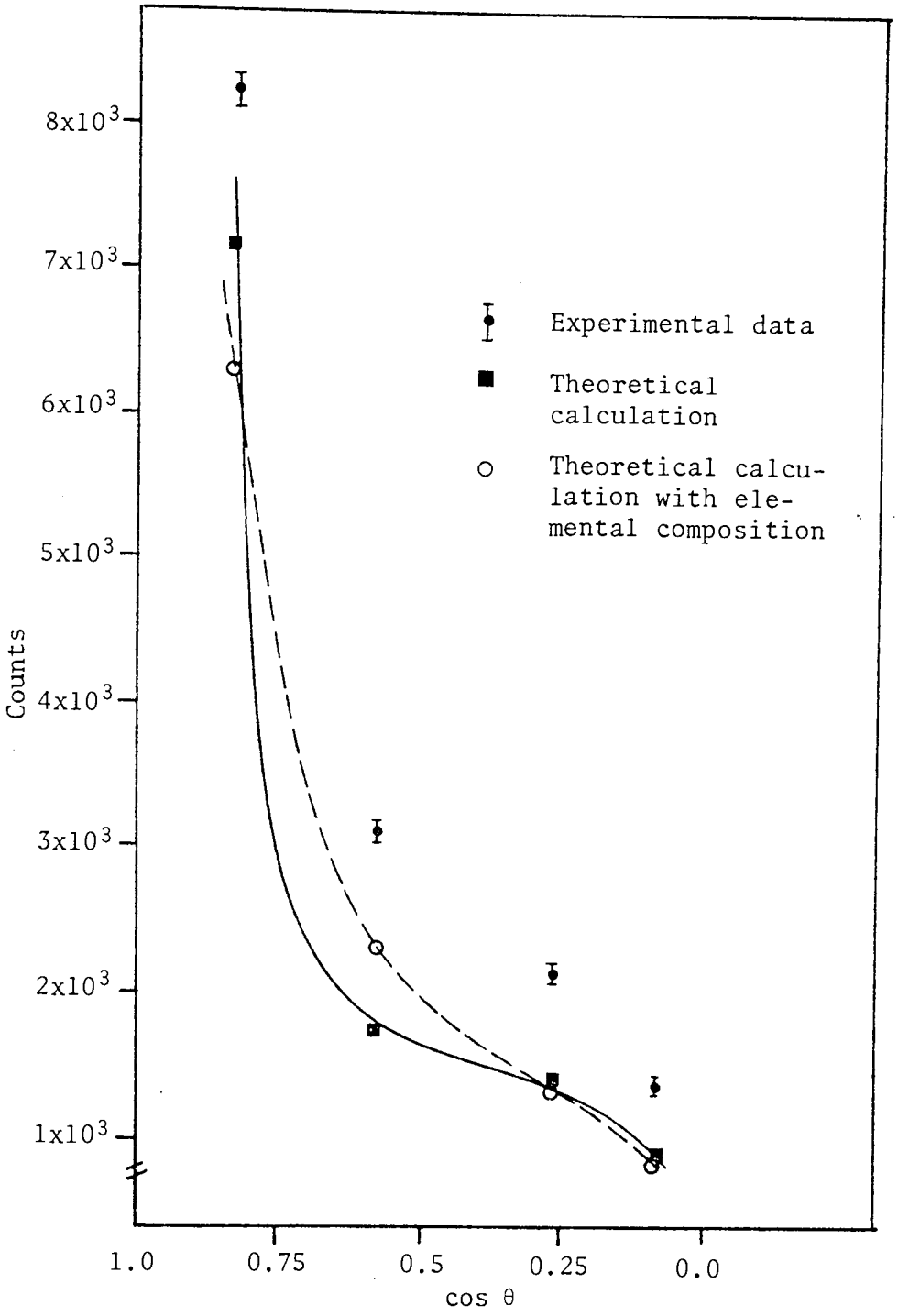

Figure (6.23) Comparison of the Experimental Measurement and Theoretical Calculation of the Number of Neutrons scattered from 5 cm. Thick Concrete Sample

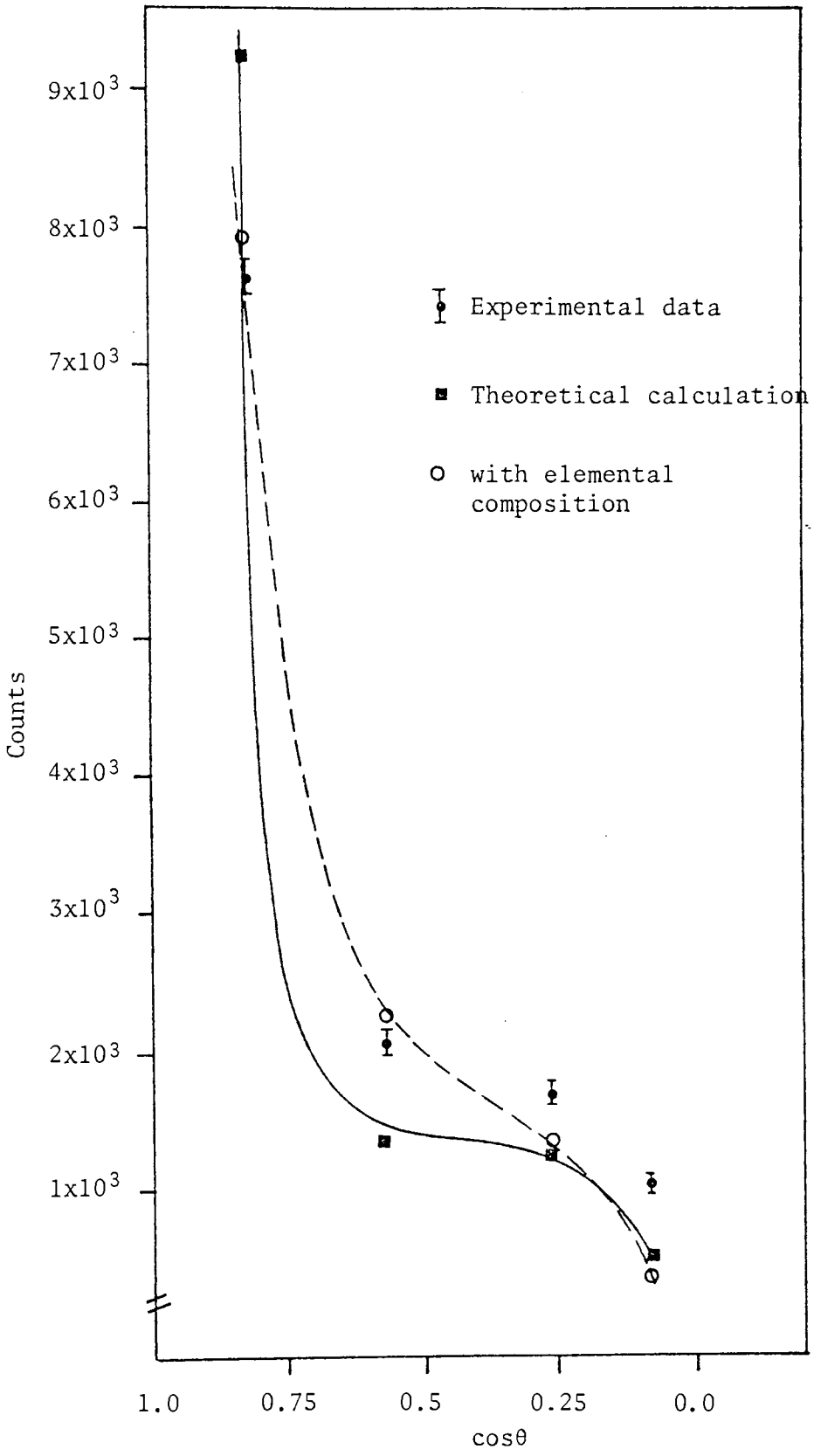

Figure (6.24) Comparison of the Experimental Measurement and Theoretical Calculation of the Number of Neutrons Scattered from 7.62 cm. Thick Concrete Sample

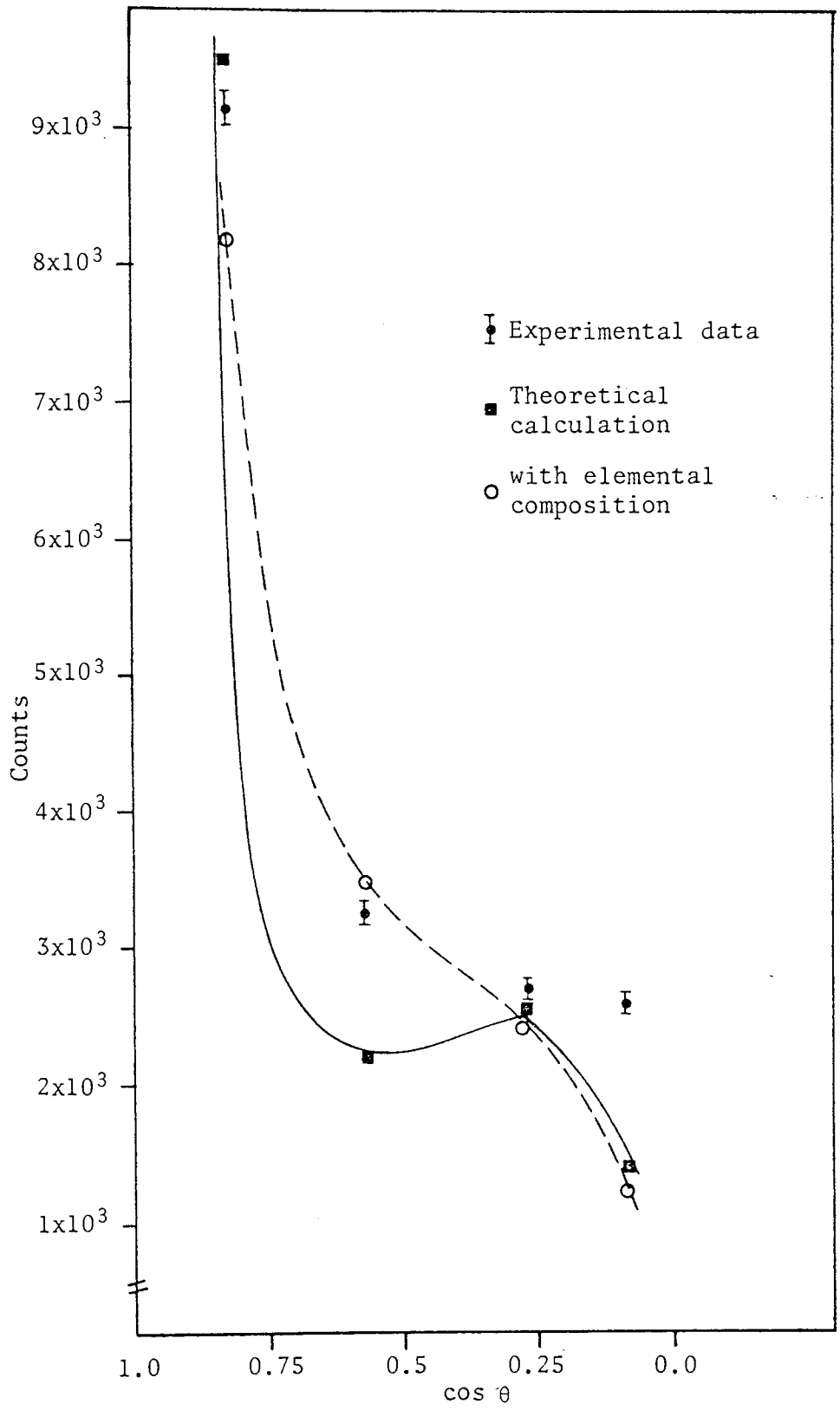

Figure (6.25) Comparison of the Experimental Measurement and Theoretical Calculation of the Number of Neutrons Scattered from 12.7 cm. Thick Concrete Sample

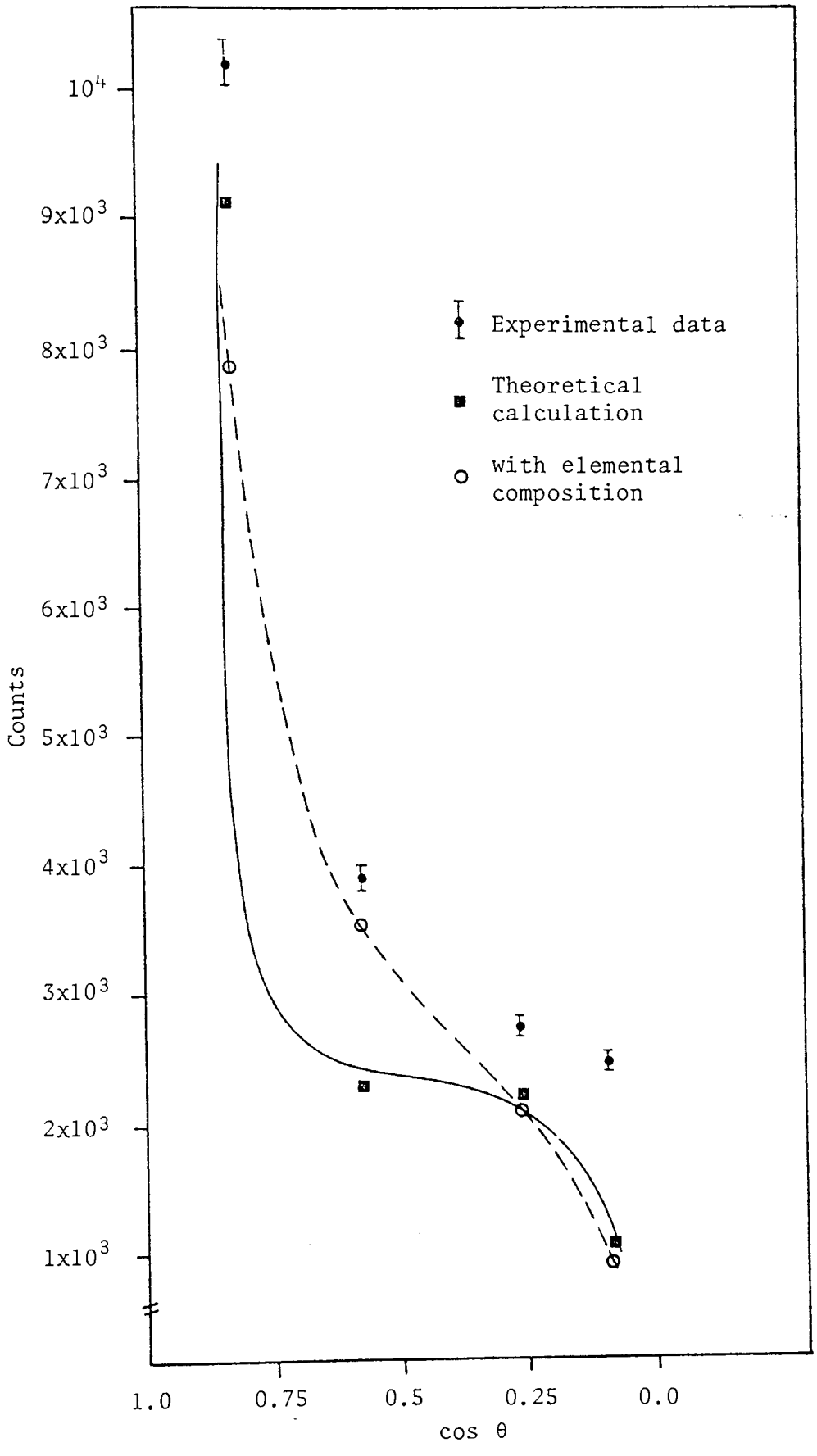

Figure (6.26) Comparison of the Experimental Measurement and Theoretical Calculation of the number of Neutrons Scattered from 17.8 cm. Thick Concrete Sample

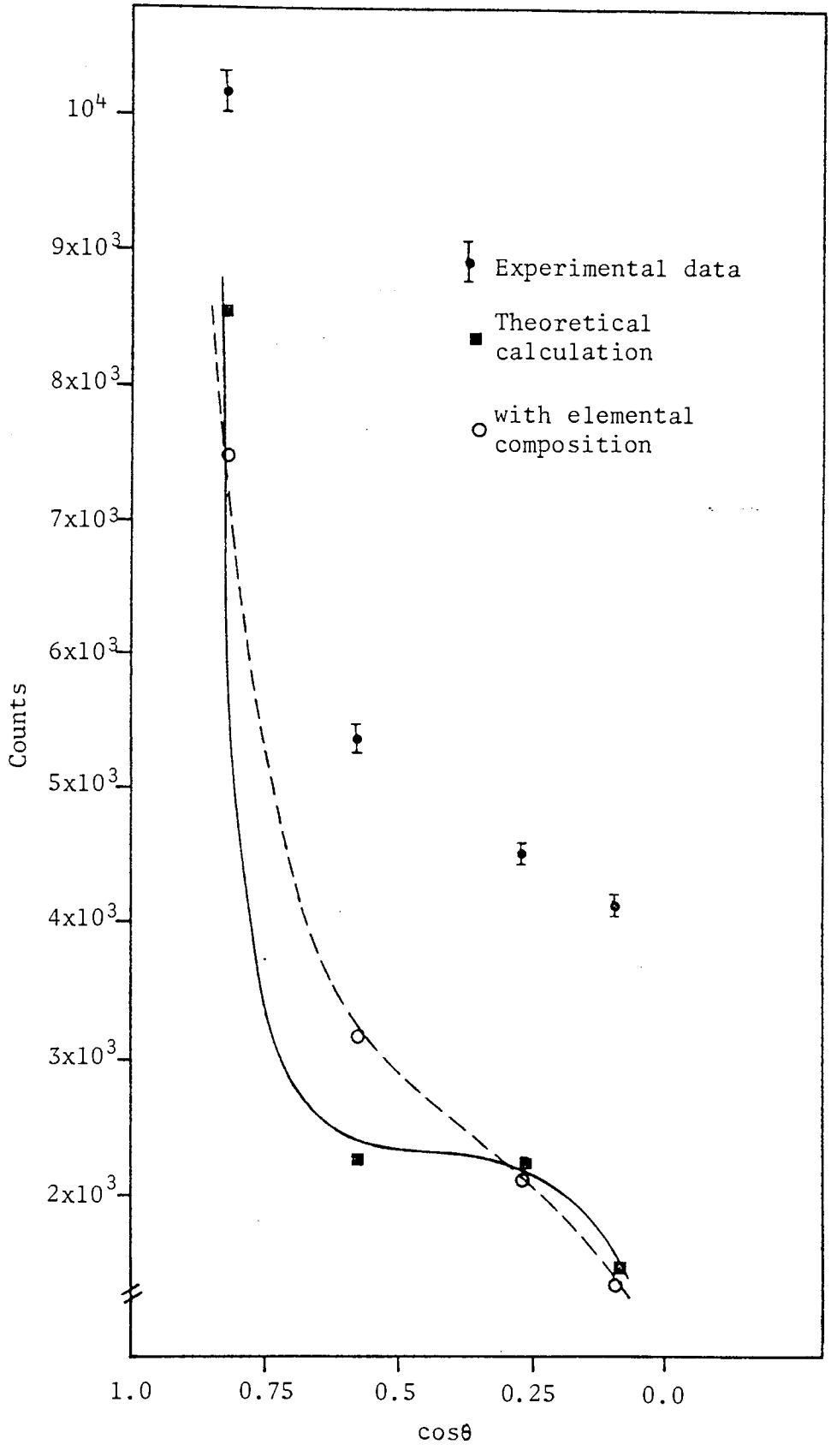

Figure (6.27) Comparison of the Experimental Measurement and Theoretical Calculation of the Number of Neutrons Scattered from 25.4 cm. Thick Concrete Samples

CHAPTER SEVEN

CHAPTER SEVEN

CONCLUSIONS

The T(d, n)^{4}He reaction was used to study the angular distribution of neutrons after being scattered from various thicknesses of iron and concrete samples. The results obtained show the usefulness of the associated particle time-of-flight technique in such measurement for fast neutrons.

The resolution of the spectrometer was 2.5 ± 0.2 n.sec. (FWHM) for the production of 14 Mev neutrons. The time resolution of the spectrometer was limited by the time uncertainty involved with the detector, because of the thickness of the scintillator, and transit time spread of the electrons in the photomultiplier tube. It is possible to improve the time resolution of the detector by choosing large sample-to-detector distances. However, the increased detector to sample distance would increase the background counts and the accumulation time of the spectrum. In future work, it would be helpful to be able to resolve the elastic and inelastic components of the scattered neutron beam. In the present work it was not possible to do this for iron and some of the elements of the concrete sample. However, as discussed in chapter five, using the Gaussian shape of the elastic peak, it was possible to "strip off" the contribution from the elastically scattered neutrons.

The differential elastic scattering cross-sections were measured for 14.0 and 14.4 Mev neutrons at several scattering angles in the angular range 0^o - 90° by moving the neutron detector through different angles with respect to the sample position. The results of the thin iron sample for 14.0 Mev neutron using flat plate geometry were in agreement within the experimental error with the data of Coon et al[12] using cylindrical geometry and data of Yuasa[12] at 90° using disk shape

scatterer. The agreement of the experimental data for the thin sample of iron and theoretically predicted cross-section using the optical model was good (x^2 = 0.34). In the prediction of cross-sections by this model, some workers [14, 132, 133, 137] have suggested that it is not necessary to assume the volume imaginary potential below E_n = 20 Mev. However, in this work the effect varying it was studied. The fit was a further improvement (x^2 = 0.29). The optical model parameters obtained to fit the elastic scattering cross-section of the thin iron sample for 14 Mev neutrons as shown in chapter six were in good agreement with the parameters obtained by Wilmore et al[13].

For 14.4 Mev neutron energy, the results of the angular distribution for the thin sample of iron were compared with the prediction of the optical model. The agreement was good (x^2 = 0.1). As discussed in chapter five, the variation of the cross section with sample thickness was explained using equation (5.26) and the univeral constant K, (K = 0.33 ± 0.20)(mean free paths)$^{-1}$. The universal constant K agreed well with the constant value reported in ref.[144]. It seems that, this equation can be used in general for all elements with extended thicknesses. The shape of spectra obtained by the calculation number of scattered neutrons from thick samples predicted, using the theory based on the continuous slowing down model, were in reasonable agreement with the data of the experimental measurements. In order to obtain accurate results the analysis should be done using the Monte Carlo calculation, which is in principle more powerful. However, the use of Monte Carlo technique presupposes a rather sophisticated computer facility. The results obtained are important from the point of view of shielding calculation and construction for fusion reactors.

The theoretically predicted differential cross-section for the thin concrete sample by the optical model was in reasonable agreement with

the experimental data. However, it was found that, by reducing the optical potentials from the Becchetti et al parameters by 25%, the experimental data were in good agreement with the theoretically predicted cross-sections, and the results were improved by 17%. In the case of the thick samples of concrete, using the continuous slowing down model, the number of scattered neutrons were determined. The discrepancy of some of the experimental data from the theoretical values was due to the presence of hydrogen and some of the light elements in the concrete, however, the shape of spectra was correct.

Finally it was shown that, by using a 1 Mev deuteron beam, the time-of-flight technique can be applied to the $^{2}H(d, n)^{3}He$ reaction. In this work, the distance between the neutron detector and sample was 0.5 m and by monitoring the proton yield, the problem of obtaining the neutron yield was overcome. The spectrometer resolution obtained was 43 ± 2 n.sec. (FWHM) for the production of 3.02 Mev neutrons. This is an improvement to the value of 65 n.sec. (FWHM) reported by Janicki for the production of 2.99 Mev neutrons. For future work, it would be helpful to study the elastic and inelastic scattering of fast neutrons with other materials such as lead and Lithium or combination of heavy and light elements which might be used for future fusion reactors.

LEAST SQUARES FIT.

```
100 INPUT"PRINTER OR VDU";Z$
110 IFZ$="V"THEN VS=3:GOTO 130
120 IFZ$="P"THENVS=4
130 OPEN1,VS:CMD1
140 DIM X(100),Y(100),C(100),N(100),E1(100),E2(100)
150 PRINT#1," LEAST SQUARES LINE FIT."
160 PRINT#1,"-----------------------"
170 PRINT#1:PRINT#1
180 PRINT#1,"X(I)"SPC(10)"Y(I)"SPC(10)"LOG(Y(I))"SPC(13)"E1"SPC(13)"E2"
190 PRINT#1,CHR$(1)"──────────────────────────────────────────────────────"
200 READ N
210 M=0
220 D=0
230 S1=0
240 S2=0
250 T0=0
260 T1=0
270 FOR I=1 TO N
280 READ X(I),Y(I),C2(I)
290 REM---- C2=ERROE OF Y(I)
300 NEXT I
310 FOR I=1 TON
320 Q(I)=LOG(Y(I))
330 C(I)=(INT(Q(I)*1000+.5))/1000
340 EM(I)=LOG(Y(I)+C2(I))
350 E1(I)=(INT(EM(I)*1000+.5))/1000
360 EI(I)=LOG(Y(I)-C2(I))
370 E2(I)=(INT(EI(I)*1000+.5))/1000
380 PRINT#1,X(I)SPC(8)Y(I)SPC(9)C(I)SPC(8)E1(I)SPC(9)E2(I)
390 S1=S1+X(I)
400 S2=S2+X(I)↑2
410 T0=T0+C(I)
420 T1=T1+X(I)*C(I)
430 NEXT I
440 AA=(N*T1-S1*T0)/((N*S2)-(S1)↑2)
450 BB=(T0*S2-S1*T1)/((S2*N)-(S1)↑2)
455 A=(INT(AA*10000+.5))/10000
456 B=(INT(BB*100000+.5))/100000
460 PRINT#1
470 PRINT#1
480 PRINT#1
490 PRINT#1,"Y=";A"X +";B
495 PRINT#1,"========================="
500 FOR I=1 TO N
510 Z(I)=A*X(I)+B
520 D1(I)=Z(I)-C(I)
530 D=D+(D1(I)*D1(I))
540 NEXT I
550 REM-----M=ALPHA
560 M=(D/(N-2))
570 REM-----Q=DELTA
580 Q=((N*S2)-(S1*S1))
590 AP1=SQR((N*M)/Q)
600 BQ1=SQR((S2*M)/Q)
610 PRINT#1
620 PRINT#1
625 A1=(INT(AP1*10000+.5))/10000
626 B1=(INT(BQ1*10000+.5))/10000
630 PRINT#1,SPC(2)"A1"SPC(13)"B1"
640 PRINT#1,"-------"SPC(10)"------"
650 PRINT#1,A1SPC(3)B1
660 REM----A1=ERROR OF A
670 REM----B1=ERROR OF B
680 REM----E1=MAX.POINT
690 REM----E2=MIN.POINT
700 CLOSE1
710 END
720 DATA 4
730 DATA .4328,28.94,2.63
740 DATA .3856,40.37,3.77
750 DATA 1.1384,23.1,3.13
760 DATA 1.7314,13.1,3.4
READY.
```

APPENDIX (B)

MATHEMATICAL RELATIONSHIPS FOR A NUCLEAR REACTION

Referring to Figure (2.11) and considering the (DT) and (DD) reactions, it is found that, the energy of neutron (E_3) can be written as:

$$E_n \equiv E_3 = E_1 \frac{M_1 M_3}{(M_3 + M_4)^2} \left\{ 2\cos^2\theta_3 + \frac{M_4(M_3 + M_4)}{M_1 M_3}\left(\frac{Q}{E_1} + 1 - \frac{M_1}{M_4}\right) \right.$$

$$\left. \pm 2\cos\theta_3\left[\cos^2\theta_3 + \frac{M_4(M_3 + M_4)}{M_1 M_3}\left(\frac{Q}{E_1} + 1 - \frac{M_1}{M_4}\right)\right]^{\frac{1}{2}} \right\} \quad \ldots\ldots \text{(B-1)}$$

where M_1 = mass of the incident particle

M_2 = mass of the bombarded particle

M_3 = mass of the lighter product particle

M_4 = mass of the heavier product nucleus

and θ_3 = Laboratory angle of M_3

Assuming

ψ = centre of mass angle of light particle

ϕ = centre of mass angle of heavy particle

θ_4 = Laboratory angle of heavy product nucleus

E_4 = Energy of heavy particle

and $E_T = E + Q$

Defining the parameters:

$$A = \frac{1}{(M_1 + M_2)(M_3 + M_4)}$$

$$B = A\, M_1\, M_4\left(1 - \frac{Q}{E_T}\right)$$

$$C = A\ M_1\ M_3\left(1 - \frac{Q}{E_T}\right)$$

$$D = A\ M_2\ M_3\left(1 + \frac{M_1\ Q}{M_2\ E_T}\right)$$

$$H = A\ M_2\ M_4\left(1 + \frac{M_1\ Q}{M_2\ E_T}\right)$$

The following useful relations may be obtained:

The Energy of the light particle:

$$E_3 = [C + H + 2(BD)^{\frac{1}{2}} \cos\psi]E_T \qquad \ldots\ldots \text{(B-2)}$$

The Energy of the heavy product nucleus in Laboratory system:

$$E_4 = [B + D + 2(BD)^{\frac{1}{2}} \cos\phi] \qquad \ldots\ldots \text{(B-3)}$$

The Laboratory Angle of the scattered heavy product nucleus can be determined from the relation:

$$\sin\theta_4 = \left(\frac{M_3\ E_3}{M_4\ E_4}\right)^{\frac{1}{2}} \sin\theta_3 \qquad \ldots\ldots \text{(B-4)}$$

The Centre of mass angle of the light particle can be found from the relation:

$$\sin\psi = \left(\frac{E_3/E_T}{H}\right)\sin\theta_3 \qquad \ldots\ldots \text{(B-5)}$$

The ratio of cross-sections for light product:

$$\frac{\sigma(\psi)}{\sigma(\theta_3)} = \frac{(BD)^{\frac{1}{2}}(H/C - \sin^2\theta_3)^{\frac{1}{2}}E_T}{E_3} \qquad \ldots\ldots \text{(B-6)}$$

And the ratio of cross-sections for heavy product nucleus:

$$\frac{\sigma(\phi)}{\sigma(\theta_4)} = \frac{(BD)^{\frac{1}{2}}(D/B - \sin^2\theta_4)^{\frac{1}{2}}E_T}{E_4} \qquad \ldots\ldots \text{(B-7)}$$

KIN. OF NUCLEAR REACT.

```
100 INPUT"PRINTER OR VDU";Z$
110 IFZ$="V"THEN VS=3:GOTO 130
120 IFZ$="P"THENVS=4
130 OPEN1,VS:CMD1
140 PRINT#1,CHR$(1)SPC(4)"KINEMATICS OF D(D,N)HE3 REACTION":PRINT#1
150 PRINT#1,CHR$(1)SPC(3)"**************************************":PRINT#1:PRINT#1
160 M1=2.014102
170 M2=2.014102
180 M3=1.008665
190 M4=3.016030
200 Q=(M1+M2-M3-M4)*931.375
210 REM------(M1,M2=DEUTERON MASS)----
220 REM------(M3=NEUTRON MASS)------
230 REM------(M4=HE3 MASS)------
240 PRINT#1,"M1=";M1;"AMU"
250 PRINT#1,"M2=";M2;"AMU"
260 PRINT#1,"M3=";M3;"AMU"
270 PRINT#1,"M4=";M4;"AMU"
280 PRINT#1,"Q=";Q;"MEV"
290 FOR E1=.1 TO 3 STEP 0.5
300 PRINT#1,CHR$(1)"DEUTRON ENERGY=";E1;"MEV"
310 PRINT#1,SPC(2)"-----------------------------------------------"
320 PRINT#1,SPC(1)"NEUTRON ANG"SPC(10)"NEUTRON E"SPC(15)"HE3 E"SPC(13)"FI"
330 PRINT#1,SPC(4)"(DEG)"SPC(14)"(MEV)"SPC(18)"(MEV)"SPC(12)"(DEG)"
340 PRINT#1,SPC(1)"------"SPC(13)"--------"SPC(15)"-------"SPC(11)"-------"
350 FOR ANG=0TO 180 STEP 5
360 IF ANG=180THEN620
370 PSI=ANG*π/180
380 K=SQR(M1*M3*E1)/(M4+M3)*COS(PSI)
390 L=(M4-M1)/(M4+M3)*E1+Q*M4/(M4+M3)
400 A1=(M1*M3*E1)/(M4+M3)↑2*COS(PSI)*COS(PSI)
410 B1=SQR(A1+L)
420 EN=(K+B1)↑2
430 E3=INT(EN*1000+.5)/1000
440 REM-------(E3=N. ENERGY)------
450 EH=E1+Q-E3
460 E4=INT(EH*1000+.5)/1000
470 REM------(E4=HE3 ENERGY)-----
480 A=(M4/M3)*((M1+M2)/M1)
490 B=A*((M2/(M1+M2))+(Q/E1))
500 C=SQR((B-(SIN(PSI)*SIN(PSI))))
510 C1=0.5*SIN(2*PSI)+SIN(PSI)*C
520 C2=COS(PSI)*C-(SIN(PSI)*SIN(PSI))-(M4/M3)
530 D=(180/π)*ATN(C1/C2)
540 REM------(FI=HEL. ANGLE)------
550 FI=INT(D*1000+.5)/1000
560 IF FI<0 THENGOTO 610
570 FI=180-FI
580 PRINT#1,SPC(1)ANGSPC(16)E3SPC(15)E4SPC(10)FI
590 NEXT ANG
600 NEXT E1
610 FI=FI*(-1):GOTO630
620 FI=0
630 PRINT#1,SPC(1)ANG SPC(16)E3SPC(15)E4SPC(10)FI
640 NEXT ANG
650 NEXT E1
660 CLOSE 1,4
670 END
READY.
```

APPENDIX (C)

THE NORMAL ERROR DISTRIBUTION

In nuclear spectroscopy, the pulse height distribution of a peak can be represented by a Gaussian function:

$$Y(x) = Y_o \exp[-(x - x_o)^2/2\sigma^2] \quad \ldots\ldots (C\text{-}1)$$

where Y_o = the peak height

x_o = the peak position or mean of the distribution

σ = standard deviation

and $Y(x)$ = the amplitude of the Gaussian at channel x.

Using the property of the Gaussian function:

$$Q(x) = \frac{Y(x-1)}{Y(x+1)} = \exp[2(x - x_o)/\sigma^2] \quad \ldots\ldots (C\text{-}2)$$

And taking logarithms of above equation, i.e.

$$\ell n\, Q(x) = 2(x - x_o)/\sigma^2 \quad \ldots\ldots (C\text{-}3)$$

a linear function of x is derived.

Equation (C-3) can be fitted to a straight line by the least squares method.

The slope "m" and intercept "b" of this linear fit then yield the standard deviation and x_o of the Gaussian function:

$$\sigma = (2/m)^{\frac{1}{2}}$$

$$\text{and } x_o = -b/m \quad \ldots\ldots (C\text{-}4)$$

In making this fit a weighting factor (W_i):

$$W_i = \left[\frac{1}{N_{i+1}} + \frac{1}{N_{i-1}}\right]^{-1} \qquad \ldots\ldots \text{(C-5)}$$

is given to each ln Q(x) point, where N_i represents the content of the ith channel

With the values of σ and x_o, the peak height Y_o can be obtained as:

$$\ell n\ Y_o = \frac{\sum_{i=1}^{N} W_i' \left[\ell n\ N_i + (x - x_o)^2/2\sigma^2\right]}{\sum_{i=1}^{N} W_i'} \qquad \ldots\ldots \text{(C-6)}$$

where W_i' is the weighted factors given by Mukoyama [143] as:

$$W_i' = \left[\frac{1}{N_i} + \frac{(x_i - x_o)^2}{\sigma^4}\{(\Delta x_o)^2 + \frac{(x_i - x_o)^2}{\sigma^2}(\Delta\sigma)^2\}\right]^{-1}$$

$\ldots\ldots$ (C-7)

Here Δx_o = standard deviation of x_o

and $\Delta\sigma$ = estimated standard deviation of σ

Finally, using the value of Y_o, the total area under the peak can be found from the relation:

$$A = (2\pi)^{\frac{1}{2}}\ \sigma\ Y_o \qquad \ldots\ldots \text{(C-8)}$$

Using the above equations, a computer programme was written and is shown in the next pages.

NORMAL ERROR DIST.

```
100 INPUT"PRINTER OR VDU";Z$
110 IFZ$="V"THEN VS=3:GOTO 130
120 IFZ$="P"THENVS=4
130 OPEN1,VS:CMD1
140 PRINT#1,SPC(1)CHR$(1)"PROGRAMME FIT.OF A NORMAL DIST."
150 PRINT#1,"----------------------------------------"
160 PRINT"HOMANY DATA POINTS"
170 INPUT N
180 DIM X(N),Y(N),Q(N),U(N),W(N)
190 A1=0
200 B1=0
210 C1=0
220 D1=0
230 E=0
240 FOR I=1 TO N STEP 1
250 READ X(I):NEXT
260 FOR I=1 TO N STEP 1
270 READ Y(I):NEXT
280 FOR I=1 TO N
290 PRINT#1,ISPC(2)X(I)SPC(5)Y(I):NEXTI
300 FOR I=2 TO N-1 STEP 1
310 K=I-1
320 J=I+1
330 L=N-2
340 Q(I)=LOG(Y(K)/Y(J))
350 U(I)=(1/Y(J)+1/Y(K))
360 U(I)=1/U(I)
370 A1=A1+X(I)*U(I)
380 B1=B1+Q(I)*U(I)
390 C1=C1+X(I)*Q(I)*U(I)
400 D1=D1+X(I)*X(I)*U(I)
410 E=E+U(I)
420 NEXT I
430 M=(E*C1-A1*B1)/(E*D1-A1*A1)
440 B=(B1*D1-A1*C1)/(E*D1-A1*A1)
450 PRINT#1,"M=";M
460 PRINT#1,"B=";B
470 REM----(S=SIGMA)----
480 S=SQR(2.0/M)
490 REM---(X0=PEAK POSITION)-----
500 X0=-(B)/M
510 PRINT#1,"PEAK POSITION=";X0
520 REM===(RESIDUAL CALCUL.)======
530 PRINT#1,"SIGMA=";S
540 REM----(S1=ERROR IN S)------
550 REM----(S2=DETERMINANT)-----
560 A2=0
570 D2=0
580 A2=A2+X(I)
590 D2=D2+X(I)*X(I)
600 S2=(L*D2)-(A2)↑2
```

```
 610 D3=0
 620 FOR I=2 TO N-1 STEP 1
 630 Z=2*(X(I)-X0)/S↑2
 640 D=(Q(I)-Z)↑2
 650 R=D3+D
 660 NEXT I
 670 REM----(P=ALPHA)-----
 680 P=(R)/(L-2)
 690 T0=SQR((L*P)/(S2))
 700 S1=(0.7071*T0)/(M)↑1.5
 710 REM----(S4=ERROR IN X0)------
 720 S3=SQR((P*D)/S2)
 730 S4=SQR((S3/M)↑2+(B*T0/M↑2)↑2)
 740 REM----X0=X0+S4------
 750 REM S=S+S1
 760 REM***EVALUATION OF PEAK HEIGHT***
 770 Z3=0
 780 G=0
 790 FOR I=1 TO N STEP 1
 800 V=(S4)↑2+((X(I)-X0)↑2)*((S1)↑2)/(S↑2)
 810 W(I)=1/Y(I)+(((X(I)-X0)↑2)*V)/(S↑4)
 820 W(I)=1/W(I)
 830 REM----(W=WEIGH. VALUE)----
 840 T1=((X(I)-X0)↑2)/(2*(S)↑2)
 850 H1=(W(I)*(LOG(Y(I))+T1))
 860 H2=H1/W(I)
 870 H=H2+Z3
 880 NEXT I
 890 REM----PEAK HEIGHT Y0
 900 Y0=EXP(H)
 910 PRINT#1,"PEAK HEIGHT=";Y0
 920 A=2.507*S*Y0
 930 PRINT#1,"PEAK AREA=";A
 940 FW=2.355*S
 950 PRINT#1,"FWHM=";FW
 960 FOR X=151 TO156 STEP 1
 970 T1=((X-X0)↑2)/(2*(S)↑2)
 980 T1=-T1
 990 Y1=Y0*EXP(T1)
 1000 PRINT#1,X,Y1
 1010 NEXT X
 1020 END
 1030 DATA 152,153,154,155,156
 1040 DATA 40,136,200,114,27
READY.
```

ELASTIC DIFF.X-SEC.OF IRON

RADIATION CENTRE

```
100 INPUT"PRINTER OR VDU";Z$
110 IFZ$="V"THEN VS=3:GOTO 130
120 IFZ$="P"THENVS=4
130 OPEN1,VS:CMD1
140 DIMN(300),A(100),X(100),P(300),Y(3000),Z(300),N1(50),N2(50),N3(50),L(50)
150 PRINT#1,CHR$(1)SPC(5)"ELASTIC DIFF X-SECTION OF IRON":PRINT#1
160 PRINT#1,SPC(30)"RADIATION CENTRE":PRINT#1
170 PRINT#1,CHR$(1)SPC(3)"**************************************":PRINT#1:PRINT#1
180 PRINT#1,CHR$(1)"DISTANCE=",L40,"CM."
190 PRINT#1,SPC(2)"-----------------------------------"
200 PRINT#1,SPC(2)"A"SPC(7)"Z1"SPC(8)"C"SPC(21)"P"SPC(9)"DS MB/STD"SPC(4)"ER"
210 PRINT#1,CHR$(1)"==================================="
220 READ NI
230 READ X
240 PRINT#1,"X=",X,"CM."
250 PRINT#1,"--------"
260 PRINT#1
270 FOR J1=1 TO III
280 D=0
282 H2=0
284 Y2=0
290 READ G,A,P,EP,N
300 REM----G=GEOMET. FACT.
310 FOR I=1 TO N
320 READ Y(I):NEXT
330 R=140
340 S=(.25*π)/R^2
350 M=0.21303
360 X1=X*(1.006)
370 Z1=1-EXP(-M*X1)
380 FOR I=1 TO N
390 D=D+EXP(-M*Y(I))
400 NEXTI
410 C1=D/N
420 SI=(P*2.51)/(95.5*Z1*C1*S*5.4*0.939*0.945*100)
425 FOR I=1 TO N
430 B=(EP/P)^2+(0.05/2.51)^2+(.65/9.55)^2+(4.1/10)^2+(.007/.939)^2+(.005/.945)^2
440 H=H2+((M*X1)^2*((.05/2.51)^2+(.015/(1.006*X))^2)
450 Y2=Y2+(M*Y(I))^2*((.05/2.51)^2+(.1/Y(I))^2)
455 NEXT I
460 DP=SI*SQR(B+H+Y2)
470 PRINT#1,A,
480 Z=Z1:GOSUB1130:Z1$=Z$:PRINT#1,Z1$,
490 Z=C1:GOSUB1130:C1$=Z$:PRINT#1,C1$,
500 Z=P:GOSUB1110:P$=Z$:PRINT#1,SPC(15)P$,
510 Z=SI:GOSUB1140:SI$=Z$:PRINT#1,SPC(5)SI$,
520 Z=DP:GOSUB1150:DP$=Z$:PRINT#1,DP$
530 NEXTJ1
540 PRINT#1,CHR$(1)"-------------------------------------"
550 READ N2,N3
560 FORJ=1 TON2
570 READ X
580 PRINT#1,"X=",X,"CM."
590 PRINT#1,"--------"
600 PRINT#1
610 FORJ=1 TO N3
620 SD=0
622 YA=0
624 HO=0
630 READ G,A,P,EP,N
640 FOR I=1 TO NSTEP1
650 READ Y(I):NEXT
660 R=140
670 S=(.25*π)/R^2
680 M=0.21303
690 X1=X*(1.006)
700 Z1=1-EXP(-M*X1)
710 FOR I=1 TO N STEP 1
```

```
720 SD=SD+EXP(-M*Y(I))
730 NEXT I
740 D1=SD/N
750 SI=(P*2.51)/(95.5*Z1*D1*S*5.4*0.939*0.945*100)
755 FOR I=1 TO N
760 B=(EP/P)↑2+(0.05/2.51)↑2+(.65/9.55)↑2+(4/140)↑2+(.007/.939)↑2+(.005/.945)↑2
770 H=H0+(M*X1)↑2*((.05/2.51)↑2+(.015/(1.006*X))↑2)
780 Y2=YA+(M*Y(I))↑2*((.05/2.51)↑2+(.1/Y(I))↑2)
785 NEXT I
790 DR=SI*SQR(B+H+Y2)
800 PRINT#1,A;
810 Z=Z1:GOSUB1120:Z1$=Z$:PRINT#1,Z1$;
820 Z=D1:GOSUB1130:D1$=Z$:PRINT#1,D1$;
830 Z=P:GOSUB1110:P$=Z$:PRINT#1,SPC(15)P$;
840 Z=SI:GOSUB1140:SI$=Z$:PRINT#1,SPC(5)SI$;
850 Z=DR:GOSUB1150:DR$=Z$:PRINT#1,DR$
860 NEXT J
870 FOR J=1 TO N2
880 PRINT#1,CHR$(1)"————————————————————————————————————————"
890 NEXT K
900 CLOSE1
910 END
915 REM==============================(1=2CM.)================================
920 DATA 5
930 DATA 2,1.30,3764,148,5,2,3,1.1
935 DATA .55,.27,.14
950 DATA 1.50,1344,115,5,3,15,1.5
955 DATA .7,.35,.17
960 DATA 1.70,592,90,7,5,2,5,9,2,9
965 DATA 1.45,.72,.36,.18
970 DATA 1.80,496,68,11,4,9,7,5,10,3,4,9,5,7,5,6
975 DATA 2.45,1.22,.61,.3,.15
980 DATA 1.90,380,45,12,4,9,7,5,10,1,4,7,10,35,4,85,10,3
985 DATA 2.42,1.21,.6,.3,.15
990 DATA 2,4
995 REM==============================(X=6 CM.)================================
1000 DATA 6,1.30,5618,169,10,6,9,4,6,2,3,3,4,1,1,5,7,5,8,.55,.27,.14
1020 DATA 1.50,2218,115,15,9,3,6,2,3,1,9,3,6,4,7,7,4,6,1,6,6,3,4,7,7,8,4,7
1025 DATA .8,.4,.2
1030 DATA 1.70,1445,73,21,5,2,11,05,4,8,8,5,10,8,5,8,5,9,10,9,8,2,9,5,15,4,9
1035 DATA 5,8,5,5,2,65,2,85,1,43,.71,.35,.18
1040 DATA 1.90,586,29,21,4,9,7,5,10,1,10,6,10,85,10,35,4,35,4,55,4,7,7,55
1045 DATA 4,85,10,3,4,6,10,5,4,45,10,75,2,22,1,11,.55,.27,.13
1046 REM==============================(X=8 CM.)================================
1050 DATA 8,1,30,6161,142,11,9,2,6,9,4,6,2,2,8,5,8,3,4,1,1,.55,.27,.14
1070 DATA1,50,2599,124,21,12,5,9,3,6,2,3,1,9,9,6,4,5,9,6,3,6,1,9,9,4,7,7,7
1075 DATA 10,85,1,6,1,5,4,6,6,2,9,25,.75,.37,.18
1080 DATA1,70,1942,121,24,5,8,5,2,8,10,8,5,4,8,11,05,11,3,4,6,5,7,8,05
1085 DATA 10,9,8,5,15,4,9,2,85,11,2,4,7,2,75,8,6,1,37,.68,.34,.17
1090 DATA 1,30,714,73,25,4,9,10,1,4,7,7,55,10,6,4,55,4,15,11,1,10,35,7,5
1095 DATA 4,85,10,3,4,6,10,5,4,45,10,75,4,3,11,2,22,1,11,.55,.27,.13
1100 DATA 10,85,4,35
1110 NN=1:GOTO1160
1120 NN=4:GOTO1160
1130 NN=4:GOTO1160
1140 NN=3:GOSUB1180
1150 NN=2:GOTO1160
1160 Z=INT(Z*10↑NN+.5)/10↑NN
1170 Z$=LEFT$(RIGHT$("          "+STR$(Z+.5/10↑NN*SGN(Z)),10),9)
1180 RETURN
READY.
```

SLOWING DOWN DENSITY

IRON SAMPLES

```
100 INPUT"P%RINTER OR VDU";Z$
110 IFZ$="V"THEN VS=3:GOTO 130
120 IFZ$="P"THENVS=4
130 OPEN1,VS:CMD1
140 DIM N(20),N1(20),E(20),T(20),Q(20,20),R(20),A(20),B(20),Z(20,20)
150 DIM S(20),W(20,20),TN(20),Y(20),P(20),AA(10),DT(20),SA(10),XS(10),C(20)
160 DIME$(20),T$(20),Q$(20,20),W$(20,20)
170 PRINT#1,CHR$(1)SPC(9)"SLOWING DOWN DENSITY":PRINT#1
180 PRINT#1,SPC(33)"IRON SAMPLE"
190 PRINT#1,CHR$(1)SPC(1)"————————————————————————————————————————":PRINT#1:PRINT#1
200 PRINT#1,SPC(3)"E"SPC(12)"T"SPC(27)"Q*1E6"
210 PRINT#1,CHR$(1)"-----------------------------------"
220 READ N,N1
230 S(I)=0
240 P=0
250 M=.2164
260 FORJ=1TON1:READ E(J):NEXTJ
270 FOR J=1 TON1:READ C(J):NEXT J
280 FOR I=1TO N
290 NN=4.7917E8
300 S0=14
310 PRINT#1
320 PRINT#1,"X=";I/2;"CM."
330 PRINT#1,"————————"
340 PRINT#1
350 FORJ=1TON1
360 R(J)=LOG(E0/E(J))
370 T(J)=(2464.8909*R(J))/(C(J)↑2)
380 A(J)=EXP(-(I/2)↑2)/(4*T(J)))
390 B(J)=S0/(4*π*T(J))
400 Q(J,I)=(NN/(A(J)*B(J)))/1E6
410 S(I)=S(I)+Q(J,I)
420 Z=E(J):GOSUB1290:E$(J)=Z$:PRINT#1,E$(J);
430 Z=T(J):GOSUB1300:T$(J)=Z$:PRINT#1,SPC(5)T$(J);
440 Z=Q(J,I):GOSUB1310:Q$(J,I)=Z$:PRINT#1,SPC(15)Q$(J,I)
450 NEXTJ
460 NEXT I
470 PRINT#1:PRINT#1
480 PRINT#1:PRINT#1
490 PRINT#1,CHR$(1)SPC(9)"AFTER NORMALIZATION":PRINT#1
500 PRINT#1,SPC(3)"E"SPC(12)"T"SPC(27)"Q*1E6"SPC(17)"W*1E6"
510 PRINT#1,CHR$(1)"-----------------------------------"
520 FORI=1TON:PRINT#1,"X=";I/2;"CM."
530 PRINT#1,"————————"
540 FORJ=1TON1:W(J,I)=(Q(J,I)*NN)/S(I)/1E6
550 Z=E(J):GOSUB1290:E$(J)=Z$:PRINT#1,E$(J);
560 Z=T(J):GOSUB1300:T$(J)=Z$:PRINT#1,SPC(5)T$(J);
570 Z=Q(J,I):GOSUB1310:Q$(J,I)=Z$:PRINT#1,SPC(15)Q$(J,I);
580 Z=W(J,I):GOSUB1320:W$(J,I)=Z$:PRINT#1,SPC(10)W$(J,I)
590 NEXT J
600 PRINT#1,SPC(35)"---------"
610 PRINT#1,SPC(40)"S="S(I)
620 PRINT#1,CHR$(1)"————————————————————————————————————————"
630 NEXT I
640 READ N2,N3
650 PRINT#1:PRINT#1:PRINT#1:PRINT#1
660 PRINT#1,CHR$(1)SPC(8)"TOTAL NO. OF NEUTRONS":PRINT#1
670 PRINT#1,SPC(1)"R"SPC(12)"AA*1E6"SPC(24)"TN*1E6"SPC(13)"DT"
680 PRINT#1,CHR$(1)"-----------------------------------"
690 FOR K=1 TO N2
700 READ X:EF
710 PRINT#1,"X=";X;"CM."
720 PRINT#1,"-------"
730 PRINT#1
740 FOR L=1 TO N3
750 READ X1,A,NA,XS
760 AA=(NN*E↑(-M*X1))/1E6
```

```
 770 BB=(1-EXP(-M*X))
 780 FOR I=1TO NA READ Y(I):NEXT
 790 DD=140
 800 SA=(25*π)/(DD)↑2
 810 P=0
 820 FOR I=1 TO NA
 830 J=1
 840 P=P+W(J,I)*EXP(-M*Y(I))
 850 NEXT I
 860 TN=AA+P
 870 DT=(P*1E6*SA*EF*BB*XS)/2550
 880 PRINT#1,A;
 890 Z=AA:GOSUB1330:AA$=Z$:PRINT#1,SPC(7)AA$;
 900 Z=TN:GOSUB1340:TN$=Z$:PRINT#1,SPC(20)TN$;
 910 Z=DT:GOSUB1350:DT$=Z$:PRINT#1,SPC(11)DT$
 920 NEXT L
 930 PRINT#1,CHR$(1)"──────────────────────────────────────────────"
 940 NEXT K
 950 CLOSE 1,4
 960 END
 970 REM******************(T=FERMI AGE)*******************
 980 REM ============(Q=SLOWING DOWN DENSITY)==========
 990 DATA 16,15
1000 DATA 13.9,13,12,11,10,9,8,7,6,5,4,3,2,1,.1
1010 DATA 1.167,1.206,1.306,1.4633,1.617,1.767,1.910,2.027,2.2,2.2,2.2,2.2,2.2
1020 DATA 2.3,2.3,3.5
1030 DATA 4,4
1040 REM******************(X=2CM.)*************************
1050 DATA 2,.095,2.2,25,3,380.55,1.6,1.05,.5
1060 DATA 2.8,45,3,77.23,2,1.45,.7
1070 DATA 4.7,65,3,28.27,3.4,2.4,1.1
1080 DATA 6.3,85,3,23.40,6.3,6.3,6.3
1090 REM******************(X=4CM.)***********************************
1100 DATA 4,.095,4.4,25,7,380.55,3.8,3.3,2.8,2.2,1.7,1.1,.5
1110 DATA 5.6,45,7,77.23,4.9,4.2,3.6,2.9,2.1,1.4,.7
1120 DATA 6.9,65,7,28.27,6.85,6.8,6.1,4.8,3.5,2.3,1.15
1130 DATA 6.3,85,7,23.40,6.3,6.3,6.3,6.3,6.3,6.3
1140 REM******************(X=6CM.)***************************************
1150 DATA 6,.095,6.6,25,11,380.55,6,5.5,5,4.4,3.85,3.3,2.8,2.15,1.6,1.1,.55
1160 DATA 8.4,45,11,77.23,7.8,7.2,6.5,5.8,4.9,4.2,3.6,2.85,2.1,1.5,.7
1170 DATA 6.9,65,11,28.27,6.85,6.8,6.8,6.8,6.85,6.85,6.1,4.9,3.6,2.5,1.2
1180 DATA 6.3,85,11,23.40,6.3,6.3,6.3,6.3,6.3,6.3,6.3,6.3,6.3,6.3,6.3,6.3
1190 REM******************(X=8CM.)*****************************************
1200 DATA 8,.095,8.75,25,15,380.55,8.2,7.75,7.2,6.6,6.1,5.5,5,4.4,3.8,3.3,2.7
1210 DATA 2.1,1.6,1.05,.55
1220 DATA 8.7,45,15,77.23,8.7,8.7,8.65,8.6,7.8,7.1,6.5,5.8,5,4.4,3.6,2.9,2.1
1230 DATA 1.5,.7
1240 DATA 6.9,65,15,28.27,6.85,6.8,6.8,6.8,6.85,6.85,6.85,6.85,6.85,6.85,6.1
1250 DATA 4.9,3.7,2.5,1.2
1260 DATA 6.3,85,15,23.40,6.3,6.3,6.3,6.3,6.3,6.3,6.3,6.3,6.3,6.3,6.3,6.3,6.3
1270 DATA 6.3,6.3
1280 REM=================================================================
1290 MM=2:GOTO1360
1300 MM=3:GOTO1360
1310 MM=3:GOTO1360
1320 MM=2:GOTO1360
1330 MM=2:GOTO1360
1340 MM=2:GOTO1360
1350 MM=2:GOTO1360
1360 Z=INT(Z*10↑MM+.5)/10↑MM
1370 Z$=LEFT$(RIGHT$("              "+STR$(Z+.5/10↑MM*SGN(Z)),10),9)
1380 RETURN
1390 STOP
READY.
```

REFERENCES

1. Bethe H.A., Phys. Rev. 47, (1935), 747 - 759

2. Bohr N., Nature, 137, (1936), 344 - 348

3. Lamarsh J.R., "Introduction to Nuclear Reactor Theory", Addison-Weseley publishing Co. Inc., (1966)

4. Weisskopf V.F., Physica, 22, (1956), 952 - 958

5. Weisskopf V.F., Rev. Mod. Phys., 29, (1957), 174 - 181

6. Hauser W., and Feshbach H., Phys. Rev. 87, (1952), 366 - 373

7. Fernbach S., Serber R., and Taylor T.B., Phys. Rev., 75, no. 9 , (1949), 1352 - 1355

8. Woods R.D., and Saxon D.S., Phys. Rev., 95, (1954), 577 - 578

9. Lee J.D., B.N.E.S. Report Paper No. 5.3, (1969)

10. Hunt S.E., "Fission, Fusion and the Energy Crisis", Pergamon Press, (1976)

11. Lamarsh J.R., "Introduction to Nuclear Engineering", Addison Weseley Publishing Co., (1975)

12. Yuasa K., J. of the Phys. Soc. of Japan, 13, no.11, (1958) 1248 - 1258

13. Wilmore D., and Hodgson P.E., Nucl. Phys., 55, (1964), 673 - 695

14. Bjorklund F., and Fernbach S., Phys. Rev. 109, no.4, (1958) 1295 - 1298

15. Elliot J.O., Phys. Rev., 101, no.2, (1956), 684 - 688

16. Coon J.H., Davis R.W., Felthauser H.E., and Nicodemus D.B., Phys. Rev., 111, no.1, (1958), 250 - 260

17. Havranek M., Nucl. Eng. and Design , 16, (1971), 249 - 252

18. Hacke J., Kerntechnik, 11, (1969), 193 - 196

19. Carter L.L., and Morford R.J., Trans. of the Amer. Nucl. Society, 30, (1978), 618 - 619

20. Allen F.J., and Futterer Arnold T., Nucleonics, 21, (1963), 120 - 121

21. Chilton A.B., Health Phys., 29, (1975), 813 - 814

22. Schmidt F.A.R., O.R.N.L. Report, Risc, 26, (1969)

23. Bozyap O., and Day L.R., Health Phys., 28, (1975), 101 - 109

24. Becchetti F.D., and Greenlees G.W., Phys. Rev., 182, no.4, (1969), 1190 - 1209

25. Murray R.I., "Nuclear Energy", (1977), 149, Pergamon Press Inc.

26. Technical Bulletin Societe Anonym de Machines Electrostateques, Grenoble, France, June (1961)

27. Baynham D.F., Ph.D. Thesis, (1971), The University of Aston in Birmingham

28. England J.B.A., "Techniques in Nuclear Structure Physics", Part I, (1975), 251, Macmillan Press Ltd.

29. Walt M., and Barschall H.H., Phys. Rev., 93, (1954), 1062 - 1068

30. Walt M., and Beyster J.R., Phys. Rev. 98, (1955), 677 - 684

31. Blech I.A., and Averbach B.L., Phys. Rev., 137, no.4A, (1965), A1113 - A1116

32. Coon J.H., and Davis R.W., Phys. Rev., 94, (1953), 785

33. Darden S.E., Haeberli W., and Walton R.B., Phys. Rev., 96, (1954), 836

34. Snowden S.C., and Whitehead W.D., Phys. Rev., 94, (1954), 1267 - 1272

35. O'Neill G.K., Phys. Rev., 95, no.5, (1954), 1235 - 1245

36. Dunning J.R., Pegram G.B., Fink G.A. ,Mitchell D.P., and Segre E., Phys. Rev. 48, (1935), 70 4

37. Alvarez L.W., Phys. Rev., 54, (1938), 609 - 617

38. Firk F.W.K., Nucl. Instr. and Meth., 162, (1979), 539 - 563

39. Day R.B., Phys. Rev., 89, (1953), 908

40. Day R.B., and Walt M.,Phys. Rev., 117, (1960), 1330 - 1333

41. Rethmeter J., Jonker C.C., Rodenburg M., Hovenier J.W., and Meulen D.R.V.D., Nucl. Inst. and Meth., 17, (1962), 273 - 285

42. Nielson G.C., and James D.B., The Rev. of Scint. Instr., 26, no.11, (1955), 1018 - 1024

43. Cranberg L., and Levin J.S., Phys. Rev., 100, (1955), 434 - 435

44. Bennett E.W., Okhuysen P.L., Ashe J.B., and Millet W.E., Bull. Am., Phys. Soci., Ser.II, 2, (1957), 232

45. Johnson P.B., Callaghan J.E., Bartle C.M., and Chapman N.G., Nucl. Inst. and Meth., 100, (1972), 141 - 148

46. Horstmann H., and Liskin H., EUR-3668 (1968), European Atomic Energy Community-Euratom

47. Benvensite J., and Zenger J., UCRL-4266 (1954)

48. Hanson A.O., Taschek R.F., and Williams J.H., Rev. Mod. Phys. 21, (1949), 635 - 649

49. Connell K.A., Ph.D. Thesis, (1972), The University of Aston in Birmingham

50. Brockmann H., Nucl. Scin. and Eng., 77, (1981), 377 - 414

51. Warshaw S.D., Phys. Rev., 76, no.12, (1949), 1759 - 1765

52. Reynolds H.K., Dunbar D.N.F., Wenzel W.A., and Whaling W., Phys. Rev., 92, no.3, (1953), 742 - 748

53. Gunnersen E.M., and James G., Nucl. Inst. and Meth., 8, (1960), 173 - 184

54. Granata L., and Lagonegro M., Nucl. Inst. and Meth., 70, (1969), 93 - 97

55. Benvensite J., Mitchell A.C., Schrader C.D., and Zenger J.H., Nucl. Inst. and Meth., 7, (1960), 306 - 314

56. Conner J.P., Bonner T.W., and Smith J.R., Phys. Rev., 88, no.3, (1952), 468 - 473

57. Arnold W.R., Phillips J.A., Sawyer G.A., Stovall E.J.J.R., and Tuck J.L., Phys. Rev., 93, no.3, (1954), 483 - 497.

58. Argo H.V., Taschek R.F., Agnew H.M., Hemmendinger A., and Leland W.T., Phys. Rev. 87, no.4, (1952), 612 - 618

59. Allan D.L., and Poole M.J., Proc. Roy. Soci., A204, (1951), 500 - 513

60. Liskin H., and Paulsen A., Nuclear Data Tables, 11, (1973), 569 - 619

61. Paulsen A., and Liskin H., EANDC(E), 144, (1972)

62. Moszynski M., and Bengtson B., Nucl. Inst. and Meth. , 158, (1979), 1 - 31

63. Birks J.B., "The Theory and Practice of Scintillation Counting" Pergamon Press, (1964)

64. Brooks F.D., Nucl. Inst. and Meth., 162, (1979), 477 - 505

65. Atam P. Arya, "Fundamental of Nuclear Physics", (1966), Allyn and Bacon, Inc.

66. Harvey J.A., and Hill N.W., Nucl. Inst. and Meth., 162, (1979), 507 - 529

67. Buck Warren L., and Swank Robert K., Nucleonics, 11, (1953), 48 - 52

68. Nuclear Enterprises Ltd., Catalogue 1980

69. Batchelor R., Gilboy W.B., Parker J.B., and Towle J.H., Nucl. Inst. and Meth., 13, (1961), 70 - 82

70. Swartz C.D., and Owen George E., "Fast Neutron Physics", Vol. IV, Part I, by Marion and J. Fowler, (1960), 211 - 246

71. Marion J.B., and Young F.C., "Nuclear Reaction Analysis, Graphs and Tables", North-Holand, Amesterdam and Wieley, (1968), New York

72. Knoll Glenn F., "Radiation Detection and Measurements", John Wiley & Sons, (1979)

73. Gammel J.L., "Fast Neutron Physics, Vol IV, Part II, Ed. by J.B. Marion and J.L. Fowler ,Interscience publ., (1963), 2185 - 2225

74. Kurz Richard J., UCRL, no.11339, (1964), "A 709/7090 Fortram II Program to Compute the Neutron-Detection Efficiency of Plastic Scintillator for Neutron Energies from 1 to 300 Mev"

75. Gul K., Nucl. Instr. and Meth., 176, (1980), 549 - 554

76. Fajer V., and Alvarez L., Nucl. Instr. and Meth., 184, (1981), 515 - 519

77. Toms M.E., Nucl. Instr. and Meth., 92, (1971), 61 - 70

78. Brannen E., and Olde G.L., Radiation Research, 16, (1962), 1 - 6

79. Smith D.L., Polk R.G., and Miller T.G., Nucl. Inst. and Meth., 64, (1968), 157 - 166

80. Wright G.T., Phys. Rev. 91, (1953), 1282 - 1283

81. Gooding T.J., and Pugh H.G., Nucl. Inst. and Meth., 7, (1960), 189 - 192

82. Chou C.N., Phys. Rev., 87, (1952), 904 - 905

83. Craun R.L., and Smith D.L., Nucl. Inst. and Meth., 80, (1970), 239 - 244

84. Evans H.C., and Bellamy E.H., Proc. Phys. Soci., 74, (1959), 483 - 485

85. Rich R., and Madey R., UCRL-2301, (1954), "Range Energy Tables"

86. Flynn K.F., Glendenin L.E., Steinberg E.P., and Wright P.M., Nucl. Instr. and Meth., 27, (1964), 13 - 17

87. Conner R.D., adn Husain M.K., Nucl. Instr. and Meth., 6, (1960), 337 - 342

88. Keil G., Nucl. Instr. and Meth., 89, (1970), 111 - 123

89. Hopkins J.C., Martin J.T., and Shagrave J.D., Nucl. Instr. and Meth., 56, (1967), 175 - 176

90. Glasgow D.W., Velkley D.E., Brandenberger J.D., Mcellistrem M.T., Hennecke H.J., and Breitenbecher D.V., Nucl. Instr. and Meth., 114, (1974), 521 - 534

91. Muga M.L., Burnsed D.J., Steeger W.E., and Taylor H.E., Nucl. Instru. and Meth., 83, (1970), 135 - 138

92. Muga M.L., Burnsed D.J. and Steeger W.E., Nucl. Instr. and Meth., 104, (1972), 605 - 610

93. Geissel H., Güttner K., Hoffmann S., and Münzenberg G., Nucl. Instr. and Meth., 144, (1977), 465 - 468

94. Fowler J.L. and Brolley J.E., Rev. of Mod. Phys., 28, no.2, (1956), 103 - 134

95. Okhuysen P.L., Bennett E.W., Ashe J.B., and Millet W.E., The Rev. of Scint. Instruments, 29, no.11, (1958), 982 - 984

96. Dixon W.R., and Aitken J.H., Nuclear Physics, 24, (1961), 456 - 464

97. Schuster D.G., Nucl. Instr. and Meth. , 76, (1969), 35 - 42

98. Put L.W., Coenders C. Bot. W.J ., Koene J.W. and Blok J., Physica, 32, (1966), 1397 - 1406

99. Cox A.J., and Holland D., Inter. J. of Appl. Radiation and Isotopes, 26, (1975), 776 - 780

100. Prade H., and Csikai J., Nuclear Physics, A123, (1969), 365

101. Galloway R.B., and Waheed A., Nucl. Instr. and Meth . , 128, (1975), 505 - 513

102. Bartle C.M., Chapman N.G., Johnson P.B., and Callagham J.E., Nucl. Instr. and Meth. , 63, (1968), 39 - 44

103. Tripard G.E., Monier L.F.C., White B.L. and Martin P.W., Nucl. Instr. and Meth. , 66, (1968), 261 - 269

104. Janicki M.C., and Cox A.J., Inter. J. of Appl. Radiation and Isotopes, 30, (1979), 439 - 445

105. Ryves T.B., and Sharma D., Nucl. Instr. and Meth. , 128, (1975), 455 - 459

106. Ruby L., and Crawford R.B., Nucl. Instr. and Meth . , 24, (1963), 413 - 417

107. Blair J. Morris, Freier G.,Lampi E., Sleator W.J R., and Williams J.H., Phys. Rev., 79, no.1, (1948), 1599 - 1603

108. White M., Vacuum, 15, (1965), 449 - 450

109. Arnison G.T.J., Nucl. Instr. and Meth. , 40, (1966), 359

110. Tripard G.E., and White B.L., Rev. of Scintific Instr., 38, (1967), 435 - 436

111. Bartle C.M., and Meyer H.O., Nucl. Instr. and Meth. , 112, (1973), 615

112. Bartle C.M., Nucl. Instr. and Meth. , 144, (1977), 599

113. Janicki M.C., Ph.D. Thesis, (1977), The University of Aston in Birmingham

114. Anderson H.H., and Ziegler J.F., "Hydrogen Stopping Power and Ranges in all Elements", Vol.3, (1977), Pergamon Press

115. Burcham W.E., "Nuclear Physics, An Introduction", Second Ed., (1973), Longman

116. Allenby K., Ph.D. Thesis, The University of Aston in Birmingham, (1974)

117. Allred J.C., Armstrong A.H., and Rosen L., Phys. Rev. 91, (1953), 90 - 99

118. Seagrave J.D., Phys. Rev., 97, no.3, (1955), 757 - 765

119. Kinney W.E., and Perey F.G., Nucl. Scien. and Eng., 40, (1970), 396 - 406

120. Hopkins J.C., and Silbert M.G., Nucl. Scienc. and Eng., 19, (1964), 431 - 436

121. Coon J.H., Davis R.W., Felthauser H.E., et al, from paper of Phys. Rev., 109, no.4, (1958), 1295 - 1298, by F. Bjorklund and S. Fernbach.

122. Hood G.A., and Johnson N.C., Concrete Engineers, Handbook, 1st Ed., McGraw-Hill, (1950)

123. McLains, and Martins, J.H. (Eds.), "Reactor Handbook", 2nd Ed., Vol. IV, "Engineering", Chapter 9 (Shielding), Interscience Publishers, (1964)

124. Tipton C.R. (Ed.) "Reactor Handbook", 2nd Ed., Vol I, "Materials" Chapter 51, "Shielding", Interscience Publishers, (1960) 1081.

125. Hansen L.F., Anderson J.D., Days R.J., Howerton R.J., Kometo T., Logan C.M. and Wong C., Nucl. Science and Eng., 55, (1974), 345 - 348

126. Jaeger R.G., (Ed.), "Engineering Compendium on Radiation Materials" Vol II, Springer-Verlag, Berlin, (1975)

127. Feshbach H., Porter C.E., and Weisskopf V.F., Phys. Rev., 96, (1954), 448 - 464

128. Perey F., and Buck B., Nucl. Phys., 32, (1962), 353 - 380

129. Engelbrecht C.A., and Fiedeldey H., Ann. Phys., 42, (1967), 262 - 295

130. RAROMP, (Regular And Reformulated Optical Model Programme), by Pyle, G.J.

131. Greenlees G.W., Pyle G.J., and Tang Y.C.,Phys. Rev., 171, no.4, (1968), 1115 - 1136

132. Perry F.G., Phys. Rev., 131, (1963), 745 - 763

133. Rosen L., Beery J.G., and Goldhaber A.S., et al, Ann. Phys., (N.Y.), 34, (1965), 96 - 152

134. Glasstone S., and Sesonke A., "Nuclear Reactor Engineering", International Student, Ed., (1967)

135. Geraseva L.A., and Vavilov V.V., J. of Nucl. Energy, 16, (1962), 123 - 124

136. Grimeland B., and Dönvold S., Nucl. Science, and Eng., 19, (1964), 245 - 248

137. Pyle G.J., and Greenlees G.W., Phys. Rev, 181, (1969), 1444 - 1454

138. Makra S., Palfalvi J., and Vertes P., Health Physics, 26, (1974), 29 - 39

139. Pierre Claude S.T., Machwe M.K., and Lorrain P., Phys. Rev., 115, no.4, (1959), 999 - 1003

140. Clarke R.L., and Cross W.G., Nuclear Phys., 53, (1964), 177 - 203

141. McDonald W.J., Robson J.M., and Malcolm R., Nucl. Phys., 75, (1966), 353 - 370

142. BNL 325, "Neutron Cross Sections", Vol II, Third Ed., (1976)

143. Mukoyama T., Nucl. Instr. and Meth., 125, (1975), 289 - 291

144. Al-Shalabi B., Ph.D. Thesis, (1981), The University of Aston in Birmingham